TUDelft

Delft University of Technology

Two-dimensional membranes in motion

Davidovikj, Dejan

Important note
To cite this publication, please use the final published version (if applicable).
Please check the document version above.

Two-dimensional membranes in motion

TWO-DIMENSIONAL MEMBRANES IN MOTION

Proefschrift

ter verkrijging van de graad van doctor
aan de Technische Universiteit Delft,
op gezag van de Rector Magnificus prof. dr. ir. T. H. J. J. van der Hagen,
voorzitter van het College voor Promoties,
in het openbaar te verdedigen op vrijdag 23 februari 2018 om 15:00 uur

door

Dejan DAVIDOVIKJ

Master of Science in Nanoscience and Nanotechnology,
KU Leuven, België en Chalmers Tekniska Högskola, Zweden,
geboren te Skopje, Macedonië.

Dit proefschrift is goedgekeurd door de

promotors: prof. dr. P. G. Steeneken
                  prof. dr. ir. H. S. J. van der Zant

Samenstelling promotiecommissie:

Rector Magnificus,	voorzitter
Prof. dr. P. G. Steeneken,	Technische Universiteit Delft
Prof. dr. ir. H. S. J. van der Zant,	Technische Universiteit Delft
Prof. dr. ir. A. van Keulen,	Technische Universiteit Delft
Prof. dr. K. I. Bolotin,	Freie Universität Berlin
Prof. dr. ir. M. Poot,	Technische Universität München
Prof. dr. A. Isacsson,	Chalmers University of Technology
Prof. dr. J. M. Parpia,	Cornell University

To my parents.

CONTENTS

SUMMARY

This thesis revolves around nanomechanical membranes made of suspended two - dimensional materials. Chapters 1-3 give an introduction to the field of 2D-based nanomechanical devices together with an overview of the underlying physics and the measurement tools used in subsequent chapters. The research topics that are discussed can be divided into four categories: characterisation (Chapters 4 and 5), sensors (Chapter 6), actuators (Chapters 7 and 8) and novel materials (Chapter 9). A short summary of each chapter is given below.

Chapter 1 starts with a historical overview of the fields of 2D materials and nanoelectromechanical systems (NEMS) and discusses how merging the two can lead to better NEM devices, but also how NEMS can be used to probe the properties of 2D materials.

Chapter 2 provides a theoretical framework of nanomechanics of ultra-thin circular membranes, both in the linear and nonlinear vibration regimes. It also explains the relation between the material properties of the membranes and their nonlinear dynamic response.

Chapter 3 is about the tools and methods that are used throughout the thesis. It starts with an explanation of the laser interferometry setup as a means to measure the displacement of 2D resonators and the underlying physical principles of transduction of the mechanical motion to an optical signal. This is followed by a discussion on electrostatic driving and fitting of nonlinear response curves. At the end of the chapter, a brief overview of the basic fabrication process flows is given.

Chapter 4 deals with spatial mapping of vibrational modes of suspended graphene nanodrums. By optimising the measurement setup, up to eight vibrational modes of the driven motion are detected. Higher order modes show spatial discrepancies compared to the theoretically predicted mode shapes, which is attributed to morphological imperfections in the nanodrum. This is validated by a finite-elements model, that confirms that mode shapes of higher order resonance modes are easily distorted by inhomogeneous tension distribution across the drum.

Chapter 5 aims at relating the nonlinear dynamic behaviour of 2D nanodrums to their mechanical properties, in particular, their Young's modulus. Using membrane theory, a mathematical link is provided between the Young's modulus of the material and the nonlinear spring constant of the drums. The method is strengthened by using a fitting algorithm that fits a set of measured nonlinear response curves at once, using a single fit parameter. This provides a basis for fast, high-frequency and contactless characterisation of the mechanical properties of 2D materials.

Chapter 6 explores the limitations of capacitive sensing using a single nanodrum. By optimising the chip design, the parasitic capacitances are minimised, which enables detection of capacitance changes down to 50 aF. The readout is implemented in a pressure sensing scheme, where a graphene nanodrum is used to detect pressure changes down to 25 mbar. The work is supported by a simplified model that investigates the possible routes for increasing the responsivity of tension-induced pressure sensors based on graphene.

Chapter 7 describes a novel way to tune the tension in graphene nanodrums using an on-chip heater structure. The heater serves both as a mechanical support for a graphene nanodrum and as a tool to tune its in-plane tension electrothermally, by running a current through the heater. The concept is demonstrated both in the ac regime, where the drum's motion is excited electrothermally and in the dc regime, where we demonstrate that the temperature increase of the heater not only causes an increase in the resonance frequency of up to 30%, but it also causes a decrease in dissipation (the quality factor increases up to 50%). By simultaneously controlling the heater and the gate voltage, we gain independent control of the resonance frequency and the quality factor, something that cannot be achieved using a gating-only approach.

Chapter 8 uses the process flow described in Chapter 6 to develop a new kind of graphene-based NEM device - a graphene gas pump. The pump system consists of two cavities coupled by a narrow trench sealed with a single graphene flake. It is shown that by employing a local gating scheme, attolitre quantities of gas can be controllably pumped between the cavities and this pumping of gas can be measured optically.

Chapter 9 is an excursion to the uncharted territories of nanomechanics using membranes made of ultra-thin epitaxially grown complex oxide films. Employing a recently published method for growing and releasing thin films of complex oxides, nanodrums of strontium titanate ($SrTiO_3$) and strontium ruthenate ($SrRuO_3$) are fabricated and mechanically characterised. The temperature dependence of the mechanical properties of $SrTiO_3$ shows signatures of structural phase transitions that seem to affect the resonance frequency, but more so the mechanical dissipation of the structures. An explanation for this behaviour is proposed, based on the polarity and configuration of domains and domain walls in the $SrTiO_3$ membranes.

Chapter 10 sublimates the entire research presented in this thesis and provides a critical overview of the work and its implications in the field of 2D-based nanomechanics.

SAMENVATTING

Dit proefschrift draait om nanomechanische membranen gemaakt van vrijhangende twee-dimensionale materialen. Hoofdstukken 1-3 geven een introductie in het gebied van 2D-gebaseerde nanomechanische apparaten samen met een overzicht van de onderliggende fysica en de meetinstrumenten die in de volgende hoofdstukken worden gebruikt. De onderzoeksonderwerpen die worden besproken, kunnen worden onderverdeeld in vier categorieën: karakterisering (Hoofdstuk 4 en 5), sensoren (Hoofdstuk 6), actuatoren (Hoofdstukken 7 en 8) en nieuwe materialen (Hoofdstuk 9). Hieronder volgt een korte samenvatting van elk hoofdstuk.

Hoofdstuk 1 begint met een historisch overzicht van 2D-materialen en nano - elektromechanische systemen (NEMS) en bespreekt hoe het samenvoegen van de twee kan leiden tot betere NEM-apparaten, maar ook hoe NEMS kunnen worden gebruikt om de eigenschappen van 2D-materialen te onderzoeken.

Hoofdstuk 2 biedt een theoretisch raamwerk van nanomechanica van ultradunne cirkelvormige membranen, zowel in de lineaire als niet-lineaire trillingsregimes. Het verklaart ook de relatie tussen de materiaaleigenschappen van de membranen en hun niet-lineaire dynamische respons.

Hoofdstuk 3 gaat over de hulpmiddelen en methoden die in de thesis worden gebruikt. Het begint met een uitleg van de laserinterferometrie-opstelling die wordt gebruikt om de verplaatsing van 2D-resonatoren te meten, en een uitleg van de onderliggende fysische principes van transductie van de mechanische beweging naar een optisch signaal. Dit wordt gevolgd door een discussie over elektrostatische actuatie en het fitten van niet-lineaire responscurves. Aan het einde van het hoofdstuk wordt een kort overzicht gegeven van het fabricatieproces.

Hoofdstuk 4 behandelt het in kaart brengen van vibrationele modi van vrijhangende grafeen-nanodrums. Door de meetopstelling te optimaliseren, kunnen tot acht vibrationele modi van de aangedreven beweging gedetecteerd worden. Hogere orde modi vertonen ruimtelijke verschillen ten opzichte van de theoretisch voorspelde modusvormen, die worden toegeschreven aan morfologische imperfecties van de nanodrum. Dit wordt gevalideerd door een model gebruikmakend van de eindige-elementenmethode, dat bevestigt dat modusvormen van hogere orde resonantiemodi gemakkelijk worden vervormd door inhomogene spanningsverdeling over de drum.

Hoofdstuk 5 heeft als doel het niet-lineaire dynamische gedrag van 2D-nanodrums te relateren aan hun mechanische eigenschappen, in het bijzonder hun Young's modulus. Met behulp van de membraantheorie wordt een wiskundige relatie gevonden tussen de elasticiteitsmodulus en de niet-lineaire veerconstante van de drums. De methode wordt verbeterd door een algoritme te gebruiken dat een reeks gemeten niet-lineaire respons curves tegelijk kan fitten met behulp van een enkele fit-parameter. Dit biedt een basis voor snelle, hoogfrequente en contactloze karakterisering van de mechanische eigenschappen van 2D-materialen.

Hoofdstuk 6 onderzoekt de beperkingen van capacitieve detectie met behulp van een enkele nanodrum. Door het ontwerp van de chip te optimaliseren, worden de parasitaire capaciteiten tot een minimum beperkt, wat detectie van capacitieve veranderingen tot 50 aF mogelijk maakt. De uitlezing is geïmplementeerd in een drukmeetschema, waarbij een grafeen-nanodrum wordt gebruikt om drukveranderingen tot 25 mbar te detecteren. Het werk wordt ondersteund door een vereenvoudigd model dat de mogelijke routes onderzoekt voor het vergroten van de responsiviteit van spanningsgeïnduceerde druksensoren op basis van grafeen.

Hoofdstuk 7 beschrijft een nieuwe manier om de spanning in grafeen-nanodrums te regelen met behulp van een on-chip verwarmingsstructuur. De verwarmer dient zowel als mechanische ondersteuning voor de grafeen-nanodrum en als een hulpmiddel om zijn spanning in het vlak elektrothermisch te regelen door een stroom door de verwarmer te sturen. Het concept wordt in het AC-regime gedemonstreerd, waarbij de beweging van de durm elektrothermisch wordt geëxciteerd, en in het DC regime, waarbij we aantonen dat de temperatuurverhoging van de verwarmer niet alleen een toename van de resonantiefrequentie van maximaal 30 % veroorzaakt, maar ook een afname in dissipatie (de kwaliteitsfactor neemt toe tot 50 %). Door gelijktijdig de verwarming en de gate-spanning te regelen, verkrijgen we onafhankelijke controle over de resonantiefrequentie en de kwaliteitsfactor, iets dat niet kan worden bereikt met behulp van een gating-only benadering.

Hoofdstuk 8 gebruikt het fabricatieproces beschreven in Hoofdstuk 6 om een nieuw soort op grafeen gebaseerd NEM-apparaat te ontwikkelen - een grafeen gaspomp. Het pompsysteem bestaat uit twee holten gekoppeld door een smalle sleuf die is afgedicht met een enkele laag grafeen. Aangetoond wordt dat, door toepassing van een lokaal gating-schema, controleerbare hoeveelheden gas tussen de holten gepompt kan worden, en dat het pompen van het gas optisch kan worden gemeten.

Hoofdstuk 9 is een excursie naar de niet in kaart gebrachte territoria van nanomechanica met behulp van membranen gemaakt van ultradunne epitaxiaal gegroeide films van complexe oxiden. Gebruikmakend van een recent gepubliceerde methode voor het groeien en scheiden van dunne films van complexe oxiden van hun substraat zijn nanodrums van strontiumtitanaat ($SrTiO_3$) en strontium ruthenaat ($SrRuO_3$) gefabriceerd en mechanisch gekarakteriseerd. De temperatuurafhankelijkheid van de mechanische eigenschappen van $SrTiO_3$ toont kenmerken van structurele faseovergangen die de resonantiefrequentie en mechanische dissipatie van de structuren lijken te beïnvloeden. Een verklaring voor dit gedrag wordt voorgesteld, gebaseerd op de polariteit en de configuratie van de domeinen en de domeinmuren in de $SrTiO_3$ membranen.

Hoofdstuk 10 sublimeert het volledige onderzoek gepresenteerd in dit proefschrift en biedt een kritisch overzicht van het werk en de implicaties ervan op het gebied van 2D-gebaseerde nanomechanica.

README.txt

It would not be a piece of 21st century literature without the essential README.txt file, a sort of a preface with the sound of the future echoing from the *.txt* extension. This is usually the place where the authors (of a piece of software, a game, a script) try to wear the shoes of the users (in this case, readers) and provide them with a manual on how to use and treat their oeuvre, be it a piece of software, a script or, in this case, a book.

First, a few words about the title. A subject of passionate discussion between me, my promotors, my friends and colleagues, this was what this book ended up with. The godfather of the book, whom I will thank for this and many other deeds at the end of the thesis, dottore Giordano Mattoni, knowing my aversion towards the serious and sterile, came up with the suggestion of a title that is correct, yet not too scientific and just a bit playful. This was assuming that in the sea of PhD theses on nanomechanics with two-dimensional materials, this one would stand out: not only by its content, but also by its title. Please do not get me wrong, dear reader, in this "sea" of theses that I mentioned, there are absolutely marvellous pieces of work [1–4] (and many others). The authors of these works simply depleted the pool of available titles.

If you are reading this it means that you either: (i) had to read this book (a big cheers to the committee members here); (ii) you are a friend or a member of my family; (iii) somebody recommended it; or (iv) the title actually worked. I take a bit of pride in all four cases, personally. I have to have done a decent job so that eight people, world renowned scientists, do me a favour by taking the responsibility to read and grade my work. If you belong to the second category, I extend my greatest respect back. Even if it was just the catchy title, it feels nice to successfully "lure" people into reading your work. This also poses a great burden, for one now feels obliged to meet and exceed the expectations of the reader, who took time to open this book. That said, I will try to do my best [1].

Dejan Davidovikj
Delft, January 2018

---

[1] Disclaimer: No matter how hard I try, whatever I write to explain the basic concepts underlying this thesis will be of worse quality than a, say, Wikipedia article. This is nowadays experts from all around the world can work together, elaborate on subjects from many different perspectives. This modern era is devoid of intellectual property–knowledge is globalised and merits are shared, resulting in literature of finest quality. Although I promised to do my best at sublimating the basics, I strongly encourage the reader to use other sources, some of which are referenced in this thesis, to fill in the gaps, or, potentially, correct my mistakes. In a hundred years from now, most of the things written here will be either obsolete or maybe even wrong. This is exactly what makes science beautiful.
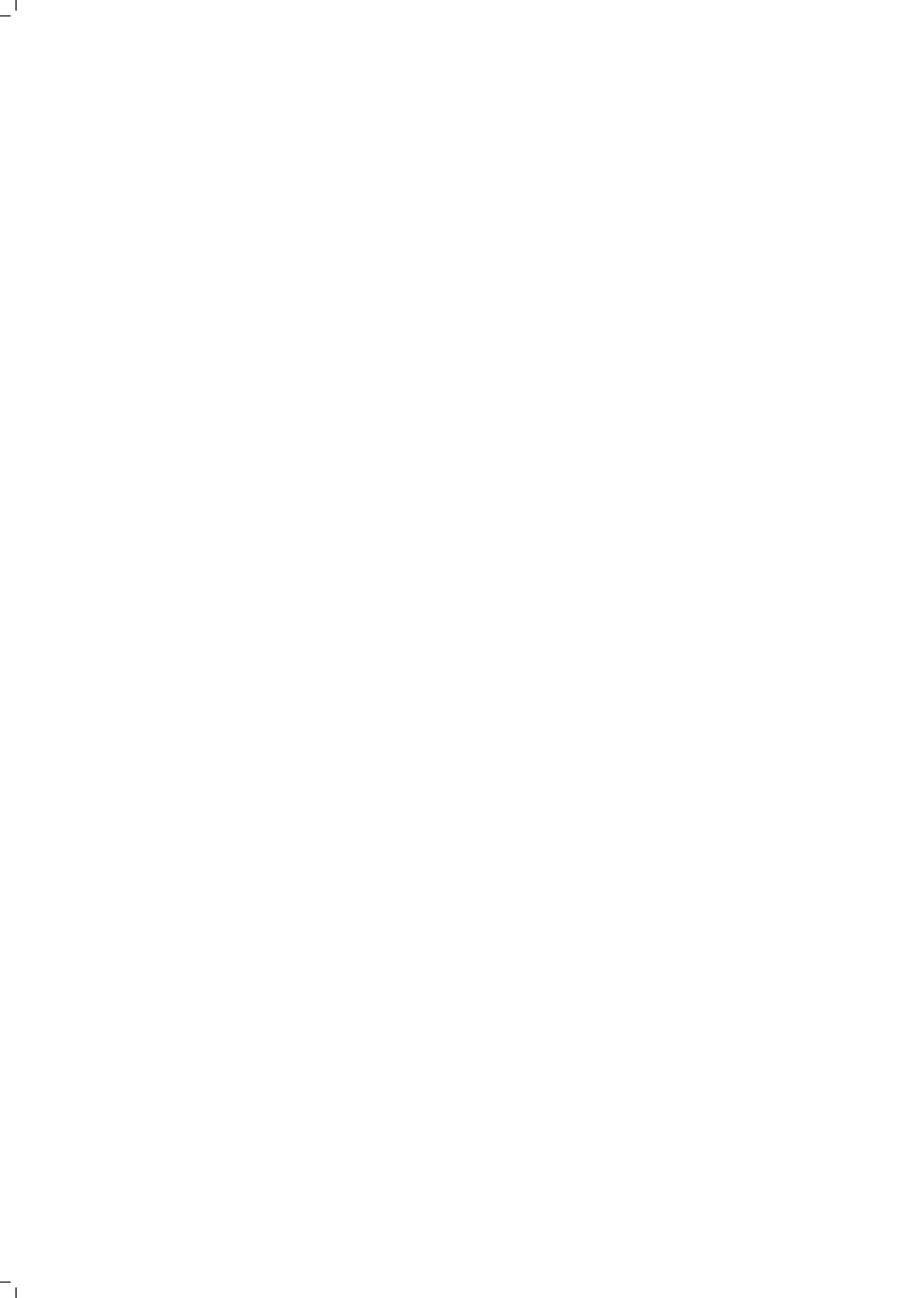
1

INTRODUCTION

In this chapter we will introduce the fields of two-dimensional (2D) materials and nano-electromechanical systems (NEMS), as well as elaborate on the synergy between the two.

1

1.1. TWO-DIMENSIONAL MATERIALS

MATERIALS are the building blocks of nature. Ultimately, these building blocks determine the durability and functionality of a device, machine or any kind of system created by nature or engineered by humans. When a new material is discovered, it triggers an avalanche of ideas and suggestions on how its special properties can provide new functionalities, how they can be used to construct new devices, how it can unveil novel physics. So was the case with graphene. The first experimental evidence of isolation and characterisation of atomically-thin carbon films [5] has more than 30 thousand citations to date. The term "graphene" has more than 1.1 million hits on Google Scholar. In the following section we will try to explain why this is the case.

1.1.1. GRAPHENE

On the macro-scale, from the standpoint of structural mechanics, it is rather obvious to conclude that the geometrical ordering of the building blocks has a strong influence on the mechanical properties of the final structure. Take a house of cards for example. Its building blocks are so thin, so easily deformable that it is even hard to believe when you see that you can keep building on and on and the cards on the bottom are able to sustain the weight of all the layers on top. By carefully choosing the angles between the cards, the distances between them, and the number of repetitions required for one layer to support the next, a deck of cards can be transformed into a beautiful periodic structure with a new functionality, using fewer building blocks than would otherwise be required to reach the same height.
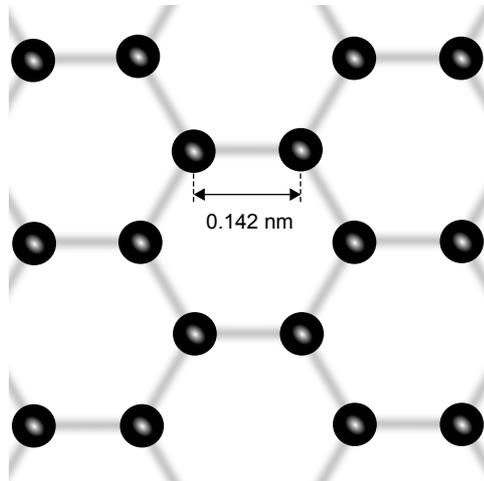
Figure 1.1: **A top view of the lattice of graphene.** The grey lines represent the bonds between the atoms.

It is somehow fascinating to think that these same rules apply at the nanoscale. We are used to thinking that the properties of matter are ultimately determined by the properties of its building blocks, be it atoms or molecules, but this is not fully true. The same chemical element can exist in more than one form, a property referred to as allotropy.

1

For example, both graphite and diamond are made entirely out of carbon. The difference is the microscopic ordering of the constituent atoms[1]. It is the shape of the crystalline lattice that makes graphite an excellent conductor, and, on the other hand, makes diamond an excellent insulator.

Graphene is an allotrope of carbon, just like diamond and graphite. As a matter of fact, graphite is just many layers of graphene stacked on top of each other. Graphene consists of a single layer of carbon atoms perfectly ordered in what resembles the structure of a beehive. This type of ordering is therefore referred to as a *honeycomb* or a *hexagonal* lattice. Again, what makes the structure stable are the carefully chosen distances and angles between the carbon atoms, much like the house of cards discussed above.

PROPERTIES OF GRAPHENE

To understand the origin of the peculiar properties of graphene, it is necessary to look at the way the atoms in the lattice form bonds. In its free form, carbon has an electron configuration $1s^2 2s^2 2p^2$, meaning that the 1s and 2s orbitals are completely filled and the two other electrons sit in two of the three 2p orbitals ($2p_x$, $2p_y$, $2p_z$). However, carbon is considered to have a valence of four. This is because an electron from the 2s orbital can be easily excited to the unoccupied 2p orbital, resulting in a $1s^2 2s^1 2p^3$ configuration[2]. In graphene, the 2s, $2p_x$ and $2p_y$ orbitals mix to form three identical sp^2 hybridised orbitals, which form a radially symmetric planar configuration, allowing each carbon atom to bond with three neighbouring atoms in a hexagonal crystal structure. Each pair of carbon atoms are 1.42 Å = 0.142 nm apart (see Figure 1.1) and form strong so-called σ bonds. These strong planar bonds give the material its exceptional strength and remarkable mechanical properties, which will be discussed in the section below. The remaining single electrons in the $2p_z$ orbitals of each carbon atom are delocalised and make up the π band of graphene - a "cloud" of electrons that enables graphene to conduct electricity with exceptional ease. The thickness of graphene is actually defined by the effective thickness of this π band - a single layer of graphene is considered to be 335 pm thick. The stacking of graphene sheets (what ultimately comprises graphite) is mediated by weak van der Waals interactions between the layers[3]. This is, naturally, a generalized picture that conceptually explains the structure of graphene and its influence on the main properties it exhibits. There are many exotic phenomena that have been predicted and/or observed in graphene, which are outside of the scope of this thesis.

A brief overview of the most remarkable properties of graphene is given below:

- **Band structure:** Graphene is a zero-gap semimetal with a linear energy dispersion. As a consequence, the charge carriers in graphene behave as massless Dirac fermions [6];

- **Carrier mobility:** Higher than 140 000 $cm^2 V^{-1} s^{-1}$ at room temperature (when encapsulated with boron nitride) [7];

---

[1]And, of course, the price.

[2]This state of carbon is energetically favourable for forming bonds, since the energy released by forming two additional bonds compensates for the energy required to excite one electron into the 2p orbital.

[3]This is why these materials are also called *van-der-Waals* or *layered* materials.

1

- **Optical properties:** Graphene is transparent, absorbing only 2.3 % of light per layer independent on the wavelength (in the visible spectrum) [8];

- **Thermostability:** Graphene has a melting point higher than 4000 K [9];

- **Thermal conductivity:** Higher than $1800\,\mathrm{Wm^{-1}K^{-1}}$ [10] and geometry-dependent [11].

  This exceptional combination of traits makes graphene attractive not only as an ultra-thin conductor, but also for applications in Hall sensors [12], as a heat sink in electronic devices [13], field-effect devices [14], and in cheap and disposable healthcare devices [15].

MECHANICAL PROPERTIES OF GRAPHENE

This thesis revolves around freely suspended membranes, hence we are mostly interested in the mechanical properties of graphene. With a Young's modulus of 1 TPa [16, 17] and an intrinsic tensile strength of 130 GPa [17], it is considered to be the strongest material ever tested. It is stable in atmospheric conditions and it can even heal itself when exposed to molecules containing carbon [18]. A unique aspect of graphene is that, despite its atomic thickness, the electrons forming the in-plane bonds are so tightly packed that a single layer of graphene is impermeable to gases [19]. In addition, it has been demonstrated that nanometre pores of controllable size can be introduced in graphene [20] which enable molecular sieving of gases through atomically thin graphene membranes [21].

1.1.2. OTHER 2D MATERIALS

Graphene's solitude at the throne came to an end soon after its discovery, when a whole new zoo of ultra-thin materials with a similar structure were discovered and isolated. These were all layered materials that also exhibit very strong in-plane bonds and can be easily mechanically exfoliated and thinned down, due to the weak van der Waals forces holding the layers together. The first materials to join graphene [22] were niobium diselenide ($NbSe_2$), a superconductor, molybdenum disulfide (MoS_2), a direct band-gap semiconductor and hexagonal boron nitride (h-BN), an exceptionally good insulator. An interesting addition to the family was black phosphorous (b-P), isolated a few years later [23, 24], which is an anisotropic semiconductor.

An overview of the mechanical properties of some of these materials is given in Table 1.1, together with the values for graphene given above.

1.2. NANOELECTROMECHANICAL SYSTEMS (NEMS)

Microelectromechanical systems (MEMS) encompass all microscopic devices with dimensions ranging from $1-100\,\mu$m that consist of moving mechanical parts and are capable of transducing an electrical signal to a mechanical motion (microactuators) or vice versa (microsensors) [29]. Their size, low operational power, negligible weight and the ability to produce many devices at once (batch fabrication) drastically lowers the cost per unit, which makes them incredibly attractive and drives the need for their further miniaturisation. MEMS are omnipresent in modern technology. Nowadays, smart mobile phones have at least a few integrated MEMS devices. For example, the microphone

Material	Young's modulus (E)	Tensile strength	N_2 permeability
graphene	430 - 1100 GPa [25]	130 GPa [17]	$<10^{-26}$ mol s^{-1}Pa^{-1} [19]
MoS$_2$	150-430 GPa [25]	16 - 30 GPa [25]	not measured
h-BN	334 GPa [26] - 865 GPa [27]	70.5 ± 5.5 GPa [27]	not measured
b-P	58.6 ± 11 GPa ($\parallel$) [28]	4.8 ± 1.4 GPa ($\parallel$) [28]	not measured
	27.2 ± 4.1 GPa ($\perp$) [28]	2.3 ± 0.7 GPa ($\perp$) [28]	

Table 1.1: **Mechanical properties of some of the most prominent 2D materials.**

is a micromembrane, typically with sizes down to 500 μm, which is used to transduce sound into an electrical signal. The accelerometer is a MEMS device, usually consisting of a microplate suspended by a tiny spring. When it experiences acceleration, the microplate is displaced and this displacement is read out electrically. This is the component responsible for the contents of the screen on the phone always being displayed upright. The state-of-the-art mobile phones are also equipped with pressure sensors - micromembranes hermetically sealing a cavity which is at a constant pressure. When the pressure on the outside changes, the membrane deflects due to the pressure difference and the amount by which it deflects can be directly related to the pressure outside.

Nanoelectromechanical systems (NEMS) are the younger and smaller, nano sibling of MEMS [30, 31]. A system is considered to be a NEMS when it is smaller than 100 nm in at least one dimension. Due to their sub-nanometre thickness, two-dimensional membranes belong to the category of NEMS. The even smaller size of NEMS is advantageous not only due to the lower cost (even more devices can be produced in a single step), but also due to the potential improvement of the sensitivity in force, mass, pressure and charge sensing devices [1, 31, 32].

1.3. TWO-DIMENSIONAL NANOELECTROMECHANICAL SYSTEMS

The field of graphene- and 2D materials-based NEMS really took off with the work by Bunch *et al.* [33], where the authors describe the fabrication of single-layer graphene mechanical resonators. This work was the first demonstration of a working graphene NEMS, a result which was quickly reproduced using other 2D materials [34–38]. In parallel, the first demonstrations of pressure [32, 39] and gas [21, 40] sensors, as well as novel concepts for mass sensing using graphene [41, 42] were reported. The exploration of graphene as a nanomechanical device was not limited to sensor applications, but it also extended to NEMS RF oscillators [43, 44] and electromechanical switches [45]. Interestingly, although graphene is impermeable, membranes of oxidised graphene (GO) have been shown to hold great promise for water filtration [46].

1

Despite the immense potential, one question still remains: can 2D materials be readily produced and commercialised [47]? To this end, a lot of effort has been put in growing graphene by means of chemical vapour deposition (CVD) [48]. Many works have focused on improving the quality of CVD graphene and developing better transfer techniques to successfully integrate it in NEMS devices [49–57]. Currently employed transfer techniques, however, allow for little processing after the transfer of the 2D material, which poses a lot of limitations on device design. Furthermore, for commercialisation of 2D NEMS, a lot of work needs to be done to improve the uniformity and reliability of the suspended membranes. There is currently no way to systematically transfer 2D materials, ensuring a homogeneous tension, little to no morphological imperfections and maximum yield.

In the section below we will give a brief overview of the synergy between 2D materials and NEMS, or, in other words, why graphene and 2D materials are important for NEMS devices, but also how NEMS devices can be used to learn something new about 2D materials.

1.3.1. OPPORTUNITIES FOR NEMS

The strong potential of 2D materials as NEMS devices stems from their remarkable mechanical properties, most attractive of which are their low mass, impermeability to gases, their high flexibility, high tensile strength, and the ability to tailor their permeability to gases. In Table 1.2 we summarise how the most important mechanical properties that make graphene (and other 2D materials) stand out can influence the performance of NEM sensors.

	pressure sensors	gas sensors	mass sensors	microphones	inertial sensors
low mass	△	△	△	△	▽
impermeability	△	∘	∘	∘	∘
flexibility	△	△	∘	△	∘
tensile strength	△	∘	∘	△	∘
controllable porosity	∘	△	∘	∘	∘

Table 1.2: **A summary of the properties of graphene and their potential for improving the performance of MEMS/NEMS sensors with respect to conventional sensors.** △ - improves performance, ▽ - degrades performance, ∘ - not relevant.

Owing to their atomic thickness, 2D materials have a very high surface-to-mass ratio. Their low mass can significantly improve the sensitivity of pressure, gas and mass sensors, as well as microphones (practically, high-frequency pressure sensors). Nevertheless, this property makes them a poor candidate for inertial sensors, where higher mass results in larger forces and therefore higher sensitivities. Tension-induced pressure sensors require a cavity that is completely sealed by the membrane, which is why the impermeability of graphene is of great importance [19, 39]. However, even though graphene itself has been shown to be impermeable [19], leakage of gas is readily observed in graphene-sealed cavities [19, 40, 58]. The exact origin of the leakage is still a subject of debate, but the generally accepted explanations are that this occurs either through the underlying silicon oxide [19] or through the graphene-substrate interface [40]. It is important to mention that pores of controllable size can be readily introduced in graphene, making it selectively permeable to gases [20, 21, 59], which gives it a great advantage as a gas-selective barrier in NEMS gas sensors once the leakage problem is solved. For pressure sensing applications, however, the need for a hermetically sealed cavity can be eliminated by employing a squeeze-film pressure sensing concept, as demonstrated in Ref. [32].

The high flexibility and high tensile strength of 2D materials enable large deflections (or vibrational amplitudes) at smaller forces without breaking, which is beneficial for sensing applications, because high amplitudes usually result in higher signal-to-noise ratios. For the same reason, however, the high flexibility poses a limit on the electrostatic force that can be applied to the membranes before pull-in [60] and can deteriorate the dynamic range of graphene- and 2D materials-based NEMS.

The high tensile strength and low mass of 2D materials make them attractive as high-speed NEMS actuators, for example, in micro-loudspeakers [61]. Although it is well known that the dynamic performance of 2D-based NEMS is drastically impaired in the presence of gas [19, 32], little has been explored in the quasi-static limit of such devices for their use as actuators to displace fluids. This is, to a large extent, the inspiration behind the device concept shown in Chapter 8, where we demonstrate pumping of gases using pneumatically coupled cavities sealed with graphene.

One of the issues that still needs to be resolved is the readout of 2D resonators. The two main readout mechanisms [4] currently employed are: (i) optical readout, using a laser interferometer setup (similar to the one described in Chapter 3.1) [32–34], or (ii) electrical readout, using either a transconductance [43, 62], piezoresistivity-based [39, 63, 64] or capacitive readout [2, 65]. It is clear that the (bulky and expensive) optical readout cannot be integrated in the devices, so its use is limited to characterisation of 2D nanodrums or proof-of-concept studies on sensing mechanisms. The electrical readout schemes, on the other hand, rely either on the change in the conductance of the membrane as a function of deflection (making them prone to variations in gas composition, humidity, light intensity, temperature and material properties), or on the change in capacitance between the drum and a bottom electrode [2, 65], which currently relies on a process flow with subsequent etching steps after the transfer of the flake. Nevertheless, for their application as tension-induced pressure sensors as well as for studying gas permeation through 2D materials, it is highly preferable to have an electrical readout

---

[4]that work at room temperature

1

scheme that allows for a process flow that does not require underetching of the cavity after the transfer of the 2D flake, i.e., the 2D material is transferred last and can be used to seal the cavity. Moreover, since the dynamic performance of 2D resonators greatly deteriorates at room temperature and atmospheric pressure [32–34], it would be beneficial that the readout circuitry is capable of detecting the static deflection of the membrane, similar to the way that conventional MEMS pressure sensors operate. This requires a complete redesign of the devices, a topic discussed in Chapter 6.

1.3.2. OPPORTUNITIES FOR 2D MATERIALS

The relationship between 2D materials and NEMS is not one-sided. The well established technology and the solid theory basis on nanomechanical systems make them an excellent platform for studying the properties of two-dimensional materials. Some examples include extracting the mechanical properties of suspended graphene drums [17, 66–68], extracting the thermal properties of 2D materials [69–74] and studying their mechanical dissipation [67, 75–77]. Nevertheless, there are still many open questions. The relation between the observed dynamic nonlinearities [33, 34] and the material properties of the resonator has not been fully explored. Moreover, the nature of mechanical dissipation in 2D resonators and its drastic decrease at low temperatures is still poorly understood [25, 43, 71]. We touch upon these topics in Chapters 5 and 7.

In Table 1.1 we showed that the mechanical properties of some 2D materials are similar in terms of tensile strength and elasticity. For the purpose of constructing mechanical devices, the choice of the 2D material makes little difference. However, some 2D materials also exhibit some more exotic properties that, in combination with their mechanical superiority can lead to hybrid nanoelectromechanical systems with added functionality. A few examples include: (i) piezoelectricity of MoS_2 [78, 79] and h-BN [80] for self-transducing [5] mechanical resonators; (ii) strain-induced bandgap tuning of transition metal dichalcogenites (TMDCs) [81, 82] for suspended tunable photodetectors or (iii) functionalisation of 2D materials [83] for selective gas and mass sensors. In this thesis, the main focus will be on graphene, the most ubiquitous of all 2D materials. Two exceptions are Chapter 5, which includes characterisation of nanodrums made of MoS_2 and in the final chapter, Chapter 9, where we fabricate and characterise nanomechanical resonators out of complex oxides, materials that exhibit a plethora of electronic and structural properties, including 2D superconductivity [84], ferroelectric/magnetic orders [85] and negative capacitance [86].

1.4. THIS THESIS

The thesis is divided into four parts. The first part revolves around mechanical characterization of the 2D membranes through their dynamic response. This includes Chapters 4 and 5. In the second part (Chapter 6) we talk about on-chip electrical readout of suspended graphene membranes and their potential as NEMS pressure sensors. The

---

[5]What is meant by "self-transducing" is that the dynamic displacement of the resonator will produce a voltage at the edges that can be read out, eliminating the need for an active external readout circuitry.

third part is about actuators: in Chapter 7 we talk about new ways of actuating graphene NEMS and in Chapter 8 we propose a new graphene-based pneumatic actuator - a gas pump. The final part consists of Chapter 9 which looks into a novel class of ultra-thin materials - membranes made of complex oxides.

1

2

NANOMECHANICS

In this chapter we talk about the physics of motion at the nanoscale. First we start by describing our ultra-thin membranes in the framework of linear harmonic oscillators. We then take a step forward and derive an expression to relate the nonlinear dynamic response of 2D resonators to an important material property: their Young's modulus.

A NY system with inertia (or finite mass) that, when displaced from its equilibrium position, experiences a restoring force F proportional to its displacement x can be modelled as a harmonic oscillator. The same goes for the vibrations of ultra-thin two-dimensional membranes studied in this thesis. In the electronics community, the word *oscillator* is reserved for systems with positive feedback, i.e., when the driving force applied to the system is proportional to either its position or to its velocity. When this is not the case, as in the measurements presented in this thesis, the system is usually referred to as a *resonator*. In this the physics community, however, the word harmonic oscillator is used for a resonator and in this thesis these words are going to be used interchangeably.

2.1. TWO-DIMENSIONAL MEMBRANES AS LINEAR HARMONIC OS-CILLATORS

We consider the motion of a driven damped linear harmonic oscillator in one dimension, x, being the axis perpendicular to the plane of the membrane, as we are mostly interested in the out-of-plane displacement of the membrane. Assuming small vibrational amplitudes ($x<h$, h being the thickness of the membrane), the restoring force that the membrane experiences after being deflected by x is:

$$F = -k_1 x, \tag{2.1}$$

where k_1 is the linear spring constant of the system. The explicit meaning of "linear" will become clearer in Chapter 2.2. The system is also characterised by its mass m and a damping factor b. The equation of motion when the system is subjected to a periodic excitation force ($f = F\cos(\omega t)$) is then given by [87]:

$$m\ddot{x} + b\dot{x} + k_1 x = F\cos(\omega t), \tag{2.2}$$

where ω is the angular frequency of the excitation force[1]. By taking the natural frequency of the system to be $\omega_0 = \sqrt{\frac{k_1}{m}}$, Equation (2.2) can be rewritten as:

$$m\ddot{x} + \frac{\omega_0 m}{Q}\dot{x} + \omega_0^2 m x = F\cos(\omega t), \tag{2.3}$$

where $Q = \frac{\omega_0 m}{b}$ is a dimensionless quantity called a quality factor (or Q-factor) of the oscillator, and it practically represents the ratio between the energy stored and the energy dissipated per vibrational cycle.

At any actuation frequency ω, the steady-state motion of the system is described by $x(t) = |X_\omega|\cos\omega t$. X_ω is the complex amplitude of the oscillator, and it can be calculated from the steady-state solution of Equation (2.3):

$$X_\omega = \frac{F/m}{\omega_0^2 - \omega^2 + i\frac{\omega_0 \omega}{Q}} \tag{2.4}$$

---

[1]Throughout this thesis the words *excitation, actuation* and *driving* shall be used interchangeably.

The oscillation amplitude and phase with respect to the actuation force are then given by:

$$|X_\omega| = \frac{F/m}{\sqrt{\left(\omega_0^2 - \omega^2\right)^2 + \left(\frac{\omega_0\omega}{Q}\right)^2}}, \tag{2.5a}$$

$$\phi_\omega = -\arctan\left(\frac{\omega_0\omega}{Q(\omega_0^2 - \omega^2)}\right), \tag{2.5b}$$

which are plotted in Figure 2.1 as a function of the damping, i.e. Q-factor. A higher Q-factor means that less energy is dissipated relative to the energy stored in the oscillator, hence the amplitude at resonance increases with increasing quality factor. At resonance, the amplitude and phase of the oscillations are given by:

$$|X_{\omega=\omega_0}| = \frac{FQ}{\omega_0^2 m}, \tag{2.6a}$$

$$\phi_{\omega=\omega_0} = -\frac{\pi}{2} \tag{2.6b}$$
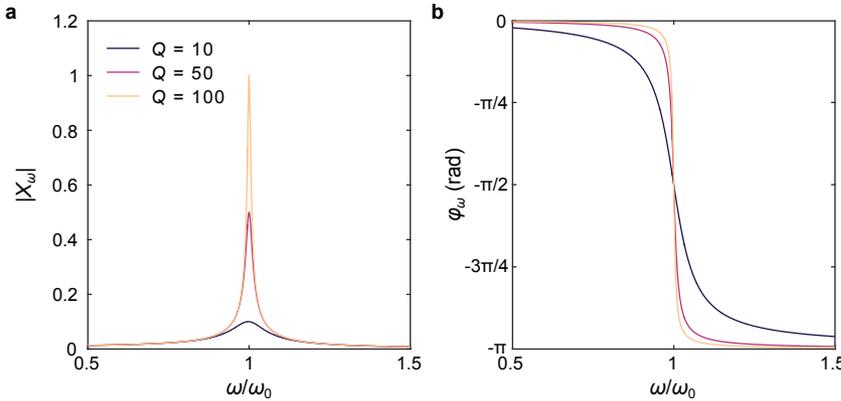
Figure 2.1: **Modelled frequency response of a driven damped harmonic oscillator. a**, Normalized oscillation amplitude $|X_\omega|$ and **b**, phase ϕ_ω of an oscillator with a varying quality factor.

In a homodyne detection scheme (see Chapter 3.1) both the real and the imaginary part of the complex amplitude can be measured and converted to amplitude and phase. For basic characterisation, we are usually interested in the resonance frequency of the resonator:

$$f_0 = \frac{\omega_0}{2\pi} = \frac{1}{2\pi}\sqrt{\frac{k_1}{m}}, \tag{2.7}$$

and its quality factor Q. These two parameters can both be extracted by fitting the measured frequency response curves using Equations (2.5a) and (2.5b).

2.2. NONLINEAR DYNAMICS OF TWO-DIMENSIONAL MEMBRANES

It is rather neat when the system under consideration is linear, i.e., an ideal spring with a spring constant k_1, which obeys Hooke's law: $F = -k_1 x$. In reality, springs are not ideal. When a spring is significantly deformed, assuming $F(-x) = -F(x)$, the spring constant itself starts to increase and becomes a function of the deflection:

$$k = k_1 + k_3 x^2 + k_{2n+1} x^{2n}, n > 1. \tag{2.8}$$

The higher-order terms of Equation (2.8) ($n > 1$) are outside of the scope of this thesis, and we will focus only on k_3, which will be referred to as the *nonlinear* spring constant. The nonlinear spring constant contains information on the added tension as a function of the deflection of the system from equilibrium, which depends on the material that the spring is made of, its geometry and the geometrical shape of the deflection (for 2D and 3D systems)[2].

The spring-mass system of interest in this thesis is an ultra-thin circular membrane resonator made of a two-dimensional material. In the dynamic case, due to the nonlinearity of the spring constant, the resonance frequency itself starts to change above a certain critical vibrational amplitude. One can see that by replacing (2.8) in (2.7), the resonance frequency becomes amplitude-dependent: $f_0(x) = \frac{1}{2\pi} \sqrt{\frac{k_1 + k_3 x^2}{m}}$. The expression for k_3, in particular, its relation to the material properties of the membrane, depends on the geometrical shape of the deformation (more details on this are given in Chapter 5).

In this section, the relation between the nonlinear spring constant k_3 of the membrane and its material properties will be extracted using the deformation shape corresponding to its fundamental resonance mode. This is necessary to relate the nonlinear frequency response of the resonators in Chapter 5 to their Young's modulus. To model it mathematically, we start by writing out the expression for the strain energy of a circular membrane as [89]:

$$U = \int_0^{2\pi} \int_0^R \frac{Eh}{2(1-v^2)} \left(\epsilon_{rr}^2 + \epsilon_{\theta\theta}^2 + 2v\epsilon_{rr}\epsilon_{\theta\theta} + \frac{1-v}{2}\gamma_{r\theta}^2 \right) r \, dr \, d\theta, \tag{2.9}$$

where E is Young's modulus, v is Poisson's ratio, h is the thickness and R is the radius of the membrane. Moreover, ϵ_{rr}, $\epsilon_{\theta\theta}$, and $\gamma_{r\theta}$ are the radial and circumferential normal and shear strains that are determined as:

$$\epsilon_{rr} = \frac{\partial u}{\partial r} + \frac{1}{2}\left(\frac{\partial w}{\partial r}\right)^2, \tag{2.10}$$

$$\epsilon_{\theta\theta} = \frac{\partial v}{r\partial\theta} + \frac{u}{r} + \frac{1}{2}\left(\frac{\partial w}{r\partial\theta}\right)^2, \tag{2.11}$$

$$\gamma_{r\theta} = \frac{\partial v}{\partial r} - \frac{v}{r} + \frac{\partial u}{r\partial\theta} + \left(\frac{\partial w}{\partial r}\right)\left(\frac{\partial w}{r\partial\theta}\right), \tag{2.12}$$

---

[2]We note that the nonlinearities discussed in this Chapter entail only changes in tension resulting from a geometrical deformation. In theory, even at a microscopic level, the "spring constant" between two atoms is nonlinear. This is because the minimum of the potential well around the equilibrium point is not perfectly quadratic (see [88]), but it deviates from a parabola for large deflections. To measure the influence of these microscopic nonlinearities, however, much larger forces are required.

where u, v and w are the radial, tangential and transverse displacements respectively. For a membrane with fixed edges u, v and w shall vanish at $r = R$. Moreover, u and v should be zero at $r = 0$ for continuity and symmetry. Assuming only axisymmetric vibrations ($v = 0$ and $\partial w/\partial\theta = \partial v/\partial\theta = \partial u/\partial\theta = 0$) and fixed edges, the w and u can be approximated as [90]:

$$w = x(t) J_0\left(\alpha_0 \frac{r}{R}\right), \tag{2.13a}$$

$$u = u_0 r + r(R-r) \sum_{k=1}^{\bar{N}} q_k(t) r^{k-1}. \tag{2.13b}$$

Here it should be noted that for axisymmetric vibrations the shear strain $\gamma_{r\theta}$ would become zero. In Equations (2.13a, 2.13b), $x(t)$ is the generalized coordinate associated with the transverse motion of the fundamental axisymmetric mode and $q_k(t)$ are the generalized coordinates associated with the radial motion. Moreover, J_0 is the Bessel function of the first kind of order zero, and $\alpha_0 = 2.40483$. In addition, $\bar{N}$ is the number of terms in the expansion of radial displacement, and u_0 is the initial displacement due to pre-tension (n_0) that is obtained from the initial stress $\sigma_0 = n_0/h$ as follows:

$$u_0 = \frac{\sigma_0(1-v)}{E}. \tag{2.14}$$

The kinetic energy of the membrane neglecting radial (i.e. in-plane) inertia, is given by:

$$T = \frac{1}{2}\rho h \int_0^{2\pi}\int_0^R \dot{w}^2 r\,\mathrm{d}r\,\mathrm{d}\theta, \tag{2.15}$$

where the overdot indicates differentiation with respect to time t.

In the presence of transverse harmonic distributed pressure $p = F_{\text{el}}\cos(\omega t)/R^2\pi$ (assuming the angle of the membrane is negligible), the virtual work done is:

$$W = 2\pi \int_0^R pwr\,\mathrm{d}r = \frac{2}{R^2}\int_0^R F_{\text{el}}\cos(\omega t)wr\,\mathrm{d}r, \tag{2.16}$$

where ω is the excitation frequency and F_{el} gives the force amplitude, positive in the transverse direction. Higher-order terms in w are neglected in Equation (2.16) [91]. The Lagrange equations of motion are

$$\frac{\mathrm{d}}{\mathrm{d}t}\left(\frac{\partial T}{\partial\dot{\mathbf{q}}}\right) - \frac{\partial T}{\partial\mathbf{q}} + \frac{\partial U}{\partial\mathbf{q}} = \frac{\partial W}{\partial\mathbf{q}}, \tag{2.17}$$

and $\mathbf{q} = [x(t), q_k(t)]$, $k = 1,...,\bar{N}$, is the vector including all the generalized coordinates.

Since radial inertia has been neglected, Equation (2.17) leads to a system of nonlinear equations comprising of a single differential equation associated with the generalized coordinate $x(t)$ and $\bar{N}$ algebraic equations in terms of $q_k(t)$. By solving the $\bar{N}$ algebraic equations it is possible to determine $q_k(t)$ in terms of $x(t)$. This will reduce the $\bar{N}+1$ set of nonlinear equations to a single Duffing oscillator as follows:

$$m_{\text{eff}}\ddot{x} + b\dot{x} + k_1 x + k_3 x^3 = \xi F_{\text{el}}\cos(\omega t), \tag{2.18}$$

where it is found that

$$m_{\text{eff}} = 0.2695\,m,\ k_1 = 4.897\,n_0,\ \xi = 0.432, \tag{2.19}$$

and b is the damping coefficient that has been added to the equation of motion to introduce linear viscous dissipation. The coefficients of m_{eff}, k_1 and the value of ξ are obtained from the numerical solution of Equation (2.17) using Equations (2.13a) and (2.13b) and are dependent on the deformation shape, i.e. the vibrational mode shape[3]. Moreover, k_3 is the cubic stiffness, which is a function of the Young's modulus and Poisson's ratio, and its convergence and accuracy is determined by using different number of terms in the expression for the radial displacement (Equation (2.13b)). The value of k_3 converges for $\bar{N} > 3$ and its relation to the Young's modulus can be determined by fixing the value of the Poisson's ratio and numerically solving the set of $\bar{N}$ Lagrange equations. k_3 can be expressed in the form:

$$k_3 = C_3(v)\frac{Eh\pi}{R^2}, \tag{2.20}$$

where C_3 is dimensionless constant which is a function of the Poisson's ratio. The so-
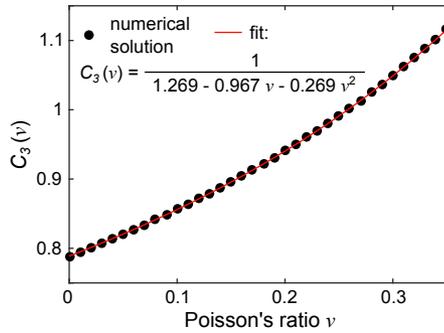
Figure 2.2: **Numerical solutions for C_3 as a function of v.** The red line represents the corresponding fit.

lutions for C_3 as a function of v are plotted in Figure 2.2 for values of the Poisson's ratio between 0 and 0.35.

The relation between C_3 and v is best described with the inverse of a second-order polynomial, namely:

$$C_3 = \frac{1}{1.269 - 0.967v - 0.269v^2}. \tag{2.21}$$

This functional dependence is similar to the one used for AFM nanoindentation measurements, often referred to as $q(v)$ [17].

Next, the following dimensionless parameters are introduced:

$$\hat{t} = \omega t, \tag{2.22a}$$

---

[3]It is important to note that the same values of m_{eff}, k_1 and ξ should be taken into consideration when describing the linear vibrations of the fundamental mode of a circular membrane.

$$\hat{x} = x/h. \tag{2.22b}$$

By using Equations (2.18) and (2.22), the following dimensionless equation of motion can be obtained:

$$r^2 \ddot{\hat{x}} + \frac{1}{Q} r \dot{\hat{x}} + \hat{x} + \eta_3 \hat{x}^3 = \lambda \cos(\hat{t}), \tag{2.23}$$

where

$$\omega_0 = \sqrt{\frac{k_1}{m}}, \, Q = \frac{m\omega_0}{b}, \, \eta_3 = \frac{k_3 h^2}{k_1}, \, \lambda = \frac{\xi F_{\text{el}}}{m\omega_0^2 h}, \, r = \frac{\omega}{\omega_0}. \tag{2.24}$$

Equation (2.23) is valid for studying nonlinear vibrations of membranes subjected to external harmonic excitation in the frequency neighbourhood of the fundamental mode. Assuming the fundamental mode of vibration is not involved in an internal resonance with other modes, then other modes accidentally excited will decay with time to zero due to the presence of damping [92]. Here we assume that this condition is preserved and therefore the response of the membrane is described by a single dimensionless Duffing equation (Equation (2.23)), which is convenient for performing the fitting (parameter identification) of nonlinear response curves (see Chapter 3.3).

3

METHODS

In this chapter we are going to describe the main tools that we use to fabricate and characterise our devices, our scientific "arsenal". First, we briefly discuss the underlying principle of interferometric motion detection and then we describe the standard configuration of the measurement setup. This is followed by a description of the calibration of motion: how to convert the voltage from the photodiode to a motion amplitude of our membranes (in nanometres) and what kind of errors arise from the assumptions that we make. We continue by describing the fitting of nonlinear frequency response curves, using a model order reduction method to reduce the number of fitted parameters to a single variable. Finally, we explain how we fabricate our devices, laying out the process flows for most of the devices used throughout this thesis.

3.1. LASER INTERFEROMETRY

Most of the measurements in this thesis are performed optically, using a laser interferometer. In this section, the working principle of the setup will be outlined, together with the underlying physics of the transduction of the motion amplitude of a 2D resonator to an electrical signal.
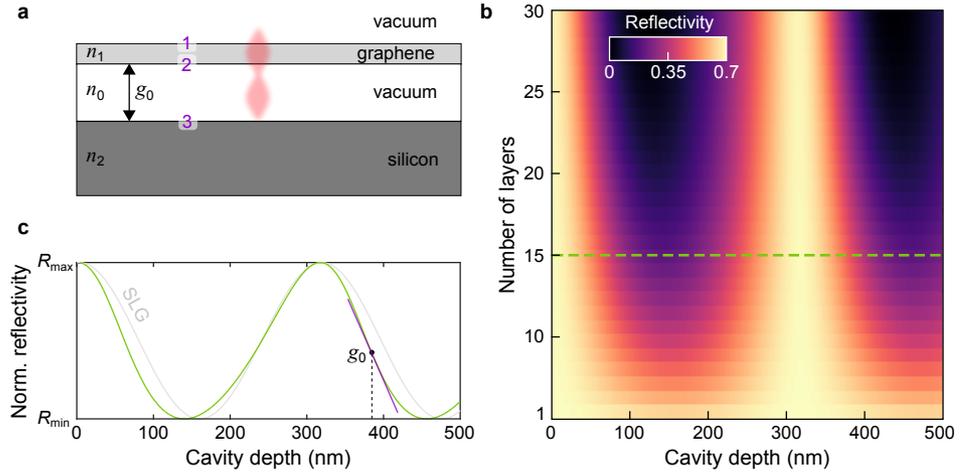

Figure 3.1: **A schematic of the optical cavity and a model of the reflectivity of the cavity as a function of drum position. a**, A schematic of the optical cavity. n_i are the refractive indices of medium i, g_0 is the cavity depth and the numbers 1-3 represent the interfaces in the system. The stationary optical field created by the laser is sketched in red. **b**, Calculated reflectivity of the silicon-vacuum-graphene optical cavity as a function of cavity depth and the number of graphene layers. **c**, Calculated reflectivity for a 5-nm thick graphene drum (green curve) as a function of the position of the drum. The calculation is based on a measurement using a λ = 632.8 nm laser. The black dot represents the initial position of the drum (cavity depth) g_0 = 385 nm. The purple line represents the linear approximation of the reflectivity (constant transduction) around g_0.

All the samples in this thesis consist of a membrane of a two-dimensional material suspended on top of a cavity. On the backside of the cavity there is a reflective surface, usually made of silicon (Si), gold (Au) or gold-palladium (AuPd). The semi-transparent membrane together with the reflective backmirror form an optical cavity, also called a Fabry-Pérot cavity (see Figure 3.1a). A red helium-neon (HeNe) laser (λ = 632.8 nm) is focused onto the membrane. The essence of the transduction of the membrane's motion to an electrical signal lies in the modulation of the power of the red laser that is reflected off of the sample. This relies on two mechanisms:

1. **Interference**: the fraction of the light that is reflected from the reflective mirror interferes with the light that is reflected directly from the membrane, which happens due to a difference in path lengths;

2. **Modulated absorption**: the light reflected from the backmirror forms a standing wave, due to the zero-electric-field condition at the metal-vacuum interface. The intensity of the reflected light is then modulated by means of modulated absorption of the light by the graphene drum moving through this optical field.

The interplay of these two mechanisms is determined by the thickness of the graphene drum and the cavity depth.

Mathematically, the intensity of the reflected light can be described using the model proposed in [93]:

$$R = \left| \frac{r_1 + r_2 e^{-i\delta_1} + r_3 e^{-i\delta_2} + r_1 r_2 r_3 e^{-i(\delta_1 + \delta_2)}}{1 + r_1 r_2 e^{-i\delta_2} + r_1 r_3 e^{-i(\delta_1 + \delta_2)} + r_2 r_3 e^{-i\delta_2}} \right|^2, \tag{3.1}$$

3

where $r_1 = \frac{n_0 - n_1}{n_0 + n_1}$, $r_2 = \frac{n_1 - n_0}{n_1 + n_0}$ and $r_3 = \frac{n_0 - n_2}{n_0 + n_2}$ represent the reflections from interfaces 1-3 and δ_1 and δ_2 are the phases that the light acquires while travelling through the graphene and the cavity (vacuum) respectively (see Figure 3.1a). A colormap of the reflectivity of the system calculated using this model as a function of the cavity depth and the number of graphene layers, based on $\lambda = 632.8$ nm, $n_1 = 2.6 - 1.3i$ and $n_2 = 3.88 - 0.02i$, is shown in Figure 3.1b. Fixing the thickness of the graphene and the laser wavelength, in Figure 3.1c we plot the reflectivity as a function of the position of the drum for a 5-nm thick graphene flake.

To measure the intensity of the reflected light we use a laser interferometer setup, schematically described in Figure 3.2. The sample is mounted inside a vacuum chamber, usually at a pressure in the order of 10^{-6} mbar. The entire sample stage is motorized and, in one of the setups used in this thesis, we also use a sample chamber that can be cooled down to 3.5 K (using a closed-cycle Montana Instruments Cryostation).

The linearly polarised laser beam (polarization perpendicular to the plane of the sketch) coming out of the HeNe laser is sent through a set of lenses (BE), which increase the beam diameter by a factor of three. This is done in order to fill the entire aperture of the objective lens (50x) in order to minimize the spot size by maximizing the angle, resulting in a laser spot smaller than 1.3 μm. The beam is then sent through a polarised beam splitter (PBS), which is transparent for vertically polarized light. The laser passes through a $\lambda/4$ plate rotated at 45 °, which gives the light circular polarization. The beam then goes through a cold mirror (CM), which is transparent for red light. The purpose of the cold mirror will become clear below in the text. The light is then focused onto the sample by a 50x objective lens. The part of the light that gets reflected off of the sample passes again through the $\lambda/4$ plate, which effectively turns its polarization from circular to horizontal (90° with respect to the light from the source). The PBS completely reflects horizontally polarised light, so all the light coming from the sample is redirected towards and focused on the photodiode (PD)[1]. Depending on the measurement, the output of the photodiode is either connected to the input of a Vector Network Analyser (VNA) for measurements of driven motion or to a Spectrum Analyser (SA) for measurements of Brownian (thermal) motion.

---

[1]The PD model used throughout this thesis is a NewPort 1801 photoreceiver with a frequency range of 0 - 125 MHz. Using an internal amplifier, it converts laser power to voltage through two outputs: a dc-coupled output (using an internal low-pass filter at 50 kHz) and an ac-coupled output (using an internal high-pass filter at 25 kHz). For most of the measurements presented in this thesis, the ac-coupled output of the photodiode is used.
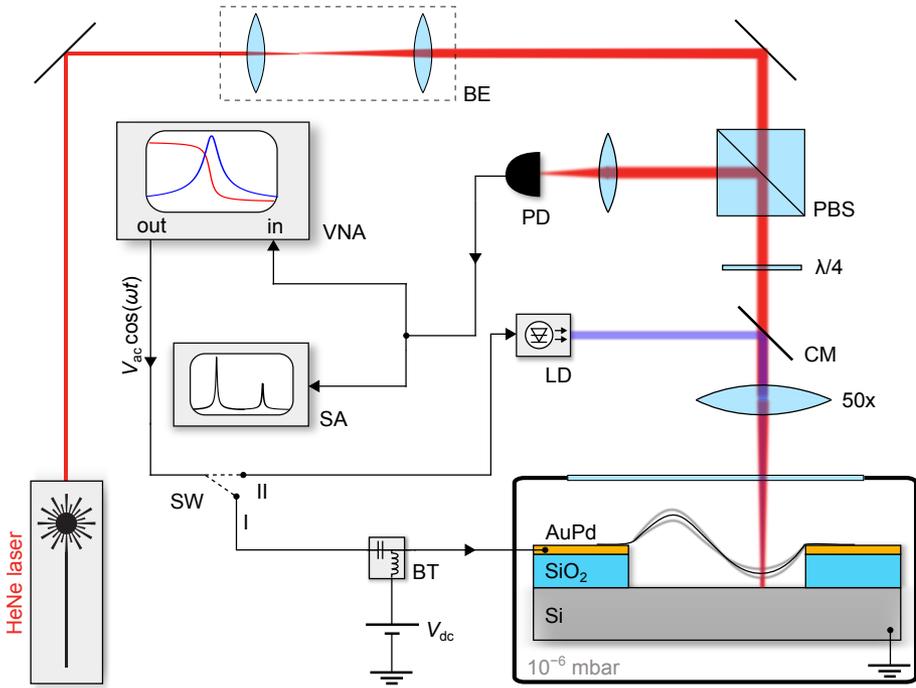
3

Figure 3.2: **Laser interferometer.** A HeNe laser is focused on the suspended graphene drum, which is mounted in a high-vacuum chamber. The motion of the drum modulates the reflected intensity of the laser, which is captured using a photodiode (PD). The drum can be driven both optothermally (using the power-modulated blue laser diode (LD)) and electrostatically (using the backgate, v_G), depending on the switch (SW) configuration. The driven motion is measured using a Vector Network Analyser (VNA) and the undriven (Brownian) motion is measured using a Spectrum Analyser (SA). BE: beam expander, PBS: polarised beam splitter, CM: cold mirror, BT: bias-tee.

Almost all measurements in this thesis rely on homodyne detection of the motion of the membrane, i.e. the membrane's motion is simultaneously actuated and measured at the same frequency. This is done using the VNA shown in Figure 3.2. For conducting materials and samples with electrical access (Au or AuPd electrode on top of which the 2D material is transferred) we use electrostatic actuation [43, 94]: the output port of the VNA is in electrical contact with the membrane through the metallic electrode on the chip. On top of this ac actuation signal, we add a dc component (V_{dc}) through a bias-tee, to avoid frequency doubling of the actuation signal due to the quadratic dependence of the electrostatic force on the applied voltage (see Chapter 3.2 for the mathematical derivation).

Alternatively, we can use another, blue laser ($\lambda = 405$ nm) to excite the motion of the membrane optothermally [33, 34]. The blue laser is coupled to the optical path through the cold mirror. The cold mirror is transparent to red light, but is highly reflective for blue light. By connecting the output of the VNA to the blue laser diode, we periodically modulate the output power of the laser, which is focused on the same spot as the

measurement laser. The periodic modulation of the LD input power causes a periodic modulation of the tension of the membrane through means of thermal expansion and contraction. More details on the microscopic mechanism of optothermal actuation can be found in [74].

3.1.1. CALIBRATION OF THE AMPLITUDE

In this section the procedure of calibration of the motion amplitude using the resonator's Brownian noise is explained. In addition, the effect of nonlinearities in the readout method on the calibration is estimated.

To convert the measured signal (in Volts) to a motion amplitude of the resonator (in metres), we use thermal calibration (we follow closely the procedure described in [95]). This means that we can relate the time-averaged undriven (Brownian) motion of the drum to its thermal energy. The following relation between the drum's amplitude and its thermal noise power spectral density (PSD) can be stated:

$$\langle x_n^2(t) \rangle = \int_0^\infty df\, S_{xx}(f),$$ (3.2)

where $\langle x_n^2(t) \rangle$ is the mean-square amplitude of motion of the n-th mode of the drum, f is the frequency, and $S_{xx}(f)$ is the measured one-sided spectral density of the drum's motion.

According to the equipartition theorem, the time averaged potential energy of a harmonic oscillator per degree of freedom $\frac{1}{2} m_{\text{eff},n} \omega_n^2 \langle x_n^2(t) \rangle$ is equal to $\frac{1}{2} k_B T$. This allows us to express the thermal noise PSD of the drum ($S_{xx}(f)$) as [95]:

$$S_{xx}(f) = \frac{k_B T f_n}{2\pi^3 m_{\text{eff},n} Q_n [(f^2 - f_n^2)^2 + (f f_n / Q_n)^2]},$$ (3.3)

where k_B is the Boltzmann constant, T is the temperature (in our case, we take $T = 293$ K), and f_n, $m_{\text{eff},n}$ and Q_n are the resonance frequency, effective mass ($m_{\text{eff}} = 0.2695\, m$ when S_{xx} is taken at the centre of the drum [95]) and quality factor of the n-th resonance mode respectively.

We start by experimentally measuring the PSD using a spectrum analyser ($S_{VV}(f)$). This is obtained as $V(f)^2 / \Delta f$, where $V(f)$ is the voltage spectrum of the resonator's motion, measured with a bandwidth Δf. The unit of the obtained signal is then V^2/Hz. $S_{VV}(f)$ represents the total PSD of the system. This includes noise from various sources in the detection system, among which the dark current noise of the photodiode (S_{VV}^{PD}, measured as voltage over a 50 Ω resistor), which can be easily measured and subtracted. Assuming all other sources of noise to be very weakly dependent on frequency in the measured bandwidth, we can consider them to be a flat additive contribution (S_{VV}^w) to the total PSD. S_{VV}^w also determines the noise floor of the measurement. The remaining signal can be entirely attributed to the thermal noise PSD of the drum ($S_{xx}(f)$) multiplied by a transduction factor α (V^2/m^2), which depends on the mechanical-optical-electrical transduction of the system. It is worth mentioning that α is highly susceptible to changes

in the measurement laser intensity, position and focus of the drum, the cavity depth and optical/electrical losses in the system. To ensure that the value of α stays constant throughout the measurements we take all measurements in one go, without changing the sample position.

We can now write a general relation between the aforementioned quantities:

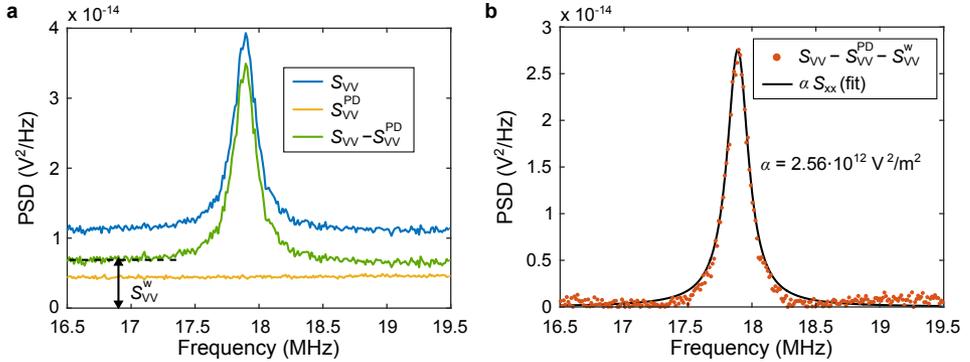$$S_{VV}(f) = S_{VV}^w + S_{VV}^{PD}(f) + \alpha S_{xx}(f) \tag{3.4}$$

3

Figure 3.3: **Calibration procedure. a**, Measured power spectral density (PSD) of the fundamental mode of a 5-nm thick MoS$_2$ drum. The blue curve is the measured PSD, the yellow curve is the PSD of the photodiode dark current and the green curve is the resulting subtraction of $S_{VV}(f) - S_{VV}^{PD}(f)$. The constant offset of the green curve accounts for all other sources of noise in the system S_{VV}^w. **b**, PSD of the motion of the drum, after subtracting the noise floor from the green curve in **a**. The black curve is the fit of the PSD of the drum, from which the transduction factor α can be obtained.

In Figure 3.3 we show an example of a calibration measurement of an MoS$_2$ drum shown in Chapter 5. The measured total PSD of the drum (S_{VV}) is shown by the blue curve in Figure 3.3a. Subtracting the photodiode dark current noise S_{VV}^{PD} (yellow curve), we get the resulting green curve. This curve contains both $\alpha S_{xx}(f)$ and a constant noise floor (S_{VV}^w), assuming a white noise background. Further subtracting this offset results in the data (red points) shown in Figure 3.3b. This curve can now be fitted using Equation (3.3) multiplied by the transduction factor α. This fit is shown by the black curve in Figure 3.3b. From this fit, we can determine 3 fit parameters: the resonance frequency f_0, the quality factor Q and, most importantly, the transduction factor α (in this case $\alpha = 2.56 \cdot 10^{12} \, V^2/m^2$).

Using this transduction factor, we can now determine the amplitude (in nanometres) of the driven motion as well. The magnitude of the driven motion at resonance is obtained from a two-port network analyser measurement and is given by $|S_{21}(f_0)|$ (in V/V). Multiplying this by the RMS value of the ac driving voltage ($V_{ac,RMS}$) gives us the RMS value of the time averaged motion amplitude of the drum in Volts ($A_{RMS}(f)$)

$$A_{RMS}(f) = \sqrt{\langle A^2(f) \rangle} = |S_{21}|(f) \cdot V_{ac,RMS}. \tag{3.5}$$

This amplitude can be converted to metres ($x_{RMS}(f)$) considering a constant transduction factor α by:

$$x_{RMS}(f) = \sqrt{\langle x^2(f) \rangle} = \frac{1}{\sqrt{\alpha}} A_{RMS}(f).$$ (3.6)

3.1.2. CALIBRATION UNCERTAINTIES

The entire calibration procedure is done assuming that the transduction factor α is constant, i.e. that the reflected intensity depends linearly on the position of the drum.

The square root of the transduction factor $\sqrt{\alpha}$ of the system is proportional to the derivative of the curve shown in Figure 3.1c with respect to the drum position at the point $g_0 = 385$ nm. Even though the cavity depth is adjusted such that we sit on the linear part of the curve, there are still higher order terms from the linearisation which can result in an error when determining the amplitude.

For thin flakes multiple reflections can be neglected and the intensity of the reflected light can be approximated by:

$$I = A + B\cos\left(4\pi\frac{g_0 + x}{\lambda}\right),$$ (3.7)

where I is the intensity of the light on the photodiode, A and B are constant coefficients, g_0 is the cavity depth, λ is the wavelength of light, and x is the vertical displacement of the drum. This equation can be now expanded around the static position of the drum ($x = 0$):

$$I = A + B\cos\left(4\pi\frac{g_0}{\lambda}\right) - B\frac{4\pi}{\lambda}\sin\left(4\pi\frac{g_0}{\lambda}\right)x - B\left(\frac{4\pi}{\lambda}\right)^2\cos\left(4\pi\frac{g_0}{\lambda}\right)\frac{x^2}{2} + B\left(\frac{4\pi}{\lambda}\right)^3\sin\left(4\pi\frac{g_0}{\lambda}\right)\frac{x^3}{6}.$$ (3.8)

Assuming a periodic motion of the membrane, the amplitude is given by: $x = x_{max}\cos\omega t$. Replacing this in Equation (3.8) gives:

$$I = A + B\cos\left(4\pi\frac{g_0}{\lambda}\right) - B\frac{4\pi}{\lambda}\sin\left(4\pi\frac{g_0}{\lambda}\right)x_{max}\cos\omega t - \frac{B}{2}\left(\frac{4\pi}{\lambda}\right)^2\cos\left(4\pi\frac{g_0}{\lambda}\right)x_{max}^2\cos^2\omega t +$$
$$+\frac{B}{6}\left(\frac{4\pi}{\lambda}\right)^3\sin\left(4\pi\frac{g_0}{\lambda}\right)x_{max}^3\cos^3\omega t.$$ (3.9)

Substituting $\gamma = 4\pi\frac{g_0}{\lambda}$, $C_0 = A + B\cos\left(4\pi\frac{g_0}{\lambda}\right)$, $C_1 = B\frac{4\pi}{\lambda}$, $C_2 = \frac{B}{2}\left(\frac{4\pi}{\lambda}\right)^2$ and $C_3 = \frac{B}{6}\left(\frac{4\pi}{\lambda}\right)^3$ we get:

$$I = C_0 - (C_1\sin\gamma)x_{max}\cos\omega t - (C_2\cos\gamma)x_{max}^2\cos^2\omega t + (C_3\sin\gamma)x_{max}^3\cos^3\omega t.$$ (3.10)

$$I = C_0 - \overbrace{\frac{C_2 \cos\gamma}{2} x_{\max}^2}^{0} + \overbrace{\left[\frac{3}{4}(C_3 \sin\gamma)x_{\max}^3 - (C_1 \sin\gamma)x_{\max}\right]}^{f} \cos\omega t -$$
$$- \underbrace{\frac{(C_2 \cos\gamma)}{2} x_{\max}^2 \cos 2\omega t}_{2f} + \underbrace{\frac{C_3 \sin\gamma}{4} x_{\max}^3 \cos 3\omega t}_{3f}. \tag{3.11}$$

Using homodyne detection with a very narrow bandwidth filter (in our case < 1kHz), we are only sensitive to the $\cos\omega t$ component of Equation (3.11) (labelled f), hence the actual intensity detected by the VNA at the resonance frequency ω_0 is:

$$I(\omega) = \frac{3}{4}(C_3 \sin\gamma)x_{\max}^3 - (C_1 \sin\gamma)x_{\max}. \tag{3.12}$$

The linear coefficient of Equation (3.12) corresponds to the transduction coefficient extracted using the calibration procedure ($\sqrt{\alpha}$). At small amplitudes, the cubic component plays little role. The error that the cubic term introduces in the amplitude calibration at large amplitudes is therefore given by:

$$\varepsilon = \frac{\frac{3}{4}(C_3 \sin\gamma)x_{\max}^3}{(C_1 \sin\gamma)x_{\max}} = \frac{3}{4}\frac{C_3}{C_1}x_{\max}^2, \tag{3.13}$$

or:

$$\varepsilon = 2\frac{\pi^2}{\lambda^2}x_{\max}^2. \tag{3.14}$$

Hence, using a laser with $\lambda = 632.8$ nm, for amplitudes of up to $x_{\max} = 10$ nm, the error that we make in the estimation of the amplitude is $|\varepsilon| < 0.5\,\%$. We note that this error is independent of the the gap size g_0. It is worth mentioning that the nonlinearities in the optical transduction can be exploited to calibrate the amplitude of nanomechanical resonators without the need of knowing their mass or temperature [96].

3.2. Determination of the electrostatic driving force

In this section the electrostatic force is determined by two methods: (i) based on the geometry and the voltage applied on the drum and (ii) based on the measured amplitudes at resonance.

The electrostatic force acting on the membrane at a frequency ω, assuming a parallel plate capacitor model, can be calculated as:

$$F_{\mathrm{calc}}(\omega) = \xi\frac{\varepsilon_0 R^2 \pi}{2g_0^2}\left[V_{\mathrm{dc}} + V_{\mathrm{ac}}\cos(\omega t)\right]^2 = \xi\frac{\varepsilon_0 R^2 \pi}{2g_0^2}\left[V_{\mathrm{dc}}^2 + \frac{1}{2}V_{\mathrm{ac}}^2 + 2V_{\mathrm{dc}}V_{\mathrm{ac}}\cos(\omega t) + \frac{1}{2}V_{\mathrm{ac}}^2\cos(2\omega t)\right], \tag{3.15}$$

where g_0 is the gap size and $\xi = 0.432$ is a correction factor that accounts for the fundamental mode shape of a fixed circular membrane (see Section 1 and main text).

In a homodyne detection scheme, only the motion resulting from a force at frequency ω can be detected. Therefore, the effective force on the drum will be:

$$F_{\text{calc}}(\omega) = \xi \frac{\varepsilon_0 R^2 \pi}{2g_0^2} \left[2V_{\text{dc}} V_{\text{ac}} \cos(\omega t) \right]. \tag{3.16}$$

It is worth mentioning that due to the fact that the output of the VNA has 50Ω impedance and the drum is a capacitor (high impedance), the ac voltage felt by the drum is double the voltage that is output by the VNA ($V_{\text{ac}} = 2V_{\text{ac,VNA}}$).

Knowing the applied driving force is crucial for fitting the nonlinear response curves and finding the Young's modulus of the membranes, and it therefore needs to be determined very accurately. Even though it can be easily calculated using Equation (3.15), there are three main sources of uncertainty that can alter the calculated value. The first one is the gap size g_0. Even though the gap size is fixed by the sample fabrication and can be easily measured, the actual position of the drum due to membrane slack and imperfections is unknown. This can change the effective gap size, and therefore the effective force by up to 5 % (assuming slack of 20 nm over a 385 nm gap). A second source of uncertainty is the dc voltage felt by the drum. It is well known that the charge neutrality point (the resonance frequency minimum in f_0 vs. V_{dc} measurements) is not at a voltage $V_{\text{dc}} = 0$ V [43, 97]. Similar effects have been observed in carbon nanotubes and are often attributed to trapped charges [43, 98, 99]. These charges manifest themselves as an added dc voltage of the drum, and can significantly affect the effective electrostatic force. Finally, due to the presence of the AuPd electrode underneath the drum, the electric field will be screened by the edges of the electrode around the perimeter of the drum. This will lower the effective capacitance of the drum and therefore also the effective electrostatic force felt by it. For a flat drum, using a gap size of 385 nm and a 100 nm-thick AuPd electrode, such fringe field effects can account for up to 15 % of overestimation of the force.

To correct for these effects, we calculate the expected peak amplitude at resonance ($x_{\text{calc,RMS}}|_{\omega=\omega_0}$) using the force calculated using Equation (3.16). In the linear vibration regime, this function is expected to be linear with the force, hence with the applied ac voltage:

$$x_{\text{calc,RMS}}|_{\omega=\omega_0} = \frac{Q}{\omega_0^2 m_{\text{eff}}} F_{\text{calc,RMS}}, \tag{3.17}$$

$$x_{\text{calc,RMS}}|_{\omega=\omega_0} = \frac{Q}{\omega_0^2 m_{\text{eff}}} \xi \frac{\varepsilon_0 R^2 \pi}{g_0^2} V_{\text{dc}} V_{\text{ac,RMS}} = \beta V_{\text{ac}}. \tag{3.18}$$

The slope of the x_{RMS} vs. $V_{\text{ac,RMS}}$ curve at low ac voltages (linear regime) will be a constant β, defined as:

$$\beta = \frac{\text{d} x_{\text{calc,RMS}}|_{\omega=\omega_0}}{\text{d} V_{\text{ac,RMS}}} = \frac{Q}{\omega_0^2 m_{\text{eff}}} \xi \frac{\varepsilon_0 R^2 \pi}{g_0^2} V_{\text{dc}}; \tag{3.19}$$

$$\beta = \frac{Q}{\omega_0^2 m_{\text{eff}} V_{\text{ac,RMS}}} F_{\text{calc,RMS}}. \tag{3.20}$$

Knowing β, we can calculate the force for any driving ac voltage:

$$F_{\text{calc,RMS}} = \beta \frac{\omega_0^2 m_{\text{eff}}}{Q} V_{\text{ac,RMS}}. \tag{3.21}$$

The actual force felt by the drum (F_{RMS}) will be modified depending on the uncertainties in determining V_{dc} (V_{dc}') and g_0 (g_0'), possibly resulting in a different slope of the x_{RMS} vs. $V_{\text{ac,RMS}}$ curve: β'. We can use this value to cross-check and correct for the actual force (F_{RMS}):

$$F_{\text{RMS}} = \beta' \frac{\omega_0^2 m_{\text{eff}}}{Q} V_{\text{ac,RMS}}. \tag{3.22}$$
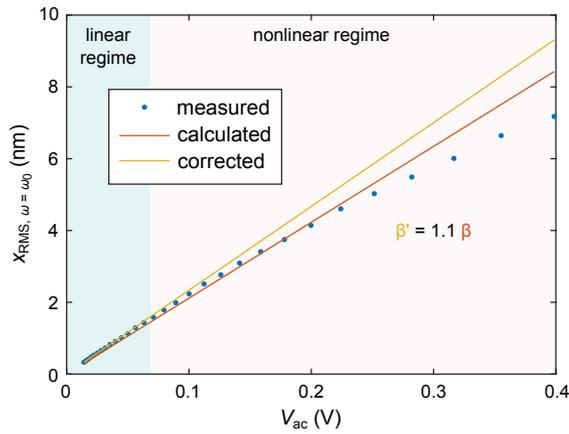

Figure 3.4: **Force estimation and correction.** The dc voltage applied is $V_{\text{dc}} = 1$ V. The blue dots represent the measured amplitude of a 8-nm thick FLG drum at resonance. The red curve is the calculated amplitude using Equation (3.18) (in the linear regime) with the force calculated from Equation (3.16). The yellow curve is the corrected force using Equation (3.22). The error in the force estimation in this case is roughly 10 %.

To visualize the procedure, in Figure 3.4, we present data from a 4-μm in diameter, 8-nm thick FLG drum. The calibrated amplitude at resonance (or $x_{\text{RMS,max}}$ in the nonlinear regime) is plotted as blue dots (similar data can be seen in [33]). The calculated expected amplitude based on Equation (3.18) is represented by the red line. To correct for the difference in slopes in the linear part (left hand side), we fit the slope of the measured amplitude to extract β'. The resulting error in the force estimation is roughly 10 %, which, assuming that the error is only due to trapped charges (neglecting effects of fringe fields), translates to a 0.1 V offset over the applied $V_{\text{dc}} = 1$ V [43].

As long as the force scales linearly with the applied driving voltage (and there are no significant nonlinearities in the actuation), this method can be easily extended to calibrate the force of other actuation methods, like optothermal actuation, since the force can be extracted from the calibrated amplitude data. This is provided that the Q-factor is known and the displacement x can be properly calibrated.

3.3. NONLINEAR IDENTIFICATION

In order to be able to numerically fit or identify the nonlinear response curves, we need an analytical solution to the Duffing equation (Equation (2.18)). To do this, here we utilize the harmonic balance method. This method is a suitable and accurate mathematical technique that entails the solution of nonlinear equations to be approximated by a truncated Fourier series. In case of the dimensionless Duffing oscillator (i.e. Equation (2.23)), a first order truncation has been shown to provide accurate results [92]. Hence,

$$\hat{x} \approx x_1 \sin \hat{t} + x_2 \cos \hat{t}. \tag{3.23}$$

Substituting Equation (3.23) into Equation (2.23) yields:

$$x_1(1 - r^2) - r\frac{1}{Q}x_2 + \frac{3}{4}\eta_3 x_1 A^2 = 0, \tag{3.24a}$$

$$x_2(1 - r^2) + r\frac{1}{Q}x_1 + \frac{3}{4}\eta_3 x_2 A^2 = \lambda, \tag{3.24b}$$

where $A = \sqrt{x_1^2 + x_2^2}$ is the amplitude of motion, $x_1 = A\sin\phi$ and $x_2 = A\cos\phi$, ϕ being the phase difference between the excitation and the response. From Equations (3.24a) and (3.24b) the following analytical frequency-amplitude relation could be found:

$$A^2\left[\left((1 - r^2) + \frac{3}{4}\eta_3 A^2\right)^2 + (\frac{r}{Q})^2\right] = \lambda^2. \tag{3.25}$$

The idea of harmonic balance based parameter estimation is to follow a reverse path [100]. In other words, the identification is conducted by assuming that the vibration amplitude A and frequency ratio r are already known for every frequency step from experiments. Therefore, in order to obtain unknown parameters, the following system should be solved for every j-th frequency step, $r^{(j)}$:

$$\begin{pmatrix} -r^{(j)}x_2 & \frac{3}{4}x_1 A^2 \\ r^{(j)}x_1 & \frac{3}{4}x_2 A^2 \end{pmatrix} \cdot \begin{bmatrix} \frac{1}{Q} \\ \eta_3 \end{bmatrix} = \begin{bmatrix} -x_1(1 - (r^{(j)})^2) \\ -x_2(1 - (r^{(j)})^2) + \lambda \end{bmatrix} \quad, j = [1:m]. \tag{3.26}$$

System (3.26) can be compactly written as $\bar{A}_h \cdot Y = \bar{B}_h$. This system is over constrained since it contains $2 \times m$ equations. In order to solve (3.26) and to estimate system parameters, least squares technique is used and the norm of the error $Er = \left(\bar{A}_h \cdot Y - \bar{B}_h\right) \cdot \left(\bar{A}_h \cdot Y - \bar{B}_h\right)^T$ should be minimized. Accordingly, here the pseudo-inverse of matrix A_h is calculated and the solution is obtained as follows:

$$Y = \left(\bar{A}_h^T \bar{A}_h\right)^{-1} \bar{A}_h \cdot \bar{B}_h. \tag{3.27}$$

A problem in utilizing the least squares technique is that the identified peak amplitudes in the frequency-response curves do not correspond to the ones obtained from the experiments. In order to resolve this issue, a correction on the quality factor is made by making use of the following expression (see Ref. [100] for the derivation details):

$$Q = \frac{1}{2}\left[\sqrt{\frac{1}{2} + \frac{3}{8}\eta_3 A_{\max}^2 - \sqrt{(\frac{1}{2} + \frac{3}{8}\eta_3 A_{\max}^2)^2 - \frac{\lambda^2}{4A_{\max}^2}}}\right]^{-1},\qquad(3.28)$$

in which $A_{\max}$ is the experimentally measured peak amplitude for each frequency–amplitude curve. This will yield the nonlinear identification procedure to a single fit parameter algorithm for the estimation of η_3.

3.4. Sample fabrication

In this section we will briefly describe the process flow for fabricating most of the devices used in this thesis. The devices usually consist of circular cavities[2] fabricated on p++ doped silicon wafers with thermally grown SiO_2 with a thickness of 285 nm. Electrical access usually means more control over the devices, since it provides an additional tuning knob during the experiments. Therefore, the majority of samples have metallic electrodes (usually made of gold-palladium (60-40) or pure gold). From our experience, the AuPd provides a very flat surface (root-mean-square surface roughness down to 100 pm) compared to pure Au, which substantially improves the subsequent transfer of the 2D flakes. The highly doped silicon makes for a convenient gating electrode. When the 2D membrane is made of an insulating material, like the ones described in Chapter 9, no electrical access is necessary and we thus work with simpler devices, consisting of circular cavities in SiO_2. Both of the process flows shall be described in detail below.

For fabricating the devices used in Chapters 6 and 8 a different process flow is used, which is described in detail in Chapter 6.

3.4.1. Si-SiO$_2$-AuPd structures

The fabrication process starts with cleaning $19 \times 19 mm^2$ Si/SiO$_2$ chips in nitric acid (HNO$_3$). Nine devices are usually patterned at once on a single chip (3×3 matrix). Two layers of poly(methyl methacrylate) (PMMA) resist are spin-coated on the chip (see Figure 3.4.1a): the bottom layer is of a lower (495 kDa) and the top layer is of a higher molecular weight (950 kDa). The chip is then patterned using electron-beam lithography (doses ranging from 900-1100 $\mu C/cm^2$). The resist is then developed for 90 seconds in a solution of methyl isobutyl ketone (MIBK) and isopropyl alcohol (IPA), MIBK:IPA 1:3, followed by 90 seconds of rinsing in IPA. The resulting resist profile is shown in Figure 3.5b. Using two layers of resist helps in getting a so-called undercut, where the profile of the bottom layer of resist (with a lower molecular weight) is slightly receded with respect to the one on top.

The metals are deposited using electron-beam metal evaporation (Figure 3.5c). At very low pressures (10^{-7} mbar) this provides for a strongly anisotropic deposition of the metals. Usually three metals are evaporated: 5 nm of titanium (used as an adhesion layer), 95 nm of gold-palladium and 30 nm of chromium (used as a hard mask for the subsequent etching step). The final cavity depth can be controlled by controlling the thickness of the AuPd layer. This is followed by a lift-off process in warm acetone (45°) for

---

[2]The device design is more complex in, for example, Chapter 7, but the process flow used is identical to what is described in 3.4.1.
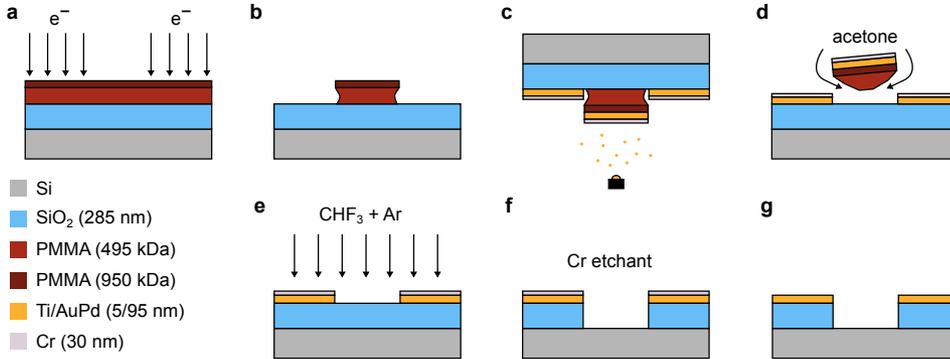
Figure 3.5: **Process flow for Si-SiO$_2$-AuPd structures. a**, E-beam patterning of the resist. **b**, The resist profile after developing. **c**, E-beam evaporation of metals (Ti-AuPd-Cr). **d**, Lift-off in acetone. **e**, RIE using the Cr as a hard mask. **f**, Wet etching of Cr using a Cr etchant. **g**, The resulting SiO$_2$-AuPd cavity.

45 minutes (Figure 3.5d). The undercut in the bottom resist layer facilitates this process, as it prevents contact between the top and bottom metallic layers and it provides easier access for the acetone. The next step is creating the cavities, i.e., etching away the SiO$_2$ in the areas that are not covered by metal. This is done using reactive ion etching (RIE) at a pressure of 7 μbar (Figure 3.5e). Two gasses are used: 50 sccm of CHF$_3$ and 2.5 sccm of Ar. This combination of gasses is selective to SiO$_2$ - the underlying silicon is left intact. The next step is the removal of Cr, which is done in Cr etchant (Figure 3.5f). The resulting chips (Figure 3.5g) are then diced into nine 6×6 mm^2 pieces.

3.4.2. SI-SIO$_2$ STRUCTURES

The process flow for samples with no electrical access is somewhat easier, but well-defined cavities with sharp vertical walls require some optimization of the process. From our experience, the best quality of samples is achieved when using CSAR 62 (AR-P 6200.09) resist, which is not only very sensitive and decreases the e-beam exposure time, but is also very resistant and can be used as a mask for the subsequent RIE step. The resist is patterned using e-beam lithography with doses ranging from $300 - 350\mu C/cm^2$ (Figure 3.6a). The resist is developed in pentyl acetate for 60 seconds followed by rinsing in MIBK:IPA 1:1 for 60s, and in pure IPA for 60s. The samples are then loaded into the RIE
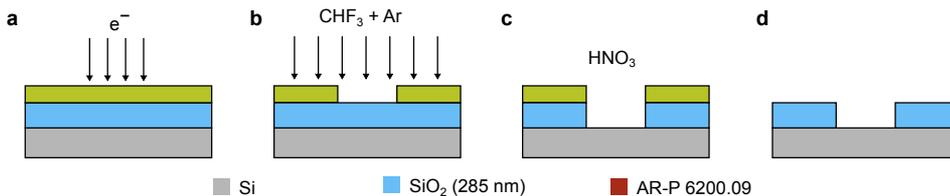

Figure 3.6: **Process flow for Si-SiO$_2$ structures. a**, E-beam patterning of the resist. **b**, RIE using the resist as a hard mask. **c**, Stripping the remaining resist in nitric acid. **d**, The resulting SiO$_2$ cavity.

system and the same recipe as in Chapter 3.4.1 is used (Figure 3.6b). The ratio of the etching rates of SiO_2 and CSAR 62 is about 2:1. The remaining resist is then removed in HNO_3 (Figure 3.6c). The resulting chips (Figure 3.6d) are then diced into nine 6×6 mm^2 pieces.

3.4.3. TRANSFER OF THE 2D MATERIALS

The flakes of the 2D materials are obtained by mechanical exfoliation from natural crystals[3] and the transfer is performed using an all-dry transfer technique, which is descibed in detail in [101]. The transfer of the 2D flakes is always done as the final step.
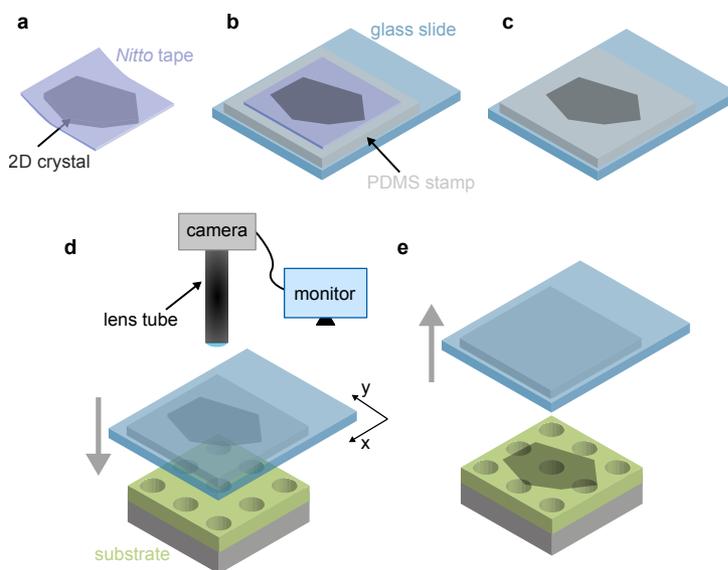

Figure 3.7: **Exfoliation and transfer of 2D materials. a**, Exfoliation from natural crystals using *Nitto* tape. **b**, Transfer of the exfoliated flakes from the *Nitto* tape onto a PDMS stamp stuck to a rigid glass slide. **c**, The flakes of the material are now transferred on the PDMS. **d**, The glass slide is turned upside down and positioned above the pre-patterned sample using a micropositioner. The process is monitored using an optical lens connected to a camera and a monitor. **e,** The glass slide with the PDMS is slowly retracted upwards, such that the 2D material flakes stay on the designated place on the substrate.

First, flakes are exfoliated from natural crystals using *Nitto* tape (Figure 3.7a). The process is repeated several times in order to thin down the flakes. A thick piece of poly-dimethylsiloxane (PDMS) is cut out and placed on a glass slide. The glass slide serves as a rigid support for the polymer piece. The *Nitto* tape with the flakes of the 2D material are then pressed onto the PDMS stamp (Figure 3.7b) and peeled off quickly. As a result, some of the flakes stay on the PDMS stamp (Figure 3.7c). The glass-PDMS stack is turned upside down and mounted onto a micropositioning stage. The process is monitored through an optical system comprising of a lens tube and a camera connected to a screen

---

[3]This does not apply for the materials used in Chapter 9.

that enables live monitoring of the whole process. The transparency of the glass slide and the PDMS facilitate the positioning of the flakes onto the substrate (Figure 3.7d). The stack is then pressed onto the pre-patterned substrate with holes and peeled off slowly (Figure 3.7e). If successful, the flakes of the 2D material stay on the substrate, forming suspended nanodrums.

3

4

VISUALIZING THE MOTION OF GRAPHENE NANODRUMS

Membranes of suspended two-dimensional materials show a large variability in mechanical properties, in part due to static and dynamic wrinkles. As a consequence, experiments typically show a multitude of nanomechanical resonance peaks, which makes an unambiguous identification of the vibrational modes difficult. Here, we probe the motion of graphene nanodrum resonators with spatial resolution using a phase-sensitive interferometer. By simultaneously visualizing the local phase and amplitude of the driven motion, we show that unexplained spectral features represent split degenerate modes. When taking these into account, the resonance frequencies up to the eighth vibrational mode agree with theory. The corresponding displacement profiles however, are remarkably different from theory, as small imperfections increasingly deform the nodal lines for the higher modes. The Brownian motion, which is used to calibrate the local displacement, exhibits a similar mode pattern. The experiments clarify the complicated dynamic behaviour of suspended two-dimensional materials, which is crucial for reproducible fabrication and applications.

NANOMECHANICAL devices from suspended graphene and other two-dimensional materials have received growing interest in the past few years [33–36], and their application in sensitive pressure, gas and mass sensors has been proposed [19, 21, 32, 39, 41, 59, 102]. Available techniques to study the mechanical properties of such membranes include quasi-static indentation [16, 103] and dynamic response analyses in frequency- and time-domains [33–35, 50, 104, 105]. These experimental studies show a large variability in the mechanical properties [34, 49, 50], and to understand the intricate dynamic behaviour of suspended graphene, it is necessary to detect its motion with spatial resolution. While initial experiments were done on structures with radial symmetry broken by design [106–108], the local phase of the membrane motion was not measured in these cases, which makes identification of the mode difficult, especially for the higher modes and in the presence of small imperfections. Moreover, previous experiments did not measure absolute displacements, which makes the acquisition of quantitative displacement profiles of the fundamental and higher modes impossible.

In this chapter we visualize the motion of two-dimensional nanodrums with unprecedented resolution and sensitivity using a phase-sensitive scanning interferometer. The driven motion and the non-driven Brownian motion of a suspended few-layer graphene resonator vibrating at very high frequencies is detected up to the eighth vibrational mode. The phase information enables a reconstruction of the time-evolution of the displacement profile. In the radially symmetric nanodrum we observe splitting of multiple degenerate modes, as well as a distortion of the mode structure. By visualizing the Brownian motion, the displacement profiles are calibrated to obtain spatially resolved displacement amplitudes. The spatially resolved measurements enable a detailed examination of the mode structure, and provide a useful tool in the efforts towards reproducible fabrication of suspended two-dimensional materials.

4.1. EXPERIMENTAL SETUP

Circular graphene nanodrums are fabricated by transferring exfoliated few-layer graphene on top of silicon substrates pre-patterned with circular holes, as is described in Chapter 3.4.1. Figure 4.1a shows the graphene nanodrum of interest, with a diameter of $5\,\mu$m and a thickness of 5 nm as confirmed by Raman spectroscopy and atomic force microscopy (Figure 4.1b). The approximate mass of the moving part equals 230 fg. The flexural motion of the nanodrum is detected using an optical interferometer, which has been used previously in frequency- and time-domain studies of the nanomechanical properties of 2D-materials [33, 34, 103, 109, 110]. Figure 4.1c shows the setup and a schematic cross-section of the graphene nanodrum. The drum is probed by a HeNe laser, and the intensity variations caused by the interfering reflections from the moving membrane and the fixed silicon substrate underneath are detected with a photodiode, as is described in more detail in Chapter 3.1.

The sample can be moved in-plane with the graphene $(x - y)$ using a motorized nanopositioning stage. Compared to a scanning mirror, moving the sample does not affect the intensity of the incident light such that the transduction gain of the setup remains constant. This makes a calibration of the displacements possible, as will be shown below. With a step size of 140 nm, the spectral response is measured at 1500 points spa-
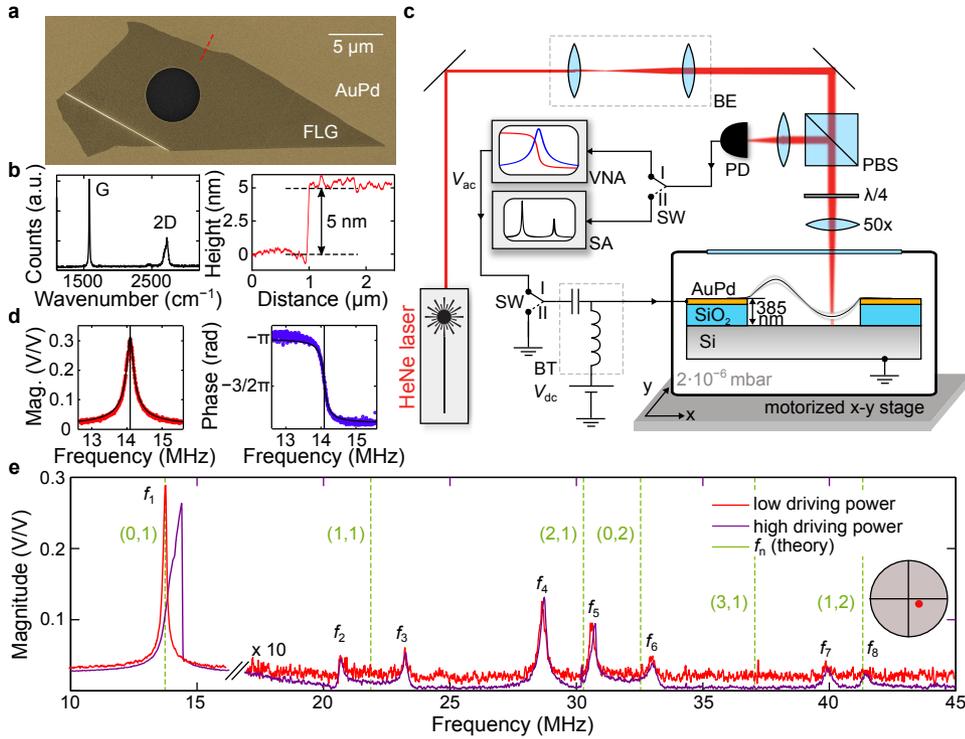
Figure 4.1: **Scanning laser interferometry of graphene nanodrums. a,** Scanning Electron Microscope (SEM) image of the graphene nanodrum. **b,** Raman spectrum (left) taken at the centre of the drum; the relative height of the G and 2D peaks is characteristic of multi-layer graphene. Atomic Force Microscope (AFM) trace (right) taken along the red dashed line from (a), showing the flake thickness of 5 nm. **c,** Interferometric displacement detection is accomplished by focusing a HeNe laser beam ($\lambda = 632.8$ nm) on the nanodrum, while recording the interfering reflections from the graphene and the Si substrate underneath using a photodiode (PD). The sample is mounted on a motorized xy nanopositioning stage that scans the sample in a serpentine fashion, with a step size of 140 nm. BE: 3× Beam Expander; PBS: Polarized Beam Splitter. Two measurement types can be selected using switch SW: SW = 1 engages a phase-sensitive Vector Network Analyser (VNA) measurement, while SW = 2 is used to detect the Brownian motion of the nanodrum using a Spectrum Analyser (SA). **d,** VNA measurement (magnitude and phase) of the fundamental resonance mode, detected while probing at the centre of the drum (black curves: fitted response). **e,** VNA measurement showing the eight lowest resonance modes of the nanodrum, when driven at $V_{ac} = 2.2$ mV (red) and $V_{ac} = 8.9$ mV (purple). Eight resonance peaks are detected, which are indexed 1-8 starting at the fundamental mode (for clarity, the magnitude of modes 2-8 is scaled 10×). The dashed green lines mark the calculated frequencies for a circular tension-dominated membrane [95].

tially distributed across the suspended part of the drum, which is sufficient to visualize the displacements associated with higher vibration modes, which exhibit an increasing number of nodal lines.

Two measurement types can be selected by setting the switch SW (see Figure 4.1c). When SW = 1, the complex response (magnitude and phase) to an electrostatic driving signal is measured using a Vector Network Analyser (VNA). When SW = 2, the driving signal is switched off, and the Brownian motion of the membrane is detected using a Spectrum Analyser (SA). Figure 4.1d shows the magnitude and phase response (SW = 1) at the fundamental resonance mode, which corresponds well to an harmonic oscillator. Figure 4.1e shows the response of the drum at higher driving frequencies, taken at low (red curve) and higher (black curve) driving voltages, when probing close to the centre of the drum. At strong driving, a multitude of peaks are detected, which are labelled f_i, in accordance with their position in the spectrum. The resonance frequencies calculated for a perfect circular membrane are also displayed[1]. The measured resonance frequencies are conspicuously different from the calculated ones, which raises the central question addressed in this work: Which mode indices correspond to each of the observed resonance peaks?
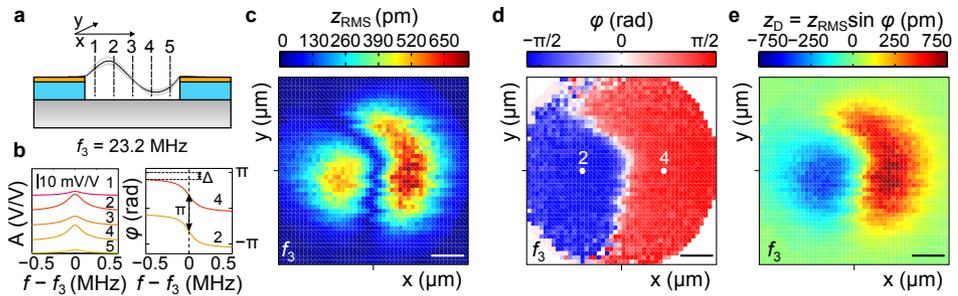

Figure 4.2: **Spatially-resolved measurements.a,** Individual frequency response lines taken at positions 1-5 using the VNA (SW = 1), while applying a driving signal at f_3. **b,** Recorded magnitude (left) and phase (right) response at f_3. A phase difference π indicates that on these locations the drum moves in opposite direction. **c,** Root-mean-square displacement z_{RMS} of mode 3, taken at a step size (x,y) of 140 nm. The diffraction-limited spot size of the probe laser is $1.3\,\mu m$, which causes some loss of spatial resolution. **d,** Local phase response, ϕ_R, of the nanodrum, showing that two halves of the drum move in opposite directions. **e,** Reconstructed displacement field map as obtained by $z_D = z_{RMS} \sin\phi$. Scale bars in **c-e**: $1\,\mu m$.

4.2. VISUALIZING DRIVEN MOTION

The motion of the graphene nanodrum is made visible using a phase-sensitive scanning interferometer. To demonstrate the technique, we set out by measuring the frequency response of mode 3 at five different positions on the drum, as illustrated in Figure 4.2a. The amplitude and phase responses are fit to a harmonic oscillator function, and the fits are shown in Figure 4.2b. From the responses it is observed that, while two halves of the drum move at a comparable amplitude, their phase differs by π.

---

[1] In a circular membrane, the mode-shapes are labelled as (m,n), where m refers to the number of nodal diameters and n to the number of nodal circles.
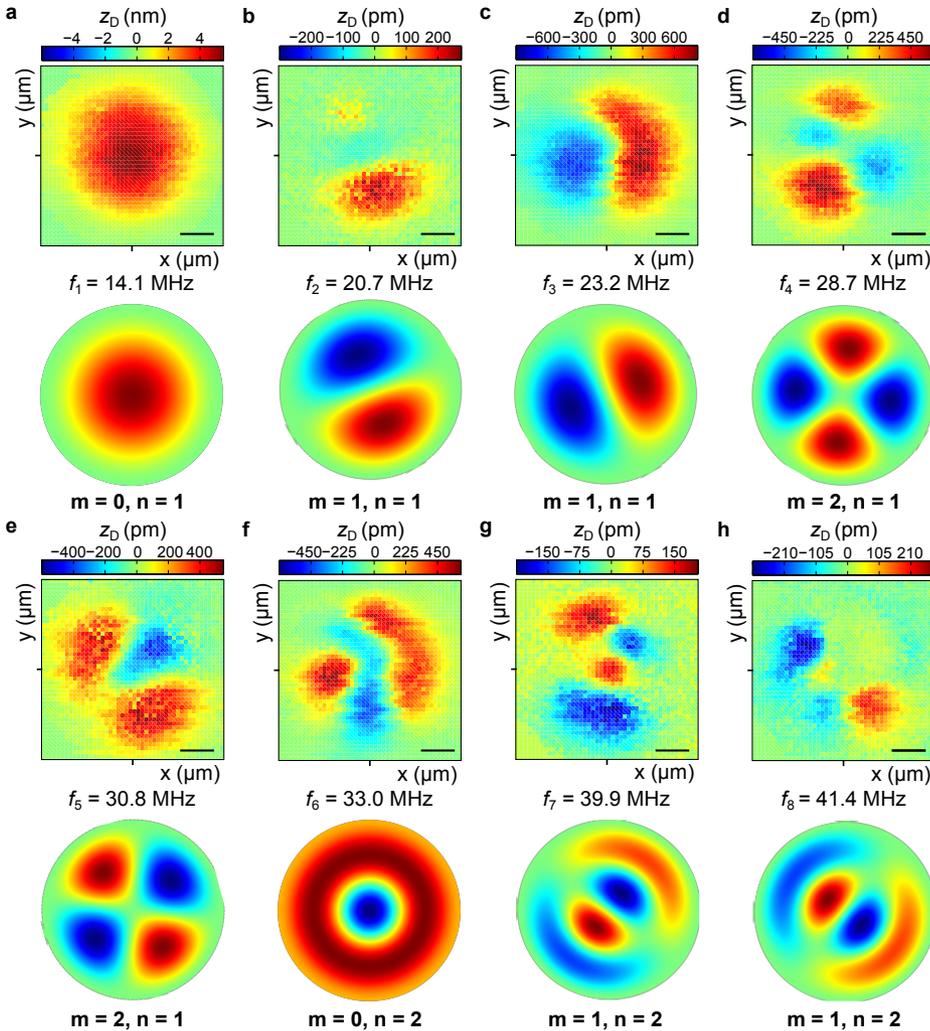
Figure 4.3: **Visualizing resonant motion. a-h,** Top: experimental data; bottom: finite-element calculation. The modes predicted by the calculation are indexed by (m,n). Panels **b** and **c** show that the nanodrum hosts a split degenerate $(1,1)$ mode, while also the $(2,1)$ mode is split, as is shown in panels **d** and **e**. The displacement profile measured in **f** resembles a $(0,2)$ mode, which is distorted due to an imperfection as will be discussed in the main text. **g** and **h** reveal a degenerate $(1,2)$ mode. Scale bars: $1\,\mu$m.

This indicates that at positions 2 and 4 the graphene moves in opposite directions, as is the case for a $(1,1)$ mode. Following this procedure, a more refined measurement is performed. Figure 4.2c-d display on a colour scale the fitted peak height, z_{RMS}, and phase responses ϕ at the resonance peak frequency, measured on a square grid with a spacing of 140 nm. The amplitude response reveals two anti-nodal points which are separated by a nodal line, and the phase response shows that on either side of the nodal line the

graphene moves in opposite directions. While for the $(1,1)$ mode this phase behaviour appears trivial, we will show below that the phase information is a requisite to understand the motion of higher modes. Figure 4.2e shows a snapshot colormap of the membrane movement, as obtained by $z_D = z_{RMS} \sin \phi$.

In a similar way, the motion at the other resonance peaks of Figure 4.1e is visualized. Figure 4.3a-h show the mode shapes that correspond to $f_1 - f_8$, together with the theoretical shapes, which were obtained by finite-element calculations for a circular membrane. The fundamental mode was probed at a reduced driving voltage, as to maintain a linear response as in Figure 4.1e, red curve. The measurements show unambiguously that the peaks observed in the spectrum of Figure 4.1e are the result of split degenerate modes $(1,1)$, $(1,2)$, and $(2,1)$. The displacement profiles of modes 1-4 (Figure 4.3a-d) are in reasonable agreement with the theoretically calculated mode shapes. Other modes, however, in particular the ones with higher indices (i.e., 5, 6 and 8 as shown in Figure 4.3e-g) show a large discrepancy. Clearly, an imperfection is present whose influence on the location of the nodal lines grows with the mode index. Note that this imperfection is not visible in the SEM image of Figure 4.1a, but has a large impact on the mode shapes. Table 4.1 summarizes the experimental and theoretical resonance frequencies and mode shapes, and will be described further in the next section.

4.3. VISUALIZING BROWNIAN MOTION

The above experiments illustrate in detail the mode structure of a driven graphene nanodrum, and it is interesting to compare these driven measurements with the displacements that are the result of thermal fluctuations. Compared to silicon carbide microdisk resonators, whose thermal motion was studied recently [111], graphene nanodrums have a very low reflectivity and a 10-100 times lower mechanical Q-factor. Nevertheless, the present technique is sensitive enough to visualize their Brownian motion.

To study the Brownian motion, the switch is set to SW = 2, in order to switch-off the driving signal and to the record displacements with a Spectrum Analyser Figure 4.4a shows an example of a thermal noise spectrum, taken close to the centre of the drum. Three vibrational modes are observed that resemble the lowest three resonances of Figure 4.1e, albeit at somewhat lower frequencies. The difference in frequency results from the absence of the electrostatic force: as $V_{dc} = 0$, no force is exerted on the graphene drum. Compared to the driven measurement, a part of the mechanical tension is released, which causes the resonance frequencies to tune to a lower value. With the same step size as in the driven measurement, we map the first three mode shapes and plot the thermal RMS displacement as a function of position. Figure 4.4b shows the Brownian motion of the fundamental $(0,1)$ mode, and Figures 4.4c and 4.4d show a splitting of the degenerate $(1,1)$ mode, in close agreement with the amplitude map of the driven motion. Note that in the absence of a driving signal the phase is not measured as it diffuses within the measurement integration time.

For applications of suspended two-dimensional materials, it is important to quantify the displacements associated with the motion. The RMS displacement of a nanomechanical resonator can be obtained by measuring its Brownian motion [112]. From the power spectral density of the signal measured at the centre of the drum, $S_{VV}(f) = S_{VV}^w +$
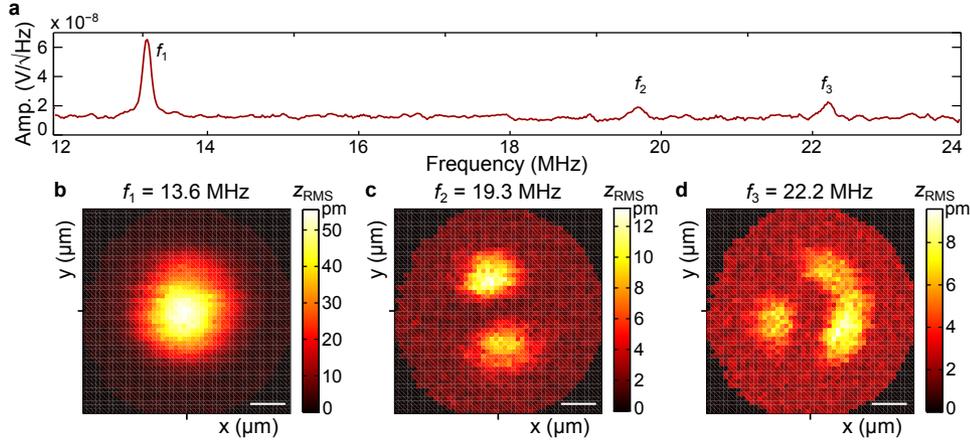
Figure 4.4: **Visualizing Brownian motion. a,** Spectrum analyser measurements (SW = 2) taken without applying a driving signal ($V_{ac} = 0$) reveal three vibrational modes. **b-d,** Spatial maps of the RMS Brownian displacements at each of the vibrational modes. The Brownian mode shapes correspond well with the ones observed when the drum is resonantly driven (Figure 4.3a-c). The slightly lower frequencies are the result of the absence of a dc voltage $V_{dc} = 0$ V, which results in a sightly lower mechanical tension in the drum.

$S_{VV}^{PD}(f) + \alpha S_{zz}(f)$, the noise floor S_{VV}^{w} and the transduction factor α (V^2/m^2) are calculated, as discussed in detail in Chapter 3.1.1. The thermal displacement noise spectral density of the fundamental mode at the drum centre is given by $S_{zz}(f)$ (referred to as $S_{xx}(f)$ in Chapter 3.1.1) [95]. Note that the temperature of the drum is up to a few K below the ambient temperature due to combined effects of laser heating and photothermal damping [113], as discussed in detail in Appendix 4.5.2. Using an incident optical power of 0.8 mW, the noise floor equals 11 fm/$\sqrt{\text{Hz}}$, which enables the detection of the three resonance modes. The transduction factor equals $\alpha = 3.75 \times 10^{11}$ V^2/m^2, and using this number, all detected displacement signals in the experiments of Figure 4.3 and Figure 4.4 are converted to absolute displacements, and indicated in the respective colour bars.

4.4. DISCUSSION

From the summary of the measurement results presented in Table 4.1, it becomes clear that the ratios of the higher harmonics to the fundamental mode, f_n/f_0, deviate from the theoretically expected frequencies for a membrane resonator[2]. Deviations range from 0.7% for mode f_8 to 8.6% for mode f_2. While the spatial maps show that the difference between the measured and theoretical mode shapes increases with the mode index, there is no obvious correlation between the differences in the resonance frequencies and the distortion of the mode shapes. For example, the mode shape of f_3 is in good agreement, while the mode shape of f_8 bears almost no resemblance to the theoretical

---

[2]The motion of mode (3,1), with an expected resonance at 37.4 MHz, is not detected. A possible explanation is that the nodal lines in this device are spaced close to the diffraction limit, resulting in a low displacement contrast.

calculation. Interestingly, comparing them in the frequency domain, f_8 differs by only 0.7 % , and f_3 by 3.3 % from its theoretical value. Similarly, the frequency of f_6 is within 2 % of the calculated value, while the corresponding shape is highly distorted due to a broken radial symmetry. Thus, the lower modes appear more robust against imperfections, possibly due to the lower number of nodal lines – a tendency that is confirmed by finite-element simulations provided in Appendix 4.5.3. These findings are of particular interest in the light of the recently proposed nanomechanical schemes to detect the *geometry* of adsorbed masses [114, 115], which rely on an accurate description of the mode shapes. In such schemes, the splitting of the degenerate modes, which is also observed in the Brownian motion and emerges from the structural imperfections in our experiments, could be used to provide information about the geometry of the adsorbed mass.

	experiment		theory		
i	f_i (MHz)	f_i / f_0	f_i / f_0	(m, n)	shape
1	14.1	1	1	(0, 1)	
2	20.69	1.467	1.593	(1, 1)	
3	23.24	1.648			
4	28.73	2.038	2.135	(2, 1)	
5	30.75	2.181			
6	33	2.340	2.295	(0, 2)	
-	-	-	2.653	(3, 1)	
-	-	-			
7	39.93	2.832	2.917	(1, 2)	
8	41.41	2.937			

Table 4.1: **Experimental and theoretical resonance frequencies of the graphene nanodrum.**

It is interesting to further investigate the origins of the mode-splitting and the progressive distortion of the mode structure for the higher modes. To this end, we map the local stiffness of the drum using peak-force AFM (measurement details provided in Appendix 4.5.3). The analysis reveals local inhomogeneities in the membrane that went unnoticed during optical and electron microscopy inspection. These may be the result of a uniaxial residual tension in the drum, introduced while 'peeling-off' the graphene flake during the transfer to the substrate [101]. Similar effects were observed in other drums studied, which include a single-layer and a 13-layer graphene device (measurements are provided in Appendix 4.5.4), and it can thus be expected from this work that these are inherent to suspended two-dimensional materials fabricated by exfoliation and dry transfer. A finite-element calculation that takes this feature into account results in a better agreement between the predicted mode shapes and the measurements, as is discussed

in Appendix 4.5.3.

Besides the displacements on resonance described above, other parameters can be visualized with spatial resolution. For example, the local resonance frequency, the *Q*-factor and the noise floor give a wealth of information about the device and the detector, such as the local temperature distribution in the device, and the local reflectivity of the substrate. These examples are discussed in more detail in Appendix 4.5.1. Spatially resolved measurements are a valuable tool to analyse the dynamic properties of two-dimensional materials, and may be used to address open questions such as the origin of their low mechanical *Q*-factors [116, 117], as well as to assess fabrication quality and reproducibility. These are essential in order to exploit opportunities that arise in new applications as hybrid nano-electromechanical systems, that fuse excellent mechanical properties with exotic traits such as a negative thermal expansion coefficient and Poisson's ratio [118, 119] and electromechanical [120, 121] and optoelectronic couplings [122].

In conclusion, we visualize the motion of micrometer-scale graphene drums vibrating at very high frequencies with a lateral resolution of 140 nm and a displacement resolution of $11\,\mathrm{fm}/\sqrt{\mathrm{Hz}}$. The driven and non-driven thermal displacement profiles of the radially symmetric drum reveal the motion associated with nanomechanical resonance peaks up to the eighth vibrational mode. The spatial technique presented in this work complements the frequency- and time-domain techniques presently available, and is crucial to obtain a complete description of the dynamic behaviour of suspended two-dimensional materials.

4

4.5. APPENDIX

4.5.1. MEASURING OTHER PARAMETERS WITH SPATIAL RESOLUTION

Besides the height of the resonance peak, other characteristics can be plot as a function of the position on the drum. For each mode and at each position, one can for instance plot the noise floor, the resonance linewidth, or derived parameters such as the ratio between the resonance frequencies. Of particular interest is the spatial distribution of the resonance frequencies, which is the result of heating of the drum by the probe laser. Figure 4.5a shows a spatial map of resonance frequency of the driven fundamental mode, f_1. Clearly the resonance frequency varies, with a minimum at the drum circumference and a maximum in its centre. This is explained by heating of the sample by the laser: as the reflectivity of the silicon is lower than that of the AuPd, the sample heats up slightly more when probing the motion at the drum centre. The thermal expansion of the substrate, together with the thermal contraction of the graphene [118], induce additional tension in the membrane, which increases its resonance frequency. The resonance frequency of the drum thus maximizes when the laser hits the centre of the drum. A map of the reflectivity of the device, shown in Figure 4.5b, confirms the increased optical absorption when probing at the centre of the drum.

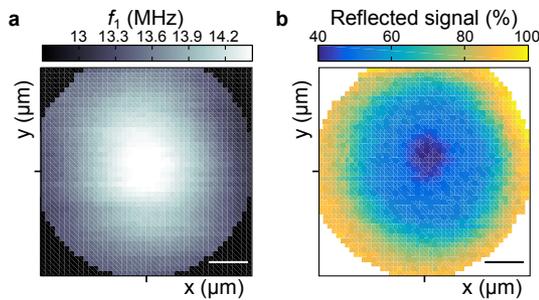Figure 4.5: **Spatial map of the resonance frequency of the fundamental mode. a,** Due to the different effective heating across the drum, its resonance frequency varies by 7 %. The scale bar is $1\,\mu$m. **b,** Reflectivity of the device, as represented by the dc output of the photodiode. The plotted signal, which is normalized to the reflectivity at the AuPd, clearly shows the increased absorption at the centre of the drum.

4.5.2. LASER POWER DEPENDENCE AND PHOTOTHERMAL EFFECTS

Heating by the probe laser and optomechanical effects [113] modify the resonance frequency and the damping of the graphene drum, and this introduces an error in the displacement calibration. To investigate these effects, we measure the undriven spectra (SW = 2, SA) of the fundamental mode at a laser power ranging from $0.25 - 2\,\mathrm{mW}$. As is shown in Figure 4.6, a significant frequency shift is observed. All spatial maps were measured at an incident power of $0.8\,\mathrm{mW}$, and and by combining the frequency and reflectivity images of Figure 4.5a-b we estimate that the drum temperature is up to $3\,\mathrm{K}$ above the ambient temperature. The error in the displacement calibration due to laser heating is then approximately $+1\%$.
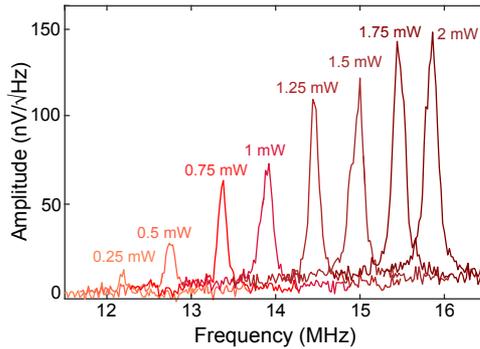
Figure 4.6: **Laser power dependence of the Brownian motion for the fundamental resonance mode.** Spectra of the undriven motion plotted as a function of incident laser power. The combined effects of laser heating and photothermal damping cause a significant increase of the resonance frequency and a slight decrease of the Q-factor with increasing laser power.

Figure 4.6 also reveals a reduction of the Q-factor, which results from photothermal damping. The effect is not very pronounced, as the optical power is mostly absorbed by the silicon. At a laser power of $0.8\,\mathrm{mW}$, the effective quality factor is reduced by approximately 6%. As the effective temperature of the mode equals $T_{\mathrm{eff}} = \frac{T Q_{\mathrm{eff}}}{Q}$ [113], the maximum error in the displacement calibration due to photothermal damping is estimated to be -6%.

4.5.3. PEAK-FORCE AFM OF THE NANODRUM SURFACE
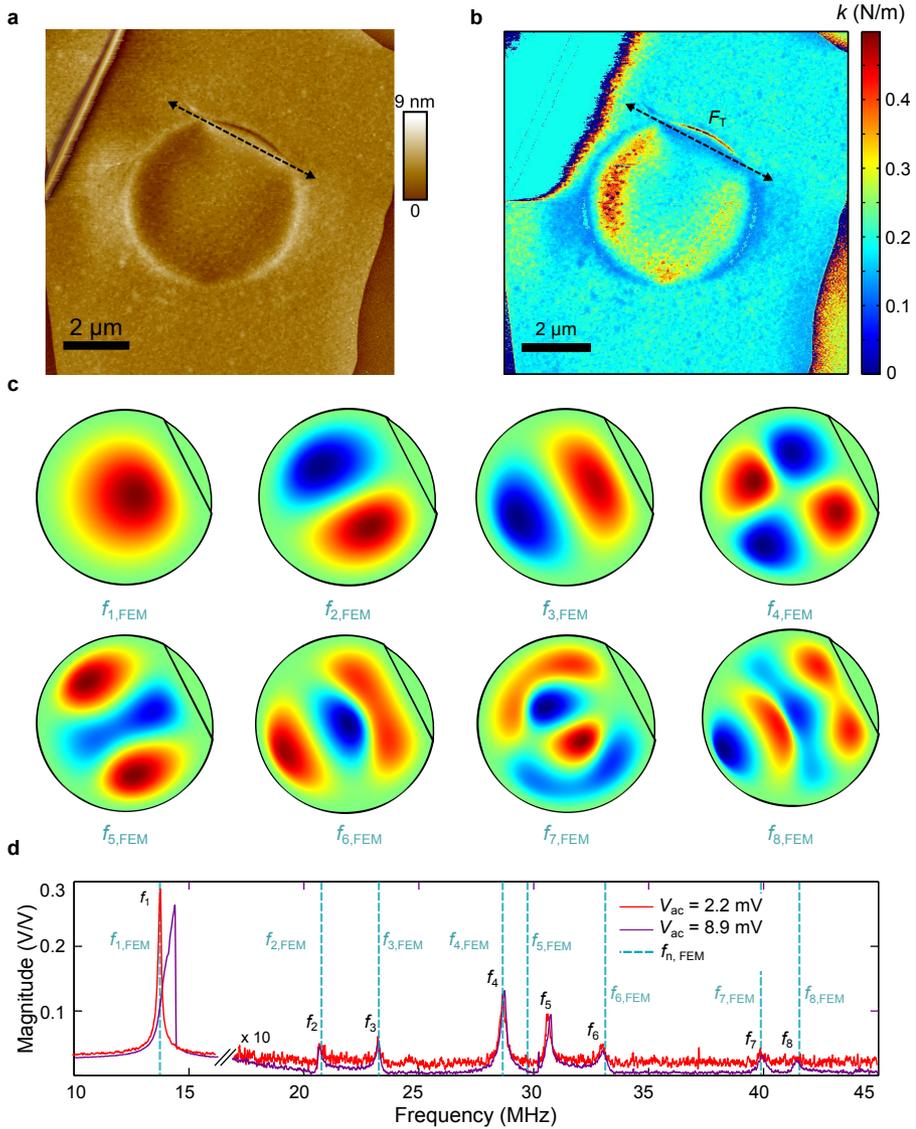
Figure 4.7: **Effect of local stiffness variations on the mode pattern. a,** Maximum displacement at a peak force of 5 nN. The AFM scan reveals a wrinkle indicated by the dashed line. **b,** Effective local linear spring constant, k, as calculated by taking the derivative of the force with respect to deflection for small deflections. **c,** Simulated mode shapes when assuming a tensile force F_T along the wrinkle, indicated by the dashed line in panel **a**. The simulated modes are labelled $f_{n,FEM}$, where n is the position of the peak in the frequency spectrum. **d,** Simulated resonance frequencies (dashed blue lines) superimposed on the frequency response measurement of Figure 4.1a.

To investigate the origin of the distortion of the higher order mode shapes, the local stiffness of the drum was mapped using Peak-Force Atomic Force Microscopy (PF-AFM). Figure 4.7a shows the maximum displacement at each point of the drum using 5 nN as a setpoint for the PF-AFM. It reveals a wrinkle-like feature, which is indicated by the black dashed line. From the force-displacement curves, the effective spring constant at every point is extracted and shown in Figure 4.7b. It reveals that the wrinkle manifests itself as a source of uniaxial tension along its direction, denoted by F_T. To qualitatively understand how this feature affects the mode shapes, we simulated the mode shapes using a finite element model (FEM). The location of the wrinkle is included by imposing a clamped boundary condition, along which a non-uniform tension is applied. As shown in Figure 4.7c, the wrinkle not only breaks the degeneracy of modes $(1, 1)$, $(2, 1)$, and $(1, 2)$, but it also defines the direction of the nodal lines for the higher mode shapes. Taking the feature into account, the simulated mode shapes more closely resemble the measured ones, and they explain the unusual shapes of mode f_6, which loses its radial symmetry, and mode f_5 which shows merging of two anti-nodes along the diameter of the drum. The resonance frequencies, which are plotted as dashed blue lines in Figure 4.7d, are in good agreement with the measurements, except for mode f_5.

4.5.4. MEASUREMENTS ON ADDITIONAL DEVICES

Measurements were performed on two additional devices under the same measurement conditions. Device 2, with a diameter of 5 μm and a thickness of 4.5 nm (13-14 layers), is shown in Figure 4.8a. A driven measurement reveals the four resonance modes indexed A-D in Figure 4.8b. The corresponding displacement profiles, shown in Figure 4.8c, illustrate that mode A corresponds to the fundamental mode. While from the resonance frequency of mode B a $(1, 1)$ mode is expected, with $f_B / f_A \approx 1.6$ for a perfect membrane, the spatial image reveals a much more complicated displacement pattern. The irregular topography of the drum, displayed in the AFM image of Figure 4.8a, is likely the cause of a distorted mode pattern.

Device 3 is a single-layer graphene drum with a diameter of 5 μm. Figure 4.9a shows an optical microscope top view and a Raman spectrum, with the pronounced 2D peak characteristic of a single layer. Figure 4.9b shows the measured frequency response (magnitude only) of the fundamental mode. The corresponding displacement profile is shown in Figure 4.9c. As in the device in the main text and in device 2 discussed above, the irregular profile may be the result of non-uniform tension or the presence of a microscopic wrinkle. As the responsivity of the interferometer reduces for thinner (low-reflectivity) devices, higher modes could not be detected for this single-layer device. Optimization of the cavity depth for single-layer graphene would enable the visualization of higher resonance modes.

4
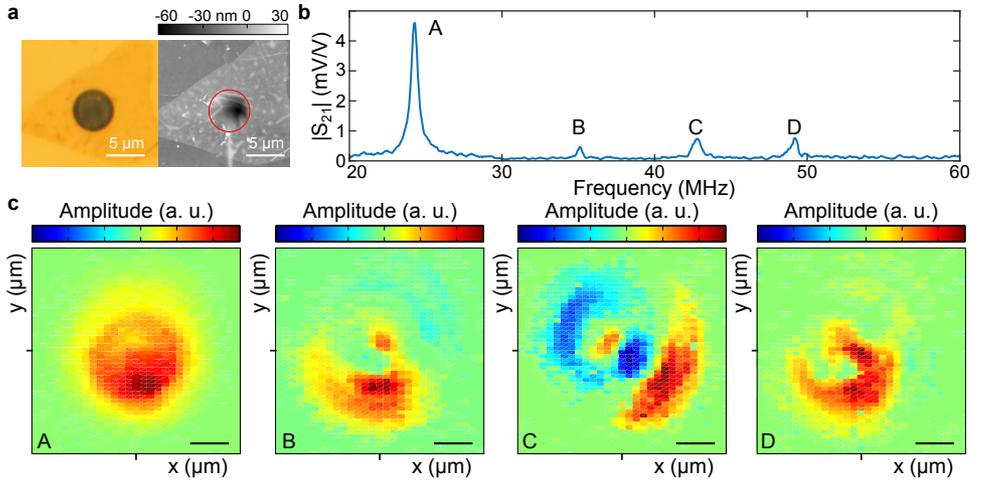
Figure 4.8: **Device 2: 13-layer graphene. a,** Optical image (left) and AFM scan (right) of device 2. The AFM measurement shows a thickness of 4.5 nm. **b,** Frequency response when driven at $V_{ac} = 8.9$ mV and $V_{dc} = 3$ V, revealing four resonance peaks labelled A-D. **c,** Visualization of the displacement profiles that correspond to peaks A-D.
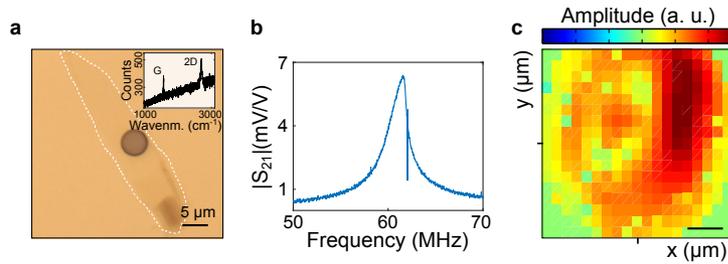
Figure 4.9: **Device 3: Single-layer graphene. a,** Optical image of device 3. Inset: Raman spectrum taken at the drum centre. **b,** Driven frequency response at fundamental resonance mode, with $V_{ac} = 70$ mV. **c,** Visualized displacement profile of the fundamental mode of the single-layer graphene drum.

5

NONLINEAR DYNAMIC CHARACTERIZATION OF TWO-DIMENSIONAL MATERIALS

Owing to their atomic-scale thickness, the resonances of two-dimensional (2D) material membranes show signatures of nonlinearities at forces of only a few picoNewtons. While the linear dynamics of membranes is well understood, the exact relation between the nonlinear response and the resonator's material properties has remained elusive. Here we show a method for determining the Young's modulus of suspended 2D material membranes from their nonlinear dynamic response. To demonstrate the method we perform measurements on graphene and MoS_2 nanodrums electrostatically driven into the nonlinear regime at multiple driving forces. We show that a set of frequency response curves can be fitted using only the cubic spring constant as a fit parameter, which we then relate to the Young's modulus of the material using membrane theory. The presented method is fast, contactless, and provides a platform for high-frequency characterization of the mechanical properties of 2D materials.

T HE remarkable mechanical properties of 2D material membranes have sparked interest for potential uses as pressure [32, 39], gas [21, 40] and mass [41, 42] sensors. For such applications it is essential to have accurate methods for determining their mechanical properties. One of the most striking properties of these layered materials is their high Young's modulus. In order to measure the Young's modulus, a number of static deflection techniques have been used, including Atomic Force Microscopy (AFM) [16, 17, 124, 125], the pressurized blister test [126] and the electrostatic deflection method [103, 127]. The most widely used method is AFM, where by performing a nanoindentation measurement at the centre of a suspended membrane, its pre-tension (n_0) and Young's modulus (E) are extracted from the force-deflection curve. Despite the large number of experimental and theoretical studies [25, 128], the exact physics behind the elasticity of 2D materials is still a subject of debate [129]. This debate is mainly motivated by the large spread in values reported in literature ($E_{graphene}$ = 430 - 1200 GPa) [25], which has been attributed to variations in the material properties and fabrication techniques [130]. As a consequence, there is a significant interest in methods for characterizing the mechanical properties of 2D materials.

Whereas AFM has been the method of choice for static studies, laser interferometry has proven to be an accurate tool for the dynamic characterization of suspended 2D materials, with dynamic displacement resolutions better than 20 fm/$\sqrt{\text{Hz}}$ at room temperature [33, 34, 97]. Since for very thin structures the resonance frequency is directly linked to the pre-tension in the membrane, these measurements have been used to mechanically characterize 2D materials in the linear limit [33–36]. At high vibrational amplitudes nonlinear effects start playing a role, which have lately attracted a lot of interest [44, 67, 75, 104, 131, 132]. In particular, Duffing-type nonlinear responses have been regularly observed [33, 34, 43, 94, 97]. These geometrical nonlinearities, however, have never been related to the intrinsic material properties of the 2D membranes.

In this chapter we introduce a method for determining the Young's modulus of 2D materials by fitting their forced nonlinear Duffing response. Using nonlinear membrane theory, we derive an expression that allows us to relate the fit parameters to both the pretension and Young's modulus of the material. The proposed method offers several advantages. Firstly, the excitation force is purely electrostatic, requiring no physical contact with the membrane that can influence its shape [133, 134]. Secondly, the on-resonance dynamic operation significantly reduces the required actuation force, compared to static deflection methods. Thirdly, the high-frequency resonance measurements allow for fast testing by averaging over millions of deflection cycles per second, using mechanical frequencies in the MHz range. Lastly, the membrane motion is so fast that slow viscoelastic deformations due to delamination, slippage, and wall adhesion effects are strongly reduced. To demonstrate the method, we measure and analyse the nonlinear dynamic response of suspended 2D nanodrums.

5.1. MEASUREMENTS

The samples consist of cavities on top of which exfoliated flakes of 2D materials are transferred using a dry transfer technique [101]. One of the measured devices, a few-layer (FL) graphene nanodrum, is shown in the inset of Figure 5.1a. The measurements are performed in vacuum at room temperature. Electrostatic force is used to actuate the membrane and a laser interferometer is used to detect its motion, as described in [33–35, 97]. A schematic of the measurement setup is shown in Figure 5.1a. The details on the sample preparation and measurement setup are described in Chapter 3.
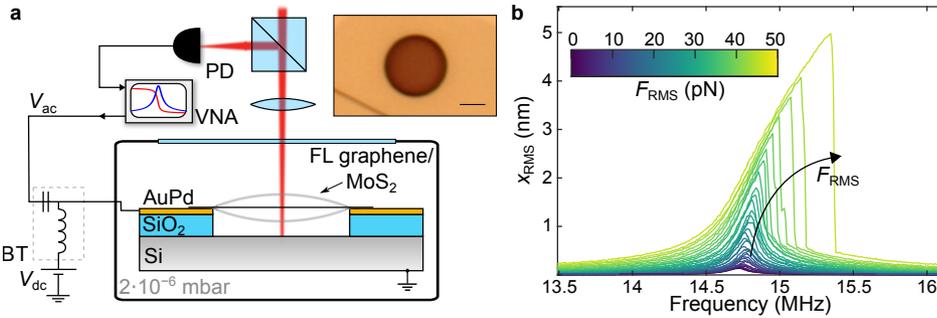

Figure 5.1: **Measurement setup and measured frequency response of device 1. a,** Schematic of the measurement setup: a laser interferometer setup is used to read out the motion of the nanodrum. The Si substrate is grounded and, using a bias-tee (BT), a combination of ac and dc voltage is applied to electrostatically actuate the motion of the drum. This motion modulates the reflected laser intensity and the modulation is read out by a photodiode. Inset: an optical image of a FL graphene nanodrum (scale bar: 2 μm). **b,** Frequency response curves of the calibrated root-mean-square (RMS) motion amplitude for increasing electrostatic driving force. The onset of nonlinearity is visible above F_{RMS} = 15 pN. The colour of the curves indicates the corresponding driving force.

Figure 5.1b shows a set of calibrated frequency response curves of the fundamental mode of a graphene drum (device 1, with thickness $h = 5$ nm and radius $R = 2.5\,\mu$m) driven at different ac voltages (V_{ac}). The dc voltage is kept constant ($V_{dc} = 3$ V) throughout the entire measurement with $V_{dc} \gg V_{ac}$. All measurements are taken using upward frequency sweeps. The RMS force F_{RMS} is the root-mean-square of the electrostatic driving force. For high driving amplitudes ($F_{RMS} > 15$pN), the resonance peak starts to show a nonlinear hardening behaviour, which contains information on the cubic spring constant of the membrane.

5.2. FITTING THE NONLINEAR RESPONSE

We can approximate the nonlinear response of the fundamental resonance mode by the Duffing equation (see Chapter 2.2):

$$m_{\text{eff}}\ddot{x} + b\dot{x} + k_1 x + k_3 x^3 = \xi F_{\text{el}} \cos(\omega t), \tag{5.1}$$

where x is the deflection of the membrane's centre, b is the damping constant, k_1 and k_3 are the linear and cubic spring constants and $m_{\mathrm{eff}} = \alpha m$ and ξF_{el} are the mass and the applied electrostatic force corrected by factors (α and ξ) that account for the mode-shape of the resonance (for a rigid-body vertical motion of the membrane α and ξ are both 1). As shown in the Chapter 2.2, for the fundamental mode of a fixed circular membrane $\xi = 0.432$ and $\alpha = 0.269$. The parameters in the Duffing equation (5.1) are related to the resonance frequency ω_0 ($\omega_0 = 2\pi f_0$) and the Q-factor by $Q = \omega_0 m_{\mathrm{eff}} / b$ and $\omega_0^2 = k_1 / m_{\mathrm{eff}}$.
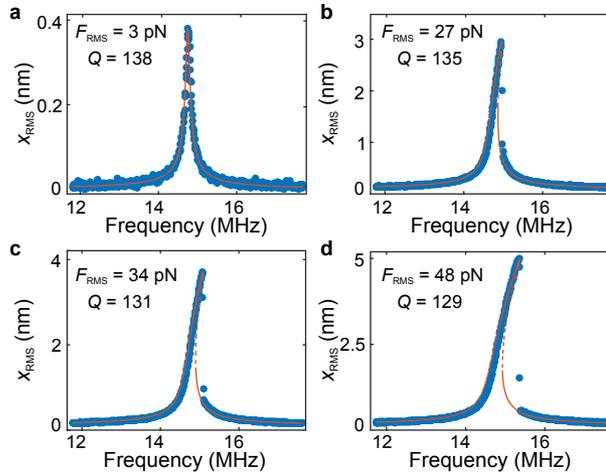
5

Figure 5.2: **Measurements and fits of the nonlinear frequency response curves of device 1.** Measured traces (blue scatter plot) and the corresponding fits (red curves) showing both the stable (solid line) and the unstable (dashed line) solutions of the Duffing equation. **a-d,** Frequency response curves of the device from Figure 5.1 at four different driving forces, denoted in the top left corner of each panel, along with the extracted Q-factors. The extracted cubic spring constant is $k_3 = 1.35 \cdot 10^{15} \mathrm{Nm}^{-3}$.

The fundamental resonance frequency ($f_0 = 14.7$ MHz) is extracted from the linear response curves at low driving powers (Figure 5.1b), and is directly related to the pre-tension (n_0) of the membrane: $n_0 = 0.69\pi^2 f_0^2 R^2 \rho h$, where ρ is the mass density of the membrane (for device 1, $n_0 = 0.107$ Nm^{-1}). In order to fit the set of nonlinear response curves, the steady-state solution of the Duffing equation (Equation (5.1)) is converted to a set of algebraic equations using the harmonic balance method (see Chapter 3.3). Using these equations, the entire set of curves can then be fitted by a least-squares optimization algorithm. Since N curves are fitted simultaneously, the expected fitting error is roughly a factor $\sqrt{N}$ lower than that of single curve fit.

The Q-factor is implicitly related to k_3 by a function $Q_i = Q_i(k_3, A_{\mathrm{max,i}}, F_{\mathrm{el,i}})$, where $A_{\mathrm{max,i}}$ are the peak amplitudes and $F_{\mathrm{el,i}}$ are the driving force amplitudes for each of the measured curves [100, 135] (see Chapter 3.3). The amplitudes $A_{\mathrm{max,i}}$ are found from the experimental data and the whole dataset is fitted using a single fit parameter: the cubic spring constant k_3. The results of this procedure are presented in Figure 5.2a-d, which shows four frequency response curves and their corresponding fits. The solutions of the

steady-state amplitude for the Duffing equation (red curves in Figure 5.2) are plotted by finding the positive real roots x^2 of:

$$
\begin{aligned}
\xi^2 F_{\text{el}}^2 \quad = \quad & (\omega^2 b^2 + m_{\text{eff}}^2 (\omega^2 - \omega_0^2)^2) x^2 \\
& -\frac{3}{2} m_{\text{eff}} (\omega^2 - \omega_0^2) k_3 x^4 + \frac{9}{16} k_3^2 x^6.
\end{aligned}
\tag{5.2}
$$

A good agreement between fits and data is found using the single extracted value $k_3 = 1.35 \cdot 10^{15}$ Nm^{-3}, which demonstrates the correspondence between the measurement and the underlying physics. We note that at higher driving amplitudes, we also observe a reduction in the Q-factor (by nearly 10% at the highest measured driving amplitude). This can be a signature of nonlinear damping mechanisms which is in line with previously reported measurements on graphene mechanical resonators [67, 104, 136]. In the following section, we will lay out the theoretical framework to relate the extracted cubic spring constant k_3 to the Young's modulus of the membrane.

5.3. THEORY

The nonlinear mechanics of a membrane can be related to its material parameters via its potential energy. The potential energy of a radially deformed circular membrane with isotropic material properties can be approximated by a function of the form:

$$
U = \frac{1}{2} C_1 n_0 x^2 + \frac{1}{4} C_3(v) \frac{Eh\pi}{R^2} x^4,
\tag{5.3}
$$

where R and h are the membrane's radius and thickness respectively. Bending rigidity is neglected, which is a good approximation for $h/R < 0.001$ [137]. C_1 and $C_3(v)$ are dimensionless functions that depend on the deformed shape of the membrane and the Poisson's ratio v of the material. The term in equation (5.3) involving C_1 represents the energy required to stretch a membrane under a constant tensile pre-stress, the C_3 term signifies that the tension itself starts to increase for large membrane deformations. The out-of-plane mode shape for the fundamental resonance mode of a circular membrane is described by a zero-order Bessel function of the first kind ($J_0(r)$). Numerical calculations of the potential energy (5.3) of this mode give $C_1 = 1.56\pi$ and $C_3(v) = 1/(1.269 - 0.967v - 0.269v^2)$ (see Chapter 2.2). Using equation (5.3) the nonlinear force-deflection relation of circular membranes is given by

$$
F = \frac{dU}{dx} = k_1 x + k_3 x^3 = C_1 n_0 x + C_3(v) \frac{Eh\pi}{R^2} x^3.
\tag{5.4}
$$

The functions C_1 and C_3 have previously been determined for the potential energies of statically deformed membranes by AFM [124, 138] and uniform gas pressure [139, 140]. Their functional dependence depends entirely on the shape of the deformation of the membrane. In Table 5.1 we summarize the functional dependences of k_1 and k_3 for the 3 types of membrane deformation.

	k_1	k_3	Def. shape
AFM	πn_0	$\dfrac{1}{(1.05-0.15v-0.16v^2)^3}\dfrac{Eh}{R^2}$	
ΔP	$4\pi n_0$	$\dfrac{8\pi}{3(1-v)}\dfrac{Eh}{R^2}$	
This work	$1.56\pi n_0$	$\dfrac{\pi}{1.27-0.97v-0.27v^2}\dfrac{Eh}{R^2}$	

Table 5.1: **Values for k_1 and k_3 for different deformation shapes.** k_1 and k_3 for AFM nanoindentation (AFM), bulge testing of membranes (ΔP) and the nonlinear dynamics method (this work) for the fundamental resonance mode. The corresponding deformation shape, which determines the functional dependence of k_1 and k_3, is shown on the right.

By combining Equation 5.4 with the obtained functions for C_1 and C_3 from Table 5.1 (last row), the Young's modulus E can be determined from the cubic spring constant k_3 by

$$E = \frac{(1.27-0.97v-0.27v^2)R^2}{\pi h}k_3. \tag{5.5}$$

From this equation, with the value of k_3 extracted from the fits, a Young's modulus of $E = 594 \pm 45$ GPa is found, which is in accordance with literature values which range from $430-1200$ GPa [25, 130]. By calculating the standard deviation out of nine repeated measurements, the measurement error was determined to be 8 %, which is comparable to other methods for determining the Young's modulus of 2D materials [17]. The numerical error in the Young's modulus from the fitting procedure is typically < 0.5 % (defined as the 95 % confidence interval of the fit), as determined from the raw data and the fits. Our measurement error is therefore mainly experimental. Using $E = 594$ GPa, the

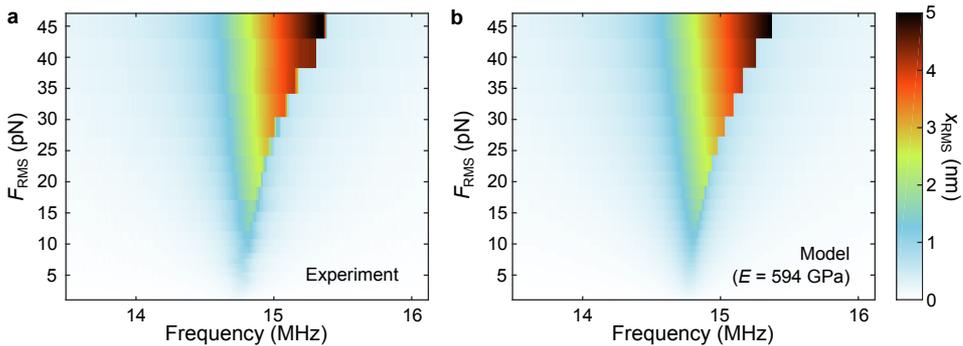Figure 5.3: **Comparison between the measured and the modelled response. a,** Measured and **b,** modelled RMS motion amplitude (x_{RMS}) using the fitted value for the Young's modulus ($E = 594$ GPa) for the device shown in Figure 5.1 (device 1).

nonlinear dynamic response of the system can be modelled for different driving powers and frequencies. Figure 5.3 shows colour plots representing the RMS amplitude of the motion of the membrane centre as a function of frequency and driving force. Excellent agreement is found between the experiment (Figure 5.3a) and the model (Figure 5.3b).

In order to confirm the validity of the method, we performed an AFM nanoindentation measurement on the same graphene drum. A force-deflection measurement, taken at the centre of the drum, is plotted in Figure 5.4 (black dots). The curve is fitted by the AFM force-deflection equation given in Table 5.1, yielding $E = 591$ GPa and $n_0 = 0.093$ Nm^{-1} (red curve in Figure 5.4). The blue curve shows the expected force-deflection curve based on the values for the Young's modulus and pre-tension extracted from the nonlinear dynamic response fits. The two curves are in close agreement.
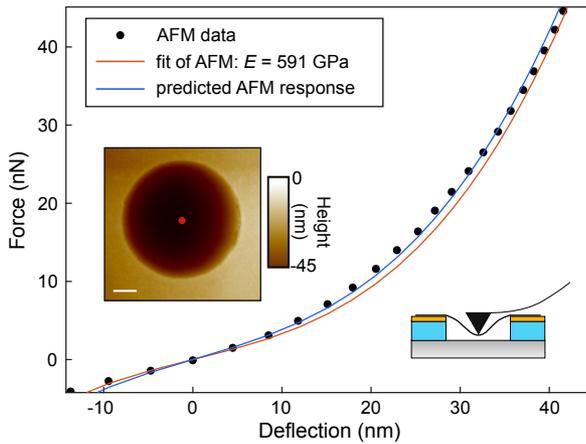
Figure 5.4: **AFM force-deflection measurement.** Force-deflection curve during tip retraction and the corresponding fit (red curve). Inset shows the AFM image of the drum (scale bar is 1 μm). The curve is taken at the centre of the drum for device 1 (marked by the red dot in inset). The blue curve represents the predicted AFM response using the $n_0 = 0.107$ Nm^{-1} and $E = 594$ GPa, obtained from the fit of the nonlinear dynamic response.

To demonstrate the versatility of the method, additional measurements on two MoS$_2$ nanodrums from the same flake are presented in Figure 5.5a-b. The extracted Young's moduli are: (a) $E = 315 \pm 23$ GPa and (b) $E = 300 \pm 18$ GPa. As with device 1, the measurement error was determined by taking the standard deviation from 9 repeated measurements. These numbers are also in agreement with literature values ($E_{MoS_2} = 140 - 430$ GPa [25, 124]). The extracted pre-tension of the drums is (a) $n_0 = 0.22$ Nm^{-1} and (b) $n_0 = 0.21$ Nm^{-1}.

5.4. DISCUSSION

There are several considerations that one needs to be aware of when applying the proposed method. In an optical detection scheme, as the one presented in this work, the cavity depth has to be optimized so that the photodiode voltage is still linearly related to the motion at high amplitudes and the power of the readout laser has to be kept low

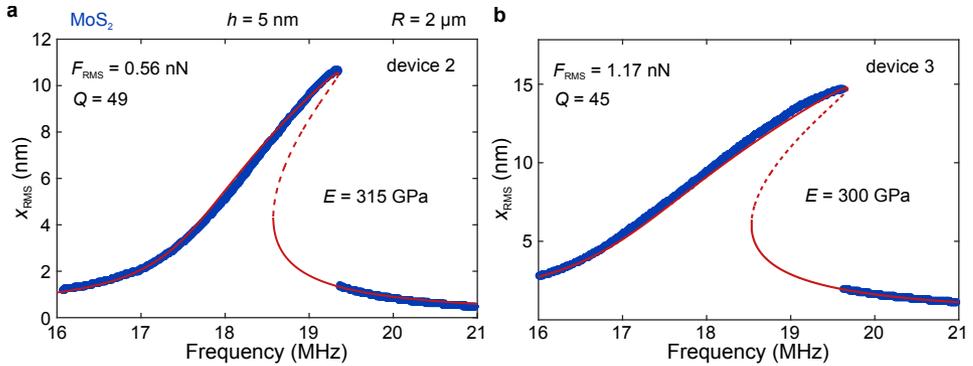Figure 5.5: **Measurements on two MoS$_2$ drums.** Measurements (blue dots) and fits (drawn red curves: stable solutions; dashed red curves: unstable solutions) of two 5 nm-thick MoS$_2$ drums with Young's moduli of: **a,** device 2: 315 GPa and **b,** device 3: 300 GPa.

to avoid significant effects of optothermal back-action [113]. The proposed mathematical model assumes that the bending energy is much smaller than the membrane energy. This is valid for membranes under tension (thickness-to-radius ratio $h/R < 0.001$) [137], as is most often the case with suspended 2D materials [33, 34, 36]. It is noted that the electrostatic force also has a nonlinear spring-softening component due to its displacement amplitude dependence. However, in the current study, the vibration amplitudes are much smaller than the cavity depth and this contribution can be safely neglected (see Appendix 5.6.1 for derivation). In addition, the method requires knowledge of the mass of the resonator, which might be affected by contamination. In the presented data, the close agreement between the extracted Young's modulus and the one determined by AFM (which is independent of the mass of the membrane) suggests that the mass estimate is accurate and effects of contamination are small.

Compared to conventional mechanical characterization methods [16, 17, 103, 124–127], the presented method provides several advantages. Firstly, no physical contact to the flake is required. This prevents effects such as adhesion and condensation of liquids between an AFM tip and the membrane, that can influence the measurements. Moreover, the risk of damaging the membrane is significantly reduced. The on-resonance operation allows the usage of very small actuation forces, since the motion amplitude at resonance is enhanced by the Q-factor. Unlike AFM, where the force is concentrated in one point, here the force is more equally distributed across the membrane, resulting in a more uniform stress distribution. Additionally, for resonators with a high quality factor, the mode shape of vibrations is practically independent of the shape or geometry of the actuator.

The high-frequency nature of the presented technique is advantageous, since it allows for fast characterization of samples, and might even be extended for fast wafer-scale characterization of devices. Every point of the frequency response curve corresponds to many averages of the full force-deflection curve (positive and negative part) which reduces the error of the measurement and eliminates the need for offset calibration of the
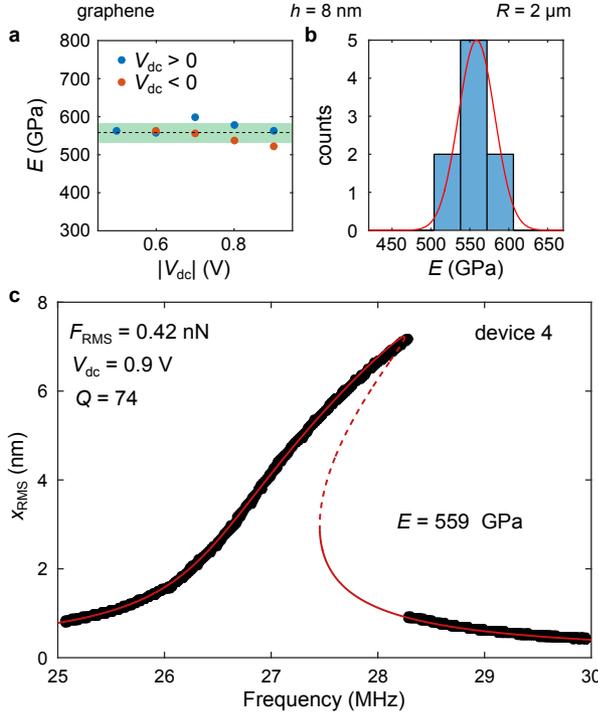
Figure 5.6: **Analysis of the robustness and repeatability of the method.** Determination of the robustness of the method using a second graphene drum (device 4). **a,** Extracted Young's modulus as a function of applied dc voltage (blue dots: positive V_{dc}, red dots: negative V_{dc}). The dashed line represents the average value of the Young's modulus and the green area represents the error in the measurement ($2\sigma_E$). Each dot represents an extracted value from fitting 8 nonlinear response curves at different driving powers. **b,** A histogram of the values extracted from **a**. The red line is a Gaussian fit to the data. **c,** Measurement (black dots) and fit (drawn red curves: stable solutions; dashed red curves: unstable solutions) of the nonlinear dynamic response of device 4, using the average value of the Young's modulus from **a** and **b**: 559 GPa.

zero point of displacement [135]. The close agreement between the AFM and nonlinear dynamics value for the Young's modulus E indicates that viscoelasticity, and other time dependent effects like slippage and relaxation, are small in graphene. Therefore, the dynamic stiffness is practically coinciding with the static stiffness. For future studies it is of interest to apply the method to study viscoelastic effects in 2D materials, where larger differences between AFM and resonant characterization measurements are expected.

To test the robustness of the method, we perform a set of nine measurements on another graphene drum (device 4, with thickness $h = 8$ nm and radius $R = 2\,\mu$m), under different conditions. Each of the measurements (blue and red dots in Figure 5.6a) represents a fit of 8 nonlinear response curves at different driving powers for a fixed dc voltage. The same set of measurements are presented in the histogram given in Figure 5.6b. The extracted average value of the Young's modulus is 559 ± 23 GPa, which is in the same order of magnitude as the one for device 1 (where all nine measurements were taken at a single dc voltage). In Figure 5.6c we plot the raw data (black dots) and the fit (red curve)

of the nonlinear response curve at $V_{dc} = 0.9$ V and $F_{RMS} = 0.42$ nN using the extracted average Young's modulus from (a) and (b). The data and the fit show good agreement, which confirms that the method is robust against measurement parameter variations. The robustness of the method can also be assessed qualitatively from the effect of the Young's modulus on the nonlinear response curve as shown in Appendix 5.6.2. There we plot the predicted response of the drum using different values of the Young's modulus to visualize its effect on the shape of the nonlinear frequency response curves.

	material	E (GPa)	σ_E (GPa)
device 1	graphene	594	45
device 2	MoS_2	315	23
device 3	MoS_2	300	18
device 4	graphene	559	23

Table 5.2: **Summary of extracted Young's moduli and corresponding errors (σ_E) of the different samples measured in this work.**

In Table 5.2 we show a summary of the measurements of the four devices presented in this chapter. In all 4 cases the error in the Young's modulus (σ_E/E) is less than 8 % and the values of the Young's moduli of the two graphene and the two MoS_2 drums are within each other's error bars. The presented method can prove to be useful for fast statistical analysis of the spread in material properties [103, 141–143] and variability of device properties in future 2D material-based products.

In conclusion, we provide a contactless method for characterizing the mechanical properties of suspended 2D materials using their nonlinear dynamic response. A set of nonlinear response curves is fitted using only one fit parameter: the cubic spring constant. Mathematical analysis of the membrane mechanics is used to relate the Duffing response of the membrane to its material and geometrical properties. These equations are used to extract the pre-tension and Young's modulus of both graphene and MoS_2, which are in close agreement with nanoindentation experiments. The non-contact, on-resonant, high-frequency nature of the method provides numerous advantages, and makes it a powerful alternative to AFM for characterizing the mechanical properties of 2D materials. We envision applications in metrology tools for fast and non-contact characterization of 2D membranes in commercial sensors and actuators.

5.5. METHODS

SAMPLE FABRICATION

The chips are fabricated using the process flow described in Chapter 3.4.1. The final depth of the cavities is $g_0 = 385$ nm and their radii are $R = 2 - 2.5$ μm. The flakes of graphene and MoS$_2$ are exfoliated from natural crystals.

MEASUREMENT SETUP

The sample is mounted in a vacuum chamber ($2 \cdot 10^{-6}$ mbar) to minimize damping by the surrounding gas. Using the silicon wafer as a backgate, the membrane is driven by electrostatic force and its dynamic motion is detected using a laser interferometer (see [97]). The detection is performed at the centre of the drum (using a laser power of 0.42 mW), using a Vector Network Analyser (VNA). A dc voltage (V_{dc}) is superimposed on the ac output of the VNA (V_{ac}) through a bias-tee (BT), such that the small-amplitude driving force at frequency ω is given by $F_{el}(t) = \xi \varepsilon_0 R^2 \pi V_{dc} V_{ac} \cos(\omega t)/g_0^2$. Even though the determination of the force is mathematically straightforward, the calculated force does not always match the force felt by the resonator, because of uncertainties in determining the gap size g_0 (due to membrane slack), the dc voltage V_{dc} (due to residual charge on the 2D flake) and the capacitance of the device (due to fringe fields). In order to cross-check the value of the driving force, we employ a second method to determine it based on the peak RMS amplitude ($x_{RMS}|_{\omega=\omega_0}$) of the calibrated linear frequency response curves using $F_{RMS} = \frac{\omega_0^2 m_{eff}}{Q} x_{RMS}$. The procedure is discussed in more detail in the Chapter 3.2 and an example of the force derivation is shown in Figure 3.4. The measured VNA signal (in V/V) is converted to x_{RMS}, using a calibration measurement of the thermal motion taken with a spectrum analyser [33, 95, 97]. The calibration procedure and the uncertainties stemming from the assumption of linear transduction are discussed in detail in Chapters 3.1.1 and 3.1.2. The temperature increase due to laser heating is estimated in Appendix 5.6.3.

5.6. APPENDIX

5.6.1. ESTIMATION OF THE ELECTROSTATIC SPRING SOFTENING

In this section the effect of nonlinearities in the electrostatic force on the nonlinear spring constant is estimated.

The electrostatic force acting on the membrane is given by

$$F_{el} = -\frac{dU_{el}}{dx} = -\frac{1}{2}\frac{dC_g}{dx}V^2, \tag{5.6}$$

where $U_{el} = \frac{1}{2}C_g V^2$ is the electrostatic energy, $V = V_{dc} + V_{ac}\cos(\omega t)$ is the applied voltage and C_g is the gate capacitance. Assuming $x \ll g_0$, where g_0 is the gap between the membrane and the backgate, the gate capacitance can be approximated using a parallel plate capacitor model:

$$C_{\mathrm{g}} = \varepsilon_0 \frac{R^2 \pi}{g_0 - x}, \tag{5.7}$$

where R is the radius of the membrane and ε_0 is the vacuum permittivity. The resulting electrostatic force is given by:

$$F_{\mathrm{el}} = \frac{1}{2} \frac{\varepsilon_0 R^2 \pi}{(g_0 - x)^2} (V_{\mathrm{dc}} + V_{\mathrm{ac}} \cos(\omega t))^2. \tag{5.8}$$

If we expand this expression around $x = 0$, using $x/g_0 \ll 1$, we get:

$$F_{\mathrm{el}} \approx \frac{1}{2} \varepsilon_0 R^2 \pi (V_{\mathrm{dc}} + V_{\mathrm{ac}} \cos(\omega t))^2 \left[\frac{1}{g_0^2} + \frac{2x}{g_0^3} + \frac{3x^2}{g_0^4} + \frac{4x^3}{g_0^5} \right]. \tag{5.9}$$

The first term ($\frac{1}{g_0^2}$) is the dominant electrostatic actuation term and the second term is what is usually described as a spring softening term ($\frac{2x}{g_0^3}$). This term influences only the linear spring constant of the resonator. The term including x^3 will have a softening effect on the cubic spring constant: $k_{3,\mathrm{soft}} = \frac{2}{g_0^5} \varepsilon_0 R^2 \pi V_{\mathrm{dc}}^2$ (for $V_{\mathrm{dc}} \gg V_{\mathrm{ac}}$ and $g_0 \gg x$). The resulting cubic spring constant $k_{3,\mathrm{tot}}$ will be given by:

$$k_{3,\mathrm{tot}} = k_3 - k_{3,\mathrm{soft}}. \tag{5.10}$$

The ratio of the two contributions (using the expression for k_3 from Equation (2.20)) is:

$$\frac{k_3}{k_{3,\mathrm{soft}}} = \frac{1}{1.269 - 0.967\nu - 0.269\nu^2} \frac{E h g_0^5}{2\varepsilon_0 R^4 V_{\mathrm{dc}}^2}. \tag{5.11}$$

For a Young's modulus $E = 594$ GPa, radius of $R = 2.5\ \mu m$, thickness of $h = 5$ nm, gap size $g_0 = 385$ nm and $V_{\mathrm{dc}} \leq 3$ V, this ratio becomes:

$$\frac{k_3}{k_{3,\mathrm{soft}}} \approx 3000, \tag{5.12}$$

which means that the electrostatic softening will have a negligible effect on the extracted Young's modulus (resulting in an error of < 0.1%). It should be noted that the cavity depth has a significant influence on the effect of electrostatic softening of the cubic spring constant. To get reasonable error margins (< 5%), the ratio of Equation (5.12) should be kept above 20.

5.6.2. The effect of the Young's modulus on the strength of the nonlinear dynamic response

In Figure 5.7 we show the frequency response of a strongly-driven graphene drum (black dots) under a constant force ($F_{\mathrm{RMS}} = 48$ pN). The coloured curves are the modelled response curves under constant force and with a fixed quality factor ($Q = 129$) and resonance frequency $f_0 = 14.7$ MHz). The different colours correspond to the frequency responses of the model using different values for the Young's modulus to show how the nonlinear response is influenced by the Young's modulus.
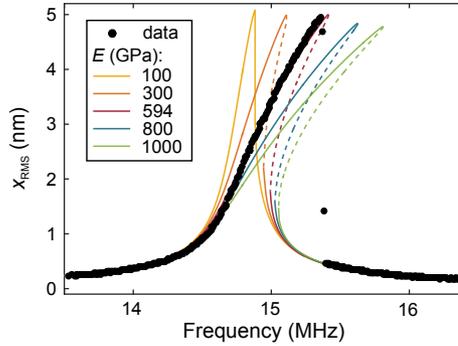
Figure 5.7: **Sensitivity of the nonlinear response to the Young's modulus**. The measured trace (at F_{RMS} = 48 pN) is represented by the black dots. The coloured lines represent the modelled response using fixed values for the damping and the driving force and varying values for the Young's modulus. The yellow line represents the modelled response using the fitted value for the Young's modulus ($E = 594$ GPa).

5.6.3. ESTIMATION OF THE TEMPERATURE OF THE DRUM

Another important parameter that may influence the calibration is the actual temperature of the membrane. Even though the measurements are conducted at room temperature, the measurement laser locally heats up the membrane. For this reason, the laser power throughout the measurement is kept relatively low (0.42 mW). To estimate the temperature increase due to the laser heating, we perform measurements at varying laser power. From the measured resonance frequency we can determine the strain of the membrane (ε). This measurement is shown in Figure 5.8.

As expected, the strain grows linearly with the laser power, due to a finite temperature increase ΔT. This can be modelled with a simple equation:

$$\varepsilon = \varepsilon_0 - \alpha_T \Delta T \tag{5.13}$$
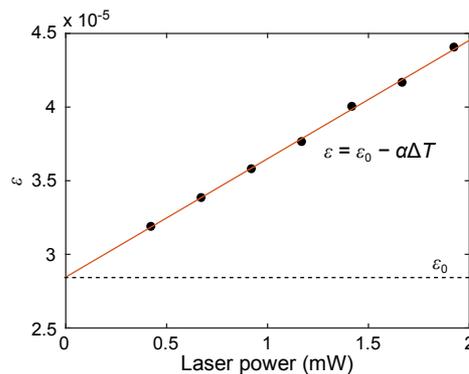
Figure 5.8: **Temperature estimation**. Extracted strain (ε) as a function of the measurement laser power. The black dots are measured pre-strain calculated from the resonance frequency. The red line is a linear fit to the data. The black dashed line is the extrapolated initial strain (ε_0).

where ε_0 is the mechanical pre-strain, α_T is the thermal expansion coefficient and ΔT is the temperature increase. The second term in the equation is the thermally induced strain. Since α_T for graphene is negative [71], the total strain of the drum increases with increasing laser power.

By fitting the measured data with a linear fit, we can extrapolate the curve and estimate ε_0 (see Figure 5.8). Using $\alpha_T \approx -6 \cdot 10^{-6} K^{-1}$, we find the temperature increase at 0.42 mW laser power to be less than 0.8 K. This temperature difference, following Equations (3.3) and (3.6), results in about 0.1 % error in the amplitude calibration.

5

6

STATIC CAPACITIVE PRESSURE SENSING USING A SINGLE GRAPHENE MEMBRANE

To realize nanomechanical graphene-based pressure sensors, it is beneficial to have a method to electrically readout the static displacement of a suspended graphene membrane. Capacitive readout, typical in micro-electro-mechanical systems (MEMS), gets increasingly challenging as one starts shrinking the dimensions of these devices, since the expected responsivity of such devices is below 0.1 aF/Pa. To overcome the challenges of detecting small capacitance changes, we design an electrical readout device fabricated on top of an insulating quartz substrate, maximizing the contribution of the suspended membrane to the total capacitance of the device. The capacitance of the drum is further increased by reducing the gap size to 110 nm. Using external pressure load, we demonstrate successful detection of capacitance changes of a single graphene drum down to 50 aF, and pressure differences down to 25 mbar.

NANOMECHANICAL devices from suspended graphene and other two-dimensional materials have been receiving growing interest in the past few years for their potential as sensitive pressure [32, 39, 62–64, 144] and gas [21, 40, 59] sensors. To realize integrated, small and low-power devices, it is necessary to have all-electrical on-chip transduction schemes, in contrast to the currently often employed laser interferometry techniques for the readout of their dynamic motion and static deflection.

Reports on electrical readout of graphene membrane nanomechanical devices have employed readout schemes based on electrical transconductance [43, 62] and piezoresistivity [39, 63, 64]. Both of these rely on the change in the conductance of the membrane as a function of deflection, which is then used to sense the motion of the membrane. Although these methods can be very sensitive, the graphene conductance can also be affected by variations in gas composition, humidity, light intensity and temperature. Moreover, the conductance is not only related to the deflection of the graphene membrane, but depends also on material parameters like the electron mobility and piezoresistive coefficients. These approaches therefore require calibration and a high degree of stability of the graphene and insensitivity to variations in its surroundings.

In contrast, the capacitance between a graphene membrane and a bottom electrode is, to first order, a function only of the geometry of the system and, therefore, the deflection of the membrane. A measurement of the capacitance of the membrane can therefore be used to calculate its deflection, which makes capacitance detection an interesting alternative method for electrical readout of nanomechanical graphene sensors. Dynamic (on-resonance) capacitive readout has been demonstrated on suspended graphene bridges [2, 65] and in suspended graphene nanodrums coupled to superconducting cavities at cryogenic temperatures [145–147]. The dynamic performance of such devices greatly deteriorates at room temperature and atmospheric pressure as the quality factor and therefore the motion amplitude at a given force are much smaller [32–34]. Capacitive readout of the *static* deflection of a graphene drum is hence a more viable solution for graphene-based devices operating in ambient conditions. This is, however, challenging to realize, mainly due to the on-chip parasitic capacitances that are usually much larger than the capacitance of the device and also because low-frequency measurements are more susceptible to noise. One way of tackling these issues is increasing the total capacitance of the device as proposed [148] and later realized [149] on a voltage tunable capacitor array comprised of thousands of unsealed graphene bridges in parallel.

In this chapter we present capacitive detection of the static deflection of a *single* few-layer graphene drum enclosing a cavity, which allows us to benchmark its performance as a pressure sensor.

6.1. DEVICE FABRICATION

The total capacitance of a suspended graphene drum and the underlying electrode in typical sample geometries (circular drum 5-10 μm in diameter, suspended over a 300 nm deep cavity), ranges from 0.5 to 2 femtoFarads. A displacement of such a drum of 1 nm would result in a capacitance change of only 2-6 attoFarads. Fabricating readout circuitry sensitive enough to detect such changes is faced with a few challenges. (i) Very
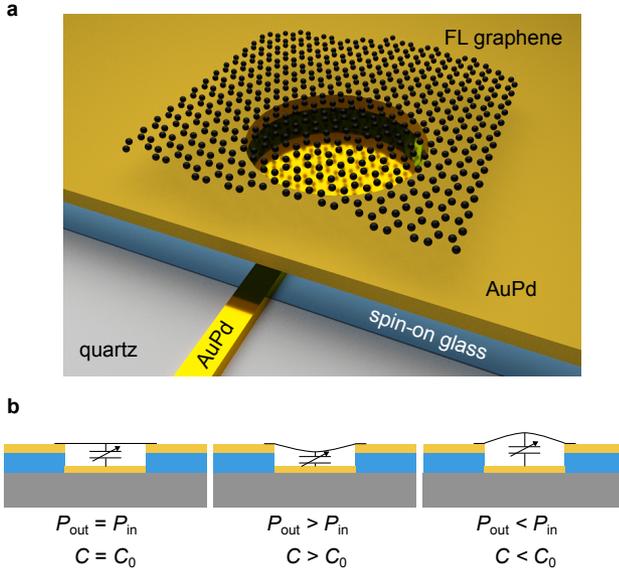
Figure 6.1: **Operating principle of the device. a,** A 3D schematic of the device: a capacitor is formed between a graphene drum suspended over a metallic cavity and a bottom metallic electrode that runs underneath an insulating (spin-on glass) oxide layer. The entire device is fabricated on top of an insulating quartz wafer. **b,** Actuation principle: external pressure load is applied. Depending on the pressure difference between the cavity and the outside environment, the nanodrum will bulge upwards or downwards resulting in a decrease or increase of the measured capacitance.

6

shallow gaps are needed in order to maximize the capacitance of the device; (ii) parasitic capacitances between the readout electrodes need to be as small as possible to improve the signal to noise ratio; (iii) the surface should be flat and adhesive to facilitate the transfer of graphene; (iv) additionally, to keep the pressure in the reference cavity constant, the cavity needs to be hermetically sealed by the graphene membrane. To address these challenges, we develop a device with electrical readout fabricated on top of a quartz substrate, which substantially reduces the parasitic capacitance of the electrical circuitry. To demonstrate the sensing concept, we transfer a few-layer graphene flake on top of the device and we use external gas pressure load to deflect the drum, reading out the corresponding change in the capacitance. A 3D schematic of the proposed device is shown in Figure 6.1a. The capacitor consists of a circular electrode on the bottom and a suspended few-layer (FL) graphene drum on top, forming a sealed cavity. The bottom electrode runs underneath a dielectric layer of spin-on-glass (SOG), which separates it from the top metal electrode. The drum is mechanically supported by the top electrode, which also serves as an electrical contact to the graphene. Figure 6.1b shows the sensing principle: when the pressure inside the cavity (P_{in}) is equal to the outside pressure (P_{out}), the capacitance of the device is given by the parallel plate capacitor formed by the graphene and the bottom electrode: C_0. When the outside pressure is higher than the pressure inside the cavity, this results in a positive pressure difference across the
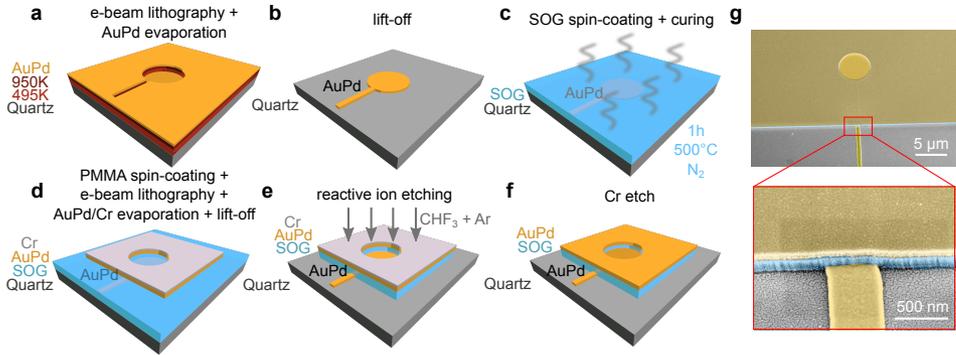
Figure 6.2: **Fabrication process flow. a-g,** Fabrication steps. **h,** A false-coloured SEM image of the device showing the top and bottom electrodes (yellow) and the separating SOG layer (blue). A zoomed-in image of the AuPd/SOG/AuPd interface is shown in the bottom panel.

membrane, causing it to bulge downwards, which manifests itself as an increase of the measured capacitance. Conversely, if the pressure inside the cavity is higher than the outside pressure, the drum bulges upwards, resulting in a decrease of the measured capacitance.

Fabrication requires two e-beam lithography steps for the bottom and top electrodes. Both lithographic steps use two layers of PMMA resist (A6 495K [300 nm] and A3 950K [100 nm]) in order to create sloped resist walls which facilitate the lift-off. To minimize charging effects during the e-beam patterning, a 10 nm layer of Au is sputtered on top of the resist prior to the e-beam exposure. The Au layer is removed before developing the resist using KI/I_2 gold etchant. Figure 6.2a shows a sketch of the sample after developing the resist in MIBK:IPA (1:3) and evaporating 5 nm of titanium (5 nm) and 60 nm of gold-palladium ($Au_{0.6}Pd_{0.4}$) to form the bottom electrode. The titanium is used as a thin adhesion layer and is not shown in the figure.

After lift-off (Figure 6.2b), a layer of FOX XR-1451 spin-on-glass (SOG) is spin-coated on the chip. In order to improve the conformity of the SOG layer to the underlying surface, the SOG layer is baked in two stages: 3 minutes at 150 °C and 3 minutes at 250 °C. Subsequently, the chip is placed in a N_2 furnace at 500 °C at 1 atm, which cures the SOG, making it mechanically harder and also improving its surface smoothness and step coverage (Figure 6.2c). The baking and curing processes are essential for obtaining a flat and smooth surface, which is important, as it largely influences the roughness of the electrode evaporated on top of it. Smooth surfaces enhance adhesion and thereby facilitate the transfer of graphene. The current process flow results in a cavity depth of 110 nm. The top electrodes are fabricated on top of the SOG layer, following the same steps of Figure 6.2a-b, with a different combination of metals: $Ti/Au_{0.6}Pd_{0.4}/Cr$ (5 nm/90 nm/30). This is shown in Figure 6.2d. The top layer of chromium is used as a hard mask for the following etching step, to avoid contamination of the underlying AuPd.

Figure 6.2e shows the formation of the cavities by using reactive ion etching (RIE) of the SOG everywhere around the top electrodes. This is done at 7 μbar in CHF$_3$:Ar (50:2.5 sccm). The remaining Cr is then etched away using Cr etchant, which results in the final device (Figure 6.2g). The cavity depth can be easily tuned by changing the thickness of the top layer of AuPd. In Figure 6.2h we show a false-coloured SEM image of the device after the removal of the Cr. The bottom panel shows a zoom-in of the interface between the two electrodes (yellow) and the SOG layer in between (blue). After the device has been fabricated, graphene flakes are transferred on top of the cavities using a dry transfer technique. The resulting graphene drums are 5 μm in diameter.

6.2. EXPERIMENTAL PROCEDURE

The measurement setup is shown in Figure 6.3. The device is mounted in a vacuum chamber connected to a membrane pump and a pressure controller. The pressure controller is connected to a N$_2$ gas bottle (purity 99.999 %) and the pressure of the gas inside the chamber can be controlled linearly by using a 0-10 V input voltage. The pressure controller has a voltage output, which enables a direct readout of the pressure inside the chamber. In this configuration, the pressure can be regulated between 1-1000 mbar (0-10 Volts on the input) with a resolution of $\approx$ 0.5 mbar. The capacitance of the graphene drum is measured using an LCR meter in a two-port configuration. All capacitance measurements are performed at a frequency of 1 MHz with a voltage amplitude of $V_p =$ 100 mV. The integration time for the capacitance readout is 1500 ms. The inset of Figure 6.3 shows an optical image of the measured device: a 6 nm - thick graphene drum.

6

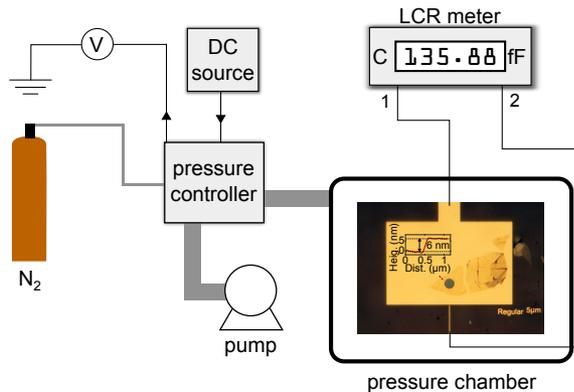Figure 6.3: **Schematic of the measurement setup.** The device is mounted in a pressure chamber connected to a pressure controller with a dc voltage control input. The voltage output of the pressure controller is proportional to the actual pressure inside the chamber (P_{out}). The capacitance of the drum is read out using an LCR meter. The figure shows an optical image of the device (a FL graphene drum with a thickness of 6 nm).

6.3. RESULTS

The measurement scheme is sketched in Figure 6.4a. Although graphene hermetically seals off the cavity, slow gas permeation usually takes place through its edges or through the underlying oxide [19]. We make use of this observation and keep the sample in vacuum for 48 h prior to each measurement to ensure that the gas from the cavity is completely evacuated ($P_{in} \approx 0$). Then a square wave is applied to the control input of the pressure controller, such that the pressure in the chamber (P_{out}) is changed in a step-like fashion. Figure 6.4b shows the measured capacitance of the device as a function of time for two values of the pressure step height: $P_{max} = 600$ mbar (blue) and 250 mbar (red). Both graphs show that the capacitance rises when the pressure inside the chamber P_{out} increases, and jumps back to the initial value upon pumping down. Despite the care taken to eliminate parasitic capacitances, by using a quartz substrate and local gate, the total capacitance of the device is ≈ 590 fF, mostly stemming from the parasitic capacitance of the wiring and the on-chip inter-electrode capacitance, since the contribution of the graphene drum is calculated to be only 1.58 fF.
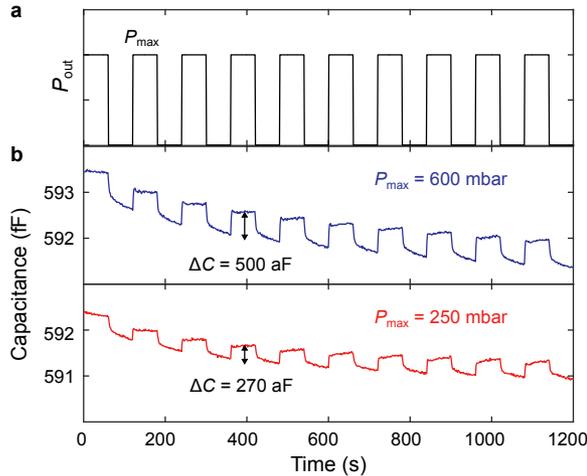
Figure 6.4: **Measurements using a square wave pressure input. a,** Experimental procedure: the pressure is changed from vacuum to P_{max} with a period of 120 s. **b,** Capacitance of the device as a function of time for two different runs using $P_{max} = 600$ mbar (top) and $P_{max} = 250$ mbar (bottom). Both panels show the extracted capacitance step height (ΔC) at the moment of changing the pressure.

Starting from $P_{in} = P_{out}$ and assuming an abrupt change in P_{out}, such that permeation effects can be neglected, the expected capacitance change can be calculated using an implicit relation between the pressure difference across the membrane (ΔP) and the deflection of the membrane's centre (x) [1]:

$$\Delta P = \frac{4 n_0}{R^2} x + \frac{8 E h}{3 R^4 (1 - \nu)} x^3, \tag{6.1}$$

where n_0 is the pre-tension of the membrane, R and h are its radius and thickness respectively and E and ν are the Young's modulus and the Poisson's ratio of the material. Knowing x and the spherical deformation shape of the membrane ($U(r) = x(1 - \frac{r^2}{R^2})$), the capacitance can be calculated using the parallel plate approximation as:

$$C = 2\pi\varepsilon_0 \int_0^R \frac{r}{g_0 - U(r)}\, dr, \tag{6.2}$$

where ε_0 is the vacuum permittivity and g_0 is the gap size. Using $n_0 = 0.1$ N/m and $E = 1$ TPa, the value of the extracted capacitance steps matches well with the numbers expected from theory. On top of the measured signal, we also measure a slow drift of the capacitance over time (see Figure 6.4). The cause of the drift is not well understood and it might be due to a combination of slow gas leakage and condensation of humidity on the electrodes [150] or on the graphene membrane itself [151].
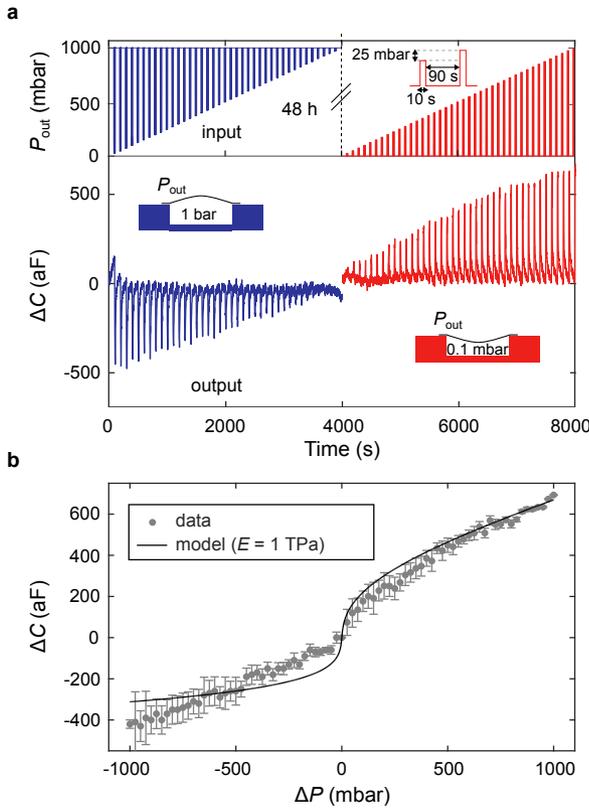
Figure 6.5: **Measurements using rising pressure steps. a,** Capacitance change as a function of time (top). Bottom: Starting from 1 bar, pressure is changed in a stepwise fashion with increasing steps of 25 mbar (10 % pulse duration with a 100 s period). The chamber is then pumped down to 1 mbar and a similar procedure is repeated with the chamber being pumped to vacuum after each step. **b,** The extracted values for ΔC as a function of the applied pressure difference across the membrane (grey dots). A theoretical fit to the data using the device dimensions, with pre-tension $n_0 = 0.1$ N/m and Young's modulus E = 1 TPa.

Using pressure pulses of increasing height we can trace out a dependence of the capacitance change on the pressure difference across the membrane. To do so, we employ a measurement protocol sketched in the inset of Figure 6.5a. The sample is kept at vacuum and short pressure steps (10 s) are applied to the sample chamber, followed by 90 s of pumping, to ensure that the cavity underneath the graphene is pumped down to vacuum before applying the next pressure step. This way, it can be safely assumed that the height of the pressure step corresponds to the actual pressure difference felt by the graphene membrane. The opposite applies for the left side of the graph (blue curve): the sample is kept at 1 bar and pressure steps of the opposite sign are applied, followed by 90 s of ambient pressure. The measured capacitance change ΔC is plotted in the bottom panel of Figure 6.5a. The aforementioned drift was subtracted for this dataset after fitting it with a polynomial (see Appendix 6.5.1).

The capacitance change is recorded as the height of the step in the measured capacitance immediately after applying the pressure pulse. Doing this for the entire span of ΔP (from -1 to +1 bar) we get a ΔC vs. ΔP curve, plotted in Figure 6.5b. The error bars at each point correspond to the RMS noise of the signal in the vicinity of the pressure step, as a measure of the uncertainty of the step determination. The black curve is the modelled response of the system for a 6 nm thick graphene membrane with a Young's modulus of 1 TPa. The model is in a good agreement with the measured response, providing further evidence that the signal is indeed coming from the displacement of the membrane. Thanks to the relatively low parasitic capacitances, despite the present drift, capacitance changes down to 50 aF could be distinguished.

6.4. DISCUSSION

The resolution of the measurement setup is limited by the resolution of the LCR meter, which is 10 aF. This corresponds to a pressure resolution of ≈ 360 Pa (or 0.36 mbar) for $\Delta P \approx 0$ and 10.6 kPa (or 106 mbar) for $\Delta P = 1$ bar. For potential application of such device as a pressure sensor, it is interesting to look at the responsivity of the device around $\Delta P = 0$. By design, the responsivity of the presented device peaks at around 0.1 aF/Pa at 0 mbar pressure difference (see Appendix 6.5.2). The root-mean-square (RMS) noise of the measurement setup is 25 aF/$\sqrt{\text{Hz}}$. However, due to the drift present in the measurements, the minimal step height that could be resolved was 50 aF. The relative error of the pressure measurement ranges from 0.6 % (for $\Delta P \approx 1$ bar) all the way up to 300 % for $-100\,\text{mbar} < \Delta P < 100\,\text{mbar}$. The accuracy of the sensor can also be influenced by morphological imperfections of the membrane itself.

There are multiple ways to increase the responsivity of the device: decreasing the thickness of the graphene (h), decreasing the pre-tension of the membrane (n_0), increasing its radius (R), or connecting N such devices in parallel. A detailed analysis of the influence of each parameter on the responsivity of the device are shown in the Appendix 6.5.2. According to the calculations, changing the thickness h does not drastically influence the responsivity. Increasing R or decreasing n_0 improve the responsivity by one or two orders of magnitude. We note that controlling the pre-tension is challenging, since it largely depends on the transfer process and usually results in large spreads [17]. Moreover, making devices with larger radii and low pre-tension would impair the yield of the devices [152] and reduce their dynamic range (due to collapse of the membrane at

high ΔP). However, increasing the number of drums in parallel N linearly increases the responsivity of the device. With more than 1000 drums in parallel (resulting roughly in a chip size of $100 \times 100 \, \mu m$) one could push the responsivity to values higher than 100 aF/Pa, resulting in a 0.1 Pa resolution using our current measurement setup.

To demonstrate the feasibility of capacitive readout of the graphene sensor with an integrated circuit, we replaced the LCR meter with an Analog Devices (AD7746) capacitance-to-digital converter chip (with dimensions $5 \times 5 \, mm^2$) which we interfaced through using the built-in I2C protocol library of an Arduino. We show an example of such measurement in the Appendix 6.5.3. Even though the signal-to-noise of this measurement is worse than the one using the LCR meter, it still serves as a proof-of-principle that on-chip detection of small capacitance changes can be realized using commercial electronic devices.

The drift in the measurement together with the poor hermeticity of the membrane hamper the long-term stability of the device. For its commercial application as a pressure sensor, the hermeticity of the device needs to be improved (e.g. by properly sealing the membrane edges) and the cross-sensitivity to the environment (humidity/gas composition) needs to be investigated more thoroughly.

In conclusion, we demonstrate on-chip capacitive readout of a single suspended graphene drum. To obtain the responsivity required for sensing such small capacitance changes, the entire fabrication is done on an insulating quartz substrate, minimizing the parasitic capacitance of the readout electrodes. We use uniform pressure load to statically deform the membrane, which results in a capacitance change of the device. Using this method, we are able to read out capacitance changes down to 50 aF and detect pressure steps down to 25 mbar. The height of the steps is consistent with predictions from the theoretical model. We also traced out a force-deflection curve by pulsing the pressure in the chamber with pulses of increasing height. The measured ΔC vs. ΔP curve matched well with theory, based on a graphene membrane with a Young's modulus of 1 TPa. We also measured a temporal drift in the capacitance, possibly originating from residual humidity in the chamber. This chapter is aimed at probing the limit of static capacitive detection of graphene nanodrums. We optimized the device to enable detection of very small capacitance changes of down to 50 aF. By combining this device design with an on-chip capacitance-to-digital converter we show a proof-of-concept demonstration of the feasibility of integrating suspended 2D membranes into next-generation pressure sensors.

6.5. APPENDIX

6.5.1. BACKGROUND DRIFT SUBTRACTION
In this section we present an example of drift subtraction using the raw data of the ΔC vs. ΔP measurement presented in Figure 6.5a of the main text (for $P_{in} \approx 0$ mbar). In Figure 6.6 the measured capacitance signal is plotted against time. As described in the main text, the pressure is increased in 25 mbar steps (with 10 s duration) followed by 90 s of pumping the chamber to vacuum. We can distinguish a background signal (defined by the minima of the measured capacitance after each pumping step) on top of which we measure sharp steps in the capacitance at the moment of introducing gas inside the

chamber. This drift can be subtracted from the measurement by fitting a (4$^{\text{th}}$ order) polynomial through these minima (red line) and subtracting it from the data (blue line). The resulting signal represents the ΔC vs. ΔP curve plotted on the right-hand side of Figure 6.5a.
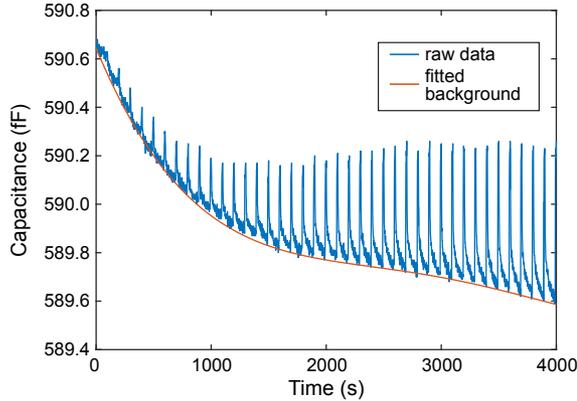

Figure 6.6: **Drift subtraction.** The blue curve represents the raw capacitance data, while the red curve is a polynomial fit of the local minima of the capacitance after each pumping step.

6.5.2. PRESSURE RESPONSIVITY

In this section we lay out the theoretical predictions of the expected capacitance change as a function of the pressure differences across the membrane, together with the expected responsivity of the device.

Using Equations (6.1) and (6.2) we model the predicted capacitance response as a function of the pressure difference across the membrane. The pressure difference ΔP is defined as $\Delta P = P_{\text{out}} - P_{\text{in}}$, where P_{out} is the pressure in the chamber and P_{in} is the pressure inside the cavity.

We start with the dimensions of the device described in the main text, namely, a single graphene membrane with a thickness of $h = 6$ nm, pre-tension $n_0 = 0.1$ N/m and a radius $R = 2.5$ μm. For each of the panels (a-d) we keep all parameters fixed, while varying only (a) the thickness, (b) the pre-tension, (c) the radius and (d) the number of identical drums connected in parallel. The top panels represent the absolute value of the expected capacitance change ($|\Delta C|$) for a given pressure difference (ΔP). The bottom panels represent the calculated responsivity ($\frac{\partial C}{\partial \Delta P}$) of the device, expressed in aF/Pa.

To be able to use such a device as a pressure sensor in mobile devices, considering the day-to-day fluctuations in the atmospheric pressure, one needs to look at the -100 mbar $\leq \Delta P \leq$ 100 mbar region of the responsivity plots, where the responsivity is usually the highest.
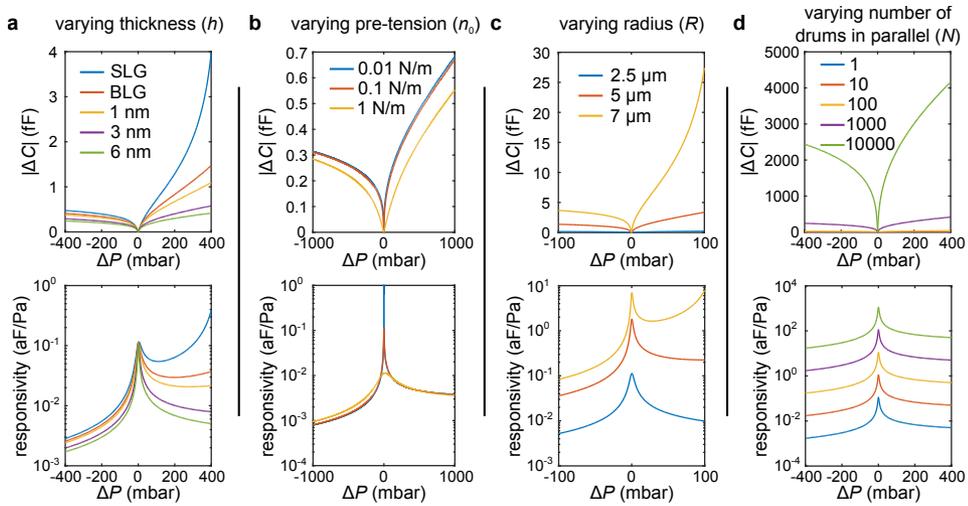
Figure 6.7: **Responsivity optimisation routes.** Calculated capacitance change (top panels) and responsivity (bottom panels) as a function of pressure difference for varying **a,** thickness; **b,** pre-tension; **c,** radius of the membrane and **d,** number of graphene drums in parallel.

It can be seen from the plots that by varying the membrane's thickness or pre-tension, one does not benefit a lot when it comes to the responsivity of the device. A larger radius, which results in a higher initial capacitance (C_0), naturally, increases the overall responsivity of the device. It has to be noted, however, that making the membranes larger, thinner or with a lower pre-tension also significantly reduces the dynamic range of the device, because it makes it easier for the membrane to collapse at a high pressure difference ΔP. Mathematically this follows directly from Equation (6.1).

One solution for increasing the responsivity of the device is increasing the number of drums connected in parallel (Figure 6.7d). This way, the dynamic range of the sensor is unchanged, whereas the overall responsivity of the system scales proportionally to the number of drums N. Using 1000 drums in parallel (resulting roughly in a $100 \times 100\ \mu m^2$ device), the responsivity peaks at 100 aF/Pa, which would, with a capacitance resolution of 10 aF, enable a pressure resolution of 0.1 Pa. Such a device could be used in next-generation pressure sensors and could have a comparable or better performance than the current state-of-the-art pressure sensors[1].

---

[1]Provided that the bottom electrodes are covered by a thin dielectric, such that the failure of a single device does not compromise the entire assembly.

6.5.3. READOUT USING AN AD7746 CHIP INTERFACED WITH AN ARDUINO

To demonstrate the integrability of the proposed device, we replaced the LCR meter with a compact, low-cost Analog Devices (AD7746) 24-bit capacitance-to-digital converter chip. According to the specifications, this chip is able to handle up to 4 pF parasitic capacitance and has a resolution of down to 4 aF. The dimensions of the readout chip are $\approx 5 \times 5$ mm^2 and it has a built-in I^{2}C interface.
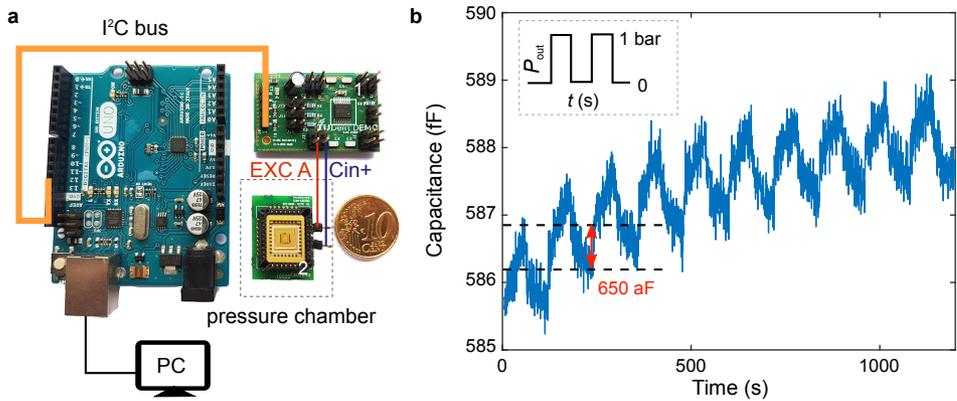

Figure 6.8: **Measurement using an AD7746 chip. a,** Schematic of the measurement setup with an AD7746 capacitance-to-digital converter chip (1). The AD7746 is connected to the sample (2) using two wires (EXC A and Cin+). The sample together with the chip carrier is mounted inside the pressure chamber. The AD chip is interfaced with I^{2}C communication using an Arduino Uno, which is connected directly to the measurement computer to read out the capacitance of the device. The 10 euro cent coin is shown for scale (20 mm in diameter). **b,** Capacitance signal measured using the AD7746 chip following the same measurement scheme from Figure 6.4. The pressure step is 1 bar and the corresponding capacitance step is 650 aF, consistent with theory.

The entire measurement setup (without the pressure chamber and the pressure controller) is shown in Figure 6.8a. The AD chip is mounted on a printed circuit board (PCB) together with a few resistors and capacitors, necessary for its basic operation. Two wires from the chip (EXC A (red) and Cin+ (blue)) are connected directly to the top and bottom electrode of our device respectively. Our entire chip (marked with (2) in the image) is mounted on a chip carrier inside the pressure chamber. The AD chip is interfaced using an Arduino Uno, which has a built-in I^{2}C protocol library. The Arduino is connected to a measurement computer, which records the capacitance value measured by the AD7746 chip.

To test the setup, we employ a measurement scheme similar to the one shown in Figure 6.4. After keeping the device for 48 hours in vacuum, we apply 1 bar pressure steps with a duration of 60 s, followed by 60 s of pumping. The measured capacitance signal is shown in Figure 6.8b. We observe a capacitance change of $\Delta C \approx 650$ aF, which is consistent with the measurement using the LCR meter for $\Delta P = 1$ bar (see Figure 6.5). The noise level of these measurements is much higher (79 aF/$\sqrt{\text{Hz}}$ RMS), as is the observed drift of the capacitance signal.

Part of the reason for the increased noise is the faster sampling time (109 ms), but also the fact that the PCB with the AD7746 chip was kept outside of the vacuum chamber (due to pressure sensitive capacitors on the PCB) and long unshielded wires were used to connect to the sample. This could be improved by redesigning the PCB and wire-bonding the graphene device directly to the PCB, in the proximity of the AD readout chip. Nevertheless, this is a proof-of-concept measurement, showing that our graphene device can be used as a pressure sensor with an all-electrical on-chip readout solution.

6

7

ON-CHIP HEATERS FOR TENSION TUNING OF GRAPHENE NANODRUMS

For the study and application of graphene membranes, it is essential to have means to control their tension, resonance frequency and temperature. Here, we present an on-chip heater platform for local tuning of in-plane tension in graphene mechanical resonators. By Joule heating of a metallic suspension ring we show thermomechanical resonance frequency tuning in a graphene nanodrum, which is accompanied by an increase in its quality factor, which we attribute to an increase of the in-plane tension. The in-situ control of temperature, in-plane tension, resonance frequency and quality factor of suspended 2D nanodrums makes this device a unique platform for investigating the origin of dissipation in these ultra-thin structures and can be of fundamental importance for studying the thermal properties of 2D materials. Moreover, by simultaneously controlling the heater and the backgate voltage, we can independently control the resonance frequency and quality factor, which is of great importance for applications in sensors and resonant mechanical filters.

S INCE the first realization of graphene mechanical resonators [33], there have been many technological achievements showcasing their successful electrical readout [43], constructing tunable mechanical oscillators [94] and voltage-controlled variable capacitors [149]. Graphene- and 2D material-based NEMS usually exhibit high and tunable resonance frequencies which makes them attractive candidates as mechanical RF filters, mixers and voltage controlled oscillators. Frequency tunability is not only of major importance for tuning the dynamic range of graphene-based pressure [32, 63] and gas sensors [21, 40, 59], but also in more fundamental studies for tuning the nonlinear coupling between mechanical resonance modes [131, 132] or coupling superconducting microwave cavities to graphene nanodrums [145–147].

Graphene-based NEMS usually incorporate a local gating scheme, where a voltage difference is applied between the suspended membrane and a bottom electrode. The resulting electrostatic force exerted on the membrane increases the tension in the membrane and can be used as a tuning knob for the mechanical resonance frequency. An interesting observation is that the tunability, in such cases, comes at a cost of increased dissipation, i.e., a decrease in the quality factor [37, 71, 153]. This is unusual, since increased tensile stress in nanomechanical devices is usually associated with a decrease in dissipation [36, 154–156]. On the other hand, when strain is applied externally, e.g. by cooling down the sample to cryogenic temperatures [37, 43, 71, 153] or by using a piezo crystal underneath the sample [117], the frequency increase is accompanied by an increase of the quality factor. Consequently, the ability to mimic this effect with an on-chip tensioning mechanism is of great interest, because it allows reaching higher $f - Q$ products, it is important for low loss sensing, low phase-noise oscillators [157] and for reaching the quantum ground state of nanomechanical resonators [156]. Achieving this will provide new insights on the dissipation mechanisms in 2D nanomechanical resonators.

In this chapter we present an on-chip heater device that is capable of tuning the *in-plane* tension of graphene nanodrums by Joule heating. Using a ring-shaped structure that undergoes thermal expansion, we demonstrate tuning of tensile strain in a suspended graphene nanodrum, which results in an increase of its mechanical resonance frequency, while at the same time reducing mechanical dissipation. In addition to the usually employed electrostatic [43, 94] and optothermal actuation mechanisms [33, 34], it is shown that the device design also allows for electrothermal actuation, where the motion of the drum is excited by a thermal ac signal. The dynamic characterization of the graphene drum is supported by in-situ Atomic Force Microscopy (AFM) measurements, that show the effects of in-plane biaxial tension on the morphology of suspended 2D materials.

7.1. DEVICE DESCRIPTION

The device is shown in Figure 7.1a. The heater consists of a narrow (2 μm wide), long AuPd electrode with a circular ring structure in the middle (inner diameter: 5 μm, outer diameter: 7 μm). The width of the heater ring is exactly one half of the width of the rest of the electrode, such that the resistance per unit length is constant, resulting in a spatially uniform heat flux. On both sides of the heater there are AuPd metallic islands that serve as mechanical support for the graphene flake. All metallic structures are sup-

ported by a SiO_2 layer (the thickness of the SiO_2-AuPd stack is 385 nm). The flake shown in Figure 7.1a is 4 nm thick few-layer graphene. When a voltage (V_H) is applied across the heater, a current I_H runs through the heater ring, causing Joule heating. As a consequence, tensile stress is generated in the suspended graphene flake due to the positive thermal expansion of the supporting heater ring and the negative thermal expansion of the graphene [71, 158]. In addition, a more conventional way of tensioning the graphene drum is available, by an out-of-plane electrostatic force that can be generated using the silicon backgate.
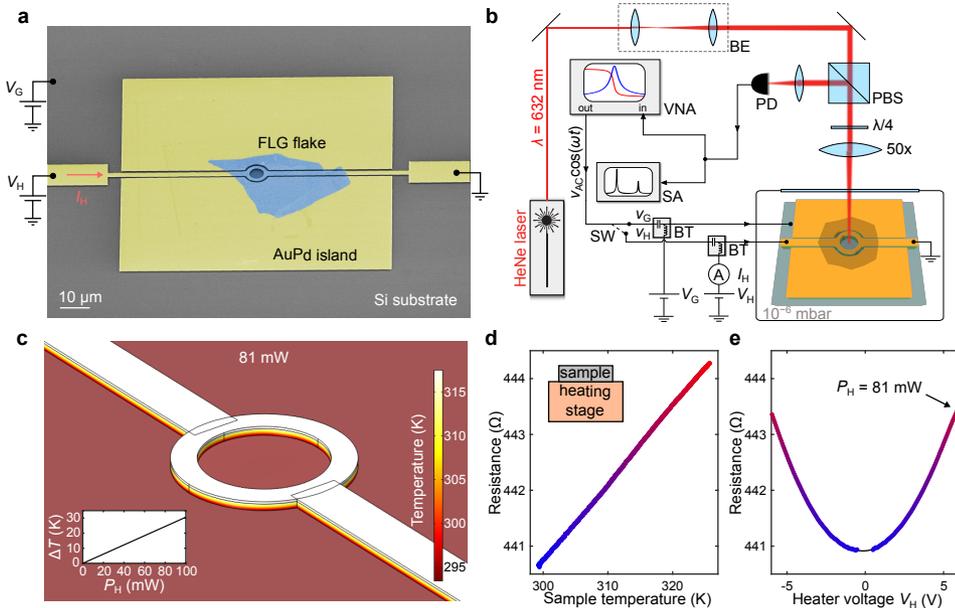

Figure 7.1: **Device characterisation and measurement setup. a,** A false-coloured scanning electron micrograph of the device. The graphene flake (blue) is suspended over the AuPd (yellow) heater and supported by the surrounding AuPd islands (electrically floating). Voltage is applied to one end of the heater (V_H) and the other end is grounded. The resulting dissipated power ($V_H I_H$) causes a temperature increase in the narrow heater structure. **b,** Measurement setup: a HeNe laser is focused on the suspended graphene drum, which is mounted in a high-vacuum chamber. The motion of the drum modulates the reflected intensity of the laser, which is captured using a photodiode (PD). The drum can be driven both electrothermally (using the heater, ν_H) and electrostatically (using the backgate, ν_G), depending on the switch (SW) configuration. The driven motion is measured using a Vector Network Analyser (VNA) and the undriven (Brownian) motion is measured using a Spectrum Analyser (SA). **c,** Finite element model of the temperature profile across the heater structure for an input Joule heating power of 81 mW. The inset shows the temperature increase (ΔT) as a function of the heater power. **d-e,** Measured heater resistance when heating the entire sample using **d,** an external stage heater and **e,** when applying a voltage across the heater. The resistance, as found from the calibration measurement in **d,** is used to estimate the heater temperature during Joule heating, shown in **e,** as indicated by assigning identical colours to data points of identical resistance.

A schematic of the measurement setup is shown in Figure 7.1b. A HeNe laser is focused onto the graphene drum, which is mounted in a vacuum chamber. The reflected laser light is interferometrically modulated by the motion of the drum and its intensity is measured by a photodiode (PD). The ac driving voltage can be applied to the heater electrode (v_H) or to the gate electrode (v_G). In both configurations, the two bias-tees (BT) also enable dc biasing of the heater (V_H) and/or of the silicon gate (V_G). Both the driven and the undriven motion of the drum is measured using a VNA and an SA respectively.

In Figure 7.1c we show a finite-element simulation of the temperature profile of the heater at a fixed input power. The details of the finite-element model are outlined in the Appendix 7.5.1. The image shows the temperature profile for a thermal power of $P_H = V_H^2/R_H = 81$ mW. In this case the temperature of the heater is 25 K higher than the ambient temperature. As expected, the calculated temperature difference ΔT is proportional to the heater power (see inset of Figure 7.1c). The temperature of the heater is also determined experimentally, by measuring the temperature-dependent resistance change of the heater itself. To calibrate it we use a heating stage to warm up the entire sample and measure the heater resistance (see Appendix 7.5.2 for details). The resulting R-T curve is shown in Figure 7.1d. The measured resistance as a function of heater voltage is shown in Figure 7.1e. Using the calibration data, we convert the measured resistance into temperature, which is colour-coded in the data points in Figures 7.1d and 7.1e. The measured temperature increase is comparable to the simulated one (Figure 7.1c).

7.2. ACTUATION MECHANISMS

The added functionality of the heater allows for three different actuation methods, which are schematically shown in Figure 7.2a. At finite temperature the motion of the drum is excited by thermal noise. A measurement of the resulting Brownian motion of the drum is shown in Figure 7.2b. From this measurement we extract the displacement sensitivity: 1.1×10^6 V/m and the noise floor of the measurement setup: 72 fm/$\sqrt{\text{Hz}}$. These numbers are comparable to our previously reported values [97], which shows that the presence of the heater structure does not deteriorate the performance of the measurement setup. Conventionally, the drum can also be driven using an out-of-plane force by applying a voltage on the backgate: $V_G + v_G \cos\omega t$ ($\omega = 2\pi f$). An example of such a measurement is shown in Figure 7.2c. The top panel shows the phase and the bottom panel shows the magnitude of the motion.

The design of the device also allows for exciting the motion of the drum with an in-plane force resulting from the thermal expansion of the heater. Although, assuming a perfectly flat membrane, an in-plane periodic force should not be able to excite out-of-plane motion, structural irregularities in the membrane (ripples, slack, wrinkles) will always give a net out-of-plane component to the in-plane force. Electrothermal actuation is performed by applying the driving voltage across the heater: $V_H + v_H \cos\omega t$ causing the heater ring to expand and contract periodically, which results in a modulation of the tension of the drum. The heat transport at a driving frequency ω can be modelled as:

$$C\Delta\dot{T} = p_{\mathrm{H}}e^{i\omega t} - \kappa\Delta T; p_{\mathrm{H}} = \frac{2V_{\mathrm{H}}v_{\mathrm{H}}}{R_{\mathrm{H}}}, \tag{7.1}$$

where C and κ are the thermal capacitance and thermal conductivity of the system, ΔT is the temperature difference with respect to the steady-state temperature and p_{H} is the applied ac heating power. The expected thermal-expansion induced amplitude is then given by:

$$x_{\omega}e^{i\omega t} = \alpha_{\mathrm{eff}}\Delta T = \alpha_{\mathrm{eff}}\frac{2V_{\mathrm{H}}v_{\mathrm{H}}}{\kappa R_{\mathrm{H}}}e^{i\omega t}\frac{1}{i\omega\tau + 1}, \tag{7.2}$$

where x_{ω} is the motion amplitude at ω, α_{eff} is the effective thermal expansion coefficient of the AuPd-graphene system and τ is the characteristic thermal delay time of the system ($\tau = C/\kappa$). A measurement using this actuation method is shown in Figure 7.2d. The bottom panel shows the measured magnitude and the top panel shows the phase. Compared with Figure 7.2c, where the drive is purely electrostatic, the resonance frequency of both measurements is roughly the same; the slight difference in resonance frequency of 0.3 MHz can be explained by the different dc values of the voltage applied
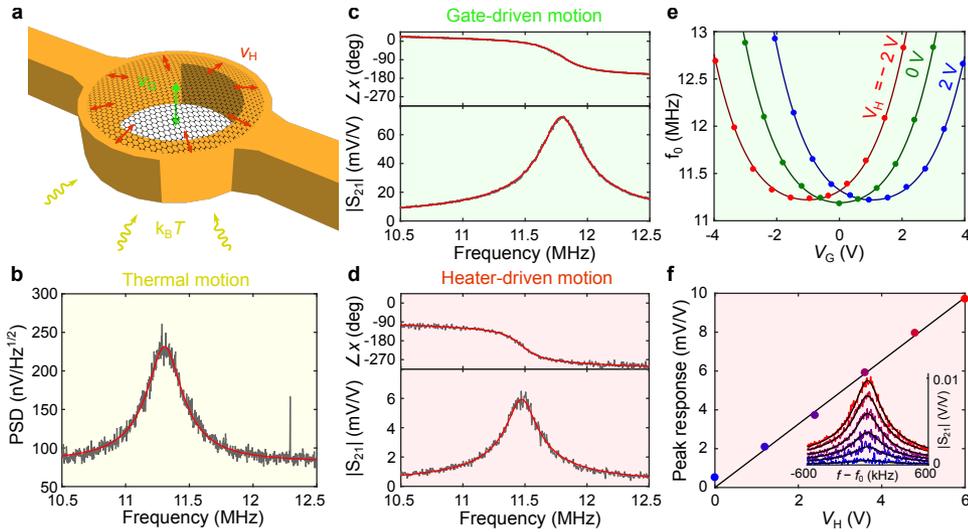

Figure 7.2: **Actuation mechanisms. a,** A schematic of the three actuation mechanisms used. The colour of each of the arrows corresponds to the background of each panel. The Brownian motion occurs due to the finite temperature of the environment (yellow arrows). The drum can be driven using electrostatic driving via the gate (V_{G}, green arrow) or using electrothermal driving via the heater (V_{H}, red arrows). **b,** Thermal (undriven) motion of the drum measured using the spectrum analyser. **c,** Phase (top) and magnitude (bottom) of the gate-driven motion at zero heater power ($V_{\mathrm{H}} = 0$ V). **d,** Phase (top) and magnitude (bottom) of the heater-driven motion at zero gate voltage ($V_{\mathrm{G}} = 0$ V). **e,** Extracted resonance frequency (f_0) as a function of the gate voltage V_{G} for three different heater voltages. The black lines are polynomial fits of the f_0 vs. V_{G} curves, as a guide to the eye. **f,** Extracted amplitude at resonance as a function of the dc voltage on the heater. The black line is a linear fit. The inset shows the data and fits for each of the colour-coded points.

to the heater V_H and the gate V_G (cf. Figure 7.2e). A striking difference between the two is the measured phase. Using electrothermal driving we observe a phase difference of approximately $-\pi/2$ between the heater-driven motion and the gate-driven motion, which is indicative of a thermal delay in the system [74, 159]. Using the phase difference at resonance, the characteristic delay time is estimated to be $\tau \gg 14$ ns ($\angle x_\omega = -\pi/2$ for $\omega \gg 1/\tau$, see Equation (7.2)). This value is in accordance with what was previously reported on graphene nanodrums [74]. This provides evidence for high-frequency driving of graphene drums by Joule heating.

By applying a dc voltage on the backgate (V_G) we can also tune the resonance frequency of the drum. Due to the out-of-plane deflection of the drum, this results in an electrostatically-induced tension, which manifests itself as an increase in the resonance frequency. Such a measurement is shown in Figure 7.2e (green points). The location of the minimum of this curve is determined by the condition at which the gate voltage equals the potential of the graphene flake, which may sometimes deviate from zero due to trapped charges on the graphene or a difference in the workfunctions of the graphene and the contacting electrode [43]. In our experiment, for $V_H = 0$ V, the parabola is centred around $V_G = 0$ V, indicating that the effect of trapped charge is negligible. For $V_H \neq 0$ V, however, we use the location of this minimum to estimate the effective potential of the graphene drum. Due to the symmetric design of the heater structure, the potential of the graphene drum is expected to raise by half of the voltage applied across the heater (V_H). The red and blue data points in Figure 7.2e represent measurements using $V_H = $ -2 V and 2 V respectively. The fact that the minima of these curves are shifted by half of the applied heater voltage (by -1 V and 1 V) confirms that the graphene flake potential is $V_H/2$. By combining voltage shifts due to the applied gate and heater voltages, the effective gate voltage across the gap, that causes electrostatic forces, becomes $V_{G,eff} = V_G - V_H/2$. This is used in subsequent measurements to decouple the influence of the heater-induced and backgate-induced tension.

To establish that the resonance in Figure 7.2d is indeed excited by high-frequency heating, a set of measurements is performed at different ac heating powers p_H by varying V_H while keeping $V_{G,eff} = 0$ V to eliminate the possibility of residual electrostatic forces. In Figure 7.2f we show the dependence of the resonance peak height of the electrothermally driven motion on the dc heater voltage (V_H). In such a configuration, if the drive was due to capacitive cross-coupling to the gate, the measured amplitude would not depend on the value of V_H. Since the ac heating power is proportional to $V_H v_H$ and the ac electrostatic force is proportional to $V_{G,eff}(v_G + \gamma v_H)$, γ being a cross-talk factor, the observation that the amplitude increases linearly with the dc heater voltage proves that the nature of the driving is electrothermal (cf. Figure 7.2d).

7.3. STATIC TENSION TUNING

A differentiating advantage of the presented device is that it provides an alternative tensioning mechanism: the force resulting from the thermal expansion of the heater causes in-plane biaxial tension in the membrane parallel to the substrate, in contrast to electrostatic forces which have a significant out-of-plane component. This concept is illustrated in Figure 7.3a-c. Figure 7.3a represents the device as-fabricated, the graphene being slightly rippled [160] and adhered to the walls [17, 19]. When using electrostatic force
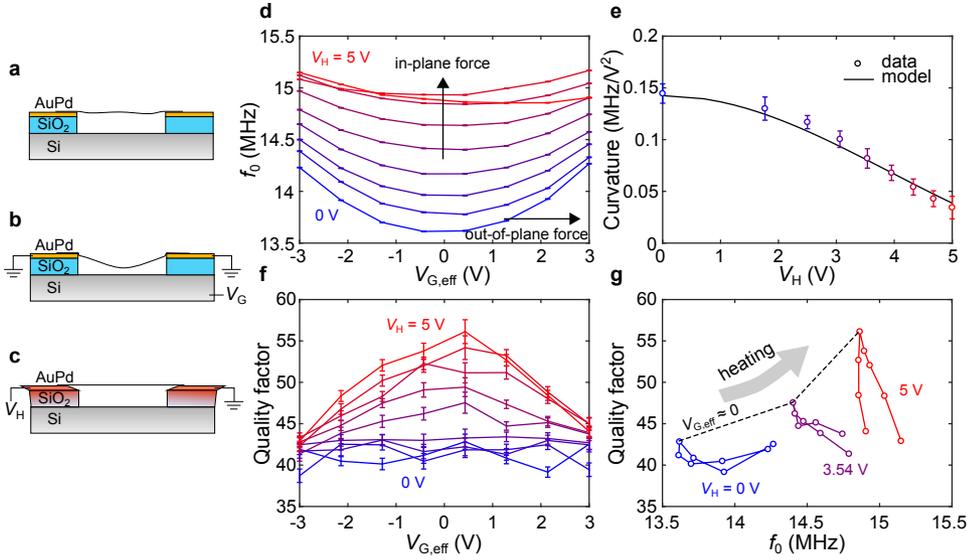
Figure 7.3: **Comparison of dc tensioning mechanisms. a-c,** Artist impression of the tensioning mechanisms. **a,** The device as-fabricated. **b,** Electrostatically induced vertical deflection. When using the heater **c,** the graphene is stretched in-plane due to the thermal expansion of the ring and contraction of the graphene flake. **d,** Resonance frequency and **f,** quality factor as a function of $V_{G,eff}$ for increasing V_H. The colour of each curve denotes the heater voltage (see x-axis of **e** for the values). **e,** Extracted curvature ($d^2 f_0/dV_G^2$) of the V_G vs. f_0 curve around $V_{G,eff} = 0$ V. The black line shows the modelled response. **g,** Quality factor vs. resonance frequency plot for gate sweeps at different heater voltages. The middle point of each curve represents the case where $V_{G,eff} \approx 0$ V (the points are connected by a black dashed line).

7

(Figure 7.3b), the drum is pulled downwards, promoting sidewall adhesion, but still contributing to the tension due to the geometrical deformation of the structure [66]. When using the heater, the drum is expected to stretch in-plane (Figure 7.3c), which increases the stiffness and flattens the membrane.

To compare the two tensioning mechanisms, we look at the frequency tuning using both the backgate (out-of-plane force) and the heater (in-plane force) and how each mechanism affects the mechanical dissipation of the resonator. In Figure 7.3d we look at the frequency tuning curves using the backgate centred around $V_{G,eff} = 0$ V. The different colours correspond to different heater voltages from zero to 5 Volts. Two effects can be observed: firstly, the resonance frequency at $V_{G,eff} = 0$ V increases with increasing heater voltage, indicating an increase in tension with V_H; secondly, we observe a decrease in the tunability of the frequency with the backgate for increasing heater voltage. The latter can be quantified by extracting the curvature of each curve at $V_{G,eff} = 0$ V, as shown in Figure 7.3e. This decrease in gate tunability can be explained by a model that takes into account the added tension due to the electrostatic force as a function of the in-plane tension. The observed trend is another confirmation that the heater-induced tension is

in-plane. The mathematical model of this behaviour, which was used to fit the data in Figure 7.3e is shown in the Appendix 7.5.3. Using this model, we extract the effective thermal expansion coefficient of the graphene-heater system: $\alpha_{eff} = 1.64 \times 10^{-6} K^{-1}$ (see Equation (7.1)).

Dissipation in 2D mechanical resonators is still poorly understood and is a subject of debate [25, 43, 71]. It is well known that the electrostatically induced shift in resonance frequency is usually accompanied by a decrease in the quality factor [37, 71] and this has been attributed to electronic Joule dissipation of the displacement current through the resonator [37]. Surprisingly, when tuning the tension electrothermally, the frequency increase of ≈ 10 % (at $V_H = 5$ V) is accompanied by a 33 % increase in the quality factor (from $Q_{0V} = 42$ to $Q_{5V} = 56$), as shown in Figure 7.3f. This is unexpected and cannot be explained in the framework of the usually observed temperature-dependence of the quality factor, which decreases with increasing temperature [37, 43, 71, 161]. Similar to our observations, simultaneous reduction in dissipation and increase in resonance frequency was observed by Kramer *et al.* when using a piezo crystal to apply in-plane tensile strain in MoS_2 nanodrums [117].This suggests that *in-plane* tension is indeed connected to an increase in Q, similar to reports on other MEMS/NEMS structures [36, 154–156].

Figure 7.3g shows an f_0 - Q plot. Each colour represents a sweep of V_G centred around $V_{G,eff} = 0$ V at a different heater voltage. The black dashed line connects the points of the curves where the effective gate voltage is close to zero to show the simultaneous increase of both the resonance frequency (i.e. tension) and the quality factor upon increasing the heater voltage. The same effect was observed in two other samples, shown in the Appendix 7.5.4. Using two control inputs, V_G and V_H, we gain access to a large portion of the $f_0 - Q$ parameter space and show that this allows independent tuning of the resonance frequency and the quality factor (see Appendix 7.5.5). The ability to control the quality factor and the frequency of the resonator independently is a rather unique feature of our device enabling applications in, for example, tunable filters, where both bandwidth and frequency need to be controlled.

7.4. In-situ AFM

Atomic force microscopy can be used to study the mechanical properties of 2D materials [16]. Hence, to gain more insight into the topography of the resonator, we perform a series of AFM measurements in peak-force mode (using a Bruker FastScan AFM) while varying the heater voltage, shown in Figure 7.4. For these measurements, the heater is connected symmetrically to a bipolar voltage source to ensure that $V_{G,eff} = 0$ V, such that no electrostatic force is exerted between the AFM tip and the resonator. The gate electrode and the AFM tip are electrically grounded. Measurements at three different heater voltages are shown in Figure 7.4a-c. Two qualitative observations can be made. Firstly, the measured membrane height in the centre of the drum increases with increasing heater voltage, indicative of a higher in-plane tension that flattens the membrane. Secondly, at high heater voltages V_H, the morphology of the drum changes substantially through the formation of what appears to be a wrinkle. Upon careful inspection, a point-like imperfection at the edge of the membrane, also observed at $V_H = 0$ V (Figure 7.4a), seems to be the cause for the formation of this wrinkle. The presented data demon-

strate, to our knowledge, the first direct observation of in-situ wrinkle formation under biaxial tension. Such measurements can be used for investigating the delicate dynamics of morphological imperfections in suspended 2D materials and their influence on the mechanical properties of these ultra-thin membranes [103, 129, 143, 162].

A total of 13 images is recorded while sweeping the heater voltage up and down in the sequence shown in Figure 7.4d. Figure 7.4d shows a horizontal cutline of the AFM height maps. It can be seen that the position of the centre of the drum moves upwards with increasing heater voltage, which is accompanied by a decrease in the membrane slack (amount of wall adhesion). The decreased wall adhesion can be the reason of the observed increase in the Q-factor of the resonator upon heating (Figure 7.3f), due to the reduced area of the wall-adhered surface and therefore reduced coupling to the substrate [76].

The extracted average height of the centre of the drum is shown in Figure 7.4e. The height is taken from the horizontal cutlines, averaging over five points just to the left of the wrinkle (grey region in Figure 7.4e). The x-axis shows the sequence of heater voltages applied. The height of the drum increases when heating up and decreases when cooling down, which is suggestive of increasing tension in the drum. Moreover, we also observe
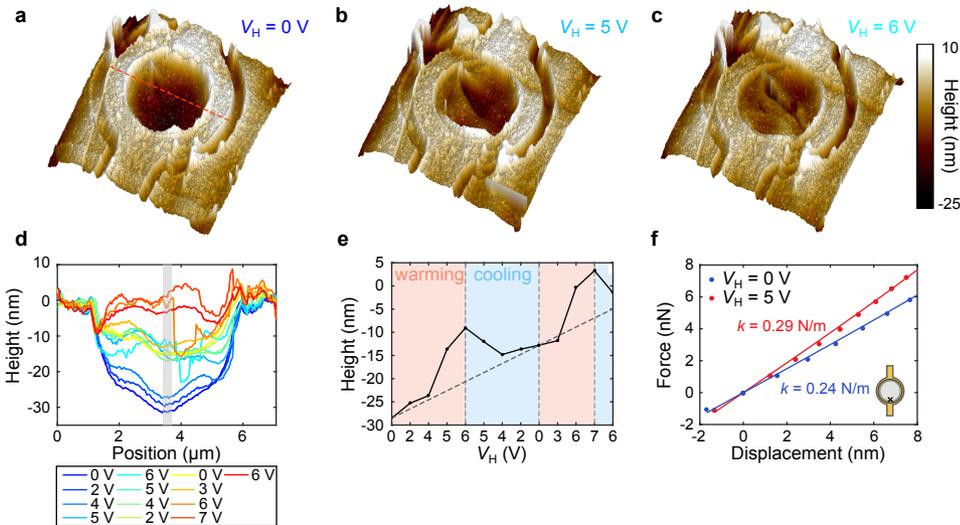

Figure 7.4: **AFM measurements. a-c,** AFM images of the flake taken at three different heater voltages. **d,** Extracted height profiles along the central cutline (dashed red line in **a**) of the drum for a sequence of heater voltages. Each colour represents a different voltage and the order of the measurements matches the order of the colours. **e,** Extracted average height of the centre of the drum (grey region in **d**) as a function of V_H. The x-axis represents the measurement sequence and shows the value of V_H (axis is not linear). The dashed line is a guide to the eye. **f,** Force-deflection curves taken near the edge of the drum (black cross in the inset) at two heater voltages: 0 V (blue) and 5 V (red).

a displacement of the centre of the drum upon a complete warmup-cooldown cycle at zero heater power. This permanent upward deformation can be a consequence of the dynamics of wrinkle formation, given that there is an energy cost associated with wrinkle unzipping.

Figure 7.4f shows two AFM force-deflection curves taken near the edge of the drum (position shown in the inset) at two different heater voltages. The slope of each curve represents the linear spring constant of the drum, which is related to the pre-tension [16]. In accordance with the frequency response measurements (Figure 7.3) and the measurements from Figure 7.4e, an increase of the tension of the drum is observed upon increasing the heater voltage. It is important to note that the ratio between the extracted spring constants ($k_{5V}/k_{0V} = 1.21$) matches the ratio of the pre-tension extracted from the measured resonance frequencies in Figure 7.3d, $\sqrt{f_{0,V_H=5V}/f_{0,V_H=0V}} = 1.21$.

In conclusion, we realized an on-chip heater device capable of tuning the in-plane tension of suspended 2D material membranes. Using dc Joule heating, we show tuning of the in-plane tension of suspended graphene membranes, which results in a resonance frequency increase of 10 %. In contrast to the case of electrostatic gating, the increase in frequency is accompanied by an increase in the quality factor of 32 %, which we attribute to the increase in in-plane tension of the graphene nanodrum. We also demonstrate that this device concept provides a new way of actuation of 2D resonators, by means of ac electrothermal modulation of the tension in the suspended structure. The presented device can serve as a platform for fundamental studies on nonlinear dynamics and thermal properties of suspended 2D materials, as well as a tool for independently tuning the resonance frequency and the quality factor in next-generation NEMS RF filters, modulators and voltage controlled oscillators.

7

7.5. APPENDIX

SYMBOLS

Used symbols (units):
V_H: heater voltage (V)
I_H: heater current (A)
R_H: heater resistance (Ω)
V_{off}: offset voltage (V)
I_{off}: offset current (A)
V_{meas}: measured voltage (V)
I_{meas}: measured current (A)
R_{meas}: measured resistance (Ω)
U_{el}: elastic energy (J)
F_{el}: restoring elastic force (N)
F_{es}: electrostatic force (N)
n_0: in-plane tension (N/m)
$n_0(0)$: pre-tension (N/m)
E: Young's modulus (Pa)
h: thickness (m)
z: displacement of the centre of the membrane (m)
R: radius (m)
v: Poisson's ratio
C: capacitance (Fa)
V_G: DC gate voltage (V)
A: area of drum (m^2)
g_0: gap size (m)
ε_0: dielectric constant
f_0: resonance frequency (Hz)
m: effective mass (kg)
k: effective stiffness (N/m)
α_{eff}: thermal expansion of the graphene-heater system (1/K)
κ: thermal conductivity of the silicon oxide (W/K)

7.5.1. TEMPERATURE PROFILE SIMULATIONS

In this section we lay out the details of the 3D finite-elements simulations of the temperature increase in the heater structure. In the simulations, we take a heat flux of 81 mW through the heater, while keeping the bottom of the silicon chip thermally anchored. In Figure 7.5a we show the temperature across the cutline running horizontally through the heater structure. This is to estimate the influence of the heat conductance through the electrodes and bonding wires on the thermal profile of the heater, the simulation is repeated for a case where the edges of the heater are also thermally anchored. It is shown that in both cases the temperature at the centre of the heater is the same (25 K), proving that heat transport through the leads is negligible and the dominant heat sink is the silicon through the thin layer of SiO_2.
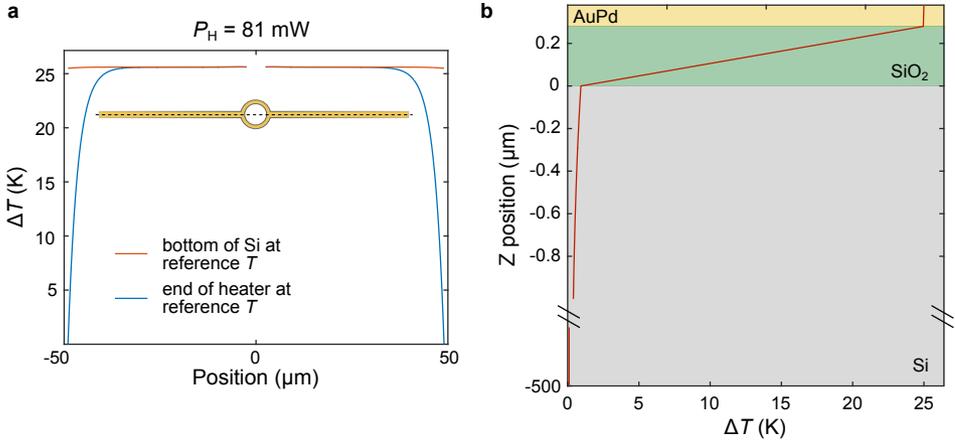
Figure 7.5: **Temperature profiles of the heater device. a,** Horizontal cutline through the heater device (dashed line in inset) for two cases: the red line is the temperature along the heater structure when the thermal reference (293 K) is at the bottom of the Si chip. The blue line shows the temperature profile when the thermal sink is at the edges of the heater electrodes, through the bonding wires. **b,** Temperature profile along the vertical direction when the Si chip is at the reference temperature (293 K). Almost the entire temperature drop is across the SiO$_2$ layer.

To evaluate the dominant thermal resistance of the system, a vertical cutline through the Si-SiO$_2$-AuPd is shown in Figure 7.5b. The thermal profile along the z-axis shows that the thermal resistance of SiO$_2$ is dominant in the system, as the total temperature drop across the silicon is less than 1 K.

7.5.2. RESISTANCE MEASUREMENT

In the experiments the resistance of the heater R_H is measured using a Keithley 2400 Sourcemeter. This is done by setting the desired voltage on the Sourcemeter and measuring both the actual heater voltage V_H as well as the current I_H that flows through it. Such monitoring is done during the mechanical measurements, as well as in separate characterization measurements where V_H is swept (cf. Figure 7.1e). Naturally, the resistance is the ratio of the voltage to the current. However, the measured values can have offsets w.r.t. their true values: $V_{meas} = V_H + V_{off}$ and $I_{meas} = I_H + I_{off}$.

This is illustrated in Figure 7.6a using the data from Figure 7.1d. The IV curve does not go through the origin, indicating that current offsets, voltage offsets, or both, are present. When with these present, simply dividing the measured voltage and current does not give the right resistance R_H:

$$R_{meas} = \frac{V_{meas}}{I_{meas}} = \frac{V_H + V_{off}}{I_H + I_{off}} = R_H \times \frac{I_H + V_{off}/R_H}{I_H + I_{off}} = R_H \times \frac{V_H + V_{off}}{V_H/R_H + I_{off}} \neq R_H. \tag{7.3}$$

In particular, Equation (7.3) shows that the measured resistance approaches R_H for large I_H, but also that it diverges at $I_H = -I_{off}$.
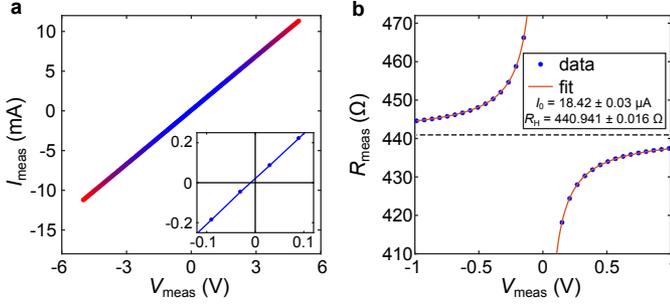
Figure 7.6: **Calibrating for the current and voltage offsets. a,** Heater current-voltage measurement. The inset shows a zoom of the data. **b,** Measured resistance and fit of Equation (7.3).

Although Equation (7.3) contains both V_{off} and I_{off}, these cannot be determined independently from a measurement of $R_{\text{meas}}(V_{\text{meas}})$ as Equation (7.3) can be rewritten as:

$$R_{\text{meas}}(V_{\text{meas}}) = \frac{V_{\text{meas}}}{V_{\text{meas}}/R_{\text{H}} + (I_{\text{off}} - V_{\text{off}}/R_{\text{H}})}, \tag{7.4}$$

after eliminating I_{meas}. This only contains the combination of I_{off} and V_{off} as a single parameter $I_0 \equiv I_{\text{off}} - V_{\text{off}}/R_{\text{H}}$.

Figure 7.6b shows the measured resistance R_{meas} as well Equation (7.4) fitted to the data. The model fits the data well, and gives the fit values for the combined offset $I_0 = 18.42\,\mu\text{A}$ and the heater resistance $R_{\text{H}} = 440.94\,\Omega$. Note that even at $V_{\text{H}} = \pm 1\,\text{V}$ the deviation between R_{meas} and R_{H} is significant, a few Ohm, especially compared to the changes that occur while changing the temperature or heater voltage as shown in Figure 7.1d. This offset is taken into account in the temperature dependence of Figure 7.1d where the current is measured at $V_{\text{H}} = -1\,\text{V}$.

Finally, Equation (7.3) can be inverted, giving:

$$R_{\text{H}} = \frac{V_{\text{meas}} - R_{\text{H}}(I_{\text{off}} - I_0)}{I_{\text{meas}} - I_0} = \frac{V_{\text{meas}}}{I_{\text{meas}} - I_0}. \tag{7.5}$$

For the last equality, the fact that $I_0 \equiv I_{\text{off}} - V_{\text{off}}/R_{\text{H}}$ holds for every combination of I_{off} and V_{off} that gives the same I_0, including for $V_{\text{off}} = 0$, is used. Now by fitting the low-voltage region (Figure 7.6b) where R_{H} is practically constant, one obtains the fit value for I_0 that can be inserted into Equation (7.5) to find the actual resistance R_{H} from the raw measurements. The results in Figure 7.1d are obtained using this procedure.

7.5.3. INTERPLAY BETWEEN IN-PLANE AND OUT-OF-PLANE TENSION

In this section, we outline the model for the influence of thermally-induced in-plane tension on the gate tunability of the resonance frequency of the membrane. The deformation of the drum under an electrostatic load is taken to be parabolic, such that its deformation shape is given by: $U(r) = 1 - \frac{r^2}{R^2}$, where R is the radius of the membrane. This is very close to the shape of the fundamental eigenmode $u(r, \phi) = J_0(kr), k \approx 2.404/R$.

The potential energy of a deformed membrane is mainly determined by the stretching energy. This is because for thin membranes we can neglect bending rigidity, provided that the condition $\frac{h^3}{d^2}\frac{E}{n_0} \ll 1$ is satisfied [137]. The potential energy of a spherically deformed membrane (by a uniform pressure load) is then given by:

$$U_{el} = 2\pi n_0 z^2 + \frac{2\pi E h}{3R^2(1-\nu)}z^4, \tag{7.6}$$

where z is the displacement of the centre of the drum. The restoring force can be calculated as:

$$F_{el} = \frac{dU_{el}}{dz} = 4\pi n_0 z + \frac{8\pi E h}{3R^2(1-\nu)}z^3. \tag{7.7}$$

To derive the electrostatic force felt by the drum, we make the parallel plate capacitor and the uniform electrostatic load approximations, which are valid for small deflections:

$$F_{es} = \xi \frac{1}{2}\frac{\varepsilon_0 A}{(g_0 - z)^2}V_G^2, \tag{7.8}$$

where ξ accounts for the projection of the force on the centre of the membrane. For a parabolic deformation $\xi = 0.5$.

Expanding this around $z = 0$, we get:

$$F_{es} = \frac{1}{4}\varepsilon_0 A V_G^2 \left(\frac{1}{g_0^2} + \frac{2z}{g_0^3} + O(z^2)\right). \tag{7.9}$$

We can now write the force-balance equation of the system:

$$F_{el} - F_{es} = 4\pi n_0 z + \frac{8\pi E h}{3R^2(1-\nu)}z^3 - \frac{1}{4}\varepsilon_0 A V_G^2\left(\frac{1}{g_0^2} + \frac{2z}{g_0^3}\right) = 0, \tag{7.10}$$

which can be rewritten as:

$$\frac{8\pi E h}{3R^2(1-\nu)}z^3 + \left(4\pi n_0 - \varepsilon_0 A V_G^2 \frac{1}{2g_0^3}\right)z - \varepsilon_0 A V_G^2 \frac{1}{4g_0^2} = 0. \tag{7.11}$$

Equation (7.11) is then used to calculate the equilibrium position $z(V_G, n_0)$ of the drum.

The effective stiffness of the system k is given by:

$$k = 4\pi n_0 - \frac{\varepsilon_0 A V_G^2}{2g_0^3} + \frac{8\pi E h}{R^2(1-\nu)}z^2, \tag{7.12}$$

which is also close to the dynamic spring constant of the fundamental mode.

The resonance frequency of the membrane can then be estimated as:

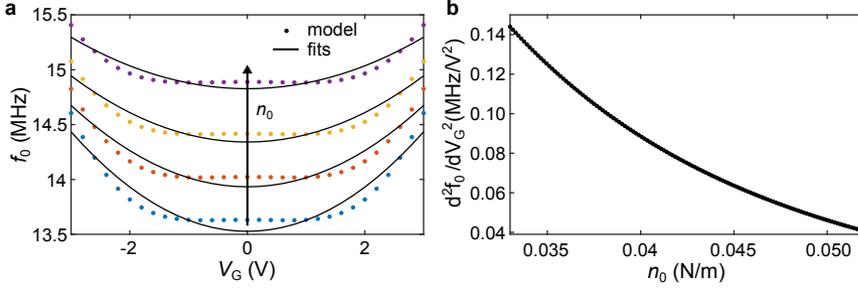$$f_0 = \frac{1}{2\pi}\sqrt{\frac{k}{m_{eff}}}, \tag{7.13}$$

Figure 7.7: **Interplay between in-plane and out-of-plane tension. a,** Modelled f_0 vs. V_G curves for increasing in-plane tension n_0 (coloured data points) together with polynomial fits (black curves). **b,** Extracted curvature from the polynomial fits of the curves shown in **a** as a function of the in-plane tension n_0.

where m_{eff} is the effective mass of the fundamental resonance mode ($m_{\mathrm{eff}} = \frac{1}{3}m$ assuming parabolic deformation). The pre-tension of the drum is calculated from the resonance frequency at zero heater- and gate-voltage: $n_0(0) = 0.033$ N/m. By substituting for z from Equation (7.11) into (7.12) and plugging this into (7.13), we numerically calculate the resonance frequency as a function of the dc voltage for varying in-plane tension. Figure 7.7a shows the simulated f_0 vs. V_G curves for four different values of the in-plane tension together with polynomial fits, which is a good approximation provided that the tension-induced hardening is much stronger than the electrostatic softening, which seems to be the case judging by the measurements presented in the main text. The effective Young's modulus E is extracted from numerical fitting of the the blue data points in panel (a), for zero heater voltage.

Panel (b) of Figure 7.7 shows the curvature at $V_G = 0$ V as a function of the in-plane tension.

By relating the pre-tension to the heater voltage, we extract the thermal expansion coefficient of the system.

The relation between the heater-induced in-plane tension and V_H can be written as:

$$n_0 = n_0(0) + \Delta n_0(V_H), \tag{7.14}$$

where $n_0(0)$ is the pre-tension of the drum at room temperature and $\Delta n_0(V_H)$ is the added tension due to heating. The thermally induced tension $\Delta n_0(V_H)$ is related to the thermally added strain (ϵ) through:

$$\Delta n_0(V_H) = \epsilon E h. \tag{7.15}$$

The strain ϵ is, in turn, related to the thermal expansion of the system:

$$\Delta n_0(V_H) = \alpha_{\mathrm{eff}} \Delta T E h. \tag{7.16}$$

The temperature increase of the system at a given voltage is determined by the total heating power and the thermal conductivity of the system:

$$\Delta T = \frac{P_{\mathrm{H}}}{\kappa} = \frac{V_{\mathrm{H}}^2}{R_{\mathrm{H}}\kappa}, \tag{7.17}$$

which yields:

$$n_0 = n_0(0) + \alpha_{\mathrm{eff}} E h \frac{V_{\mathrm{H}}^2}{R_{\mathrm{H}}\kappa}. \tag{7.18}$$

The factor $\frac{1}{R_{\mathrm{H}}\kappa} = 0.72\,\mathrm{K/V^2}$ is experimentally determined from the temperature calibration of the heater shown in Figure 7.1. Since E is known from fitting the curve of Figure 7.7a, the pre-factor $\frac{Eh}{R_{\mathrm{H}}\kappa}$ is found to be $\frac{Eh}{R_{\mathrm{H}}\kappa} = 432\,\mathrm{NK/V^2 m}$.

We now use this relation to numerically fit the measured resonance frequency as a function of heater voltage to estimate α_{eff}. The net thermal expansion coefficient of the system is found to be: $\alpha_{\mathrm{eff}} = 1.64 \times 10^{-6}\,\mathrm{K^{-1}}$. Substituting this value in the expression for n_0 in Figure 7.7b, we get a good agreement with the extracted curvature from Figure 7.3e.

7.5.4. OTHER DEVICES

In this section we present data on two other graphene devices. Similarly to Figure 7.3g, Figure 7.8 shows $f_0 - Q$ plots for (a) a 5-nm thick and (b) a 18-nm thick graphene drum. Both drums show the same trend: upon increasing the heater voltage (i.e. the temperature of the heater), both the frequency and the quality factor go up. The thin drum (Figure 7.8a) shows a ≈30 % frequency increase accompanied by a 56 % increase in the
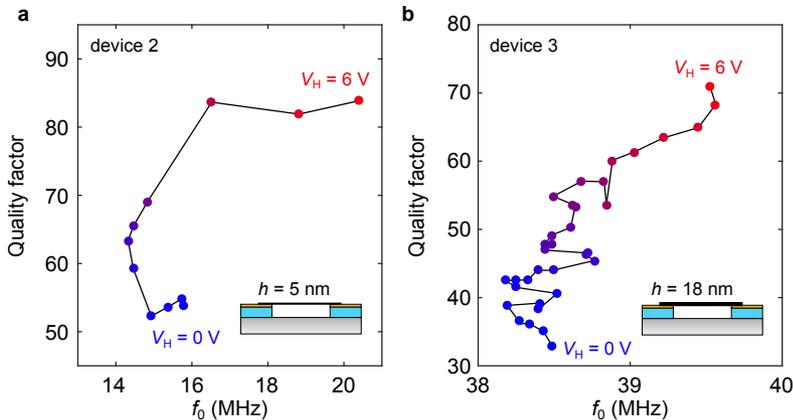

Figure 7.8: **Thermal tuning of two other graphene devices. a,** a 5-nm thick few-layer graphene and **b,** a 18-nm ultra-thin graphite drum. The resonance frequency is plotted against the quality factor while heating the device up. The colour of each dot corresponds to the temperature of the device.

quality factor. The 18-nm thick sample shows a minute frequency increase of 3 %, probably owing to the fact that the resonance of thicker drums is determined by their bending rigidity, rather than the tension. The quality factor, however, shows an increase of 121 %, which is a significant improvement of the mechanical dissipation.

7.5.5. INDEPENDENT TUNING OF f_0 AND Q

In this Section we demonstrate that we can independently tune the resonance frequency and the quality factor. Figure 7.9a shows the accessible range in the $f_0 - Q$ space, showing all the measurement curves of Figure 7.3. The area in grey represents the accessible $f_0 - Q$ space by using the dc heater and gate voltages, V_H and V_G, as control parameters. However, from this plot, as well as the data in Figure 7.3, it is clear that when changing either $V_{G,eff}$ or V_H, both the quality factor and the resonance frequency change simultaneously.

In Figure 7.9b we visualize the same data using contour plots. These lines of constant f_0 and Q are calculated using the contour function of Matlab R2017a. The x-axis shows the gate voltage $V_{G,eff}$ and the y-axis is the (square of the) heater voltage V_H^2. The blue curves are lines of equal resonance frequency and the orange curves are lines of equal
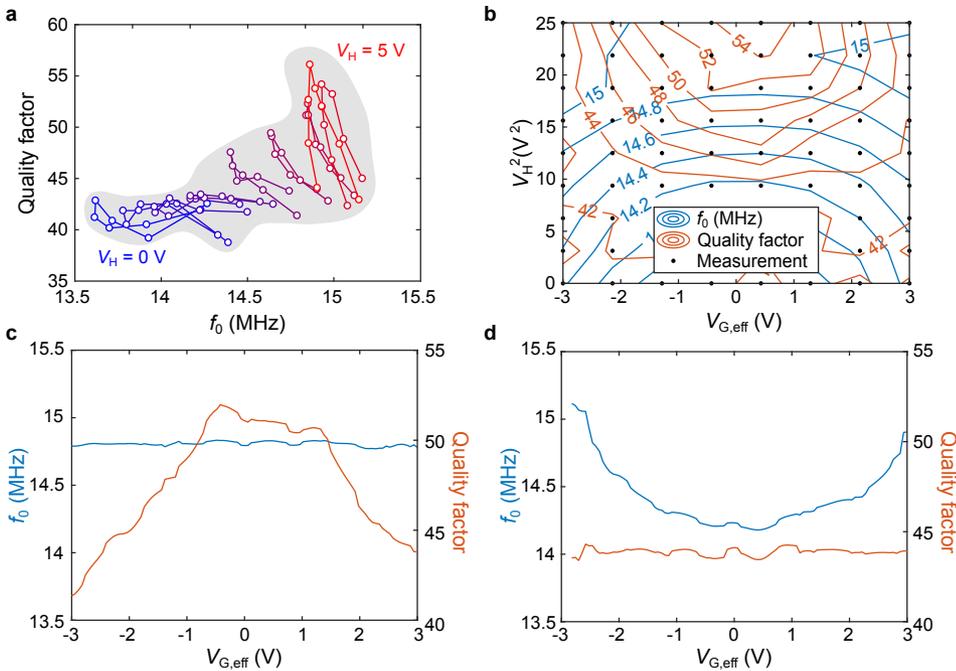

Figure 7.9: **Independent tuning of resonance frequency and quality factor. a,** $f_0 - Q$ plot for varying heater and gate voltage. The grey area indicates the accessible region. Each colour represents a different heater voltage. **b,** A double contour plot of the resonance frequency and the quality factor for varying $V_{G,eff}$ and V_H. Experimental values are measured at the locations of the black dots. Independent tuning of **c,** the quality factor and **d,** the resonance frequency by following one of the contour lines in **b**.

quality factor. By definition, when following a contour line of either f_0 or Q, the value of it remains constant. The fact that a single blue contour intersects more than one orange contour and vice versa shows that for a given value of one parameter, the other can be tuned independently in the range given by the outermost intersection points of the two curves. Using a combination of V_H and V_G, we can follow either contours of constant frequency or have constant quality factors, as shown in Figure 7.9c-d. In Figure 7.9c we show that we can keep the resonance frequency constant (blue curve), while lowering the quality factor (orange curve). The opposite effect is observed in Figure 7.9d, where we follow a contour of constant Q, while the resonance frequency increases.

Technically, the contour curves are parameterised with the $V_{G,eff}$ as control parameter and the corresponding value of V_H^2 is calculated from the output of the `contour` function using `interp1` with the `'pchip'` option. Next, for each point along the curve a 2D interpolation is performed to find the local values of f_0 and Q. Due to the difference in the interpolation algorithm and that in the `contour` function, small fluctuations in the "constant" parameter are still visible. However, the changes in the other, i.e, "varying" parameter is much larger. This clearly demonstrates the power of our system to have independent control over the resonance frequency and damping of the graphene nanodrum.

7

8

GRAPHENE GAS PUMPS

We report on the development of a pneumatically coupled graphene membrane system, comprising of two circular cavities connected by a narrow trench. Both cavities and the trench are covered by a thin few-layer graphene membrane to form a sealed dumbbell shaped chamber. Local electrodes at the bottom of each cavity allow for actuation of each membrane separately, enabling electrical control and manipulation of the gas flow inside the channel. Using laser interferometry, we measure the displacement of each drum at atmospheric pressure, as a function of the frequency of the electrostatic driving force and provide a proof-of-principle of using graphene membranes to pump attolitre quantities of gases at the nanoscale.

P UMPS have been of importance for humanity since early civilization. The Egyptians used a contraption called "shadoof" to take out water from the Nile that was used for irrigation. As technology progressed, better pumps usually meant higher pressure, larger flow, and hence, higher power. Micro- and nanofluidics in the past thirty years have substantially changed the way these devices are benchmarked. Microscale pumps are an essential ingredient in a microfluidic system, and the rapid advancements of biosciences require continually more devices capable of accurate micromixing and microdosing. This, in turn, imposes better controllability, better accuracy, lower operational power, and much smaller flow rates [165–167]. With respect to the first electrostatically actuated membrane pumps [168, 169], that were presented more than 25 years ago, a tremendous reduction in size has been achieved. Pumps are also of interest for driving pneumatic actuators in micro- and nanoelectromechanical motors. The properties of graphene, like its atomic scale thickness and extreme flexibility, are very promising for further miniaturization of such nanofluidic devices.

Since the first realization of mechanical graphene devices [33], suspended 2D materials have attracted increasing attention in the MEMS/NEMS communities. Many device concepts have been proposed, including pressure sensors [32, 39], gas sensors [21, 40], mass sensors [41, 42], and graphene microphones [170, 171]. The high tension and low mass of graphene membranes have also inspired their implementation as high-speed actuators in micro-loudspeakers [61]. Another attractive aspect of graphene membranes is their hermeticity [19] and the ability to controllably introduce pores that are selectively permeable to gases [21]. Although gas damping forces limit graphene's Q-factor at high frequencies, they provide a useful but little explored route towards graphene pumps and nanofluidics. For efficient pumps and pneumatics it is essential that most of the available power is used to move and pressurize the fluid, while minimizing the power required to accelerate and flex the pump membrane while minimizing leakage of the fluid outside of the system. In these respects, the low mass and high flexibility, combined with the impermeability of graphene membranes [19] provide clear advantages.

In this chapter we realise a system of two nanochambers (with a total volume of 7 fl) coupled by a narrow trench and sealed using a few-layer graphene flake. By designing a chip with individually accessible electrodes we construct a graphene micropump, capable of manipulating the gas flow between the two chambers using small driving voltages ($V_{dc} \leq 1$ V). Increasing the gas pressure in one of the nanochambers results in pneumatic actuation of the graphene drum that covers the other nanochamber via the connecting gas channel. To measure the displacement of the drums, we use laser interferometry and demonstrate successful pumping of gas between the two pneumatically coupled graphene nanodrums.

8.1. DEVICE DESCRIPTION

The device concept is presented in Figure 8.1a. Two circular AuPd electrodes (thickness: 60 nm) at the cavity bottom (one for addressing each of the membranes) are separated by a thin layer (130 nm) of spin-on-glass (SOG) silicon oxide from the metallic (AuPd) top electrode (thickness: 85 nm). The few-layer (FL) graphene flake (black), with a thickness of 4 nm, is in direct electrical contact with this top electrode. The entire device is fabricated on top of a quartz substrate to minimize capacitive cross-talk. The device fab-
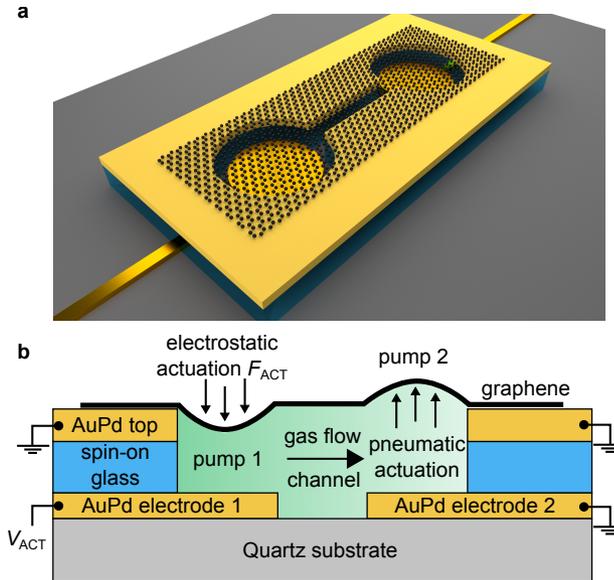
Figure 8.1: **Working principle of the pump. a,** A 3D schematic of the device: the graphene flake is covering two circular cavities that are connected through a narrow trench. **b,** Schematic cross-section of the pumps and actuation mechanism for the case that pump 1 is actuated.

rication is described in detail in [58] and in Chapter 6. A cross-section along the direction of the trench of the device is shown in Figure 8.1b, which illustrates the working principle. The actuation voltage $V_{ACT,1}$ is applied between AuPd electrode 1 and ground, while keeping AuPd electrode 2 and the AuPd top electrode grounded. As a result, pump 1 experiences an electrostatic force F_{ACT}, causing it to deflect downward. This compresses the gas underneath the membrane and the induced pressure difference causes a gas flow through the channel between the two nanochambers. This results in a pressure increase that causes the other membrane (pump 2) to bulge upward.

Figure 8.2a shows a false-coloured SEM image of the device after fabrication. The AuPd is shown in light (bottom electrodes) and dark (top electrode) yellow. The diameter of each drum is 5 μm and the trench connecting them is 1 μm wide and 3 μm long. Figure 8.2b shows an optical image of the measured device. The image shows the two bottom electrodes, together with the top metallic island on which the dumbbell shape is patterned. Graphene is transferred last (as described in Chapter 3.4.3) and it is visible in the image as a darker area on top of the metallic island.

8.2. READOUT

The readout of the drum motion of the is performed using a laser interferometer, shown schematically in Figure 8.3a. A red HeNe laser is focused on one of the graphene membranes, and the sample is mounted in a pressure chamber in a N_2 environment at ambient pressure and room temperature. When the membrane moves, the optical interfer-
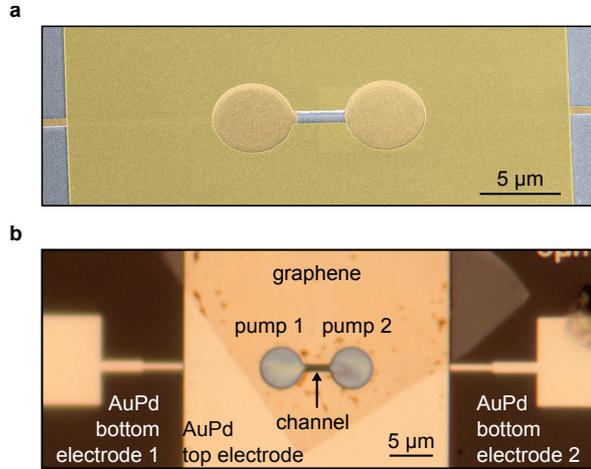
Figure 8.2: **Images of the fabricated device. a,** Scanning electron microscopy (SEM) image of the device prior to graphene transfer. **b,** Optical micrograph of the device after graphene transfer.

ence between the light reflected from the bottom electrode and the light reflected from the graphene causes the light intensity on the photodiode detector to depend strongly on the drum position. By lateral movement of the laser spot, the motion of either of the pumps can be detected. The photodiode signal is read out via an internal first-order low-pass filter with a cut-off frequency of 50 kHz.

For electrostatic actuation, the two bottom electrodes are connected to two channels of an arbitrary waveform generator, where one is grounded and the other one is actuated (Figures 8.1b and 8.3a). The actuation voltage (V_{ACT}) on each of the drums and the photodiode voltage (V_{PD}) are measured using an oscilloscope. The top electrode (i.e., the graphene flake) is electrically grounded during the measurements. Since there are 2 pumps that can be actuated (pump 1 and pump 2) and either of them can be detected with the red laser there are 4 measurement configurations indicated by $V_{PD,11}, V_{PD,21}, V_{PD,12}$ and $V_{PD,22}$, where the first number indicates the pump that is actuated and the second number indicates the pump that is read out.

We first characterize the responsivity of the system by applying a triangular voltage signal to one of the drums while measuring its motion with the laser. The measurement is shown in Figure 8.3b. The force acting on the drum scales quadratically with V_{ACT} and therefore, for small amplitudes, it is expected that the amplitude of the drum would also depend quadratically on V_{ACT} (assuming $F_{ACT} = -kz$, see Appendix 8.4.2). The fact that the voltage read out from the photodiode matches the scaled square of the input voltage (blue curve in Figure 8.3b) confirms that the assumption of linear transduction ($V_{ACT}^2 \propto V_{PD}$) of the motion is valid.
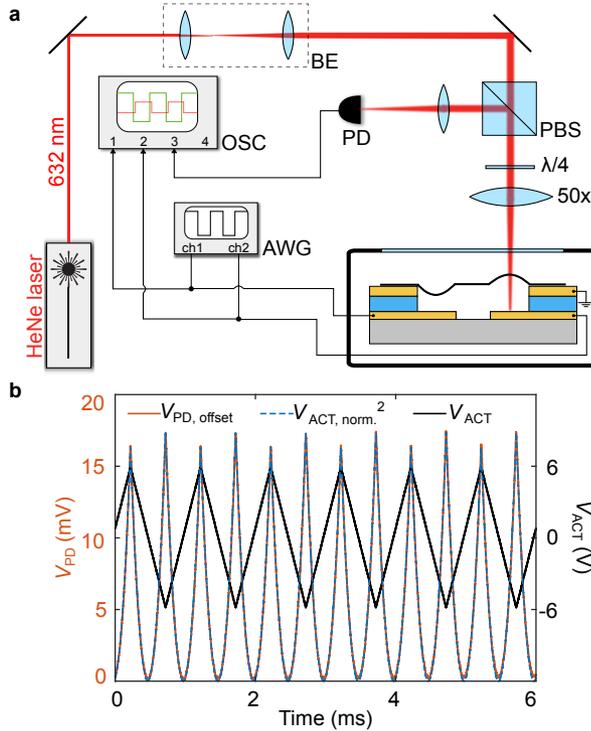
Figure 8.3: **Measurement setup. a,** Setup for electrostatic actuation and interferometric motion readout of either of the pumps. PD: photodiode, OSC: oscilloscope, AWG: arbitrary waveform generator, BE: beam expander and PBS: polarized beam splitter. **b,** Offset photodiode voltage (red curve) for a triangular input signal V_{ACT} (black curve). The dashed blue curve represents the input voltage squared, normalized to the photodiode voltage: $V^2_{ACT,norm.} = \alpha(V_{ACT} + \beta)^2$. The term $\beta = -0.13$ V accounts for residual charge on the graphene flake [43].

8

8.3. GAS PUMP AND PNEUMATIC ACTUATION

Pneumatic actuation is one of the most efficient ways to transfer force over large distances in small volumes. At the microscale, the pneumatic coupling also has the advantage of converting the attractive downward electrostatic force on pump 1 to an upward force on the graphene membrane of pump 2 (Figure 8.1b). Thus, proof for gas pumping and pneumatic actuation can be obtained by detecting that the drums move in opposite directions.

The drums are actuated using a square-wave voltage input $V_{AC,p-p} = 1$ V with a frequency of 1.3 kHz, plotted in Figure 8.4a and Figure 8.4b (grey curves). Figure 8.4a shows a measurement of the displacement of pump 1, when applying V_{ACT} on pump 1 while keeping pump 2 grounded (dark blue curve) or when actuating pump 2 while keeping pump 1 grounded (light blue curve). Both curves show a main frequency component that is coinciding with the frequency of the driving signal, meaning that the detected motion is a consequence of the applied actuation. However, when switching the actua-

tion to pump 2 it is seen that the photodiode voltage ($V_{PD,21}$) is 180 degrees out of phase with respect to $V_{PD,11}$. This is indicative of an out-of-phase motion of the two drums. Such effect is possible only if the actuation of pump 1 (in the 21 configuration) is pneumatic, i.e., mediated by gas displacement from one chamber to the other.

The same experiments are repeated in Figure 8.4b when moving the laser spot to pump 2. The red curve represents the case when pump 2 is electrically actuated while keeping pump 1 grounded and the pink curve represents the case when pump 1 is electrically actuated and pump 2 is kept grounded. The same conclusion can be drawn: the two curves are 180 degrees out-of-phase, confirming that the drums move in opposite directions.

The differences in signal amplitudes in Figure 8.4 are attributed to differences in the effective cavity depths between the pumps that affect the actuation/detection efficiency (this may happen due to morphological imperfections in the graphene flake). To confirm that the coupling is mediated by gas, the experiment is repeated at low pressure. After keeping the sample at 0.1 mbar for 48 hours, the gas is completely evacuated from the cavity [19]. In this case no sign of motion of the second drum is observed in the $V_{PD,12}$ signal, showing that pneumatic actuation is absent in vacuum (see Appendix 8.4.1).

Assuming that the cavities are hermetically sealed by the graphene (valid for very low permeation rates [19]), the pneumatically coupled graphene pump system can be modelled in the quasi-static regime by a set of two linear differential equations describing the pressure increase ΔP_i in each of the chambers. The pressure difference can then be related to the displacement z_i of the drums (details of the model and the derivation are given in Appendix 8.4.1). In the frequency domain the solutions of these differential equations can be written in terms of the Fourier transforms $\mathscr{F}$ of the solutions: $z_1(\omega) = \mathscr{F}(z_1)$, $z_2(\omega) = \mathscr{F}(z_2)$ and $F(\omega) = c\mathscr{F}(V_2^2)$, where F is the actuation pressure and c is a function of the squeeze number and the gap size $g_0 = 155$ nm. When the actuation signal is applied to pump 2, the response is given by:

8
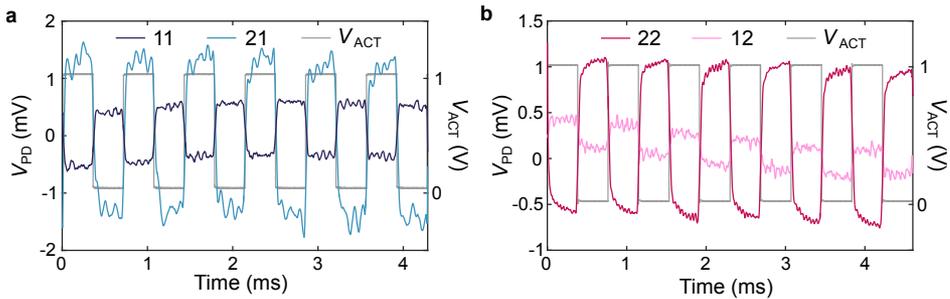
Figure 8.4: **Time domain measurements. a,** Measured displacement (photodiode voltage) of pump 1 when actuating pump 1 (measurement 11) and drum 2 (measurement 21). **b,** Measured displacement (photodiode voltage) of drum 2 when actuating pump 1 (measurement 12) and drum 2 (measurement 22). The actuation voltage is shown on the right y-axis. Measurements of each of the drums are performed at constant laser position to ensure that the transduction of the system (V_{PD}/z) is constant.
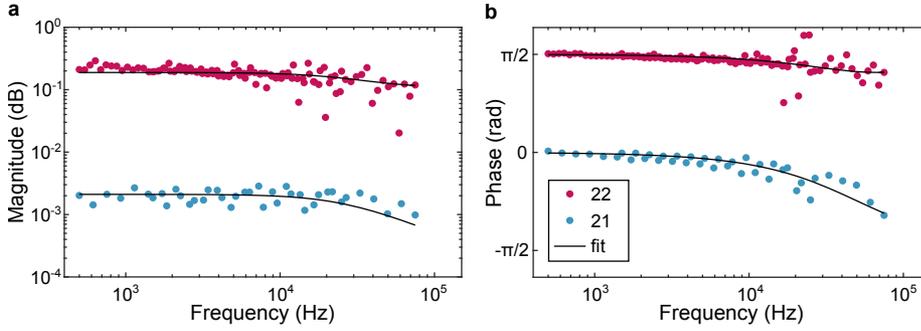
Figure 8.5: **Frequency domain measurements.** Bode plots (**a,** magnitude and **b,** phase) of the system for actu-ation of pump 2. The data points are coloured according to the measurement scheme: the red points represent actuation and detection at pump 2, while the light blue represent actuation at pump 2 and measurement of pump 1. The fit is according to the model represented with Equations (8.1) and (8.2).

$$z_1(\omega) = \frac{1}{2} \frac{1}{1 + i\omega\tau} \frac{A}{k} F(\omega); \tag{8.1}$$

$$z_2(\omega) = -\left(\frac{1}{2} \frac{1}{1 + i\omega\tau} + \frac{1}{a}\right) \frac{A}{k} F(\omega), \tag{8.2}$$

where z_1 and z_2 are the displacements of pump 1 and pump 2 respectively, ω is the ac-tuation frequency, A is the area of each drum, k is the spring constant of the drums and a is the squeeze number. The time constant τ is then given by:

$$\tau = \frac{1 + a}{2b}, \tag{8.3}$$

where the constant b is related to the gas flow through the channel. Assuming a laminar Poiseuille flow, b is dependent on the geometry of the channel and the effective viscosity of the gas, in this case nitrogen (see Appendix 8.4.2).

To investigate the nanoscale gas dynamics experimentally, the frequency response of the system is measured. The actuation voltage is applied on pump 2. The frequency of the square-wave input signal ($V_{ACT}(t)$, see Figure 8.4) is varied from 510 Hz to 23 kHz. For each actuation frequency, the Fourier transform is taken of both the input and output signal. By taking the ratio of the input and output at each of the driving frequencies a frequency response plot is obtained. We make use of the fact that the input square-wave contains higher harmonics to increase the amount of data acquired by a single time response signal, thereby increasing the frequency resolution.

The resulting Bode plots are shown in Figure 8.5. It can be seen that both the mag-nitude and phase of the resulting frequency response curves are flat up to a frequency of 10 kHz. At higher frequencies the amplitude of the motion of the second drum drops, which suggests that at these frequencies the pumping efficiency starts to become limited

by gas dynamics through the narrow channel. Fits using the model described by Equations (8.1) and (8.2) show that the response of the pumps correspond to a first-order RC low-pass filter with a characteristic time constant of $\tau = 39.3 \pm 3.4\,\mu$s, resulting in a cut-off frequency of 25.4 ± 2.2 kHz.

The demonstrated graphene-based pump system is not only of extraordinarily small size (total volume of 7 fl), but it is also capable of pumping very small amounts of gas: assuming the spring constant to be in the order of $k \approx 1$ N/m, less than 80 al of gas is pumped through the channel each cycle. The thermal noise, due to charge fluctuations on the capacitor plates, sets a lower limit to the pump rate of less than 1 zl/$\sqrt{\text{Hz}}$, which is equivalent to less than 30 N_2 molecules/$\sqrt{\text{Hz}}$ at ambient pressure and room temperature. The maximum electrostatic pressure that can be generated by the graphene pump with the given geometry is 0.5 bar, limited by the breakdown voltage of the dielectric ($V_{\text{b}} = 16$ V). The typical force exerted at $V_{\text{ACT}} = 1$ V is 4 nN, corresponding to an electrostatic pressure of 2 mbar.

Besides the pneumatic actuation and pumping, the system also allows the study of gas dynamics in channels of sub-micron dimensions, where the free path length of molecules is smaller than the channel height, even at atmospheric pressure. By controllably introducing pores in the graphene, the graphene pump can be used for molecular sieving of gases, or even aspiration and dispensing of liquids. The presented system can therefore be used as a platform for studying anomalous viscous effects in narrow constrictions as well as graphene-gas interactions at the nanoscale. It thus provides a route towards scaling down nanofluidic systems by using graphene membranes coupled by nanometre-sized channels.

8.4. APPENDIX

8.4.1. MODEL OF THE PUMP SYSTEM

EQUATIONS OF MOTION

In this section the model for the two drum system will be explained, starting with the assumptions that were made in order to arrive at the model.

The drums are modelled as simple harmonic oscillators. A parallel plate capacitor model is taken to model the electrostatic force on the drum, which holds for small deflections of the membrane with respect to gap. The gas inside the circular cavities is modelled as an ideal gas and gas inertia is neglected. The interactions of the gas are considered to be isothermal. Poiseuille flow through the trench between the two drums is considered.

The mechanics of the drums are described using Newton's second law of motion. The forces that act on the drums are the tension force of the drums (assuming equal spring constants k and masses m), the pressure force acting on the drum and the electrostatic forces coming from the charge stored in the membrane-electrode capacitor. No damping is considered apart from damping due to the gas pressure. The electrostatic force is applied to the first drum (pump 1). We name deflection of drum i with respect to the gap z_i, such that a positive value of z_i corresponds to the drum bulging upward. We con-

sider the outside air to be at ambient pressure P, while the pressure inside chamber i is P_i. The pressure difference across the drum is be called ΔP_i. The gap size is denoted as g_0, ε_0 is the vacuum permittivity and $A = r^2\pi$ is the area of each of the drums. In terms of these quantities the equations of motion are:

$$\begin{cases} m\dfrac{d^2 z_1}{dt^2} = -kz_1 + \Delta P_1 A - \dfrac{V^2 \varepsilon_0 A}{2(g_0 + z_1)^2}; & (8.4) \\[4mm] m\dfrac{d^2 z_2}{dt^2} = -kz_2 + \Delta P_2 A. & (8.5) \end{cases}$$

With this, the mechanics are fully described. These equations have one driving force, the electrostatic force experienced by pump 1. The pressure force due to the gas is not a driving force and should react to the motion of the membrane. In order to describe the pressure in the drums, the ideal gas law is taken:

$$\begin{cases} P_1 = P + \Delta P_1 = \dfrac{n_1 \bar{R} T}{V_1} = \dfrac{n_1 \bar{R} T}{A(g_0 + z_1)}; & (8.6) \\[4mm] P_2 = P + \Delta P_2 = \dfrac{n_2 \bar{R} T}{V_2} = \dfrac{n_2 \bar{R} T}{A(g_0 + z_2)}. & (8.7) \end{cases}$$

The quantity n_i in these equations stands for the amount of moles of gas in chamber i. These two equations, together with Equations (8.4) and (8.5) give a set of equations in which the membranes are coupled to the gas pressure in the drums. The pressures are now coupled to one another using the Poiseuille flow equation. This equation determines the rate of pressure induced flow of a viscous fluid across a channel. In the pump
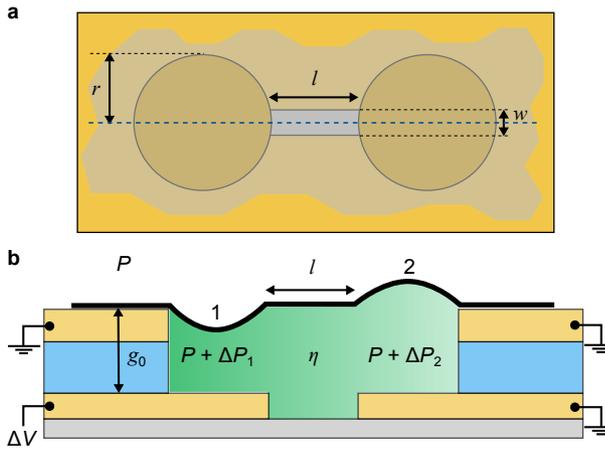
Figure 8.6: **Schematic of the device. a,** Top view of the pump system. **b,** A side view of the cross section through the dashed blue line in **a**. A potential ΔV is applied on pump 1 that results in the membrane compressing the gas, causing an increase of pressure in the chamber $P_1 = P + \Delta P_2$. This causes gas flow through the channel and results in pump 2 bulging upward. Since the channel is smaller than the chamber, it will obstruct the flow of gas, hence the pressure in the other chamber $P_2 = P + \Delta P_2$ will lag.

system, this fluid is the nitrogen gas in the cavity. The Poiseuille flow equation describes both n_1 and n_2 through the following differential equation:

$$\Phi = (1 - 0.63\frac{g_0}{w})\frac{(\Delta P_1 - \Delta P_2)g_0^3 w}{12\eta l} = \frac{dn_2}{dt}\frac{V_2}{n_2} = \frac{dn_2}{dt}\frac{\bar{R}T}{P + \Delta P_2} = -\frac{dn_1}{dt}\frac{\bar{R}T}{P + \Delta P_1}. \tag{8.8}$$

In this equation Φ is the volumetric flux of gas through the channel, $\bar{R}$ is the ideal gas constant, and η is the dynamic viscosity of the gas. The Poiseuille flow equation acts as the coupling between the two cavities. In using this equation to express the change in the amount of gas molecules in the cavities we have implicitly added the condition that the total amount of gas molecules in the pump system is conserved, which holds assuming no gas permeation outside the cavities. In order to incorporate Equation (8.8) into the model, the time derivatives of the ideal gas laws are taken:

$$\begin{cases} \dfrac{d\Delta P_1}{dt}V_1 + (P + \Delta P_1)A\dfrac{dz_1}{dt} = \dfrac{dn_1}{dt}\bar{R}T; & (8.9) \\[2ex] \dfrac{d\Delta P_2}{dt}V_2 + (P + \Delta P_2)A\dfrac{dz_2}{dt} = \dfrac{dn_2}{dt}\bar{R}T. & (8.10) \end{cases}$$

Filling in Equation (8.8) results in the following set of equations:

$$\begin{cases} \dfrac{d\Delta P_1}{dt} = -\dfrac{(P + \Delta P_1)}{g_0 + z_1}\dfrac{dz_1}{dt} \\[2ex] \qquad + (1 - 0.63\dfrac{g_0}{w})\dfrac{(\Delta P_2 - \Delta P_1)(P + \Delta P_1)g_0^3 w}{12\eta l A(g_0 + z_1)}; & (8.11) \\[3ex] \dfrac{d\Delta P_2}{dt} = -\dfrac{(P + \Delta P_2)}{g_0 + z_2}\dfrac{dz_2}{dt} \\[2ex] \qquad + (1 - 0.63\dfrac{g_0}{w})\dfrac{(\Delta P_1 - \Delta P_2)(P + \Delta P_2)g_0^3 w}{12\eta l A(g_0 + z_2)}. & (8.12) \end{cases}$$

To neatly express the model of the two drum system, the four differential equations that describe the system are given together. The following set of equations describe the two drum system:

$$\begin{cases} \dfrac{d^2 z_1}{dt^2} = -\dfrac{k}{m}z_1 + \dfrac{A}{m}\Delta P_1 - \dfrac{V^2\varepsilon_0 A}{2m(g_0 + z_1)^2}; & (8.13) \\[3ex] \dfrac{d^2 z_2}{dt^2} = -\dfrac{k}{m}z_2 + \dfrac{A}{m}\Delta P_2; & (8.14) \\[3ex] \dfrac{d\Delta P_1}{dt} = -\dfrac{(P + \Delta P_1)}{g_0 + z_1}\dfrac{dz_1}{dt} \\[2ex] \qquad + (1 - 0.63\dfrac{g_0}{w})\dfrac{(\Delta P_2 - \Delta P_1)(P + \Delta P_1)g_0^3 w}{12\eta l A(g_0 + z_1)}; & (8.15) \\[3ex] \dfrac{d\Delta P_2}{dt} = -\dfrac{(P + \Delta P_2)}{g_0 + z_2}\dfrac{dz_2}{dt} \\[2ex] \qquad + (1 - 0.63\dfrac{g_0}{w})\dfrac{(\Delta P_1 - \Delta P_2)(P + \Delta P_2)g_0^3 w}{12\eta l A(g_0 + z_2)}. & (8.16) \end{cases}$$

8

Quasi-static equations

The quasi-static limit of these equations is taken. In this case the second derivatives in Equations (8.4) and (8.5) are negligible. Newton's law is now equivalent to a force balance, indicating that at all times the drums are at an equilibrium position. This equilibrium position changes in time due to the changing gas pressure and voltage. As such there is still a response to the driving force. In order to find approximate solutions to the differential equations, Equations (8.13) and (8.14) are linearised. The force balance that is found is:

$$
\begin{cases}
kz_1 = A\Delta P_1 - \dfrac{V^2 \varepsilon_0 A}{2g_0^2}; & (8.17) \\[4mm]
kz_2 = A\Delta P_2. & (8.18)
\end{cases}
$$

The linearised differential equations for the pressure are:

$$
\begin{cases}
\dfrac{d\Delta P_1}{dt} = -\dfrac{P}{g_0}\dfrac{dz_1}{dt} + (1-0.63\dfrac{g_0}{w})\dfrac{(\Delta P_2 - \Delta P_1)Pg_0^2 w}{12\eta l A}; & (8.19) \\[4mm]
\dfrac{d\Delta P_2}{dt} = -\dfrac{P}{g_0}\dfrac{dz_2}{dt} + (1-0.63\dfrac{g_0}{w})\dfrac{(\Delta P_1 - \Delta P_2)Pg_0^2 w}{12\eta l A}. & (8.20)
\end{cases}
$$

Now filling the force balance into this differential equation eliminates all displacement terms and yields the following differential equations for the pressure:

$$
\begin{cases}
\dfrac{d\Delta P_1}{dt}(1 + \dfrac{PA}{kg_0}) = (1-0.63\dfrac{g_0}{w})\dfrac{(\Delta P_2 - \Delta P_1)Pg_0^2 w}{12\eta l A} \\[2mm]
\quad + \dfrac{PA}{kg_0}\dfrac{\varepsilon_0}{2g_0^2}\dfrac{dV^2}{dt}; & (8.21) \\[4mm]
\dfrac{d\Delta P_2}{dt}(1 + \dfrac{PA}{kg_0}) = (1-0.63\dfrac{g_0}{w})\dfrac{(\Delta P_1 - \Delta P_2)Pg_0^2 w}{12\eta l A}. & (8.22)
\end{cases}
$$

For simplicity, we define the following constants:

$$
a = \frac{PA}{kg_0};
$$

$$
b = (1-0.63\frac{g_0}{w})\frac{Pg_0^2 w}{12\eta l A}.
$$

Here a is the squeeze number and b is related to the gas flow dynamics through the channel. This allows us to put the differential equations into the following simple form:

$$
\frac{d}{dt}\begin{bmatrix}\Delta P_1 \\ \Delta P_2\end{bmatrix} = \frac{-b}{1+a}\begin{bmatrix}1 & -1 \\ -1 & 1\end{bmatrix}\begin{bmatrix}\Delta P_1 \\ \Delta P_2\end{bmatrix} + c\frac{d}{dt}\begin{bmatrix}V^2 \\ 0\end{bmatrix}; \tag{8.23}
$$

$$
c = \frac{a}{1+a}\frac{\varepsilon_0}{2g_0^2}. \tag{8.24}
$$

8

FREQUENCY SPECTRUM OF THE SYSTEM

In order to investigate the behaviour of this differential equation, a Fourier transform of the differential equations is taken:

$$i\omega \begin{bmatrix} \mathscr{F}(\Delta P_1) \\ \mathscr{F}(\Delta P_2) \end{bmatrix} = \frac{-b}{1+a} \begin{bmatrix} 1 & -1 \\ -1 & 1 \end{bmatrix} \begin{bmatrix} \mathscr{F}(\Delta P_1) \\ \mathscr{F}(\Delta P_2) \end{bmatrix} + ci\omega \begin{bmatrix} \mathscr{F}(V^2) \\ 0 \end{bmatrix}. \qquad (8.25)$$

The frequency spectra found from these equations are given by

$$\mathscr{F}(\Delta P_1) = \frac{\frac{1}{2} + i\omega\tau}{1 + i\omega\tau} c\mathscr{F}(V^2); \qquad (8.26)$$

$$\mathscr{F}(\Delta P_2) = \frac{\frac{1}{2}}{1 + i\omega\tau} c\mathscr{F}(V^2), \qquad (8.27)$$

with $\tau = \frac{1+a}{2b}$. This time also defines the cutoff frequency of the gas pump system $\omega_0 = \frac{2b}{1+a}$. The function Fourier transform of ΔP_2 takes the form of a low pass filter. We are more interested in the Fourier transform of P_1, whose magnitude and phase of $\mathscr{F}(\Delta P_1)$ are given below.

$$|\mathscr{F}(\Delta P_1)| = \frac{1}{2} \sqrt{\frac{1 + \omega^2 4\tau^2}{1 + \omega^2\tau^2}} c|\mathscr{F}(V^2)|; \qquad (8.28)$$

$$\phi = Arg[\mathscr{F}(\Delta P_1)] = \arctan\left(\frac{\omega\tau}{1 + \omega^2 2\tau^2}\right). \qquad (8.29)$$

Finally, we examine the behaviour of the drum displacement. The algebraic equations found for the displacement allow us to directly calculate the Fourier transform of the displacement from the pressures and the square of the electrostatic potential.

$$\mathscr{F}(z_1) = -\left(\frac{1}{2}\frac{1}{1 + i\omega\tau} + \frac{1}{a}\right)\frac{A}{k} c\mathscr{F}(V^2); \qquad (8.30)$$

$$\mathscr{F}(z_2) = \frac{1}{2}\frac{1}{1 + i\omega\tau}\frac{A}{k} c\mathscr{F}(V^2). \qquad (8.31)$$

Once more it can be seen that $\mathscr{F}(z_2)$ is given by applying a low pass filter on the driving force. The magnitude and phase of $\mathscr{F}(z_1)$ and find:

$$|\mathscr{F}(z_1)| = \sqrt{\frac{1}{a^2} + \left(\frac{1}{a} + \frac{1}{4}\right)\frac{1}{1 + \omega^2\tau^2}}\frac{A}{k} c|\mathscr{F}(V^2)|; \qquad (8.32)$$

$$\phi_1 = Arg(\mathscr{F}(z_1)) = \pi - \arctan\left(\frac{a\omega\tau}{2 + a + 2\omega^2\tau^2}\right). \qquad (8.33)$$

We now use these equations to model the curves from Figure 8.5.

8.4.2. MEASUREMENT IN VACUUM

A comparison of "12" measurements in vacuum and in N_2 is shown in Figure 8.7. In ambient pressure, the motion of pump 2 responds to the actuation of pump 1, mediated by the gas in the chamber. The absence of motion of pump 2 in vacuum (orange curve in Figure 8.7) is another confirmation of pneumatic actuation in the system.
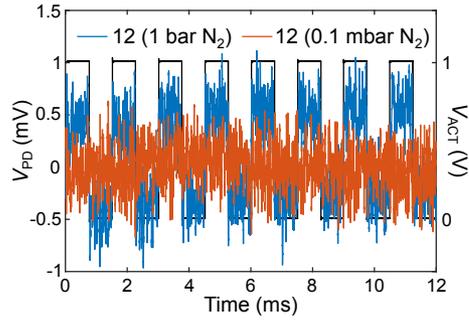

Figure 8.7: **Measurement in vacuum.** Measurement of the motion of pump 2 when actuating pump 1 at atmospheric pressure (blue curve) and in vacuum (orange curve).

9

SUSPENDED ULTRA-THIN COMPLEX OXIDE MECHANICAL RESONATORS

Thin films of complex oxides and their heterostructures exhibit a profusion of exotic transport phenomena, including two-dimensional (2D) superconductivity [84], ferroelectric/magnetic order [85] and negative capacitance [86], which often result from the intricate interplay between the film and the substrate. Recently a milestone work was published [172] showing transfer of epitaxially grown single-crystal freestanding layers of these materials. The importance of this technique lies not only in its potential for studying the transport properties of isolated films of complex oxides, but also for studying their mechanical properties in their ultrathin form. In this work, we present a study of suspended 2D mechanical resonators made out of epitaxially grown $SrTiO_3$ (STO) and $SrRuO_3$ (SRO) films. By measuring the temperature dependence of the mechanical properties of these resonators we observe signatures of structural phase transitions which affect their strain and mechanical dissipation. This approach can be extended to study phase transitions in a wide range of complex oxide materials but also greatly expands the class of exfoliable materials for implementation in nanoelectromechanical systems (NEMS), whose unique properties can be engineered in an epitaxial fashion.

T HE electronic and magnetic properties of complex oxides are very sensitive to lattice deformation due to the strong coupling between lattice, charge, spin, and orbital degrees of freedom. This coupling stems from rotations and distortions of the corner-connected BO_6 octahedra[1], which determine the overlap between O $2p$ and B d-orbitals. The B–O–B bond lengths and rotation angles are routinely controlled by strain engineering through heteroepitaxy, which forms a powerful tool to tune the properties of ultrathin films. However, the possibilities for mechanical manipulation are limited by the requirement of a substrate for the epitaxial growth, which could not be circumvented until recently. On the other hand, a wide variety of mechanical manipulation techniques are well established for the van der Waals materials, where weak interlayer bonding enables exfoliation of single- and few-layer films. Owing to their flexibility, low mass and remarkable strength, these ultrathin materials have proven to be exceptionally promising for nanomechanical sensing applications [21, 32, 42, 63]. Conversely, the well-developed field of nanomechanics has established a solid basis for characterising their thermal and mechanical properties [17, 74, 123]. In a pioneering work, Lu et al. [172] have shown that epitaxially grown oxide films can be released from the substrate, opening up the possibility of applying these techniques to ultrathin films of complex oxides.

In this chapter, we demonstrate the fabrication and mechanical characterization of 2D mechanical resonators made of single-crystal complex oxide films suspended over circular cavities. By investigating the temperature dependence of the mechanical properties of these resonators we detect signatures of phase transitions, and discuss the influence of ferroelectric domain walls on the mechanical dissipation mechanisms in different temperature regimes.

9.1. FABRICATION OF $SrTiO_3$ AND $SrRuO_3$ NANODRUMS

The fabrication of the $SrTiO_3$ (STO) and $SrRuO_3$ (SRO) mechanical resonators is described in Figure 9.1. To isolate the epitaxial thin film from the STO substrate, a water-soluble $Sr_3Al_2O_6$ (SAO) layer is first deposited by pulsed laser deposition (see Methods (9.4)). Figure 9.1a shows the reflection high-energy electron diffraction (RHEED) intensity of the specular spot during the growth of SAO and STO. Oscillations are observed during the growth of both films, indicating that the growth occurs in layer-by-layer mode. An atomic force microscopy (AFM) topographic map shows that the STO film has a step-and-terrace structure, corroborating the growth mode.

To dissolve the sacrificial layer and release the thin film from the substrate, a PDMS layer is attached to the surface before the entire stack is immersed in deionized water. After the dissolution of the SAO layer (approximately 1 hour for a 5 x 5 mm^2 50 nm-thick SAO film), the film can be transferred onto other substrates such as Si/SiO_2 using a deterministic dry-transfer technique [101]. X-ray diffraction (XRD) measurements show that the films are of excellent crystalline quality after the release and transfer process.

---

[1] The general chemical formula for perovskite materials is ABO_3, where A and B are two cations of very different sizes (usually A > B) and O are the oxygen atoms.
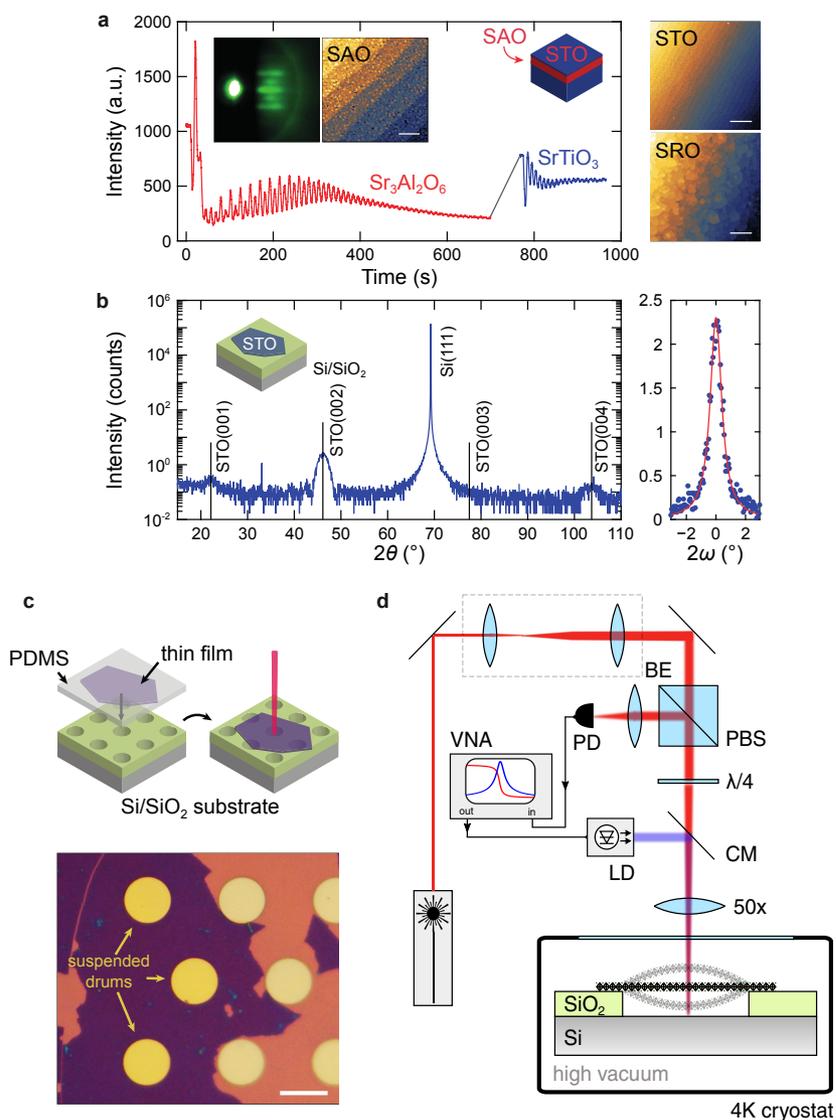
Figure 9.1: **Sample fabrication and basic characterisation. a,** RHEED intensity oscillations during the growth of $Sr_3Al_2O_6$ and $SrTiO_3$. Inset: RHEED diffraction pattern (left) and AFM image (right) of the $Sr_3Al_2O_6$ surface. The scale bar is 200 nm. Right: AFM images of the $SrTiO_3$ (top) and $SrRuO_3$ (bottom) film surfaces. The scale bar is 1 μm. **b,** X-ray diffraction measurement of a 10 unit cell (u.c.) $SrTiO_3$ film transferred on a Si/SiO₂ substrate. Right: rocking curve around the (002) reflection. **c,** Top: Schematics of the transfer of a thin $SrRuO_3$ film onto a pre-patterned Si/SiO₂ substrate. Bottom: Optical image of a 9 u.c. $SrRuO_3$ single-crystal flake on Si/SiO₂. The scale bar is 10 μm. **d,** Setup for interferometric displacement detection (VNA: Vector Network Analyser, PD: Photodiode, LD: Laser Diode, BE: Beam Expander, PBS: Polarised Beam Splitter, CM: Cold Mirror).

An XRD measurement of a 10 u.c. STO flake on a Si/SiO$_2$ substrate is shown in Fig. 9.1b (left), where Laue oscillations are clearly visible. Since the film is no longer epitaxial on a substrate, the rocking curve (right) is a measure of the morphology of the STO film lying on the SiO$_2$. The small full width at half maximum (FWHM = 0.95°) indicates that the film lies very flat on the Si/SiO$_2$ substrate.

In this chapter the technique is extended by transferring the films of STO and SRO onto Si/SiO$_2$ substrates pre-patterned with circular cavities, demonstrating the feasibility of creating suspended membranes of complex oxides. The tension applied during the transfer process is sufficient to obtain a high yield of suspended nanodrums. An optical image of 9 u.c. ($h = 3.6$ nm) thick SRO drums ($2R = 13$ μm) is shown in Figure 9.1c. It is remarkable that these materials, much like their van der Waals counterparts, have the flexibility and tensile strength required to be suspended with aspect ratios exceeding $R/h > 1800$. The open question is whether these nanodrums can act as mechanical resonators and whether their motion can be actuated and detected by optical means.

Figure 9.1d shows the measurement setup. The membranes are mounted in the vacuum chamber (10^{-6} mbar) of a closed-cycle cryostat with optical access. The readout of the motion of the suspended nanodrums is performed using a red HeNe laser ($\lambda = 632.8$ nm). The drum and the silicon underneath form a Fabry-Pérot cavity. The motion of the drum modulates the intensity of the reflected light, which is measured by a photodiode. The drums are actuated optothermally, using a blue laser that is coupled into the optical path via a cold mirror [33, 34]. The readout is performed in a homodyne detection scheme using a Vector Network Analyser (VNA), simultaneously sweeping the actuation and detection frequencies.

9.2. Mechanical characterisation

Figure 9.2 shows the mechanical resonances of several STO and SRO drums. Even though STO is transparent in the visible range [173], the motion of the drums can still be actuated and measured optically due to the fact that its refractive index is significantly different than the one of vacuum ($n_{STO} = 2.39$). Figure 9.2a-b shows measurements of two STO drums, and Figure 9.2d-e of two SRO drums of different diameters. Measurements in a wider frequency range show that higher order resonances of the drums can also be detected in both materials. Two examples are shown in Figure 9.2c,f, where up to four higher harmonics are visible. By taking the ratio of the second harmonic to the fundamental mode, we can estimate if the mechanical properties are dictated by the in-plane tension (ratio 1.59) or if they are dominantly determined by the bending rigidity (ratio 2.09). It can be seen from Figure 9.2c that STO is in a cross-over regime (ratio 1.81), which is similar to what has been observed in drums of similar dimensions made of MoS$_2$ [34] and TaSe$_2$ [36]. On the other hand, the mechanical properties of the SRO drums are almost entirely determined by their pre-tension, because $f_1/f_0 = 1.47$, which is close to the theoretical value of 1.59. Statistics on 18 STO drums are included in the Appendix 9.5.1.
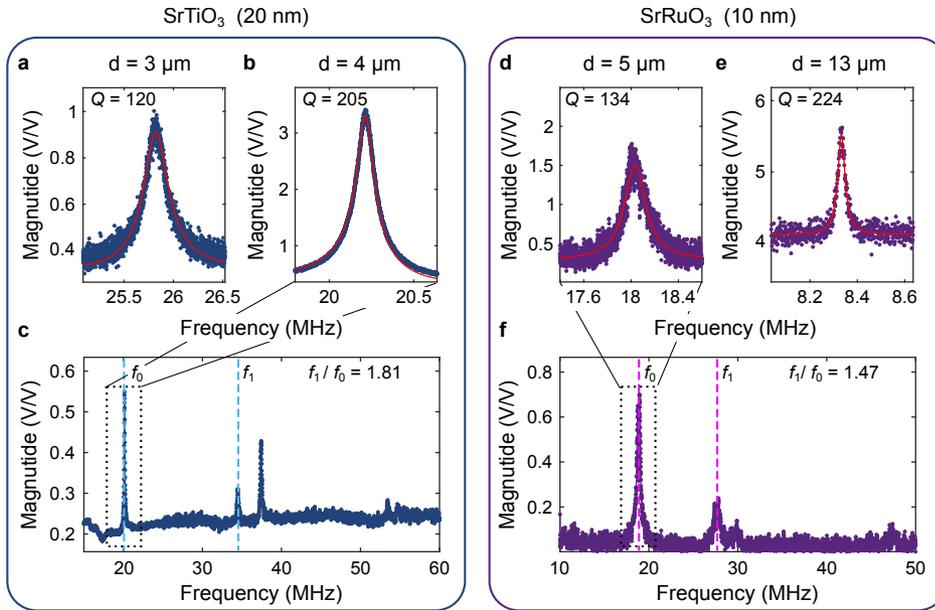
Figure 9.2: **Mechanical characterisation of STO and SRO nanodrums.** Resonance frequency measurements of 20 nm-thick $SrTiO_3$ and 10 nm-thick $SrRuO_3$ nanodrums. **a-b,** Frequency spectra of two $SrTiO_3$ drums with diameters of **a**: 3 μm and **b**: 4 μm. The red lines are linear harmonic oscillator fits. The extracted quality factors are shown in the top left corners of the panels. **c,** A wide-range frequency spectrum of the drum shown in **b**. The positions of the fundamental resonance mode (f_0) and the second harmonic (f_1) are marked with vertical dashed lines. **d-e,** Frequency spectra of two $SrRuO_3$ drums with diameters of **d**: 5 μm and **e**: 13 μm. The red lines are linear harmonic oscillator fits. The extracted quality factors are shown in the top left corners of the panels. **f,** A wide-range frequency spectrum of the drum shown in **d**. The positions of the fundamental resonance mode (f_0) and the second harmonic (f_1) are marked with vertical dashed lines.

9.3. TEMPERATURE DEPENDENCE

It is well established that STO undergoes a number of phase transitions as a function of temperature. The most studied one is the cubic-to-tetragonal transition (T_c = 105 K for bulk STO), where the STO breaks up into locally ordered tetragonal domains, joined by ferroelastic domain walls [174, 175]. Having confirmed that the membrane resonators can be mechanically characterised at room temperature, it is interesting to see if and in what way their mechanical properties are affected when the material undergoes a phase transition. Therefore, in Figure 9.3 we present the temperature-dependence of the mechanical properties of an STO nanodrum. A total of 14 temperature sweeps are recorded in different temperature ranges, shown in Appendix 9.5.2. Figure 9.3a shows the resonance frequency of the drum as a function of temperature. The functional dependence has a parabolic shape, commonly observed in 2D materials [37, 43, 71]. This is usually ascribed to the difference in thermal expansion coefficients of the membrane and the substrate, which results in thermally induced tensile stress. Two anomalies are observed upon warming up: (i) at 165 K there is a clear deviation from the parabolic behaviour and (ii) f_0 shows a kink around 30 K (see inset of Figure 9.3a).

The aforementioned cubic-to-tetragonal phase transition is expected to change the mechanical properties of the material, owing to elastic softening of the STO due to the appearance of domain walls [176]. Such a feature, however, is expected around $T_c = 105$ K for bulk STO crystals. The low thickness[2] and thermally induced strain can cause an elevated transition temperature (compared to bulk) [178] and thus account for the observation of the phase transition at 165 K instead of 105 K. Additional evidence for an elevated transition temperature is found from second harmonic generation measurements that show a feature at 157K (see Appendix 9.5.3). A similar deviation in the $f_0 - T$ dependence was measured in another sample, also at a temperature much higher than 105 K (see Appendix 9.5.3). In order to establish the temperatures at which this phase transition occurs, a second harmonic generation measurement was performed (see Appendix 9.5.4), which shows a feature at around 157 K. The second anomaly at ≈ 30 K may be related to the the onset of the so-called quantum paraelectricity, as it is usually accompanied by an anomaly in the mechanical properties of the material [176, 179–182]. It is worth noting that, although this transition is not structural [180], we still measure its influence on the resonance frequency.

While these features only lead to small shifts in the resonance frequency, they greatly impact the measured mechanical dissipation, as shown in Figure 9.3b. To characterize dissipation we use the quality factor of the resonator, which is extracted from the frequency domain measurements as $Q = f_0/\Delta f$ (Δf is the full width at half maximum of the resonance peak). Whereas the resonance frequency is influenced both by the pretension n_0 and the Young's modulus E, the quality factor should be strongly dependent on the intrinsic losses in the material ($Q \propto \frac{E_1}{E_2}$ for $E = E_1 + iE_2$ [183]). In Figure 9.3b we show the extracted quality factor for 7 subsequent temperature sweeps. In the temperature regions below 30 K and above 165 K the measurement points fall on top of each other. At intermediate temperatures, two distinct branches are observed: a low dissipation branch, traced out by the red data points (belonging to the first two temperature sweeps, including the one from Figure 9.3a), and a high-dissipation branch traced out by the blue data points, which correspond to the 5 subsequent temperature sweeps. The light blue points correspond to measurements taken during cooling down and the red and dark blue points are measurements taken during warmup. The overlap between the measurements in both directions implies that there is no correlation between the dissipation and the direction of the temperature sweep. Moreover, the functional dependence of the resonance frequency on temperature during all 7 measurements remains unchanged (see Appendix 9.5.2), which suggests that the observed effect does not influence the mechanical stiffness of the nanodrum. While the bottom branch is well-defined, evidenced by the 5 overlapping measurement sets, the low-dissipation branch only marks the upper limit of the Q-factor in the measured data. In the Appendix 9.5.2 we show that values of the Q-factor in between the two branches were also measured. Once the system enters the high-dissipation branch, it needs to be warmed up above the transition temperature for it to be able to return to the low-dissipation state. Nevertheless, the system does not always return to that state (red data points in Figure 9.3b), as

---

[2]Even in the case of bulk STO, the transition temperature of the first few layers at its surface is significantly higher [177].
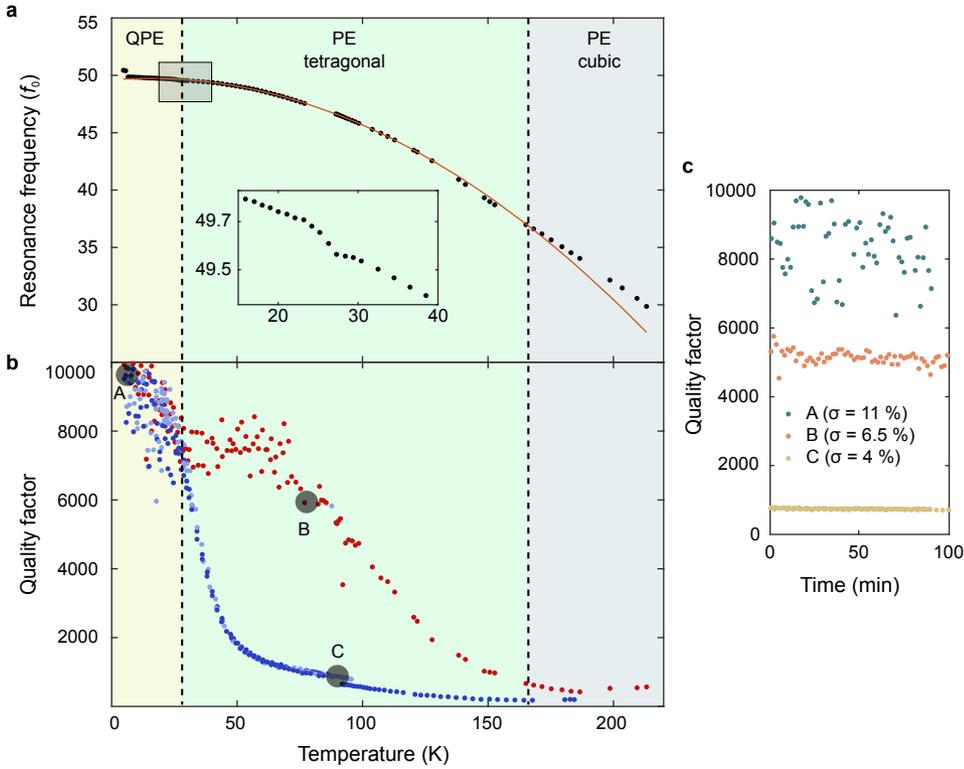
Figure 9.3: **Temperature dependence of the mechanical properties of a 4 μm STO drum. a,** Resonance frequency as a function of temperature. The red line is a parabolic fit to the data. The inset shows a zoomed-in region in the range between 15–40 K. **b,** Quality factor as a function of temperature for seven measurement cycles. Two distinct branches are distinguishable in the region between 30–165 K (dashed lines), coloured in red and blue. The light blue points correspond to cooling cycles. **c,** Quality factor as a function of time at a constant temperature, taken at the points shown in **b**.

it often ends up in one of the branches in between (see Figure 9.6). It is worth noting that switching from a low-dissipation to a high-dissipation branch has been observed (between runs 2 and 3 at around 80 K, see Appendix 9.5.2), but the opposite could not be achieved.

The general trend of decreasing dissipation (increasing Q) at lower temperatures is often observed in 2D materials [37, 43, 153][3] and its origin is a subject of ongoing discussion. A proposed explanation for this effect is the increased in-plane tension which is known to lower dissipation by increasing the energy stored per vibrational cycle in nanomechanical structures [36, 154, 156]. On top of this general trend we observe different states in the dissipation of the STO drums in the temperature region between 30 and 165 K (this effect has also been observed in another drum, shown in Appendix 9.5.3). It is well known that below the transition temperature, STO breaks up into tetragonal

---

[3]and MEMS [184]

domains, joined by ferroelastic domain walls [174, 175]. It has been experimentally determined that these domain walls also become polar (ferroelectric) below a temperature T^*, the exact value of which depends largely on the strain in the film [185–187]. Furthermore, after a minimum amount of polarity is accumulated in the domain walls they become highly mobile [187] and their motion has been linked to increased mechanical dissipation in STO [186].

In this context, we can speculate on possible explanations for the presence of two (or more) $Q(T)$ branches in the intermediate temperature range (30 - 165 K). We discuss two different scenarios, both based on the assumption that the nature of polarity of domains and domain walls in the STO membranes as a function of temperature is not substantially different than in the case of bulk STO. In the first scenario, the dissipation that the system exhibits is related to the polarity of the domain walls. As the temperature drops, domain walls gradually start to become ferroelectric. When a critical polarity is accumulated in the domain walls, they become mobile and introduce significant dissipation (blue data points in Figure 9.3b). The other branches belong to states of the STO where only some of the domain walls are polar and mobile, which manifests itself as lower mechanical dissipation. Below 40 K, all the domain walls become polar [187], and all measurement points fall on top of each other. This scenario would also enable sudden switching from a low dissipation to a high dissipation state, as polarity of the domain walls can be induced by dynamic strain [185]. Even a slight change of the position of the actuation laser (for example, due to mechanical drift) could result in a higher actuation efficiency and, therefore, a higher vibrational amplitude. When the resonator reaches a critical amplitude (i.e. a critical dynamic strain), all domain walls become polar and the system switches to the low Q branch. The polarity of the domain walls is then preserved up to the transition temperature, which is why, once the system enters this state, it needs to be thermally cycled above T_c to be able to return to one of the other branches. The resonance frequency of the membrane is not susceptible to this effect, as the polarity of the domain walls mainly influences the losses in the material.

The second scenario for explaining the $Q(T)$ branches is related to the configuration, i.e., spatial distribution of domain walls upon cooling down below the transition temperature. This is assuming that the amount of accumulated polarity in the domain walls as a function of temperature has the same functional dependence for all the measured curves. One manifestation of the effect of the domain configuration on the dissipation state can be the exact location of the domain walls. The motion of the drum causes a high concentration of dynamic stress at its circular edge. If the domain walls are accumulated at this edge of the drum, the high stress can result in switching of the polarity of the walls, which will drastically increase dissipation (blue data points in Figure 9.3b). Conversely, if the domain walls are randomly occupying the surface of the drum, the stress-induced switching would be less efficient, resulting in lower dissipation. Another manifestation of this scenario would be the location-dependent mobility of the domain walls. Previous works have reported that crossing of domain walls can result in pinning sites that hinder their propagation in the material, which results in "jamming" of the do-

mains [188]. Under this assumption, if these pinning cites are located in the proximity of the drum's centre, it would be easier for the domain walls to move radially, resulting in higher dissipation (blue data points in Figure 9.3b). Any other configuration would result in a lower dissipation, or a higher quality factor (upper branches of Q).

In Figure 9.3c we show the time dependence of the measured quality factor at three different temperatures, indicated as A-C in Figure 9.3b. The standard deviation of the dissipation over time at low temperatures (point A) is 11 %, almost a factor of 2 higher than the scatter at higher temperatures, regardless of the dissipation state of the system in the intermediate regime (points B and C). This phenomenon is consistent with both scenarios, as the measured scatter of the quality factor at low temperatures can be explained by the erratic movement of the domain walls at low temperatures [188].

Finally, in Figure 9.4 we show the measured amplitude at resonance, normalised to the dc voltage measured by the photodiode. This normalisation ensures that changes in the optical properties of the STO at $\lambda = 632.8$ nm (the wavelength of the measurement laser) do not influence the extracted amplitude. The amplitude at resonance decreases with increasing temperature, which can be explained by the significant decrease in the quality factor, because $|A|_{\omega=\omega_0} = \frac{FQ}{\omega_0^2 m}$, where F is the driving force, ω_0 is the natural frequency and m is the effective mass of the resonator. Interestingly, only the measurement points that belong to the high-dissipation branch (blue points in Figures 9.3b and 9.4) exhibit a large peak at around 34 K. This is counterintuitive, because, as the resonance frequency at a given temperature does not depend on the dissipation state of the system, one would expect that a lower quality factor (blue data points) should result in a lower amplitude. The only possible explanation is that, when the system is in the low Q branch, the driving force F (or the actuation efficiency) becomes larger, and this increase in actuation efficiency is much greater than the decrease in the Q-factor. The increased actuation efficiency cannot be caused by a change in the absorption of STO at $\lambda = 405$ nm, which is constant as a function of temperature in the measured range [189]. Therefore, the remaining interpretation is that the cause of the increased driving efficiency is a change in the thermal properties of the material (thermal expansion coefficient, heat conductivity, etc.). The so-called Debye term (C_p/T^3, where C_p is the specific heat of the material), which is also closely related to the thermal expansion of the material (α) [190], has been measured to peak at around 30 K [191]. The width of the peak in C_p/T^3 [191] is also consistent with the width of the amplitude peak in our measurements (blue curve in Figure 9.4), which means that the change in the thermal properties is likely the underlying reason for the increase in actuation efficiency. Nevertheless, the absence of the peak in all the other traces is challenging to explain within any of the thus far proposed scenarios.

A macroscopic interpretation of both the different dissipation states and the peak in vibrational amplitude could involve the strong dependence of the imaginary part of the Young's modulus (E_2) on the static and dynamic stress. In the work of Kityk *et al.* [176] the temperature dependence of E_2 as a function of both static in-plane and out-of-plane load and low-frequency dynamic load is measured. It is shown that in the temperature region between 25 K and 45 K the material shows a nonlinear elastic behaviour, where the losses increase with increasing dynamic load. In this framework, the results from Figures 9.3 and 9.4 could be interpreted as follows. The vibrational amplitude is coupled
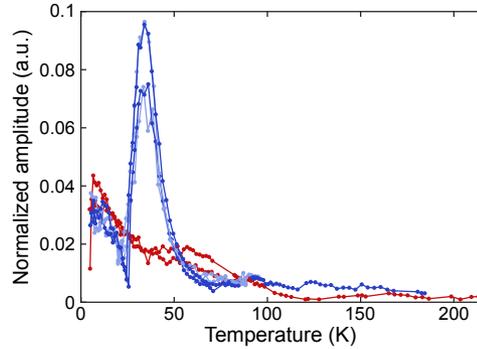
9

Figure 9.4: **Normalized motion amplitude at resonance for the data from Figure 9.3c.** The y-axis shows the resonance peak amplitude divided by the dc voltage on the photodiode to compensate for changes in the reflectivity of the sample.

to the mechanical losses of the drum. Around 30 K, the system enters a metastable state, where depending on the initial conditions, it can either enter a high-amplitude state which results in high dissipation, or a low-amplitude state, which results in lower dissipation. Two effects cannot be incorporated in this explanation, namely, the existence of multiple low dissipation branches (whereas the amplitude seems to exhibit only two, see Figure 9.6) and the fact that the system gets "locked" in the low dissipation branch, despite the thermal cycling between 5 and 165 K (upon warming up above 30 K, occupation of either state should be possible, despite the measurement history). The ultimate explanation probably lies in a combination of two or more of the proposed mechanisms.

In conclusion, we demonstrated the fabrication of ultrathin mechanical resonators made of epitaxially grown STO and SRO films. Using laser interferometry, we mechanically characterized the nanodrums and showed that they can be used as nanomechanical devices, much like drums made of van-der-Waals materials [33–38]. The temperature dependence of the resonance frequency of STO drums showed clear anomalies at 30 K and at 165 K which we ascribed to the onset of quantum paraelectricity and the cubic-to-tetragonal phase transition of STO respectively. These have an even stronger effect on the dissipation in this intermediate temperature range, exhibiting different dissipation regimes, for which we proposed several explanations based on the polarity and/or configuration of the domain walls in the film. We hereby show that ultrathin complex oxide resonators can be used to probe the intricate changes in the material and gain more insight in the domain wall physics when it undergoes a phase transition. This work makes important contributions to two fields: (i) to the field of complex oxides it adds a new tool to probe their mechanical properties, which are often strongly coupled to their structural order parameters; (ii) to the field of nanomechanics it adds a plethora of new materials with exotic properties that can be engineered by PLD growth techniques, e.g., by growing epitaxial multilayer heterostructures, something that is not easily achieveable with van der Waals materials. These materials can be used in self-transducing mechanical devices, suspended optical modulators, biomorphic actuators and novel thermomechanical and piezoelectric sensing concepts.

9.4. METHODS

$Sr_3Al_2O_6$, $SrTiO_3$, and $SrRuO_3$ films were grown by pulsed laser deposition on TiO_2-terminated $SrTiO_3$ (001) substrates. The pulses were supplied by a KrF excimer laser and the substrate was mounted using two clamps and heated by an infrared laser. $Sr_3Al_2O_6$ and $SrTiO_3$ were deposited using a laser fluence of 1.2 J/cm^2, a substrate temperature of 850°C and an oxygen pressure of 10^{-6} mbar. $SrRuO_3$ was deposited at 600°C, with a fluence of 1.1 J/cm^2 and an oxygen pressure of 0.1 mbar. The growth occurred in layer-by-layer mode for $Sr_3Al_2O_6$ and $SrTiO_3$, while $SrRuO_3$ was grown in step-flow mode. After the deposition, the heterostructures were annealed for one hour at 600°C in 300 mbar O_2, and cooled down in the same atmosphere.

The thin films were released by adhering a polydimethylsiloxane (PDMS) layer to the film surface and immersing the stack in water. Dissolution of a 50 nm $Sr_3Al_2O_6$ layer was found to take approximately 60 minutes. After releasing the substrate, the PDMS layer with the thin film was dried using dry N_2. The $SrTiO_3$ and $SrRuO_3$ films were transferred onto pre-patterned Si/285 nm SiO_2 substrates using an all-dry deterministic transfer technique [101]. The crystallinity of the thin films before and after their release was investigated by X-ray diffraction (see Fig. 9.1b).

9

9.5. APPENDIX

9.5.1. STATISTICS OF SRTIO$_3$ NANODRUMS

In Figure 9.5 we show statistical data of eleven 3-μm and seven 4-μm drums measured at room temperature and at 4.4 K. In all the drums we see a drastic increase in the quality factor at low temperatures: an average of 75-fold increase in the 3-μm drums and 88-fold increase in the 4-μm drums. The resonance frequency is affected more strongly in the 4-μm drums, which is expected, because for larger drums the pre-tension has a stronger influence on the dynamic behaviour.
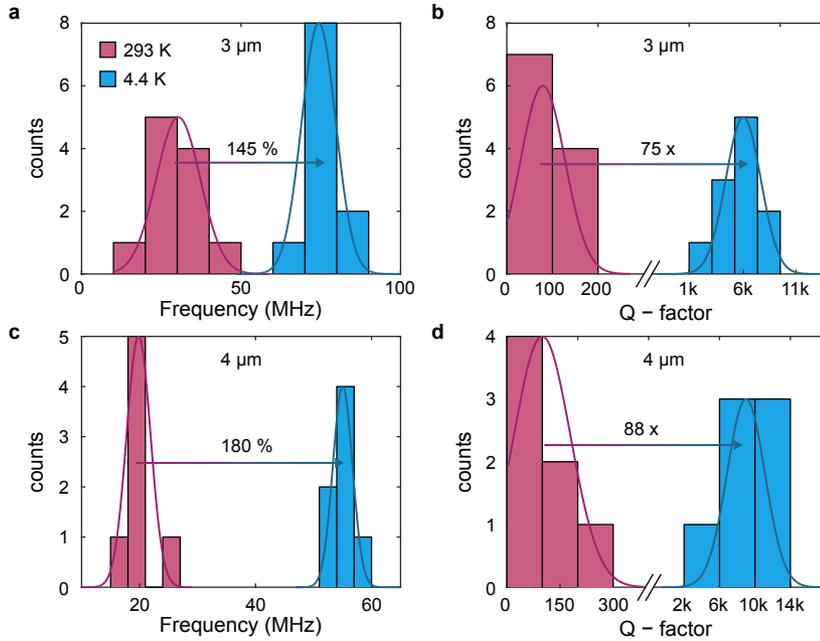

Figure 9.5: **Statistical comparison of many STO drums between room- and low-temperature.** Histograms of the resonance frequencies of **a,** 3 μm and **c,** 4 μm STO drums. Histograms of the quality factor of **b,** 3 μm and **d,** 4 μm STO drums.

9

9.5.2. MAIN DEVICE FULL DATASET

Figure 9.6 shows the full measurement set for the device shown in Figure 9.3, comprising of 14 runs. Figure 9.6d shows the derivative of the resonance frequency with respect to temperature, which is flat below 30 K and shows a change in slope above 150 K (illustrated by the dashed blue line in Figure 9.6d).
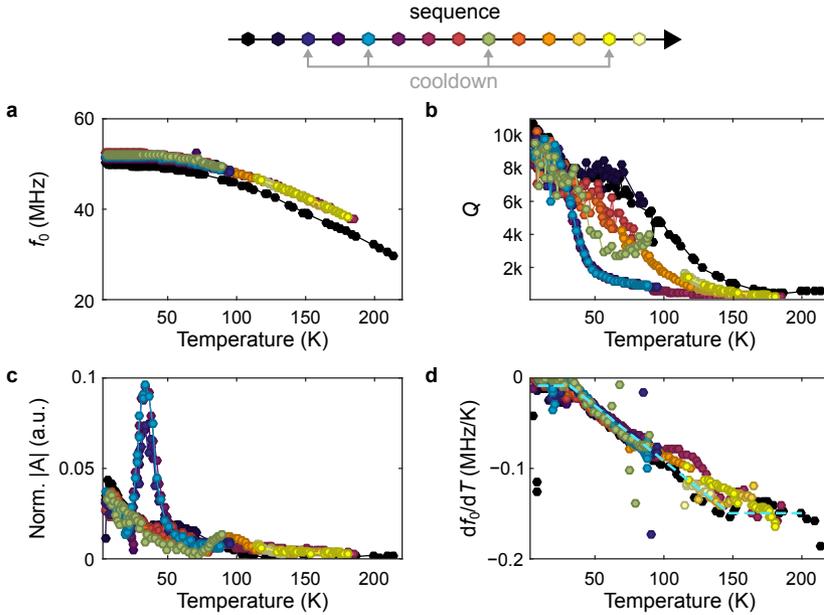

Figure 9.6: **Temperature dependence for the STO drum from Figure 3 in the main text for all 14 runs. a,** Resonance frequency, **b,** Q-factor, **c,** Normalised peak amplitude and **d,** df_0/dT vs. temperature. The measurement sequence is given above. The dashed blue line in **d** is a guide to the eye.

9

9.5.3. OTHER DEVICES

Temperature dependent measurements were performed on two additional STO drums (20 nm thick, 4 μm in diameter), shown in Figure 9.7. Drum 2 shows a deviation of the parabolic behaviour of the resonance frequency (Figure 9.7a), similar to the one shown in Figure 9.3, but at a lower temperature. Both samples show anomalies around 30 K, as shown in the insets of Figure 9.7a-b. The Q-factor of drum 3 also shows two distinct dissipation branches for the two temperature sweeps, plotted in different colours in Figure 9.7b,d,f. The low Q branch is, as in the case for the main device, accompanied by an increase in the vibrational amplitude, as can be seen in Figure 9.7f. It is important to point out that the amplitude plotted in Figure 9.7e-f is not normalised with respect to the photodiode voltage, so any effects stemming from changes in the optical properties of the material for the wavelength of the measurement laser (λ = 632.8 nm) are not compensated in these plots.
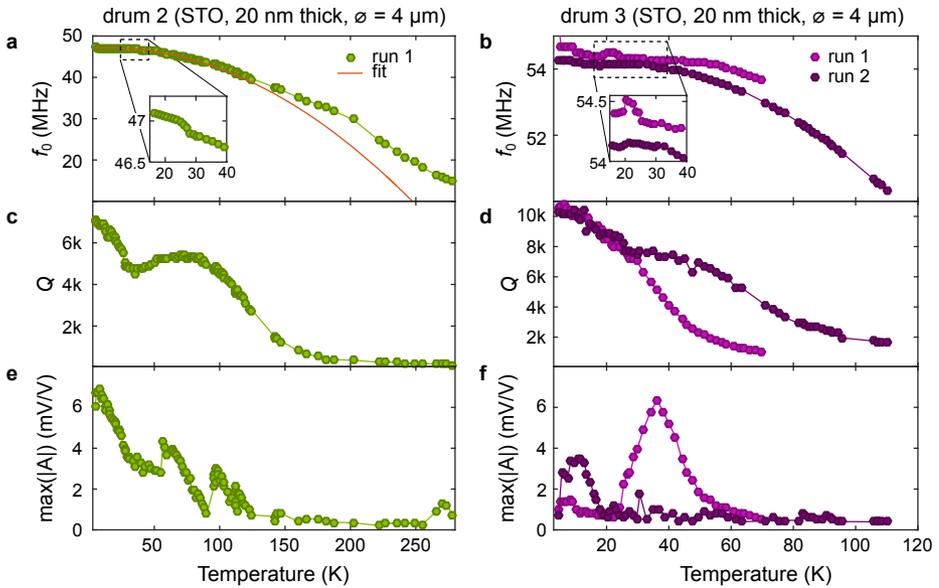

Figure 9.7: **Temperature dependence for two other STO drums.** Resonance frequency vs. temperature for **a,** drum 2 and **b,** drum 3. The red curve in **a** is a parabolic fit to the data. The insets show a zoomed-in region around 30 K. Q-factor vs. temperature for **c,** drum 2 and **d,** drum 3. Peak amplitude (not normalised) vs. temperature for **e,** drum 2 and **f,** drum 3.

9.5.4. SECOND HARMONIC GENERATION

A second harmonic generation (SHG) measurement was performed on the Si/SiO$_2$ sample with the 20 nm thick STO film transferred on top. The measurement area is determined by the laser spot size in the setup, which is estimated to be around 100 μm. The measurements were taken during cooldown (blue curve in Figure 9.8) and during

warmup (orange curve in Figure 9.8). The measurements show two features, one at 105 K, which corresponds to the transition temperature of bulk STO (potentially stemming from regions with multiple STO flakes stacked on top of each other), and another one at 157 K.
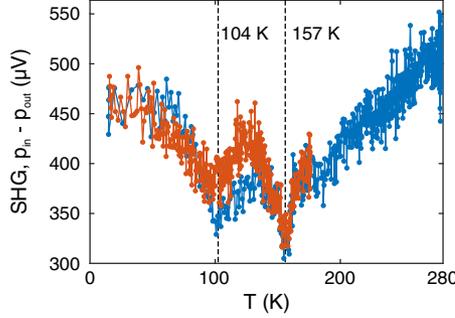

Figure 9.8: **SHG signal from the STO film.** SHG signal using a $p_{\text{in}} - p_{\text{out}}$ beam configuration taken while warming up (orange) and cooling down (blue).

9.5.5. PEAK-FORCE ATOMIC FORCE MICROSCOPY

In Figure 9.9 we use peak-force atomic force microscopy (AFM) to extract the pre-tension and the Young's modulus of the STO drum shown in Figure 9.2b. The resonance frequency in the cross-over regime can be approximated as [34]:

$$f_0 = \sqrt{f_{0,\text{membrane}}^2 + f_{0,\text{plate}}^2} \tag{9.1}$$

where $f_{0,\text{membrane}} = \frac{2.4}{\pi d} \sqrt{\frac{n_0}{\rho h}}$ and $f_{0,\text{plate}} = \frac{10.21}{\pi} \sqrt{\frac{E}{3\rho(1-\nu^2)}} \frac{h}{d^2}$. Using the numbers obtained from Figure 9.9, we get $f_0 = 19.4$ MHz, similar to the measured value for the same drum (see Figure 9.2b).
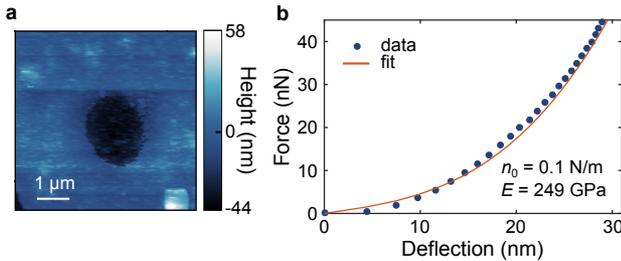
Figure 9.9: **Peak-force AFM of a suspended 4 μm STO drum. a,** Height profile. **b** Force-deflection curve taken in the centre of the drum. The red line is the fitted model, from which the Young's modulus and pre-tension are extracted.

10

CONCLUSIONS AND OUTLOOK

In this chapter, we give a brief overview of the entire thesis together with an outlook on how these findings could be integrated into new devices or serve as a platform for studying novel fundamental aspects in a wide class of 2D materials.

W^E started with a broad introduction of the topic of 2D materials, we looked into membranes made of these layered materials and gave an overview on how they could be implemented into NEMS devices. We also underlined some aspects of the physics of 2D membranes that were still not fully understood and some technological issues that were not resolved. In this chapter, we will look back and try to connect all the chapters in one whole, explain how the solution to one problem led to a new device, how that new device shed some light on an underlying physical phenomenon and how this physical phenomenon helped us solve another problem. In this process, we will try give answers to some of the questions that were posed at the beginning, many of which will be new questions altogether.

In Chapter 2 we laid out the basics on the dynamics of nanomechanical resonators. Part of it described the 2D membranes in the framework of the ubiquitous linear harmonic oscillator model, while in the second half we focused on describing a way of relating the nonlinear dynamics of the membranes to their material properties. Chapter 3 described most of the methods that we use for measurements, data processing and fabrication, our scientific arsenal.

In the Chapters 4 and 5 our main focus was on characterisation of 2D materials, in particular graphene and MoS_2. In Chapter 4, we image the vibrational mode shapes of a few-layer graphene membrane to discover that they are not exactly what one would expect them to be. By optimising the cavity depth and automatising the stage motion, we could image eight vibrational mode shapes of the nanodrum, with a lateral resolution of 140 nm [97]. The displacement sensitivity was sufficient to also image the thermal motion of the first three resonance modes. Whereas some of the mode shapes resembled closely the ones expected from theory, others showed weak correspondence to their theoretical counterparts. We ascribed this discrepancy to morphological imperfections of the nanodrum: AFM measurements showed a small wrinkle at its edge. What was really astonishing was that we could put in the exact location of the wrinkle in a finite-elements model, add uniaxial tension along the wrinkle and get an almost exact match of the simulated mode shapes to the measured ones. This was not only true for the vibrational shapes but also for the frequencies of almost all higher harmonics.

It is rather clear that these wrinkles arise from the transfer process of 2D materials: this is an aspect of the field that requires a lot of improvement. It is currently performed manually, in an unreliable, non-reproducible way, which means that wrinkles will likely be an ominous phenomenon in these devices until the transfer process is standardised. The bad news is that, taking this into consideration, it would be challenging to use 2D membranes as mass sensors due to two main issues: (i) the morphology of the membrane slightly changes the effective mass of each vibrational mode, which would hamper the mass resolution of the device and (ii) due to the distorted mode shapes, it would be very challenging to use 2D nanodrums as inertial imaging devices, a neat concept proposed in Ref. [115], where the authors develop a theoretical framework to predict the exact shape and mass distribution of adhered particles based on the vibrational mode shapes. The good news is that the conclusion that the vibrational shapes can be directly related to a wrinkle opens up a new research route. With an accurate model, one could extract the exact morphology of the drum from its vibrational mode shapes. Or what would be even more exciting to see is if, from a single frequency spectrum (the discrep-

ancies between the positions of the peaks and the expected theoretical values), one can deduce the position of a wrinkle by using its distance to the centre as a single fit parameter. This would enable *a priori* knowledge of the morphology that can be later used to predict the dynamic behaviour of the membrane.

The issue with the transfer-induced wrinkles did not stop us from trying: one of the motivations behind the heaters described in Chapter 7 was to see if we could iron them out. It turned out that using biaxial tension this was not possible: instead of ironing out the membrane, the in-plane tension just promoted the creation of a wrinkle. It is mathematically impossible to do this in a circular geometry: the wrinkle "has nowhere to go", to put it in layman's terms[1].

Morphological imperfections are very likely the reason for the large spread in reported values for the mechanical properties of 2D materials [17, 25, 58, 130]. It has been shown that wrinkles and ripples affect the observed (effective) mechanical properties of 2D materials [103, 129, 143, 162]. This was the motivation behind the work presented in Chapter 2 and Chapter 5, in which we introduced a method to probe the mechanical properties in a non-invasive way: using their nonlinear dynamic response [123]. This is a valuable addition to the exhaustive theoretical work on nanomechanics of 2D materials [17, 66–68], because we can now measure the Young's modulus of 2D nanodrums at high frequencies in a non-invasive manner. Despite these efforts, one question still remains: are we probing the Young's modulus or the Poisson's ratio? There is, to-date, no systematic way to measure these two mechanical properties independently: one needs to assume a Poisson's ratio to extract a Young's modulus.

It has been theoretically predicted that some 2D materials, like MoS_2 have intrinsic nonlinear dissipation mechanisms [192]. It would be interesting to see whether, by performing a statistical study on many MoS_2 nanodrums, we could measure different Young's moduli using the static (AFM) and the dynamic method and then use this extract the viscoelasticity of the material.

This brings us to damping: how much of the (high) dissipation of 2D resonators can be ascribed to intrinsic losses? Dissipation is a burning question in the field of 2D resonators. The generally accepted theory is that the main source of losses are the clamping points, backed up by a study by Rieger *et al.* [76]. A curious phenomenon is observed when cooling down the resonators: the resonance frequency increases, which is ascribed to the difference in thermal expansion coefficients between the 2D material and the SiO_2 or metallic cavity. However, the net stress upon cooling always seems to be tensile, regardless of the material and its thermal expansion coefficient [37, 43, 71, 153]. Moreover, the increase in f_0 was always accompanied by an increase in the quality factor, which is again attributed to thermally-induced tensile stress [43, 71]. In Chapter 7 we tried to mimic this effect at room temperature by constructing a heater ring on top of which a graphene flake would be suspended. Now, contrary to the usual approach of applying tension via an out-of-plane electrostatic force, we were finally able to apply tension in-plane electrothermally, by running a current through the heater. The result? Both the frequency and quality factor increase. Where is the catch? Are we doomed to have low

10

---

[1]This result might be counter-intuitive, but it can be reproduced by suspending a thin plastic bag over a paper cup. Just push gently with a finger at the edge of the cup and then try to stretch the bag in all directions. You will see that instead of ironing out the small wrinkle that you created, you are just making it bigger.
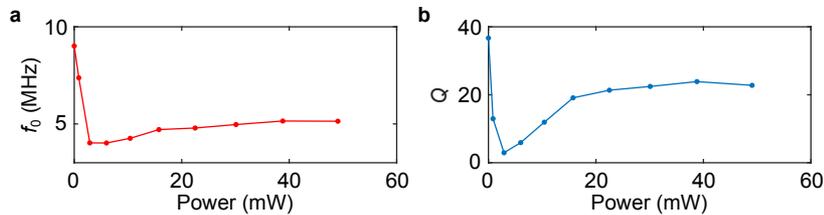
Figure 10.1: **Measurements on a multilayer MoS$_2$ membrane suspended on a heater ring. a,** Resonance frequency and **b,** quality factor as a function of heater power.

quality factors at room temperature? Does it have to do with the fact that the flakes are usually transferred at room temperature? Is it a pure tensile effect or is it related to the fact that in-plane tension also reduces membrane slack? There is still no clear evidence as to which of the dissipation routes prevails and how dissipation at room temperature can be reduced.

An interesting observation is that when we replace the graphene with MoS$_2$, which has a high positive thermal expansion coefficient, we observe the opposite effect (see Figure 10.1). Both the frequency and the quality factor show a sharp decline, reach a minimum and then slowly start to rise. This is indicative of buckling [193], which is an interesting topic by itself. Around the buckling point (minima in Figure 10.1a-b), the system is metastable: the compressive stress forces the membrane to bulge either upwards or downwards. By raising the effective temperature of the system, one could promote switching between these two states, similar to works on MEMS devices [194]. The advantage of using 2D materials is that, due to their size, the energy scales required to do so are much lower. Therefore, switching can be potentially achieved at room temperature and, in combination with electrostatic tuning, can be used to measure some fundamental concepts of the physics of information, like the Landauer limit [195].

Another attractive point of the heater device shown in Chapter 7 is that it allows for electrothermal actuation, by dynamic modulation of the tension in the suspended drum. This can be used to excite the motion of 2D resonators parametrically, similarly to what was reported using an optothermal drive [196]. The heater is advantageous because it eliminates optical backaction effects from the driving laser [113].

In terms of device fabrication, the paramount achievement was the process flow shown in Chapter 6, which enabled us to fabricate devices on an insulating quartz substrate. Another strong point was the usage of spin-on-glass as a dielectric, which provided an extremely smooth interface between the top and bottom electrode. The parasitic capacitance in these devices was in the order of 500 fF, sufficient to allow detection of capacitance changes down to a few tens of attoFarads. Using this device, we demonstrated capacitive readout and pressure sensing using a single graphene drum [58]. The measurement was successfully repeated with a cheap (10 euros) AD7746 capacitance-to-digital converter, which proved that such devices can be used in a combination with integrated readout circuits. An unresolved issue is the drift in the measured capacitance, that also hampered the measurement of gas permeation using the same method.
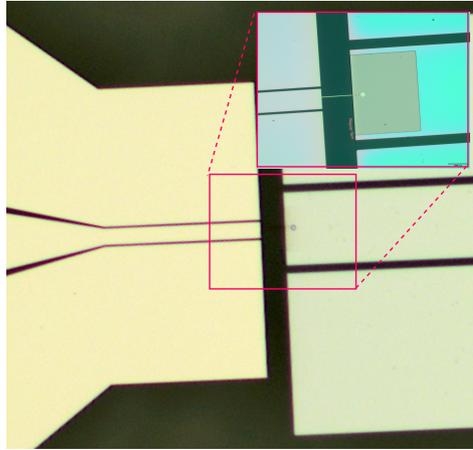
10

Figure 10.2: **Optical image of an electrical readout chip for dynamic capacitive detection at room temperature.** The inset shows a zoom-in of the device.

We also tried to extend this idea to a dynamic capacitive readout circuit (see Figure 10.2) employing the same process flow from Chapter 6 in order to get closed cavities. The concept is rather simple: two 50 Ω transmission lines are coupled by a suspended 2D membrane, which acts as a coupling capacitor. The fabrication is done on quartz, to minimize the parasitic capacitance of the electrodes. The motion of the suspended drum would modulate a GHz carrier signal sent through one of the transmission lines, which will get demodulated at the other side. In interest of time, this readout scheme was not fully explored. It would be, nevertheless, interesting to see if a hermetically sealed nanodrum could be read out capacitively. This would solve many annoying issues of laser heating, photothermal backaction and drift and would pave the way towards on-chip integration of resonant tension-induced pressure sensors.

Full hermeticity using a single-layer membrane has still not been achieved. This is partly because, even at permeation rates of $10^{-26}\,\mathrm{molPa^{-1}s^{-1}}$, the cavity volumes are so small that gas leaks out within 24–48 hours. A way to seal the cavities better (e.g., by using a metallic clamping ring) would at least eliminate one possible culprit for the poor hermeticity of 2D membranes: the membrane-substrate interface.

The fabrication process developed in Chapter 6, however, turned out to be very fruitful for experimenting in terms of the design freedom it offered. Using the same process, we fabricated individually addressable cavities coupled by a trench. By transferring graphene on top, we could seal these cavities and couple the two graphene drums pneumatically. This, together with a simplified model of the behaviour of these graphene gas pumps was described in Chapter 8. The advantage that this system offers is not only that that low mass and flexibility of graphene provide good pumping efficiency, but also in the fact that graphene's porosity can be easily modified, so one can envision nanosyringes based on porous graphene pumps. Such systems could be used for translocation of, e.g. denatured proteins, composed of amino acids of different polarities. The pump

10

concept can also be used in the absence of pneumatic actuation, as two individually-tunable resonators coupled through a graphene trench. This is useful for fundamental studies, like coherent phonon manipulation [197], but also for measuring the mechanical impedance of graphene ribbons.

Finally, in Chapter 9 we looked into a completely new kind of nanodrum resonators - ones made of complex oxides. The ability to grow these materials epitaxially and then release the ultra-thin films in water was just too tempting. We made tens of resonators of STO and SRO, described in Chapter 9 and we managed to get nanodrums of up to 21 μm in diameter with surprisingly high yield. The dynamic characterisation was focused on the STO, since it is famous for undergoing a couple of phase transitions, which significantly influence its properties [198–201]. Despite STO being fully transparent, we could successfully actuate and measure the drums optically. The temperature dependence of their mechanical resonance frequency showed discontinuities, which we ascribe to structural phase transitions in the STO. The quality factor, on the other hand, showed two distinct branches in the range between 30–165 K, which we speculate to be connected to the polarity and/or the configuration of domains and domain walls in the nanodrums. This study, even though not fully completed, suggests that ultra-thin complex oxide membranes can be used to probe the intricate changes in these materials when they undergo a phase transition. It is also a valuable expansion of the palette of ultra-thin materials with exotic properties that can be used in future NEM systems.

Finally, a short disclaimer on the title. After reading the thesis, the reader might feel deceived with the exact wording used in the title: "two-dimensional". By convention, a two-dimensional material is a single layer of a van-der-Waals material. By now the reader might have noticed that throughout the entire thesis only a single measurement has been presented on a monolayer graphene device (Chapter 4). Is the title a lie? Well, not exactly. Technically, there are no conclusive studies showing that the mechanical properties (Young's modulus, Poisson's ratio) of thicker flakes differ from the single- or 10-layer case. It is, of course, always better to work with single-layer materials, as this makes the study more credible and relevant, especially when characterising the materials, as we did in Chapters 4, 5 and 7. Exfoliating and transferring these monolayers, on the other hand, is a very time-consuming process which requires a lot of patience. The alternative is using CVD-grown monolayers, which are, again, not always representative of the naturally occurring materials as CVD growth often comes at the cost of quality [54]. Instead of doing that, we chose to focus on novel methods, concepts and devices, which we hope to prove useful for future advancements of the field of 2D nanomechanics. Which one(s) will eventually turn out to be the most useful, we have to wait and see.

REFERENCES

[1] J. S. Bunch, *Mechanical and electrical properties of graphene sheets* (Cornell University Ithaca, NY, 2008).

[2] C. Chen, *Graphene NanoElectroMechanical Resonators and Oscillators* (Columbia University, 2013).

[3] S. P. Koenig, *Graphene Membranes: Mechanics, Adhesion, and Gas Separations* (University of Colorado, Boulder, 2013).

[4] R. J. T. Nicholl, *Non-Hookean Mechanics of Crystalline Membranes* (Vanderbilt University, 2017).

[5] K. S. Novoselov, A. K. Geim, S. V. Morozov, D. Jiang, Y. Zhang, S. V. Dubonos, I. V. Grigorieva, and A. A. Firsov, *Electric field effect in atomically thin carbon films,* Science **306**, 666 (2004).

[6] K. S. Novoselov, A. K. Geim, S. Morozov, D. Jiang, M. Katsnelson, I. Grigorieva, S. Dubonos, and A. A. Firsov, *Two-dimensional gas of massless dirac fermions in graphene,* Nature **438**, 197 (2005).

[7] L. Wang, I. Meric, P. Y. Huang, Q. Gao, Y. Gao, H. Tran, T. Taniguchi, K. Watanabe, L. M. Campos, D. A. Muller, J. Guo, P. Kim, J. Hone, K. L. Shepard, and C. R. Dean, *One-dimensional electrical contact to a two-dimensional material,* Science **342**, 614 (2013).

[8] A. B. Kuzmenko, E. van Heumen, F. Carbone, and D. van der Marel, *Universal optical conductance of graphite,* Physical Review Letters **100**, 117401 (2008).

[9] E. Ganz, A. B. Ganz, L.-M. Yang, and M. Dornfeld, *The initial stages of melting of graphene between 4000 K and 6000 K,* Physical Chemistry Chemical Physics **19**, 3756 (2017).

[10] J.-U. Lee, D. Yoon, H. Kim, S. W. Lee, and H. Cheong, *Thermal conductivity of suspended pristine graphene measured by raman spectroscopy,* Physical Review B **83**, 081419 (2011).

[11] X. Xu, L. F. Pereira, Y. Wang, J. Wu, K. Zhang, X. Zhao, S. Bae, C. T. Bui, R. Xie, J. T. Thong, B. H. Hong, K. P. Loh, D. Donadio, B. Li, and B. Özilmaz, *Length-dependent thermal conductivity in suspended single-layer graphene,* Nature Communications **5**, 3689 (2014).

[12] J. Dauber, A. A. Sagade, M. Oellers, K. Watanabe, T. Taniguchi, D. Neumaier, and C. Stampfer, *Ultra-sensitive hall sensors based on graphene encapsulated in hexagonal boron nitride,* Applied Physics Letters **106**, 193501 (2015).

[13] Z. Yan, G. Liu, J. M. Khan, and A. A. Balandin, *Graphene quilts for thermal management of high-power gan transistors,* Nature Communications **3** (2012).

[14] T. Echtermeyer, M. C. Lemme, J. Bolten, M. Baus, M. Ramsteiner, and H. Kurz, *Graphene field-effect devices,* The European Physical Journal-Special Topics **148**, 19 (2007).

[15] C. S. Boland, U. Khan, G. Ryan, S. Barwich, R. Charifou, A. Harvey, C. Backes, Z. Li, M. S. Ferreira, M. E. Möbius, R. J. Young, and J. N. Coleman, *Sensitive electromechanical sensors using viscoelastic graphene-polymer nanocomposites,* Science **354**, 1257 (2016).

[16] M. Poot and H. S. van der Zant, *Nanomechanical properties of few-layer graphene membranes,* Applied Physics Letters **92**, 063111 (2008).

[17] C. Lee, X. Wei, J. W. Kysar, and J. Hone, *Measurement of the elastic properties and intrinsic strength of monolayer graphene,* Science **321**, 385 (2008).

[18] R. Zan, Q. M. Ramasse, U. Bangert, and K. S. Novoselov, *Graphene reknits its holes,* Nano Letters **12**, 3936 (2012).

[19] J. S. Bunch, S. S. Verbridge, J. S. Alden, A. M. van der Zande, J. M. Parpia, H. G. Craighead, and P. L. McEuen, *Impermeable atomic membranes from graphene sheets,* Nano Letters **8**, 2458 (2008).

[20] S. Huh, J. Park, Y. S. Kim, K. S. Kim, B. H. Hong, and J.-M. Nam, *UV/ozone-oxidized large-scale graphene platform with large chemical enhancement in surface-enhanced raman scattering,* ACS Nano **5**, 9799 (2011).

[21] S. P. Koenig, L. Wang, J. Pellegrino, and J. S. Bunch, *Selective molecular sieving through porous graphene,* Nature Nanotechnology **7**, 728 (2012).

[22] K. Novoselov, D. Jiang, F. Schedin, T. Booth, V. Khotkevich, S. Morozov, and A. Geim, *Two-dimensional atomic crystals,* Proceedings of the National Academy of Sciences **102**, 10451 (2005).

[23] L. Li, Y. Yu, G. J. Ye, Q. Ge, X. Ou, H. Wu, D. Feng, X. H. Chen, and Y. Zhang, *Black phosphorus field-effect transistors,* Nature Nanotechnology **9**, 372 (2014).

[24] A. Castellanos-Gomez, L. Vicarelli, E. Prada, J. O. Island, K. Narasimha-Acharya, S. I. Blanter, D. J. Groenendijk, M. Buscema, G. A. Steele, J. Alvarez, H. W. Zandbergen, J. J. Palacios, and H. S. J. van der Zant, *Isolation and characterization of few-layer black phosphorus,* 2D Materials **1**, 025001 (2014).

[25] A. Castellanos-Gomez, V. Singh, H. S. van der Zant, and G. A. Steele, *Mechanics of freely-suspended ultrathin layered materials,* Annalen der Physik **527**, 27 (2015).

[26] L. Song, L. Ci, H. Lu, P. B. Sorokin, C. Jin, J. Ni, A. G. Kvashnin, D. G. Kvashnin, J. Lou, B. I. Yakobson, and P. M. Ajayan, *Large scale growth and characterization of atomic hexagonal boron nitride layers,* Nano Letters **10**, 3209 (2010).

[27] A. Falin, Q. Cai, E. J. Santos, D. Scullion, D. Qian, R. Zhang, Z. Yang, S. Huang, K. Watanabe, T. Taniguchi, M. R. Barnett, Y. Chen, R. S. Ruoff, and L. H. Li, *Mechanical properties of atomically thin boron nitride and the role of interlayer interactions,* Nature Communications **8**, 15815 (2017).

[28] J. Tao, W. Shen, S. Wu, L. Liu, Z. Feng, C. Wang, C. Hu, P. Yao, H. Zhang, W. Pang, X. Duan, J. Liu, C. Zhou, and D. Zhang, *Mechanical and electrical anisotropy of few-layer black phosphorus,* ACS Nano **9**, 11362 (2015).

[29] M. Gad-el Hak, *The MEMS handbook* (CRC press, 2001).

[30] A. N. Cleland, *Foundation of Nanomechanics: From Solid-State Theory to Device Applications* (2003).

[31] K. Ekinci and M. Roukes, *Nanoelectromechanical systems,* Review of scientific instruments **76**, 061101 (2005).

[32] R. J. Dolleman, D. Davidovikj, S. J. Cartamil-Bueno, H. S. J. van der Zant, and P. G. Steeneken, *Graphene squeeze-film pressure sensors,* Nano Letters **16**, 568 (2016).

[33] J. S. Bunch, A. M. Van Der Zande, S. S. Verbridge, I. W. Frank, D. M. Tanenbaum, J. M. Parpia, H. G. Craighead, and P. L. McEuen, *Electromechanical resonators from graphene sheets,* Science **315**, 490 (2007).

[34] A. Castellanos-Gomez, R. van Leeuwen, M. Buscema, H. S. J. van der Zant, G. A. Steele, and W. J. Venstra, *Single-layer MoS$_2$ mechanical resonators,* Advanced Materials **25**, 6719 (2013).

[35] Z. Wang, H. Jia, X. Zheng, R. Yang, Z. Wang, G. Ye, X. Chen, J. Shan, and P. X.-L. Feng, *Black phosphorus nanoelectromechanical resonators vibrating at very high frequencies,* Nanoscale **7**, 877 (2015).

[36] S. J. Cartamil-Bueno, P. G. Steeneken, F. D. Tichelaar, E. Navarro-Moratalla, W. J. Venstra, R. van Leeuwen, E. Coronado, H. S. J. van der Zant, G. A. Steele, and A. Castellanos-Gomez, *High-quality-factor tantalum oxide nanomechanical resonators by laser oxidation of TaSe$_2$,* Nano Research **8** (2015).

[37] N. Morell, A. Reserbat-Plantey, I. Tsioutsios, K. G. Schädler, F. Dubin, F. H. Koppens, and A. Bachtold, *High quality factor mechanical resonators based on WSe$_2$ monolayers,* Nano Letters **16**, 5102 (2016).

[38] S. J. Cartamil-Bueno, M. Cavalieri, R. Wang, S. Houri, S. Hofmann, and H. S. van der Zant, *Mechanical characterization and cleaning of CVD single-layer h-BN resonators,* npj 2D Materials and Applications **1**, 16 (2017).

[39] A. Smith, S. Vaziri, F. Niklaus, A. Fischer, M. Sterner, A. Delin, M. Östling, and M. Lemme, *Pressure sensors based on suspended graphene membranes,* Solid-State Electronics **88**, 89 (2013).

[40] R. J. Dolleman, S. J. Cartamil-Bueno, H. S. van der Zant, and P. G. Steeneken, *Graphene gas osmometers,* 2D Materials **4**, 011002 (2016).

[41] A. Sakhaee-Pour, M. Ahmadian, and A. Vafai, *Applications of single-layered graphene sheets as mass sensors and atomistic dust detectors,* Solid State Communications **145**, 168 (2008).

[42] J. Atalaya, J. M. Kinaret, and A. Isacsson, *Nanomechanical mass measurement using nonlinear response of a graphene membrane,* Europhysics Letters **91**, 48001 (2010).

[43] C. Chen, S. Rosenblatt, K. I. Bolotin, W. Kalb, P. Kim, I. Kymissis, H. L. Stormer, T. F. Heinz, and J. Hone, *Performance of monolayer graphene nanomechanical resonators with electrical readout,* Nature Nanotechnology **4**, 861 (2009).

[44] S. Houri, S. Cartamil-Bueno, M. Poot, P. Steeneken, H. van der Zant, and W. Venstra, *Direct and parametric synchronization of a graphene self-oscillator,* Applied Physics Letters **110**, 073103 (2017).

[45] X. Liu, J. W. Suk, N. G. Boddeti, L. Cantley, L. Wang, J. M. Gray, H. J. Hall, V. M. Bright, C. T. Rogers, M. L. Dunn, *et al.*, *Large arrays and properties of 3-terminal graphene nano-electromechanical switches,* Advanced Materials **26**, 1571 (2014).

[46] R. Nair, H. Wu, P. Jayaram, I. Grigorieva, and A. Geim, *Unimpeded permeation of water through helium–leak–tight graphene–based membranes,* Science **335**, 442 (2012).

[47] A. Zurutuza and C. Marinelli, *Challenges and opportunities in graphene commercialization,* Nature Nanotechnology **9**, 730 (2014).

[48] K. S. Kim, Y. Zhao, H. Jang, S. Y. Lee, J. M. Kim, K. S. Kim, J.-H. Ahn, P. Kim, J.-Y. Choi, and B. H. Hong, *Large-scale pattern growth of graphene films for stretchable transparent electrodes,* Nature **457**, 706 (2009).

[49] R. A. Barton, B. Ilic, A. M. van der Zande, W. S. Whitney, P. L. McEuen, J. M. Parpia, and H. G. Craighead, *High, size-dependent quality factor in an array of graphene mechanical resonators,* Nano Letters **11**, 1232 (2011).

[50] A. M. van der Zande, R. A. Barton, J. S. Alden, C. S. Ruiz-Vargas, W. S. Whitney, P. H. Q. Pham, J. Park, J. M. Parpia, H. G. Craighead, and P. L. McEuen, *Large-scale arrays of single-layer graphene resonators,* Nano Letters **10**, 4869 (2010).

[51] S. C. O'Hern, C. A. Stewart, M. S. Boutilier, J.-C. Idrobo, S. Bhaviripudi, S. K. Das, J. Kong, T. Laoui, M. Atieh, and R. Karnik, *Selective molecular transport through intrinsic defects in a single layer of CVD graphene,* ACS Nano **6**, 10130 (2012).

[52] G.-H. Lee, R. C. Cooper, S. J. An, S. Lee, A. van der Zande, N. Petrone, A. G. Hammerberg, C. Lee, B. Crawford, W. Oliver, J. W. Kysar, and J. Hone, *High–strength chemical–vapor–deposited graphene and grain boundaries,* Science **340**, 1073 (2013).

[53] K. Celebi, J. Buchheim, R. M. Wyss, A. Droudian, P. Gasser, I. Shorubalko, J.-I. Kye, C. Lee, and H. G. Park, *Ultimate permeation across atomically thin porous graphene,* Science **344**, 289 (2014).

[54] Y. Hwangbo, C.-K. Lee, S.-M. Kim, J.-H. Kim, K.-S. Kim, B. Jang, H.-J. Lee, S.-K. Lee, S.-S. Kim, J.-H. Ahn, and S.-M. Lee, *Fracture characteristics of monolayer CVD graphene,* Scientific Reports **4** (2014).

[55] D. Metten, F. Federspiel, M. Romeo, and S. Berciaud, *All-optical blister test of suspended graphene using micro-raman spectroscopy,* Physical Review Applied **2**, 054008 (2014).

[56] Y. Shin, M. Lozada-Hidalgo, J. L. Sambricio, I. V. Grigorieva, A. K. Geim, and C. Casiraghi, *Raman spectroscopy of highly pressurized graphene membranes,* Applied Physics Letters **108**, 221907 (2016).

[57] A. A. Sagade, A. I. Aria, S. Edge, P. Melgari, B. Gieseking, B. C. Bayer, J. C. Meyer, D. Bird, P. Brewer, and S. Hofmann, *Graphene-based nanolaminates as ultra-high permeation barriers,* npj 2D Materials and Applications **1**, 35 (2017).

[58] D. Davidovikj, P. H. Scheepers, H. S. J. van der Zant, and P. G. Steeneken, *Static capacitive pressure sensing using a single graphene drum,* ACS Applied Materials & Interfaces **9**, 43205 (2017).

[59] L. Wang, L. W. Drahushuk, L. Cantley, S. P. Koenig, X. Liu, J. Pellegrino, M. S. Strano, and J. S. Bunch, *Molecular valves for controlling gas phase transport made from discrete ångström-sized pores in graphene,* Nature Nanotechnology **10**, 785 (2015).

[60] W.-M. Zhang, H. Yan, Z.-K. Peng, and G. Meng, *Electrostatic pull-in instability in MEMS/NEMS: A review,* Sensors and Actuators A: Physical **214**, 187 (2014).

[61] Q. Zhou and A. Zettl, *Electrostatic graphene loudspeaker,* Applied Physics Letters **102**, 223109 (2013).

[62] R. N. Patel, J. P. Mathew, A. Borah, and M. M. Deshmukh, *Low tension graphene drums for electromechanical pressure sensing,* 2D Materials **3**, 011003 (2016).

[63] A. D. Smith, F. Niklaus, A. Paussa, S. Vaziri, A. C. Fischer, M. Sterner, F. Forsberg, A. Delin, D. Esseni, P. Palestri, M. Östling, and M. C. Lemme, *Electromechanical piezoresistive sensing in suspended graphene membranes,* Nano Letters **13**, 3237 (2013).

[64] A. D. Smith, F. Niklaus, A. Paussa, S. Schröder, A. C. Fischer, M. Sterner, S. Wagner, S. Vaziri, F. Forsberg, D. Esseni, M. Östling, and M. C. Lemme, *Piezoresistive properties of suspended graphene membranes under uniaxial and biaxial strain in nanoelectromechanical pressure sensors,* ACS Nano **10**, 9879 (2016).

[65] Y. Xu, C. Chen, V. V. Deshpande, F. A. DiRenno, A. Gondarenko, D. B. Heinz, S. Liu, P. Kim, and J. Hone, *Radio frequency electrical transduction of graphene mechanical resonators,* Applied Physics Letters **97**, 243111 (2010).

[66] J. Atalaya, A. Isacsson, and J. M. Kinaret, *Continuum elastic modeling of graphene resonators,* Nano Letters **8**, 4196 (2008).

[67] A. Croy, D. Midtvedt, A. Isacsson, and J. M. Kinaret, *Nonlinear damping in graphene resonators,* Physical Review B **86**, 235435 (2012).

[68] N. Lindahl, D. Midtvedt, J. Svensson, O. A. Nerushev, N. Lindvall, A. Isacsson, and E. E. Campbell, *Determination of the bending rigidity of graphene via electrostatic actuation of buckled membranes,* Nano Letters **12**, 3526 (2012).

[69] S. Ghosh, I. Calizo, D. Teweldebrhan, E. P. Pokatilov, D. L. Nika, A. A. Balandin, W. Bao, F. Miao, and C. N. Lau, *Extremely high thermal conductivity of graphene: Prospects for thermal management applications in nanoelectronic circuits,* Applied Physics Letters **92**, 151911 (2008).

[70] A. A. Balandin, S. Ghosh, W. Bao, I. Calizo, D. Teweldebrhan, F. Miao, and C. N. Lau, *Superior thermal conductivity of single-layer graphene,* Nano Letters **8**, 902 (2008).

[71] V. Singh, S. Sengupta, H. S. Solanki, R. Dhall, A. Allain, S. Dhara, P. Pant, and M. M. Deshmukh, *Probing thermal expansion of graphene and modal dispersion at low-temperature using graphene nanoelectromechanical systems resonators,* Nanotechnology **21**, 165204 (2010).

[72] E. Pop, V. Varshney, and A. K. Roy, *Thermal properties of graphene: Fundamentals and applications,* MRS bulletin **37**, 1273 (2012).

[73] X. Xu, J. Chen, and B. Li, *Phonon thermal conduction in novel 2D materials,* Journal of Physics: Condensed Matter **28**, 483001 (2016).

[74] R. J. Dolleman, S. Houri, D. Davidovikj, S. J. Cartamil-Bueno, Y. M. Blanter, H. S. J. van der Zant, and P. G. Steeneken, *Optomechanics for thermal characterization of suspended graphene*, Physical Review B **96**, 165421 (2017).

[75] A. Eriksson, D. Midtvedt, A. Croy, and A. Isacsson, *Frequency tuning, nonlinearities and mode coupling in circular mechanical graphene resonators*, Nanotechnology **24**, 395702 (2013).

[76] J. Rieger, A. Isacsson, M. Seitner, J. Kotthaus, and E. Weig, *Energy losses of nanomechanical resonators induced by atomic force microscopy-controlled mechanical impedance mismatching*, Nature Communications **5**, 3345 (2014).

[77] J. Güttinger, A. Noury, P. Weber, A. M. Eriksson, C. Lagoin, J. Moser, C. Eichler, A. Wallraff, A. Isacsson, and A. Bachtold, *Energy-dependent path of dissipation in nanomechanical resonators*, Nature Nanotechnology **12**, 631 (2017).

[78] W. Wu, L. Wang, Y. Li, F. Zhang, L. Lin, S. Niu, D. Chenet, X. Zhang, Y. Hao, T. F. Heinz, *et al.*, *Piezoelectricity of single-atomic-layer MoS_2 for energy conversion and piezotronics*, Nature **514**, 470 (2014).

[79] H. Zhu, Y. Wang, J. Xiao, M. Liu, S. Xiong, Z. J. Wong, Z. Ye, Y. Ye, X. Yin, and X. Zhang, *Observation of piezoelectricity in free-standing monolayer MoS_2*, Nature Nanotechnology **10**, 151 (2015).

[80] K. Michel and B. Verberck, *Theory of elastic and piezoelectric effects in two-dimensional hexagonal boron nitride*, Physical Review B **80**, 224301 (2009).

[81] H. J. Conley, B. Wang, J. I. Ziegler, R. F. Haglund Jr, S. T. Pantelides, and K. I. Bolotin, *Bandgap engineering of strained monolayer and bilayer MoS_2*, Nano Letters **13**, 3626 (2013).

[82] R. Frisenda, M. Drüppel, R. Schmidt, S. M. de Vasconcellos, D. P. de Lara, R. Bratschitsch, M. Rohlfing, and A. Castellanos-Gomez, *Biaxial strain tuning of the optical properties of single-layer transition metal dichalcogenides*, npj 2D Materials and Applications **1**, 10 (2017).

[83] V. Georgakilas, M. Otyepka, A. B. Bourlinos, V. Chandra, N. Kim, K. C. Kemp, P. Hobza, R. Zboril, and K. S. Kim, *Functionalization of graphene: covalent and non-covalent approaches, derivatives and applications*, Chemical Reviews **112**, 6156 (2012).

[84] N. Reyren, S. Thiel, A. D. Caviglia, L. F. Kourkoutis, G. Hammerl, C. Richter, C. W. Schneider, T. Kopp, A.-S. Rüetschi, D. Jaccard, M. Gabay, D. A. Muller, J.-M. Triscone, and J. Mannhart, *Superconducting interfaces between insulating oxides*, Science **317**, 1196 (2007).

[85] S. Farokhipoor, C. Magén, S. Venkatesan, J. Íñiguez, C. J. Daumont, D. Rubi, E. Snoeck, M. Mostovoy, C. De Graaf, A. Müller, M. Döblinger, C. Scheu, and B. Noheda, *Artificial chemical and magnetic structure at the domain walls of an epitaxial oxide*, Nature **515**, 379 (2014).

[86] P. Zubko, J. C. Wojdeł, M. Hadjimichael, S. Fernandez-Pena, A. Sené, I. Luk'yanchuk, J.-M. Triscone, and J. Íñiguez, *Negative capacitance in multidomain ferroelectric superlattices*, Nature **534**, 524 (2016).

[87] J. Lemaitre and J.-L. Chaboche, *Mechanics of solid materials* (Cambridge university press, 1994).

[88] J. E. Jones, *On the determination of molecular fields. ii. from the equation of state of a gas,* in *Proceedings of the Royal Society of London A: Mathematical, Physical and Engineering Sciences*, Vol. 106 (The Royal Society, 1924) pp. 463–477.

[89] M. Amabili, *Nonlinear vibrations and stability of shells and plates* (Cambridge University Press, 2008).

[90] S. Timoshenko and S. Woinowsky-Krieger, *Theory of plates and shells* (McGraw-Hill, 1959).

[91] M. Amabili and I. D. Breslavsky, *Displacement dependent pressure load for finite deflection of doubly-curved thick shells and plates,* International Journal of Non-Linear Mechanics **77**, 265 (2015).

[92] A. H. Nayfeh and D. T. Mook, *Nonlinear oscillations* (John Wiley & Sons, 2008).

[93] P. Blake, E. Hill, A. Castro Neto, K. Novoselov, D. Jiang, R. Yang, T. Booth, and A. Geim, *Making graphene visible,* Applied Physics Letters **91**, 063124 (2007).

[94] C. Chen, S. Lee, V. V. Deshpande, G.-H. Lee, M. Lekas, K. Shepard, and J. Hone, *Graphene mechanical oscillators with tunable frequency,* Nature Nanotechnology **8**, 923 (2013).

[95] B. Hauer, C. Doolin, K. Beach, and J. Davis, *A general procedure for thermomechanical calibration of nano/micro-mechanical resonators,* Annals of Physics **339**, 181 (2013).

[96] R. J. Dolleman, D. Davidovikj, H. S. van der Zant, and P. G. Steeneken, *Amplitude calibration of 2D mechanical resonators by nonlinear optical transduction,* Applied Physics Letters **111**, 253104 (2017).

[97] D. Davidovikj, J. J. Slim, S. J. Cartamil-Bueno, H. S. van der Zant, P. G. Steeneken, and W. J. Venstra, *Visualizing the motion of graphene nanodrums,* Nano Letters **16**, 2768 (2016).

[98] V. Sazonova, Y. Yaish, H. Üstünel, D. Roundy, T. A. Arias, and P. L. McEuen, *A tunable carbon nanotube electromechanical oscillator,* Nature **431**, 284 (2004).

[99] B. Witkamp, M. Poot, and H. S. van der Zant, *Bending-mode vibration of a suspended nanotube resonator,* Nano Letters **6**, 2904 (2006).

[100] M. Amabili, F. Alijani, and J. Delannoy, *Damping for large-amplitude vibrations of plates and curved panels, part 2: Identification and comparisons,* International Journal of Non-Linear Mechanics **85**, 226 (2016).

[101] A. Castellanos-Gomez, M. Buscema, R. Molenaar, V. Singh, L. Janssen, H. S. J. van der Zant, and G. A. Steele, *Deterministic transfer of two-dimensional materials by all-dry viscoelastic stamping,* 2D Materials **1**, 011002 (2014).

[102] K. Jensen, K. Kim, and A. Zettl, *An atomic-resolution nanomechanical mass sensor,* Nature Nanotechnology **3**, 533 (2008).

[103] R. J. Nicholl, H. J. Conley, N. V. Lavrik, I. Vlassiouk, Y. S. Puzyrev, V. P. Sreenivas, S. T. Pantelides, and K. I. Bolotin, *The effect of intrinsic crumpling on the mechanics of free-standing graphene,* Nature Communications **6**, 8789 (2015).

[104] A. Eichler, J. Moser, J. Chaste, M. Zdrojek, I. Wilson-Rae, and A. Bachtold, *Nonlinear damping in mechanical resonators made from carbon nanotubes and graphene,* Nature Nanotechnology **6**, 339 (2011).

[105] R. van Leeuwen, A. Castellanos-Gomez, G. A. Steele, H. S. J. van, and W. J. Venstra, *Time-domain response of atomically thin MoS$_2$ nanomechanical resonators,* Applied Physics Letters **105**, 041911 (2014).

[106] D. Garcia-Sanchez, A. M. van der Zande, A. S. Paulo, B. Lassagne, P. L. McEuen, and A. Bachtold, *Imaging mechanical vibrations in suspended graphene sheets,* Nano Letters **8**, 1399 (2008).

[107] Z. Wang, J. Lee, K. He, J. Shan, and P. X.-L. Feng, *Embracing structural nonidealities and asymmetries in two-dimensional nanomechanical resonators,* Scientific reports **4**, 3919 (2014).

[108] C.-H. Liu, I. S. Kim, and L. J. Lauhon, *Optical control of mechanical mode-coupling within a MoS$_2$ resonator in the strong-coupling regime,* Nano Letters **15**, 6727 (2015).

[109] N. O. Azak, M. Y. Shagam, D. M. Karabacak, K. L. Ekinci, D. H. Kim, and D. Y. Jang, *Nanomechanical displacement detection using fiber-optic interferometry,* Applied Physics Letters **91**, 093112 (2007).

[110] J. Lee, Z. Wang, K. He, J. Shan, and P. X.-L. Feng, *High frequency MoS$_2$ nanomechanical resonators,* ACS Nano **7**, 6086 (2013).

[111] Z. Wang, J. Lee, and P. X.-L. Feng, *Spatial mapping of multimode Brownian motions in high-frequency silicon carbide microdisk resonators,* Nature Communications **5**, 5158 (2014).

[112] M. Li, H. X. Tang, and M. L. Roukes, *Ultra-sensitive NEMS-based cantilevers for sensing, scanned probe and very high-frequency applications,* Nature Nanotechnology **2**, 114 (2007).

[113] R. A. Barton, I. R. Storch, V. P. Adiga, R. Sakakibara, B. R. Cipriany, B. Ilic, S. P. Wang, P. Ong, P. L. McEuen, J. M. Parpia, and H. G. Craighead, *Photothermal self-oscillation and laser cooling of graphene optomechanical systems,* Nano Letters **12**, 4681 (2012).

[114] S. Dohn, R. Sandberg, W. Svendsen, and A. Boisen, *Enhanced functionality of cantilever based mass sensors using higher modes,* Applied Physics Letters **86**, 233501 (2005).

[115] M. S. Hanay, S. I. Kelber, C. D. O'Connell, P. Mulvaney, J. E. Sader, and M. L. Roukes, *Inertial imaging with nanomechanical systems,* Nature Nanotechnology **10**, 339 (2015).

[116] E. E. Helgee and A. Isacsson, *Scattering of flexural acoustic phonons at grain boundaries in graphene,* Physical Review B **90**, 045416 (2014).

[117] E. Kramer, D. J. J. Van Dorp, R. Van Leeuwen, and W. J. Venstra, *Strain-dependent damping in nanomechanical resonators from thin MoS$_2$ crystals,* Applied Physics Letters **107**, 091903 (2015).

[118] D. Yoon, Y.-W. Son, and H. Cheong, *Negative thermal expansion coefficient of graphene measured by Raman spectroscopy,* Nano Letters **11**, 3227 (2011).

[119] J.-W. Jiang and H. S. Park, *Negative Poisson's ratio in single-layer black phosphorus,* Nature Communications **5**, 4727 (2014).

[120] K.-A. N. Duerloo and E. J. Reed, *Flexural electromechanical coupling: A nanoscale emergent property of boron nitride bilayers,* Nano Letters **13**, 1681 (2013).

[121] W. Wu, L. Wang, Y. Li, F. Zhang, L. Lin, S. Niu, D. Chenet, X. Zhang, Y. Hao, T. F. Heinz, J. Hone, and Z. L. Wang, *Piezoelectricity of single-atomic-layer MoS$_2$ for energy conversion and piezotronics,* Nature **514**, 470 (2014).

[122] K. F. Mak, C. Lee, J. Hone, J. Shan, and T. F. Heinz, *Atomically thin MoS$_2$: A new direct-gap semiconductor,* Physical Review Letters **105**, 136805 (2010).

[123] D. Davidovikj, F. Alijani, S. J. Cartamil-Bueno, H. Zant, M. Amabili, and P. G. Steeneken, *Nonlinear dynamic characterization of two-dimensional materials,* Nature Communications **8**, 1253 (2017).

[124] A. Castellanos-Gomez, M. Poot, G. A. Steele, H. S. J. van der Zant, N. Agraït, and G. Rubio-Bollinger, *Mechanical properties of freely suspended semiconducting graphene-like layers based on MoS$_2$,* Nanoscale Research Letters **7**, 1 (2012).

[125] A. Castellanos-Gomez, M. Poot, G. A. Steele, H. S. J. van der Zant, N. Agraït, and G. Rubio-Bollinger, *Elastic properties of freely suspended MoS$_2$ nanosheets,* Advanced Materials **24**, 772 (2012).

[126] S. P. Koenig, N. G. Boddeti, M. L. Dunn, and J. S. Bunch, *Ultrastrong adhesion of graphene membranes,* Nature Nanotechnology **6**, 543 (2011).

[127] C. Wong, M. Annamalai, Z. Wang, and M. Palaniapan, *Characterization of nanomechanical graphene drum structures,* Journal of Micromechanics and Microengineering **20**, 115029 (2010).

[128] D. Akinwande, C. J. Brennan, J. S. Bunch, P. Egberts, J. R. Felts, H. Gao, R. Huang, J.-S. Kim, T. Li, Y. Li, K. M. Liechti, N. Lu, H. S. Park, E. J. Reed, P. Wang, B. I. Yakobson, T. Zhang, Y.-W. Zhang, Y. Zhou, and Y. Zhu, *A review on mechanics and mechanical properties of 2D materials - graphene and beyond,* Extreme Mechanics Letters **13**, 42 (2017).

[129] J. Los, A. Fasolino, and M. Katsnelson, *Mechanics of thermally fluctuating membranes,* npj 2D Materials and Applications **1**, 9 (2017).

[130] A. Isacsson, A. W. Cummings, L. Colombo, L. Colombo, J. M. Kinaret, and S. Roche, *Scaling properties of polycrystalline graphene: a review,* 2D Materials **4**, 012002 (2017).

[131] R. De Alba, F. Massel, I. Storch, T. Abhilash, A. Hui, P. McEuen, H. Craighead, and J. Parpia, *Tunable phonon-cavity coupling in graphene membranes,* Nature Nanotechnology **11**, 741 (2016).

[132] J. P. Mathew, R. N. Patel, A. Borah, R. Vijay, and M. M. Deshmukh, *Dynamical strong coupling and parametric amplification of mechanical modes of graphene drums,* Nature Nanotechnology **11**, 747 (2016).

[133] J. Han, N. M. Pugno, and S. Ryu, *Nanoindentation cannot accurately predict the tensile strength of graphene or other 2D materials,* Nanoscale **7**, 15672 (2015).

[134] D. Vella and B. Davidovitch, *Indentation metrology of clamped, ultra-thin elastic sheets,* Soft Matter (2017).

[135] R. Lifshitz and M. Cross, *Nonlinear dynamics of nanomechanical and micromechanical resonators,* Review of nonlinear dynamics and complexity **1**, 1 (2008).

[136] V. Singh, O. Shevchuk, Y. M. Blanter, and G. A. Steele, *Negative nonlinear damping of a multilayer graphene mechanical resonator,* Physical Review B **93**, 245407 (2016).

[137] E. H. Mansfield, *The bending and stretching of plates* (Cambridge University Press, 2005).

[138] U. Komaragiri, M. Begley, and J. Simmonds, *The mechanical response of freestanding circular elastic films under point and pressure loads,* Transactions of the ASME-E-Journal of Applied Mechanics **72**, 203 (2005).

[139] H. Hencky, *Uber den spannungszustand in kreisrunden platten mit verschwindender biegungssteiflgkeit,* Zeitschrift fur Mathematik und Physik **63**, 311 (1915).

[140] N. G. Boddeti, X. Liu, R. Long, J. Xiao, J. S. Bunch, and M. L. Dunn, *Graphene blisters with switchable shapes controlled by pressure and adhesion,* Nano Letters **13**, 6216 (2013).

[141] G. López-Polín, C. Gómez-Navarro, V. Parente, F. Guinea, M. I. Katsnelson, F. Pérez-Murano, and J. Gómez-Herrero, *Increasing the elastic modulus of graphene by controlled defect creation,* Nature Physics **11**, 26 (2015).

[142] I. Gornyi, V. Y. Kachorovskii, and A. Mirlin, *Anomalous Hooke's law in disordered graphene,* 2D Materials **4**, 011003 (2016).

[143] R. J. T. Nicholl, N. V. Lavrik, I. Vlassiouk, B. R. Srijanto, and K. I. Bolotin, *Hidden area and mechanical nonlinearities in freestanding graphene,* Physical Review Letters **118**, 266101 (2017).

[144] Y.-M. Chen, S.-M. He, C.-H. Huang, C.-C. Huang, W.-P. Shih, C.-L. Chu, J. Kong, J. Li, and C.-Y. Su, *Ultra-large suspended graphene as a highly elastic membrane for capacitive pressure sensors,* Nanoscale **8**, 3555 (2016).

[145] P. Weber, J. Güttinger, I. Tsioutsios, D. E. Chang, and A. Bachtold, *Coupling graphene mechanical resonators to superconducting microwave cavities,* Nano Letters **14**, 2854 (2014).

[146] V. Singh, S. Bosman, B. Schneider, Y. M. Blanter, A. Castellanos-Gomez, and G. Steele, *Optomechanical coupling between a multilayer graphene mechanical resonator and a superconducting microwave cavity,* Nature Nanotechnology **9**, 820 (2014).

[147] X. Song, M. Oksanen, J. Li, P. Hakonen, and M. A. Sillanpää, *Graphene optomechanics realized at microwave frequencies,* Physical Review Letters **113**, 027404 (2014).

[148] M. AbdelGhany, E. Ledwosinska, and T. Szkopek, *Theory of the suspended graphene varactor,* Applied Physics Letters **101**, 153102 (2012).

[149] M. AbdelGhany, F. Mahvash, M. Mukhopadhyay, A. Favron, R. Martel, M. Siaj, and T. Szkopek, *Suspended graphene variable capacitor,* 2D Materials **3**, 041005 (2016).

[150] L. Ford, *The effect of humidity on the calibration of precision air capacitors,* Journal of the Institution of Electrical Engineers-Part II: Power Engineering **95**, 709 (1948).

[151] E. J. Olson, R. Ma, T. Sun, M. A. Ebrish, N. Haratipour, K. Min, N. R. Aluru, and S. J. Koester, *Capacitive sensing of intercalated H_2O molecules using graphene,* ACS Applied Materials & Interfaces **7**, 25804 (2015).

[152] S. J. Cartamil-Bueno, A. Centeno, A. Zurutuza, P. G. Steeneken, H. S. J. van der Zant, and S. Houri, *Very large scale characterization of graphene mechanical devices using a colorimetry technique,* Nanoscale **9**, 7559 (2017).

[153] M. Will, M. Hamer, M. Müller, A. Noury, P. Weber, A. Bachtold, R. V. Gorbachev, C. Stampfer, and J. Güttinger, *High quality factor graphene-based two-dimensional heterostructure mechanical resonator,* Nano Letters **17**, 5950 (2017).

[154] S. S. Verbridge, J. M. Parpia, R. B. Reichenbach, L. M. Bellan, and H. Craighead, *High quality factor resonance at room temperature with nanostrings under high tensile stress,* Journal of Applied Physics **99**, 124304 (2006).

[155] J. D. Teufel, J. W. Harlow, C. A. Regal, and K. W. Lehnert, *Dynamical backaction of microwave fields on a nanomechanical oscillator,* Physical Review Letters **101**, 197203 (2008).

[156] R. A. Norte, J. P. Moura, and S. Gröblacher, *Mechanical resonators for quantum optomechanics experiments at room temperature,* Physical Review Letters **116**, 147202 (2016).

[157] J. Van Beek and R. Puers, *A review of MEMS oscillators for frequency reference and timing applications,* Journal of Micromechanics and Microengineering **22**, 013001 (2011).

[158] D. Yoon, Y.-W. Son, and H. Cheong, *Negative thermal expansion coefficient of graphene measured by raman spectroscopy,* Nano Letters **11**, 3227 (2011).

[159] C. Metzger, I. Favero, A. Ortlieb, and K. Karrai, *Optical self cooling of a deformable Fabry-Pérot cavity in the classical limit,* Physical Review B **78**, 035309 (2008).

[160] A. Fasolino, J. Los, and M. Katsnelson, *Intrinsic ripples in graphene,* Nature Materials **6**, 858 (2007).

[161] A. M. van der Zande, R. A. Barton, J. S. Alden, C. S. Ruiz-Vargas, W. S. Whitney, P. H. Q. Pham, J. Park, J. M. Parpia, H. G. Craighead, and P. L. McEuen, *Large-scale arrays of single-layer graphene resonators,* Nano Letters **10**, 4869 (2010).

[162] J. Los, A. Fasolino, and M. Katsnelson, *Scaling behavior and strain dependence of in-plane elastic properties of graphene,* Physical Review Letters **116**, 015901 (2016).

[163] D. Davidovikj, D. Bouwmeester, H. S. J. van der Zant, and P. G. Steeneken, *Graphene gas pumps,* Proceedings IEEE MEMS (2018).

[164] D. Davidovikj, D. Bouwmeester, H. S. J. van der Zant, and P. G. Steeneken, *Graphene gas pumps,* arXiv preprint arXiv:1801.07527 (2018).

[165] D. J. Laser and J. G. Santiago, *A review of micropumps,* Journal of Micromechanics and Microengineering **14**, R35 (2004).

[166] B. D. Iverson and S. V. Garimella, *Recent advances in microscale pumping technologies: a review and evaluation,* Microfluidics and Nanofluidics **5**, 145 (2008).

[167] S. Lee, R. An, and A. J. Hunt, *Liquid glass electrodes for nanofluidics,* Nature Nanotechnology **5**, 412 (2010).

[168] W. Judy, T. Tamagawa, and D. L. Polla, *Surface-machined micromechanical membrane pump,* Proceedings IEEE MEMS , 182 (1991).

[169] R. Zengerle, A. Richter, and H. Sandmaier, *A micro membrane pump with electrostatic actuation,* Proceedings IEEE MEMS , 19 (1992).

[170] D. Todorović, A. Matković, M. Milićević, D. Jovanović, R. Gajić, I. Salom, and M. Spasenović, *Multilayer graphene condenser microphone,* 2D Materials **2**, 045013 (2015).

[171] Q. Zhou, J. Zheng, S. Onishi, M. Crommie, and A. K. Zettl, *Graphene electrostatic microphone and ultrasonic radio,* Proceedings of the National Academy of Sciences **112**, 8942 (2015).

[172] D. Lu, D. J. Baek, S. S. Hong, L. F. Kourkoutis, Y. Hikita, and H. Y. Hwang, *Synthesis of free-standing single-crystal perovskite films and heterostructures by etching of sacrificial water-soluble layers,* Nature Materials **15**, 1255 (2016).

[173] M. Cardona, *Optical properties and band structure of $SrTiO_3$ and $BaTiO_3$,* Physical Review **140**, A651 (1965).

[174] F. W. Lytle, *X-ray diffractometry of low-temperature phase transformations in strontium titanate,* Journal of Applied Physics **35**, 2212 (1964).

[175] H. Unoki and T. Sakudo, *Electron spin resonance of Fe3+ in $SrTiO_3$ with special reference to the 110 K phase transition,* Journal of the Physical Society of Japan **23**, 546 (1967).

[176] A. Kityk, W. Schranz, P. Sondergeld, D. Havlik, E. Salje, and J. Scott, *Nonlinear elastic behaviour of $SrTiO_3$ crystals in the quantum paraelectric regime,* Europhysics Letters **50**, 41 (2000).

[177] E. D. Mishina, T. V. Misuryaev, N. E. Sherstyuk, V. V. Lemanov, A. I. Morozov, A. S. Sigov, and T. Rasing, *Observation of a near-surface structural phase transition in $SrTiO_3$ by optical second harmonic generation,* Physical Review Letters **85**, 3664 (2000).

[178] J. Haeni, P. Irvin, W. Chang, R. Uecker, P. Reiche, Y. Li, S. Choudhury, W. Tian, M. Hawley, B. Craigo, A. K. Tagantsev, X. Q. Pan, S. K. Streiffer, L. Q. Chen, S. W. Kirchoefer, J. Levy, and D. G. Schlom, *Room-temperature ferroelectricity in strained $SrTiO_3$,* Nature **430**, 758 (2004).

[179] H. Ledbetter, M. Lei, and S. Kim, *Elastic constants, debye temperatures, and electron-phonon parameters of superconducting cuprates and related oxides,* Phase Transitions: A Multinational Journal **23**, 61 (1990).

[180] J. Scott and H. Ledbetter, *Interpretation of elastic anomalies in $SrTiO_3$ at 37 K,* Zeitschrift für Physik B Condensed Matter **104**, 635 (1997).

[181] E. Balashova, V. Lemanov, R. Kunze, G. Martin, and M. Weihnacht, *Interdigital transducer application for ultrasonic study of $SrTiO_3$ in the quantum paraelectric region,* Solid State Communications **94**, 17 (1995).

[182] C. Ang, J. F. Scott, Z. Yu, H. Ledbetter, and J. L. Baptista, *Dielectric and ultrasonic anomalies at 16, 37, and 65 K in $SrTiO_3$,* Physical Review B **59**, 6661 (1999).

[183] Q. P. Unterreithmeier, T. Faust, and J. P. Kotthaus, *Damping of nanomechanical resonators,* Physical Review Letters **105**, 027205 (2010).

[184] B. Kim, M. A. Hopcroft, R. N. Candler, C. M. Jha, M. Agarwal, R. Melamud, S. A. Chandorkar, G. Yama, and T. W. Kenny, *Temperature dependence of quality factor in MEMS resonators,* Journal of Microelectromechanical systems **17**, 755 (2008).

[185] P. Zubko, G. Catalan, A. Buckley, P. R. L. Welche, and J. F. Scott, *Strain-gradient-induced polarization in SrTiO$_3$ single crystals,* Physical Review Letters **99**, 167601 (2007).

[186] J. F. Scott, E. K. H. Salje, and M. A. Carpenter, *Domain wall damping and elastic softening in SrTiO$_3$: Evidence for polar twin walls,* Physical Review Letters **109**, 187601 (2012).

[187] E. K. H. Salje, O. Aktas, M. A. Carpenter, V. V. Laguta, and J. F. Scott, *Domains within domains and walls within walls: Evidence for polar domains in cryogenic SrTiO$_3$,* Physical Review Letters **111**, 247603 (2013).

[188] E. K. H. Salje, X. Ding, Z. Zhao, T. Lookman, and A. Saxena, *Thermally activated avalanches: Jamming and the progression of needle domains,* Physical Review B **83**, 104109 (2011).

[189] D. J. Kok, K. Irmscher, M. Naumann, C. Guguschev, Z. Galazka, and R. Uecker, *Temperature-dependent optical absorption of SrTiO$_3$,* Physica Status Solidi A **212**, 1880 (2015).

[190] J. Garai, *Correlation between thermal expansion and heat capacity,* Calphad **30**, 354 (2006).

[191] A. Durán, F. Morales, L. Fuentes, and J. Siqueiros, *Specific heat anomalies at 37, 105 and 455 K in SrTiO$_3$:Pr,* Journal of Physics: Condensed Matter **20**, 085219 (2008).

[192] S. De, K. Kunal, and N. Aluru, *Nonlinear intrinsic dissipation in single layer MoS$_2$ resonators,* RSC Advances **7**, 6403 (2017).

[193] M. T. A. Saif, *On a tunable bistable MEMS – theory and experiment,* Journal of Microelectromechanical systems **9**, 157 (2000).

[194] W. J. Venstra, H. J. Westra, and H. S. Van Der Zant, *Stochastic switching of cantilever motion,* Nature Communications **4**, 2624 (2013).

[195] R. Landauer, *Irreversibility and heat generation in the computing process,* IBM journal of research and development **5**, 183 (1961).

[196] R. J. Dolleman, S. Houri, A. Chandrashekar, F. Alijani, H. S. van der Zant, and P. G. Steeneken, *Graphene multi-mode parametric oscillators,* arXiv: 1711.08798 (2017).

[197] H. Okamoto, A. Gourgout, C.-Y. Chang, K. Onomitsu, I. Mahboob, E. Y. Chang, and H. Yamaguchi, *Coherent phonon manipulation in coupled mechanical resonators,* Nature Physics **9**, 480 (2013).

[198] T. Sakudo and H. Unoki, *Dielectric properties of SrTiO$_3$ at low temperatures,* Physical Review Letters **26**, 851 (1971).

[199] R. Neville, B. Hoeneisen, and C. Mead, *Permittivity of strontium titanate,* Journal of Applied Physics **43**, 2124 (1972).

[200] R. G. Geyer, B. Riddle, J. Krupka, and L. A. Boatner, *Microwave dielectric properties of single-crystal quantum paraelectrics KTaO$_3$ and SrTiO$_3$ at cryogenic temperatures,* Journal of Applied Physics **97**, 104111 (2005).

[201] D. Davidovikj, N. Manca, H. S. J. van der Zant, A. D. Caviglia, and G. A. Steele, *Quantum paraelectricity probed by superconducting resonators,* Physical Review B **95**, 214513 (2017).

CURRICULUM VITÆ

Dejan DAVIDOVIKJ

13-05-1988 Born in Skopje, Macedonia.

2002–2006 High School
Gimnazija "*Josip Broz–Tito*"
Skopje, Macedonia

2006–2010 Bachelor of Science in Electrical Engineering
Ss. Cyril and Methodius University, Skopje, Macedonia
Thesis: Automation and modernisation of a thermal power plant
Supervisor: Prof. dr. M. Stankovski

2010–2012 Master of Science in Electrical Engineering
Ss. Cyril and Methodius University, Skopje, Macedonia
Thesis: Advanced mapping and navigation algorithms
Supervisor: Prof. dr. M. Stankovski

2011–2013 Master of Science in Nanoscience and Nanotechnology (*magna cum laude*)
KU Leuven, Leuven, Belgium
Chalmers University of Technology, Gothenburg, Sweden
Thesis: Superconducting resonators for electric control of molecular spins
Supervisors: dr. A. Danilov and Prof. dr. S. Kubatkin

2012   Internship
imec, Leuven, Belgium
Project: Design and optimization of a MEMS micromirror
Supervisors: dr. X. Rottenberg and dr. H. Tilmans

2014–2018 Ph.D. in Applied Physics
Delft University of Technology, Delft, the Netherlands
Thesis: Two-dimensional membranes in motion
Promotors: Prof. dr. P. G. Steeneken and Prof. dr. ir. H. S. J. can der Zant

LIST OF PUBLICATIONS

14. **D. Davidovikj***, D. J. Groenendijk*, *et al.*, *Suspended ultra-thin complex oxide mechanical resonators*, manuscript in preparation

13. J. López-Cabrelles, S. Mañas-Valero , I. Vitórica-Yrezábal , P. Bereciartua , J. A. Rodríguez-Velamazán , J. Waerenborgh , B. Vierira, **D. Davidovikj**, P. G. Steeneken, H. S. J. van der Zant, G. Mínguez Espallargas, E. Coronado, *Defect-free functionalized magnetic monolayers based on coordination polymers*, under peer review

12. **D. Davidovikj***, M. Poot*, S. J. Cartamil-Bueno, H. S. J. van der Zant, P. G. Steeneken, *On-chip heaters for tension tuning of graphene nanodrums*, under peer review

11. **D. Davidovikj**, D. Bouwmeester, H. S. J. van der Zant, P. G. Steeneken, *Graphene gas pumps*, IEEE 31th International Conference on Micro Electro Mechanical Systems (2018), arXiv 1801.07527

10. R. J. Dolleman, **D. Davidovikj**, H. S. J. van der Zant, P. G. Steeneken, *Amplitude calibration of 2D mechanical resonators by nonlinear optical transduction*, Applied Physics Letters, **111**, 25, 253104 (2017)

9. B. Sajadi, F. Alijani, **D. Davidovikj**, J. Goosen, P. G. Steeneken, F. van Keulen, *Experimental characterization of graphene by electrostatic resonance frequency tuning*, Journal of Applied Physics, **122**, 23, 234302 (2017)

8. **D. Davidovikj**, P. H. Scheepers, H. S. J. van der Zant, P. G. Steeneken, *Static capacitive pressure sensing using a single graphene drum*, ACS Applied Materials & Interfaces, **9**, 49, 43205–43210 (2017)

7. **D. Davidovikj**, F. Alijani, S. J. Cartamil-Bueno, H. S. J. van der Zant, M. Amabili, P. G. Steeneken, *Nonlinear dynamic characterization of two-dimensional materials*, Nature Communications, **8**, 1, 1253 (2017)

6. R. J. Dolleman, S. Houri, **D. Davidovikj**, S. J. Cartamil-Bueno, Y. M. Blanter, H. S. J. van der Zant, P. G. Steeneken, *Optomechanics for thermal characterization of suspended graphene*, Physical Review B, **96**, 16, 165421 (2017)

5. **D. Davidovikj***, N. Manca*, H. S. J. van der Zant, A. D. Caviglia, G. A. Steele, *Quantum paraelectricity probed by superconducting resonators*, Physical Review B, **95**, 21, 214513 (2017)

4. **D. Davidovikj**, J. J. Slim, S. J. Cartamil-Bueno, H. S. J. van der Zant, P. G. Steeneken, W. J. Venstra, *Visualizing the motion of graphene nanodrums*, Nano Letters, **16**, 4, 2768-2773 (2016)

3. R. J. Dolleman, **D. Davidovikj**, S. J. Cartamil-Bueno, H. S. J. van der Zant, P. G. Steeneken, *Graphene squeeze-film pressure sensors*, Nano letters, **16**, 1, 568-571 (2015)

2. S. E. de Graaf, **D. Davidovikj**, A. Adamyan, S. E. Kubatkin, A. V. Danilov, *Galvanically split superconducting microwave resonators for introducing internal voltage bias*, Applied Physics Letters, **104**, 5, 052601 (2014)

147

1. T. Yager, A. Lartsev, S. Mahashabde, S. Charpentier, **D. Davidovikj**, A. V. Danilov, R. Yakimova, V. Panchal, O. Kazakova, A. Tzalenchuk, *Express optical analysis of epitaxial graphene on SiC: impact of morphology on quantum transport*, Nano Letters, **13**, 9, 4217-4223 (2013)

* Authors contributed equally

ACKNOWLEDGEMENTS

This is the part where I can finally express my gratitude to the people who made these four years fruitful and, even more importantly, fun. There are no referees, no feedback, no scientific mumbo jumbo. There are no constraints of having to sound formal, objective or scientifically correct[1]. Needless to say, not much can be said in a few pages, but I will try to summarise it as well as possible. A few of my friends and colleagues have set the bar quite high when it comes to writing this important chapter, so I hope my reflections live up to the standards.

The list starts with my academic fathers: Peter and Herre[2]. I'm not talking about just regular supervisors here. I'm talking about people available any time, at any place. I'm talking about people whose question isn't: "Have you measured this yet?", but: "Are you happy?". Without them, none of this would have been possible.

Peter, you showed me that the weight of words is correlated with neither pitch nor volume. It took me some time to realise that the best advice comes in the form of modest and objective opinions rather than blunt orders. You created an atmosphere where I felt supported in everything I did, silently steering me so that I don't get lost. This invaluable trait that you possess will serve me as an elementary example of how a leader should behave. You never seized to surprise me with the broadness of your knowledge, as if there was nothing you know nothing about; and all this lore was elegantly hidden behind a thick layer of modesty. I admired your patience in listening to me during our passionate scientific discourses even when you knew I was wrong; just trying to calmly convince me over and over that what I was saying was "not exactly true". Thank you for the continuous support in every aspect of my professional life. I am honoured to have you as my promotor.

Likewise, nothing less can be said about of our glorious leader, the glue of MED, the one-and-only, Herre. I am not sure if it was his easy-going attitude or the actual wording, but you were able to convert any problem into an obvious solution. Wise as a monk, with the energy of a teenager, a man of unprecedented intuition, a teacher, a life mentor. I always had the feeling that we shared a strong mutual admiration (or at least I want to think it was not one-sided). Thank you for your immense support.

Speaking of supervision, Warner, who took me under your guardianship when I was lost. Thank you for showing me that one can treat science as a hobby, thank you for constantly fuelling my curiosity and for teaching me that good science requires much more creativity than money.

---

[1] It was widely believed that one could actually write *anything* one pleased in this part. Recently, a dear colleague of ours disproved that notion.

[2] They live apart.

The next in line is Gary, my platonic supervisor. Even though the supervising trinity never worked out as anticipated, we have had numerous opportunities to discuss, debate and even work together. A knock-on-the-door away, always available, was your broad knowledge, powered by your firm attitudes and sharp criticism. You taught me how to be systematic, (even more) self-criticizing and scientifically objective. You taught me to plot data over and over again, manually check the fits, you made me to question every word that I write (I'm not sure I actually learned that) and taught me how to read with the eyes of a (native English) reader. I hope you didn't develop a reflex when you hear a knock on your door. I wish you a lot of success with your ever-expanding team.

Menno [3], your picture should stand next to the word *systematic* in the dictionary. You are certainly one of the most knowledgeable and thorough scientists that I have met. A *hooggeleerde* in the true sense of the word. We didn't have a lot of time to hang out, but the few months we worked together have been amazing: you taught me how to anticipate, stay relaxed and "seal all the holes" in advance. I wish you an über-successful career. Thank you for accepting the holy duty of being a member of my committee.

I extend my sincere gratitude to the (independent) members of my committee in alphabetic order. Andreas, you probably don't remember this, but you opened one of your talks with a slide showing our work. That was the first time I saw that what I do is actually appreciated by someone outside of our group and I had never felt that proud before. It gave me a lot of courage and self-confidence. For this and for being a part of the committee I am deeply grateful. Fred, you accepted to be one of the judges of my work without a moment of hesitation. People say that you are a tough opponent, which is why I chose to approach you in the first place. Thank you for accepting this duty. Jeevak, apart from all the wine juggling in La Thuile, we managed to have very inspiring discussions. Your knowledge, friendliness and openness convinced me then and there that I would like to have you among the eight. You proved your open-mindedness by promptly and cordially replying to my nonchalant invitation in the manner of the great person and scientist you are. Kirill, some of your works have served as examples in our group. It is a great pleasure and honour to have you in the committee. Thank you for accepting the invitation and for the detailed feedback on the thesis. Yaroslav, every time I had the opportunity to talk to you I learned something new. I was even more astonished that next to your brilliant scientific mind there lies a huge talent for languages. Thank you for all the support and for being an extra committee member.

Next in line is our SteenekenLab. It was a great satisfaction to witness the small lab consisting of a part-time professor and two PhDs turning into a very serious player that continues gaining recognition from all around. Robin, I really saw you transform from a naïve Master's student to a serious, self-criticising, objective scientist. I am very happy that you found your way and I truly hope that your stars will stay aligned in the future. I can now say that I am confident that you will become a great academic and you should not give up your dreams. Samer, thank you for the 3-year senior support and for all the crazy jokes. Even though we never managed to push our concepts to the very end, I am sure that it will happen in the near future. In the meantime, I wish you a pleasant and fruitful ride in Japan and watch out for their solitons, they can get quite big. It may

---

[3]Prof. Dr. Poot in German.

sound immodest, but I am really proud of our group and I am happy that the legacy will continue with even more brilliant people. Makars [4] and Martin, you really showed some solid knowledge and attitude. Trust me, we didn't have that when we first arrived. Keep it up and I'm sure it will lead to a Nature (a Nature - Nature) in the near future!

Farbod, had you not been so persistent, who knows where our work would have ended up. You helped me a great deal in understanding the importance of what we were doing and I will never forget the private lectures on nonlinear dynamics that you gave me. I still owe you for that. Thank you for treating me as a friend, rather than as a student or collaborator. Thank you for introducing us to Marco and thank you both for your invaluable contributions to our research.

I learned a lot from supervising students and I hope that the feeling was mutual. Jesse, Mark, Stefani, Paul, Damian, thank you for being a part of our group and thank you all for your great work. A special thanks goes to Jesse, Paul and Damian, who significantly contributed to some of the work in this thesis.

Now for the paranymphs. For those not familiar with (Dutch) academic traditions, a paranymph is a ceremonial assistant, kind of like a best man at a wedding. The difference is that here you are allowed to have two of them. I have to admit that even with this alleviation, being the absurdly indecisive person that I am, this was incredibly difficult. I therefore decided to take a more extensive, polygamic approach to this matter.

I will start with the ones wearing the suits, the expensive paranymphs. The first one comes from a parallel, pink universe, an incredibly charming and radiantly charismatic alien, full of wisdom, knowledge, modesty and carelessness, Rocco Magno. This is a person I got introduced to while stuffing my mouth with some leftovers from lunch, a custom that would later on define our friendship. Where to start and where to stop telling you about him I don't really know: should it be the endless philosophical discussions, the epic trips* and adventures, his desperate tries to make me read and do sports... Signore Gaudenzi represents a symbol of purity[5], unreserved altruism and infinite oratorical capabilities. Rocco, thank you for the contagious positive energy, for all the shared wisdom and for being an example to many of us. Kati, please keep an eye on this wandering Wuppertalian soul!

The second one comes from a very familiar universe, a border away from my home, the el Greco of MED (sorry Marios). This is a person who never failed to smile and never failed to make others smile. His folksy approach pierced the thickest armours, giving him access to anyone's heart. Never have I seen a more likeable person, a friendlier Buddha than our Nikolaki, a person on an eternal quest to do good. Niko, thank you for all the get-togethers, for all the "Breaking Bad" moments of growing crystals[6] in the weekends, for your genuine accent, for your unique gestures, for being my gym partner (remember that deep inside we both have muscles!) and for all the delicious barbecues! I wish you many weak localisations, broken inversion symmetries, spin-orbit couplings and fractional quantum Hall effects. Andrea, it's 18 more months, stay strong!

---

[4]It's one guy, not plural.

[5]I'm talking about spiritual purity.

[6]of MoS_2

The list of undercover paranymphs starts with the hairy paranymph, il Padrino della Tesi, Giovanni. I now realise that I have already paid back for the baptism of my book by immediately reinventing his name. Though in shadier circumstances, our early memories were also shaped by wine bottles. As intelligent and benevolent as unmalleable, dottore Mattoni made it clear from the beginning that the throne of stubbornness is something that I'd have to fight for. He constantly astonished me with his ability to learn and perfect skills in a matter of hours, just uploading new ones to his brain on demand. This doesn't apply only to science - volleyball, guitar, piano, painting, you name it. Thank you for all your support, for peacefully accepting my KJ, for all the coding, the pre- and post-processing of the thesis, for introducing me to the concept of double consonants[7], for all the spontaneous travelling arrangements and for being an amazing friend.

The ex-YU paranymph, Ranko, with whom I share the longest history. Arguably one of the most selfless people I have met, Ranko is the kind of person who is always there for you, no matter what you need. Rancice, thank you for all the nightclubs, dinners, trips together and the infinite times you helped me out. We share amazing memories, you were always there for me, no matter what I asked. Thank you for being my personal banker, even though you never succeeded in teaching me how to actually manage money. Nevertheless, at the risk of sounding cheesy, having you as a friend is a treasure by itself.

The conspiranymph, my office-, lab- and gossip-mate, el Marqués de Mil Cartas. "Nice to pre-meet you!" was the beginning of the first e-mail I got from him, subtly hinting at his grand talent for inventing neologisms (and use of language in general). He was so genuinely happy when I joined the lab, much like a kid who is finally allowed to get a dog. I will not forget how much he cared about me and my well-being, how he introduced me to the world of conferences and "business trips" and how he taught me to appreciate myself more. As turbulent as his journey was, I want to believe that I was there to dampen out his emotional spikes – a tough duty, which every now and then resulted with success. Santi, I am happy that you found happiness in the oddest of places (sorry Gabi) and that you found the love of your life. I wish both of you a life full of smiles, selflessness, gadgets, start-ups, trips, esweets, Japanese memorabilia and, very importantly, one deprived of hidden agendas.

Next is a paranymph in exile, my Ottoman soulmate with whom I undoubtedly share genes, thanks to his great-great-grandfathers. Although in the US, the smoke near the balcony is still reminiscent of your existence, reminding us how one can find a perfect balance between science, tobacco, moustache, clothes, hairstyle and social life. This kind Turkish gentleman had his unique ways of expressing love: "Makkkedonija, you have to go now", "That's not my problem", "I don't give a ...". Now a part of the Ivy League, the story of the passionate Effendi serves as an example of how far one can get with the proper vision and attitude. Mulazi, my deepest respect. May the Turkish dream be with you.

---

[7]Shared credit with RG.

The silent paranymph, Dirk. Currently unable to take your call. The text colour is to illustrate how difficult it is to hear him when he speaks. I want to believe that I reached the limit of how close a foreigner[8] can get to him. Few people know this, but DJ actually enshrines a double personality: the serious, silent, measured Dirk on the one hand and the laughing, passionate, southern version of him that you can only unlock after a critical content of alcohol. Not many have witnessed the latter, but I can guarantee it exists. Dirk, thank you for your well-balanced thoughts, for taming my southern spirit from time to time, all the translations, advice, the wild Scheveningen[9] experience(s, I hope), for being the symbol of organisation, efficiency and collaboration. You are a person with an undoubtedly bright future, so all I'm going to wish you is hodl!

The paranymph-in-law, the officemate of many names[10] – sharing an office with her was nothing short of harmony. Our story can be generally divided into two parts: the first few months, when she was being constantly agonised by my phone calls, and the rest, when she bought noise-cancelling headphones. Talking to her required breaching not only this auditory, but also a visual barrier, a set of perfectly aligned monitors that compelled me to put both hands in the air when I wanted to establish communication. Nevertheless, once on board, the big-hearted designer of quantum matter was always eager to talk, help, laugh, give counsel and, from time to time, exchange a rumour or two. Maf, thank you for all the advice for plots, colours, words, science, finance, fashion, presents, jobs, for all the deep discussions about life, for not panicking at my "alla(o)" and for not physically harming me for 3 years.

Papa Max, the man of a thousand smiles, with a disturbingly similar personality to my own was one of the people I shared my deepest thoughts with. Maximilian, thank you for helping us integrate faster, thank you for not killing when we complained about your country and thank you for being the first Dutch who took me as one of your own. I'll be patiently waiting for "Where is Max? Episode 2". Riki, thank you for the best laughs, the private phytology lectures, the IFFR movie selections, the MED gatherings and the amazing parties!

Now the post-docs. First in line is the eldest, our French Silent Bob - Julien. While you failed to teach my amorphous body the art of parkour, I learned a lot from you about life, society and philosophy. You drastically influenced my perception on many global issues. Thank you for being one of my life mentors. Holger, the overly objective and blunt Deutsch with a great heart, our Dalai Lama. I was delighted to spend countless hours with him, both in his office and in Bebop. He was the ultimate checkpoint of wisdom before anything got out; for if Holger gives you the nod[11], then you are good to go. Conversely, you would hear: "this is crap", which usually meant "proceed at your own risk". Needless to say, this piece of text was also run by him. Upon careful inspection, he noticed that the holy grail of his research, the SMIM of all SMIMs was missing from the text. Normally I don't work with orders, but I got a sense of superstition in his remarks. Therefore, I feel obliged to say it: it will never work Holger! Just kidding, how can it not work with such a team behind it. I feel that your terahertz beast is well on its way and

---

[8] with a higher salary
[9] It was actually Rotterdam, wasn't it?
[10] vulgarly reduced to Maf
[11] Happens very rarely.

I can't wait to see how it reacts to percolation (speaking of which, Matvey I'm confident you'll make the most sophisticated SMIM tips!). What I'm worried about a bit is the spin entropy. By now you are probably so sick of my BS, so I will have to leave you with this. Ale, you had to suffer Santi and myself through our scientific puberty. Thank you for always listening me out, for the continuous support and the wisest advice and for taking such good care of us.

Joshua, thanks for the double tribute in your thesis. I'm sure your name will also recur below in the text. Nicola, our joint publication was arguably the toughest academic achievement of all times. For working together with me and for all the deep conversations outside working hours I am very grateful. Andres, you served and will serve as my example for efficiency and vision. I wish you best of luck in your career and I thank you for the trust you had in me, even though we didn't manage to really work on a project together in the end. I still owe you a SL MoS_2 on a cantilever, which I promised to deliver until Christmas, not specifying the year. Daniel and Mark, thank you for all the long explanations of cavity QED, CPWs, fitting and data analysis. You'll always be my resonator gurus. Richard, you are one of the people who suffered me for rather long (until you moved offices that is). Always available for help, extremely knowledgeable and very friendly. I hope your scientific endeavours continue to flourish in the future. Mickaël spent more time at MED than many of the PIs, which is why he is a constituent part of its spirit. Mike, thanks for the skiing, the French food, the nice photos and thanks for showing us that *cum laude* is an achievement that can actually be unlocked. Mark (the German one), your precious laugh left a permanent trace in the auditory cortex of my brain, which I want to believe was for the best. For if not you, who else would I explore the boundaries of humour with? Stay German, stay smart, and, most importantly, take care of Makars and Martin for me, will you? Alessandro, a big grazie for showing me that one can do science and stay normal and for having confidence in me. Enrique, stay pure. Dima, best of luck with your research. Srijit, oh you are a PI now, I forgot... Anyway, keep up the great work!

MED (QN) has one of the best and most diverse line-up of PIs in the world, some of which I had the pleasure of interacting with. Teun, a man of legendary wisdom, boundless knowledge, wit and charm. I am proud to say that through you I am three-handshakes away from the most powerful people in the world. I want to be you when I get wise. Kobus, you have been entrusted with a big task: bringing the restructured MED to new heights. I am certain you will sustain the great spirit of the group. Simon, it was a pleasure teaching with you. Sorry for constantly bugging you with questions, I hope you finally found your peace on the first floor. Andrea, thank you for introducing me to the world of complex oxides and all the one-on-one lectures. Diana, thank you for cheering up the group and helping us get through the the tough Dutch winters. Sander, thanks for your balanced opinions, for your correctness and for taking good care of MED. Anton, thank you for your burning spirit and your brilliant mind. Gao, thank you for all the opportunities and the great respect. Sonia and Toeno, my best wishes for your new beginnings.

A very important role was played by a group of wonderful people who made me proud of my nationality. Marko, Marija, invading your place for 3 long weeks felt so bad at the time, but looking back it was probably one of the best things that could happen to me. Ivo, Ufo, Goce[12], I cannot thank you enough for taking such good care of me. Thank you all for being my family.

A big thanks to the eighty+ friends from back home and from all around the globe who visited me during the last four years (some of them more than once): you made me feel loved and made my time here even more delightful. An even greater gratitude to the ones who decided to come all the way from Skopje (+ Delcevo, London, Frankfurt): Dale, Ljubo, Vic, Filjo, Denka, Marice, Iva, Ljupko, Rosica and Jasna & Nenad[13], to support me during the showdown[14].

Davor, through you I realised that the success of others can be sweeter than your own. Thank you for making me the proudest cousin in the world. Dado, thank you for being an uncle and a friend. Thanks to all my lovely grandparents who have always believed in me. To my sister, Nadja, for being my best friend and for bringing Eli along; it means a lot to me. Nena, Stefan, thank you for your unreserved trust and constant appraisal. Thanks to all the friends of my parents who live in the Netherlands for treating me like their own child.

Halfway through my PhD I was joined by my better half, the sweetest creature on Earth, who has offered me her indispensable support throughout the entire journey. Magdush, thank you for enduring me in good times and bad, for the unconditional love, for the inspiration, patience, trust and harmony.

Finally, there are two people without whom I would not be here (at all). The first one is my mother, who constantly gave me love, motivation, inspiration and support and genuinely contributed to Chapter 7. The second one is my father, whose love, charisma, advice and encouragement helped me push further. Without them I would not have made it this far.

Delft, January 2018

---

[12] ma koj te vrti ustvari

[13] for the initiative

[14] A warm welcome and deep gratitude to the ones who I might have left out and to the ones coming from all over the Netherlands.